Investigation of Sub-Systems for Dynamic Wavelength-Routed Optical Networks

Benjamin James Puttnam

Submitted to University College London for the degree of Ph.D.

Department of Electronic and Electrical Engineering

University College London

March 2008

ProQuest LLC
789 East Eisenhower Parkway
P.O. Box 1346
Ann Arbor, MI 48106-1346

I, Ben Puttnam, confirm that the work presented in this thesis is my own. Where information has been derived from other sources, I confirm that this has been indicated.

Abstract

This thesis describes an investigation of technologies and sub-systems required for physical layer implementation of a range of dynamic wavelength-routed optical networks with a specific focus on acknowledged optical-burst-switching (OBS) architectures where burst lengths are expected to be in the millisecond regime. The key sub-systems are identified and examined both individually and in terms of their interoperability. The feasibility of the existing sub-system technologies is investigated and new control systems are developed where appropriate.

The initial focus is the tunable transmitter required to provide wavelength agility at the network edge. The switching operation of fast widely tuneable lasers is investigated in the context of dynamic optical networks. Using novel probe channel BER measurements, it is shown that additional control systems are required to provide adequate wavelength stability and prevent crosstalk caused by spurious modes excited during the switching process. Based on these findings, a tunable burst transmitter using SOA blanking and a wavelength locking control loop is developed and its performance is described.

Next, the reception of the transmitted bursts is explored and the operation and characterisation of the first 10Gb/s digital burst-mode receiver is described. The receiver uses an AC-coupled photodiode, asynchronous digital sampling at 20GS/s and digital signal processing for clock and data recovery. The investigation reveals that the burst-to-burst dynamic range is ultimately limited by quantization noise and methods to improve the dynamic range are investigated and implemented.

In the core network, an experimental investigation of optically gain-clamped erbium-doped-fiber-amplifiers shows that the optimum feedback cavity designs depends on a trade off between gain transient suppression and reduced signal gain. Cascaded operation is investigated using an experimental OBS link model comprising burst-mode transmitter, receiver, amplifier and router within a recirculating transmission loop. These experiments reveal the importance of network size in feedback cavity design and that, for small networks, the use of the adaptive threshold receiver may negate all gain clamping requirements and allow maximum signal gain.

Acknowledgements

The work presented in this thesis would not have been possible without the efforts and talents of many people who deserve my sincere thanks. Firstly, I owe my thanks to my supervisor, Polina Bayvel. I am grateful for being given the opportunity to join such a talented group, for the discussions on how to conduct research, amongst many other subjects, and for all the guidance and support along the journey. In addition, I also thank her for encouraging me to attend many meetings and conferences, finding collaborators, arranging funding (EU Nobel, EPSRC and Marconi) and so much more. I wish her and her family all the best.

I am indebted to Benn Thomsen from whom I learnt a great deal about how to do experiments and apply an engineering perspective to all situations. His wide ranging knowledge, enthusiasm and skill, particularly with the burst receiver software made all of the work in the latter part of this thesis possible. I would also like to thank Michael Düser. His work provided the background for the project and his vision, knowledge and patience helped me through the transition back to university and let me believe what was possible. I am pleased to have had the opportunity to work with both of them.

I have been fortunate to undertake collaborative work with a number of visiting researchers during my time here. I am grateful to Alessandro Bianciotto, whose control loop modelling and electronics skills made the implementation of the burst-mode transmitter possible and whose squash skills lead to the creation of the White 8 Trophy. He also developed a simulator used to investigate analogue burst receiver schemes. Thanks are also due to Alicia Lopez with whom I worked primarily on burst amplification but who also contributed to the work on both the transmitter and receiver. I am also grateful to Cyril Renaud, with whom I worked on tunable lasers and who was always the first stop when experiencing unusual laser behaviour was observed in the lab. I would also to thank ONGs industrial collaborators from Bookham Technologies in Caswell. In particular, David Robbins, Neil Whitbread, Giacinto Busico and Lalitha Ponnampalam, for their tunable laser expertise and the donation of devices that enabled made much of the work. Additionally, despite some dubious musical

choices, I would like to thank Giancarlo Gavioli for his help with the transmission experiments and for providing a logical opinion in times of stress. Equally, to Yannis Benlachter who also assisted with these measurements and in many other areas, not least in printing this thesis! I would also like to thanks Vitaly Mikhailov for his help in using the free-space grating router and to Raimund Mückstein for his recent tunable laser work.

In addition to those above, there also need to thank many of the people with whom I have shared an office, lab space and, most importantly, a kettle with during my time at UCL. Andrea Del Duce, Yannis Benlachter, Chin-Pang Lui, Shamil Apparturai, Alejandra Zapata, Phil Watts, Seb Savory, Lamia Baker, Robert Killey, John Mitchell and Darren Shea. These people have provided fruitful discussion, lab equipment, computer support and much more, making everyday life in the Roberts Building an enjoyable time. I would also like to thank Scott Landers and everyone at the ULU football league for providing a welcome distraction.

Outside of UCL, I would like to thank my parents, my proud grandmother and all my family for supporting me in everything I choose to do, for always providing me somewhere else to go and for all of the wonderful cooking. I always appreciate being with them and cherish the memories of all the family occasions. Equally, I am grateful to Eva for her help, understanding and ability to make me appear punctual. She was always supportive and talking to her made the difficult moments easier. Finally, I would like to thank all my friends that have made these years so much fun. Tom, K and co. from the Patty Winters Show and all of The So Salad Crew; Christmas Holiday, Rik Van Der Magnum, Tony One Peroni, Elmo, Abbey, Pling, Catherine, Wuss, Dan, Kate, Nick, Ralph, Andrew. I love you all.

Contents

List of tables

List of figures

Abbreviations

AC	Alternating current
ADC	Analogue to digital conversion
AGC	Automatic gain control
AOGC	All-optical gain-clamping
APD	Avalanche photodiode
ASE	Amplified spontaneous emission (noise)
ATM	Asynchronous transfer mode
AWG	Arrayed waveguide grating
BER	Bit-error rate
BERT	Bit-error rate test set
BLW	Baseline wander
BMRx	Burst-mode receiver
C-band	Communications band
CDR	Clock and data recovery
CID	Consecutive identical digits
CIE	Carrier induced effects
CW	Continuous wave
DA	Differential amplifier
DAC	Digital to Analogue converter
DBMRx	Digital burst-mode receiver
DBR	Distributed-Bragg-reflector
DC	Direct current
DCF	Dispersion-compensating-fibre
DFB	Distributed feedback (laser)
DG	Data generator
DON	Dynamic optical network
DPSK	Differential phase shift keying
DS-DBR	Digital supermode-distributed-Bragg-reflector
DSP	Digital signal processing
EDFA	Erbium-doped-fibre-amplifier
EPON	Ethernet passive optical network
FBGs	Fibre Bragg gratings
FCL	Feedback cavity loss
FEC	Forward error correction
FP	Fabry-Perot
FPGA	Field programmable gate arrays
FPI	Fabry-Perot interferometer
FSR	Free spectral range
FTTH	Fibre-to-the-home
GC	Gain control

GC-EDFAs	Gain-clamped-erbium-doped-fibre-amplifier
GCSR	Grating coupler with rear sampled-grating reflector
GPIB	General purpose interface bus (IEEE-488)
I	Integral (control)
IC	Integrated circuit
ITU	International Telecommunication Union
ITU-T	ITU-Telecommunication Standardization
JET	Just-enough time
JIT	Just-in-time
LA	Limiting amplifier
LDC	Laser diode controller
MEMS	Micro-electrical-mechanical system
MG-Y	Modulated grating-Y branch
MZI	Mach Zender Interferometers
NOBEL	Next generation optical network for broadband European leadership
NRZ	Non-return-to-zero
OBS	Optical burst switching
OCS	Optical circuit switching
OEO	Optical-electrical-Optical
OIPLL	Optical injection phase-locked-loop
OPS	Optical packet switching
OSA	Optical spectrum analyzer
OSNR	Optical signal-to-noise ratio
PCB	Printed circuit board
PD	Photo diode/detector
PI	Proportional-Integral (control)
PID	Proportional-Integral-Differential (control)
PLC	Planar lightwave circuit
PON	Passive optical network
PPG	Pulse pattern generator
PRBS	Pseudo-random-bit-sequence
QCSE	Quantum confined Stark effect
RC	Resistance/capacitance
RF	Radio frequency
RO	Relaxation oscillations
Rx	Receiver
RZ	Return-to-zero
SD	Standard deviation
SG	Sampled grating
SG-DBR	Sampled grating-distributed-Bragg-reflector
SHB	Spectral hole burning
SMF	Standard single-mode fibre

SMSR	Side mode suppression ratio
SOA	Semiconductor optical amplifier
SONET/SDH	Synchronous optical networking/ Synchronous digital hierarchy
SSG-DBR	Super structure grating-distributed-Bragg-reflector
SSPF	Steady state power fluctuation
TDM	Time division multiplexing
TEC	Temperature controller
TIA	Transimpedance amplifier
Tx	Transmitter
UCLF AWG	Uniform-loss cyclic-frequency arrayed waveguide grating
VCSEL	Vertical cavity surface emitting laser
VGA	Variable gain amplifier
VOA	Variable optical attenuator
WDM	Wave division multiplexing
WLL	Wavelength locking loop
WR-OBS	Wavelength-routed optical burst switching
WRON	Wavelength-routed optical network
8B/10B	8 bit to 10 bit (coding)

Chapter 1 Introduction

1.1 Optical networking

Optically-routed communication networks on a metro or national scale form the solution to the increasing demand for high bit rate services. They exploit the huge transmission capacity of optical fibre and WDM systems whilst providing the versatility of optical routing. The amount of global data traffic carried by telecommunications networks is already measured in exabits (10^{18}) per second with predicted annual growth rates ranging from 20% to 100% [Des06, Lee06, O'Ma06, Yoo06, Fro06, Des05, Tel03, Cof02]. Additionally, short-term growth exceeding 400% is occurring in some geographical areas [Des06, Tel06] while some European operators are predicting that 50% of their revenue will be from data traffic as soon as 2010 [Lee06].

At the consumer level this growth is driven by the emergence of bandwidth hungry network applications such as interactive TV, grid computing, data storage, video-on-demand, online gaming and multimedia-conferencing [Czy06, O'Ma06, Bra06, Cav05, San04, Wei03]. In addition to the residential and business customers familiar to traditional communication networks, high bandwidth fibre based networks will also be required to accommodate scientific users currently using custom dedicated network resources for demanding research applications that require processing by distributed computing resources. In particular, the next generation of radio interferometers, the low frequency array, square kilometre array and the very long base interferometer [Ast07, Smi00] will require data transmission rates up to Tb/s on demand with guaranteed resource availability and data transfer on a similar scale may also be required for particle physics experiments at collaborative particle accelerators such as CERN [Par07].

The demand for high bandwidth services from residential and business users has led to rapid growth in data access networks with significant international roll out of fibre-to-the-home (FTTH) reaching speeds of 100Mbit/s in countries such as Japan [Bra06, Dus05, Shi04, Jhu03]. In the network core the demand for capacity has been met by moving away from traditional time division multiplexed (TDM) used in SONET/SDH networks operating with a single

channel per fibre to wavelength division multiplexing (WDM) with up to 80 optical channels to improve the efficiency of deployed fibre [Des06, Siv04, Col03, Fal02, Shi00, Mar96]. Meanwhile in research labs transmission capacity in excess of 10Tb/s has been demonstrated for a single fibre [Gna08, Nak07, Fri02, Var02], highlighting the potential of optical fibre communication to meet the ever growing demand for bandwidth.

In order to fully exploit the traffic-carrying potential of optical fibre-based networks it is advantageous to utilise WDM for more than a point-to-point transport systems and perform network functions such as routing and switching without limiting the throughput. Conventional electronic processing is unlikely to be able to match the potential offered by optical WDM due to heat dissipation and power consumption which grow exponentially as router sizes scale upwards [Ber06, Tuc06a/b, Nei05, Muk00], although there is some evidence that electronic routing may be able to keep pace with fibre carrying capacity [Tuc06a/b]. Indeed, the growth rate of electronic routers followed Moore's law throughout the 1990s with an average growth rate of 46% compared to 73% for optical transport [Tar00], and there is, as yet, no sign of this trend levelling out. The additional cost of optical-electronic-optical (OEO) conversion required to combine optical transport with electronic routing together with the forecast traffic growth has driven research into new WDM based all-optical networks where signals may be routed according to carrier frequency and remain in the optical domain.

All-optical WDM networks have the advantage of eliminating costly OEO conversion whilst being transparent to bit rate, modulation format and protocol. However, in the absence of mature optical processing and buffering technology [Won06, Kun06, Ber06, O'Ma06, Nei05, El-B02], all-optical networks cannot offer the same functionalities as their electronic counterparts and new network architectures, ideas and systems are required to fully exploit the optical bandwidth.

1.2 Static vs dynamic networks and related timescales

A number of approaches to optical networking have been proposed with the simplest being static, or quasi-static, wavelength-routed optical network

(WRONs) where light-paths are set up between node pairs, analogously to conventional circuit-switched telephony, with electronic buffering and processing taking place at the network edge. Such networks have a number of attractive features. The creation of quasi-permanent light paths means WRONS ensure zero blocking probability [Bar97a] for a stable traffic matrix and they do not require wavelength agility, and hence fast-tunable lasers at the network edge, although they may be used to improve performance by increasing resilience [Bar97b]. Since the traffic demand is fixed, optimised wavelength and resource allocation can be performed offline, allowing for efficient use of network resources. It has also been shown that performance is not significantly improved by including wavelength conversion in the network core, making such networks relatively simple to operate [She04, Ass02, Bar97].

However, the nature of WRONS means that resource allocation is only possible in units of whole wavelengths which can cause resource utilization inefficiency which may outweigh the advantages of quasi-static WRONS, particularly for networks with varying traffic demands. Idle periods in data paths allocated a permanent connection, or, mismatches between the bit rate of the light-path and the transmitter, mean allocated bandwidth can be wasted. Additionally, it is believed that the largest cost of the wavelength granularity occurs for cases where the traffic demand may change significantly over short time intervals [Gon05, Err02]. For such cases, as predicted for future data driven networks, the static network would need to be heavily over provisioned to be able to meet the maximum traffic demand at each point in the network with acceptable network resilience [Koz03, Düs05, Bha01]. The desire to overcome the static allocation inefficiencies has driven much research in to dynamic WDM based optical networks to utilize the available bandwidth with greater efficiency by allowing data to be assigned to fractions of wavelengths. As with the replacement of circuit-switched telephone networks with packet-based core networks in existing voice and data networks, it is widely believed that splitting wavelength in to smaller units, usually called packets or bursts, could potentially provide the same service quality as that of a static network with far fewer resources [Lel06, Düs05, Ger03, Sen03, Ass01, O'Ma01, Zan01, Hun00, Spa00].

Dynamic networks are generally defined by the reconfiguration timescale. WRONs may be considered similar to optical circuit switching (OCS) and reconfigurable over the longest timescales, (for example hours to days) [Dus05]. At the opposite end of the spectrum with the highest resource granularity is optical packet switching (OPS). OPS, in its purest form, is the long-term aim of dynamic optical networking with the ultimate goal for today's internet protocol (IP) dominated data plane being true IP-over WDM where ingress IP packets are routed across all-optical IP networks with minimal electronic processing. Between these 2 groups is optical burst switching (OBS) which refers to architectures where ingress packets are aggregated into larger 'bursts' at the network edge but may equally be considered as fast reconfigurable OCS. The main network architecture categories are summarised in Figure 1-1, which shows the projected evolution of dynamic optical networking as has been defined by the Next Generation Optical Network for Broadband European Leadership (NOBEL) European Union Project. NOBEL is a research collaboration between industrial and academic partners into future evolution of European transport networks in terms of architectures, traffic engineering, economics, control plane and transmission technology [Car05].

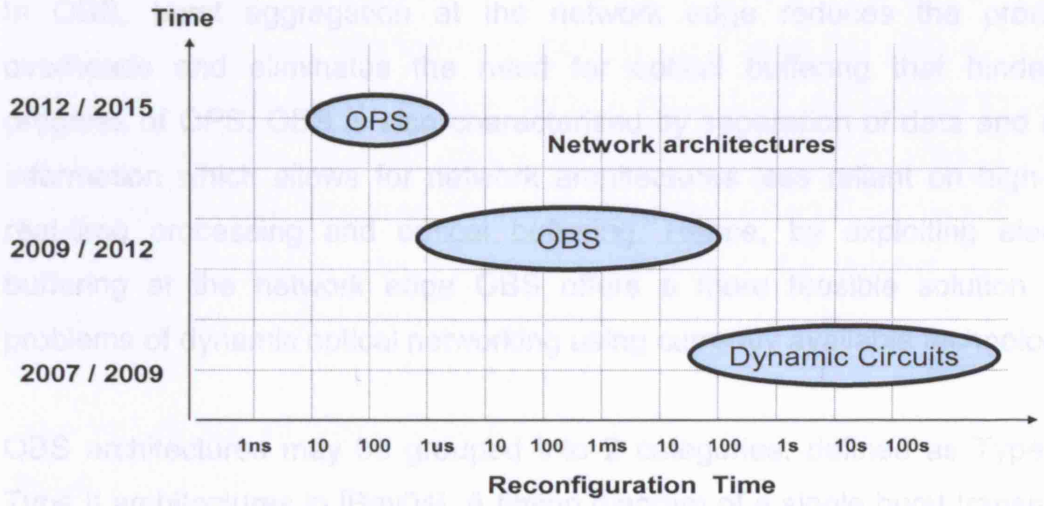

Figure 1-1 Evolution of optical networking and resource granularity for EU NOBEL project

OPS is the optical equivalent of electronic packet switching where packets are forwarded on a packet-by-packet basis depending on available resource with packets originating from the same node able to take different paths to the same destination. The header containing the control information is read to extract its destinations and the payload is held in memory until sufficient resource is

available. Aside from improved transmission speed the advantage of OPS, compared to its electronic counterpart, is the transparency to the payload data. Since router line-cards only need to be configured to read packet headers, a wide variety of payload bit rates and formats can be supported simultaneously.

Although OPS networks provide the finest bandwidth granularity and potentially offer efficient resource utilization, they can not be easily implemented. The technical issues currently preventing pure all-optical packet networks are varied and include the lack of adequate optical buffering (or memory), wavelength conversion across the C-band and scalability of optical packet switches able to operate on the nanosecond timescale required to send IP packets at current transmission speeds [Yoo06, Kun06, Nie05, Tuc05, Won03, O'Ma01, Hun00, Tar00, Hun98]. However, the potential benefits of OPS mean that overcoming these technical challenges is the focus of widespread research. To date, experimental demonstrations have been reported with header processing carried out in the optical domain [Ran06, Wol06, Pou06, Jeo03] or electronically [Gau05, Xue04, dit03 Whi03, Gui00, Hun99].

In OBS, burst aggregation at the network edge reduces the processing overheads and eliminates the need for optical buffering that hinders the progress of OPS. OBS is also characterised by separation of data and control information which allows for network architectures less reliant on high-speed real-time processing and optical buffering. Hence, by exploiting electronic buffering at the network edge OBS offers a more feasible solution to the problems of dynamic optical networking using currently available technology.

OBS architectures may be grouped into 2 categories, defined as Type I and Type II architectures in [Bay04]. A timing diagram of a single burst transmission is shown for both architecture types in Figure 1-2 and the burst assembly times and burst sizes predicted from the key theoretical studies of both types of OBS schemes are shown in Table 1-1.

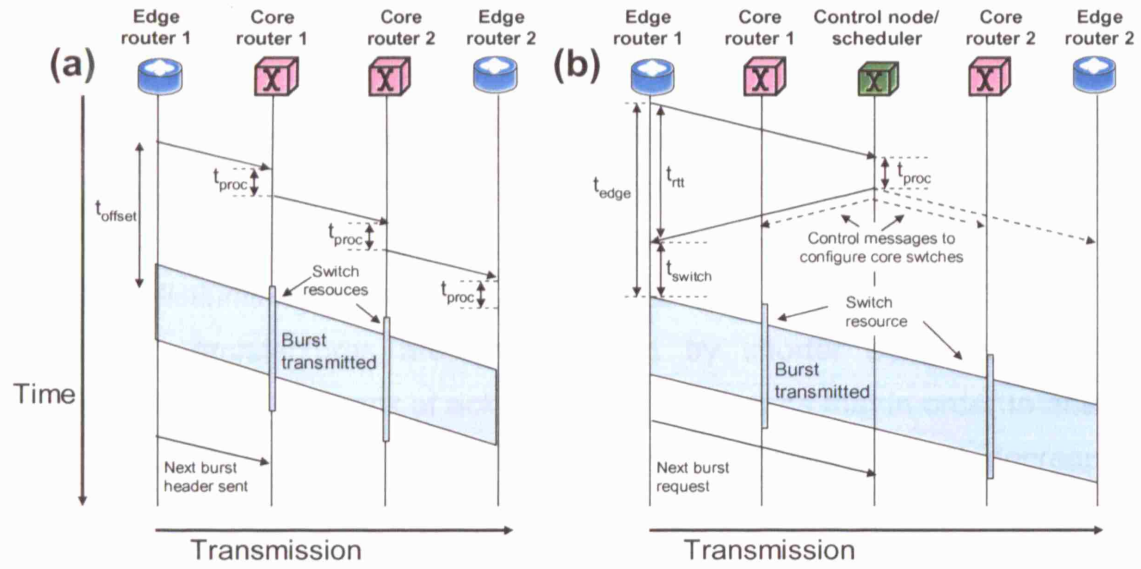

Figure 1-2 Timing diagram of burst transmission in (a) Type I OBS network and (b) Type II OBS network

Type I OBS networks, Figure 1-2(a), differ from the OPS networks in that control information recorded in the header of optical packets is sent from the edge routers ahead of the payload, on a specific control channel, to configure the network in advance of burst transmission, [Tur99, Qia99]. For example in the Just-Enough-Time (JET) architecture [Yoo97,Yoo99] packets/bursts are accumulated until they reach a set threshold of time or size at which point a control packet is sent into the network to pre-configure the core routers. The burst payload is then transmitted some time (t_{offset}) later and passes through the network without the need for optical buffering. The minimum offset time for a given packet can be calculated in terms of the time taken to process the control packet and allocate a free wavelength (t_{proc}) and the number of hops (N) between the source and destination nodes:

$$T_{offset}\,(\min) = t_{proc}.N \qquad (1.1)$$

However, additional offset times may be added to increase the probability of arrival.

Table 1-1 Timescales of burst lengths and sizes in OBS schemes

OBS scheme	OBS Type	Burst Length	Burst size @40GB/sec	Burst size @10GB/sec	Ref
Horizon	I	0.2 μs	1 kB	250B	Tur99
JET	I	3.1 μs	15 kB	3.75kB	Yoo00
Adaptive Periodic Burst	I	0.1-1 ms	0.5-5MB	0.125-1.25MB	Dus02b
JIT	II	2.5μs– 250s	12.2kB-1.1TB	3.5kB-275GB	Wei00
WR-OBS	II	5.24 ms	25MB	6.25MB	Dus02a
Segmented OBS	II	25 ms	1 GB	250MB	Vok03

In Type I OBS, there are no acknowledgements of transmitted bursts and if contention occurs in the core routers, the packet is lost without a resend request. This means that a guaranteed quality of service is not possible but the burst loss probability can be reduced if wavelength conversion is used at core routers to reduce contention. The absence of acknowledgements sets an important distinction between these and other OBS architectures. Such 'send and forget' architectures are characterized by shorter burst lengths and aggregation times. The lack of acknowledgement means that in order to ensure a low probability of packet loss, the initial offset times are increased, decreasing the overall network throughput.

This problem is addressed in Type II OBS networks, Figure 1-2(b), which refer to network architectures where the availability of a requested route is acknowledged by the control plane. This idea is typified in the best known such architecture, which is called wavelength-routed-optical burst switching (WR-OBS) [Düs02]. Here, bursts are aggregated at the ingress node according to destination and/or the required class of service until a specified time or capacity threshold is met. A request for reservation of an end-to-end light-path is then sent to a central control node. After a processing time (t_{proc}), the control node assigns a light-path and sends an acknowledgement to the ingress node with the route information and instruction to transmit the burst. If required, the core node also sends control information to the core routers. After this round-trip-time, t_{rtt}, the burst is then transmitted after a further time, t_{switch}, which is the time taken for the transmitter to tune to the correct wavelength. In such a scheme, the resource reservation and acknowledgement ensures there is no burst loss and allows for quality of service guarantees. For this type of architecture the burst assembly process is longer than that of Type I architectures, since its lower limit is set by the sum of the network round trip time and the laser tuning time:

$$T_{edge} = t_{rtt} + t_{switch} \qquad (1.2)$$

For a European size network, $T_{edge,}$ would be of the order of milliseconds. A schematic of a WR-OBS network architecture that typifies Type II OBS is shown in Figure 1-3.

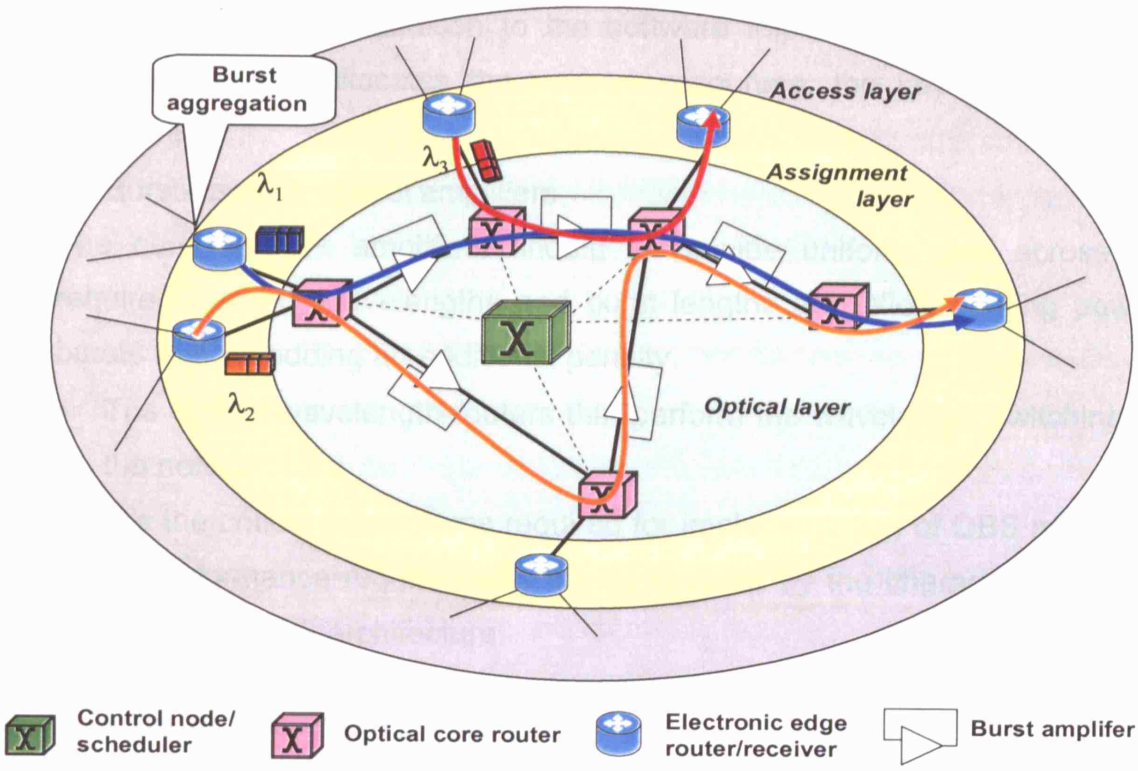

Figure 1-3 Schematic of Wavelength-Routed Optical Burst-Switching architecture

The WR-OBS architecture and OBS networks in general, rely on several key physical sub-systems for successful implementation. Most importantly, located at the network edge these are:

- The tunable transmitter onto which the bursts are assigned

This transmitter must be able to generate a sufficient number of wavelength channels to satisfy network wavelength requirements. Its wavelength-tuning time must be fast enough to satisfy the dynamic network operational requirements, determined, for example, by burst lengths and the edge delays in OBS networks.

- The burst-mode receiver that converts signals back to the electrical domain

The receiver must be able to respond to large power, timing and phase fluctuations of the incoming signal, on a burst-by-burst basis. The receiver should satisfy the appropriate network overhead requirements and burst lengths and place no restriction on the frequency content of transmitted data.

In the network core in addition to the software implemented central control node/scheduler that allocates the network resources, the key physical sub-systems are:

- Burst-capable optical amplifiers

  The core network amplifiers should to provide uniform gain across all required network wavelengths and burst lengths and allow varying power bursts without adding an additional penalty.

- The optical wavelength-routers that perform the wavelength switching in the network core

These are the critical subsystems required for implementation of OBS networks and their performance requirements are determined by the characteristics and timescales of network architecture.

1.3 Aims of research

The work described in this thesis examined the physical layer issues of implementing dynamic optical networking. Its aim was to answer the questions of how dynamic optical networks should be designed. The primary research focus is Type II OBS architectures and in particular WR-OBS. The aim was to complement and test the assumptions made in the large body of theoretical work carried out on WR-OBS, proposed and investigated theoretically at UCL [Zap05, Zap05a, Dus04 Bay04, Zap04, Kos03, Zap03, Zap03a, Dus02, Dus01]. To do this, it was necessary to identify the important design parameters, operation timescales and unsolved issues for each of the key sub-systems described in section 1.2, as defined by the appropriate network architecture. The overall goal of the work was to implement a first experimental model of an OBS link in order to study the interaction of the key sub-systems and understand the physical limits of the constituent devices.

At the transmitter, the key parameter is the time taken to tune to a stable wavelength. For the shorter burst length schemes of Type I OBS networks, the tuning time represents an overhead on each burst and has a direct effect on the network efficiency. For Type II networks, the laser cannot begin to tune until after the round trip-time, t_{rtt} in Figure 1-2(b), of the processed request and acknowledgement. Hence, the tuning time determines the total edge delay (t_{edge}), which directly affects the buffer overflow and burst loss probability

[Düs02]. Whilst switching times in the nanosecond regime, suitable for both OBS flavours have been widely reported, potential sources of impairment arising from the switching characteristics have not been explored in experimental demonstrations. Spurious laser emission which occurs during the switching process has the potential to interfere with other channels in a multi-wavelength network, manifesting itself as channel crosstalk. Similarly, the millisecond burst lengths of Type II OBS schemes require a more detailed consideration of the thermal transients. These transients, which arise from heating effect caused by step changes of tuning currents, need not be addressed in timescales of Type I architectures, shown in Table 1-1, but are critical for Type II architectures where they can extend the time required to tune to a stable wavelength into the millisecond regime. A second important parameter for the transmitter is the tuning range which determines the maximum number of wavelengths available for use in the network.

Equally, the operation of the burst-mode receiver has a direct implication for network efficiency since the size of any required preamble or control bits set the system overhead on each transmitted burst. In addition to minimising the required overhead, the major design problem lies in how the receiver is coupled to the decision-circuit and how this affects the setting of the decision-threshold which, for OBS networks, must be performed on a burst-by-burst basis. A DC-coupled decision-circuit requires fast determination and setting of the decision-threshold for each burst whilst AC-coupled receivers allow for a zero level decision-threshold but lead to large DC-offsets across each burst from the charging and discharging of the coupling capacitor.

In the network core, the key sub-systems are the burst amplifier and wavelength router. The slow gain dynamics of erbium-doped-fibre-amplifiers (EDFAs) mean that input power fluctuations, characteristic of burst data, lead to gain transients that need to be suppressed or compensated for prior to reception, to prevent transmission penalties. These transients are particularly damaging over the timescales of Type II OBS networks since the burst length is the same order of magnitude as the EDFA response time. For the core network routers the cascadabilty, port count and, where appropriate, the reconfiguration time are

the key physical parameters limiting the scalability of dynamic network architectures [Zap03].

Since the primary distinction between network architectures is the timescale over which light-paths are maintained or reconfigured, much of the component technology discussed for OBS networks may be equally applicable to OPS and OCS. Hence, experimental measurements were not only restricted to timescales applicable to Type II OBS network but performed over as wide a range of time scales as possible. Similarly, many of the issues discussed in subsequent chapters are equally applicable to optical access networks. For example, passive optical networks (PONs) rely on multiplexed burst WDM signals or time-division multiplexed (TDM) signals sharing fibres between custom premises and central offices. Like the dynamic network architectures, these schemes also require receivers capable of recovering asynchronously arriving bursts of varying power [ITU03a/b IEEE04] and, in the long reach case, optical amplifiers insensitive to input power variations [She07a/b]. Hence, although not the primary motivation for the work presented, where possible the proposed subsystems are also be discussed in the context of optical access networks.

1.4 Thesis outline

The remainder of this thesis is organised as follows. Chapters 2 and 3 investigate the tunable wavelength transmitters located in the edge routers that are the interface between electronic and optical domains for the incoming data. Chapter 2 assesses the available laser technology and identifies the key physical parameters of interest for OBS applications. An experimental study of the characterization and switching transition of widely tunable multi-section DBR-based lasers quantifies the primary sources of impairment in WDM based networks. The impacts of these impairments, arising from the thermal response to high tuning current switching and the generation of spurious modes during switching, are quantified for the first time. Chapter 3 describes the operation and implementation of a wavelength-locked burst-mode tunable transmitter that is able to compensate for thermally-induced transients and shield the laser output during switching to eliminate the spurious modes identified in chapter 2.

Chapter 4 describes the operation of the first 10 Gb/s digital burst-mode receiver. The receiver is based upon a standard AC-coupled photodiode and asynchronous digital sampling at 20GS/s with clock and data recovery performed in digital signal processing. A full experimental characterization shows the burst-to-burst dynamic range is ultimately limited by quantization noise and methods to improve the dynamic range are investigated and implemented.

Chapter 5 switches the attention to the network core. Burst amplification is investigated and a detailed experimental investigation of optically gain-clamped EDFAs in a realistic network environment is presented. The transmitter and receiver described in the previous chapters are used in a novel experimental set-up which uses BER measurements to determine optimum performance.

This idea is further extended in chapter 6 which considers the interoperability of the 3 key sub-systems described in the previous chapters using an end-to-end. OBS link test-bed. The experimental test-bed allowed the study of accumulated gain transients in a realistic dynamic optical network environment for the first time. The test-bed was used to study the effect of gain transients accumulated across a varying number wavelength-routing nodes linked by amplified fibre spans where bursts are added and dropped at each node. Next, the role of the additional receiver processing in reducing the amount of optical feedback and the inherent BER penalty of burst-mode EDFA operation are also studied. Finally, Chapter 7 presents a summary of the main conclusions of the research and provides suggestions for future work.

1.5 Original contributions of the thesis

The novel contributions of this thesis, as supported by the list of refereed publications in section 1.6, are as follows:

- First investigation of the potential impairments caused by switching crosstalk from tunable lasers in WDM networks [11,12]
- Study of the switching characteristics of semiconductor tunable lasers over the previously unexplored millisecond timescales applicable to acknowledged OBS schemes, where wavelength deviation, due to thermal switching transients, occurs [8-12]

- Development of a wavelength-locked burst-mode transmitter with SOA shuttering, suitable for dynamic optical networks, based on a DS-DBR semiconductor tunable laser [7]
- Experimental development and characterisation of a novel digital 10 Gb/s burst-mode receiver for dynamic optical networks with burst-to-burst dynamic range of 16.5dB [4,5]
- Development of an OBS link test-bed comprising burst-mode transmitter, burst-mode receiver, wavelength routers and amplified fibre spans with burst-adapted EDFAs [1-3]
- Optimisation of optically gain-clamped EDFAs for use in dynamic optically burst-switched network by novel measurements of burst quality factor [2,3,6]
- Demonstration of post-reception digital signal processing to correct for transmission impairments in burst-switched networks [1]

1.6 Publications arising from the work described in this thesis

[1] **Performance of an adaptive threshold receiver in a dynamic optical burst-switched network**
B.J.Puttnam, B.C.Thomsen and P.Bayvel, IEEE Photonic Technology Letters, Vol. 20 (3), pp 228-230, February 2008

[2] **Experimental investigation of optically gain-clamped EDFAs in dynamic optical burst-switched networks**
B.J.Puttnam, B.C.Thomsen, A.Lopez, P.Bayvel. IEEE/OSA Journal of Optical Networking special edition 'Transmission in Optically Transparent Core Networks' Vol. 7 (3), pp 197-207, January 2008

[3] **Optically gain-clamped EDFAs in dynamic burst-switched networks**
B.J.Puttnam, B.C.Thomsen, P.Bayvel. Tech. Proceedings of European Conference on Optical Communication, Sept. 2008

[4] **Optically equalized 10 Gb/s NRZ digital burst-mode receiver for dynamic optical networks**
B.C.Thomsen, B.J.Puttnam, P.Bayvel. OSA Optics Express, Vol. 15 (15), pp 9520-9526, July 2007

[5] **10 Gb/s AC-coupled digital burst-mode optical receiver**
B.C.Thomsen, B.J.Puttnam, P.Bayvel. Tech. Digest of Optical Fibre Communication Conf, paper OThK5, February 2007.

[6] Optically gain-clamped EDFAs for next generation optical amplifiers

A.Lopez, B.J.Puttnam, P.Bayvel. Tech Digest of Opto-electronics conference, Bilbao, 5th-11th March 2007

[7] **Burst-mode operation of a DS-DBR widely tunable laser for wavelength agile system applications**
B.J.Puttnam, A.Bianciotto, M.Düser, B.Thomsen, R.Gaudino, G. Busico, L.Ponnampalam, D.Robbins, N.Whitbread. P.Bayvel, Tech. Digest of Optical Fibre Communication Conf., 05-10 March 2006

[8] **Experimental investigation of the signal degradation in WDM transmission through coherent crosstalk caused by a fast tunable SG-DBR laser**
B.J.Puttnam, M.Düser, P.Bayvel. Tech. Digest of Optical Fibre Communication Conf., Vol. 3, pp 444-446, March 6-11 2005

[9] **Nanosecond channel-switching exact optical frequency synthesizer using an optical injection phase-locked loop (OIPLL)**
C.C.Renaud, M.Düser, C.F.C.Silva, B.J.Puttnam, T.Lovell, P.Bayvel, A.J Seeds. IEEE Photonic Technology Letters, Vol. 6, pp 903-905, March 2004

[10] **Nanosecond switching time, uncooled, zero frequency DWDM source**
C.C.Renaud, M.Düser, B.J.Puttnam, T.Lovell, P.Bayvel, A.J.Seeds. Tech. Digest of Optical Fibre Communication Conf., Vol.1, 23-27 Feb. 2004

[11] **Dynamic optical network architectures for future IP traffic**
M.Düser, B.J.Puttnam, P.Bayvel, N.Nagatsu, Proc. of SPIE International IT Com Information Technology and Communications, Philadelphia, 2004

[12] **Experimental investigation of rapid wavelength-switching (≤80ns) in fast tuneable lasers for applications in optical packet and burst switched networks**
B. J. Puttnam, M. Düser, P. Bayvel, T. Mullane, T. Farrell, and D. McDonald. Proc. London Comm. Symposium, pp. 241–244, London, 2003.
URL:http://www.ee.ucl.ac.uk/lcs/papers2003/index.html

1.7 References

Ass01 **Optical networking and real-time provisioning: an integrated vision for the next-generation Internet**
C.Assi, A.Shami, M.Ali, IEEE Networks magazine, vol. 15 (4), pp 36-45, April 2001

Ast07 **Express Production Real-time e-VLBI Service**
http://www.expres-eu.org/
Square Kilometre Array
http://www.skatelescope.org/
Low Frequency Array
http://www.lofar.org/

Bar97a **Wavelength requirements in arbitrarily connected wavelength-routed optical networks**
S.Baroni and P.Bayvel, IEEE Journal of Lightwave Technology, Vol. 15 (2), pp 242-251, February 1997

Bar97b **Link failure restoration in WDM optical transport networks and the effect of wavelength conversion**

S.Baroni, P.Bayvel, Proc. Optical Fibre Communication 16-21 Feb.1997 pp123-124

Bay04 **Optical burst switching: research and applications**
P.Bayvel, M.Düser, Proc. Optical Fibre Communication, Vol. 2, 23-27 Feb. 2004

Ber06 **Architecture of an integrated router interconnected spectrally (IRIS)**
P. Bernasconi, J.Gripp, D.Neilson, J.Simsarian, D.Stiliadis, A.Varma, M.Zirngibl. Tech. Digest of High Performance Switching and Routing Workshop pp.8 7-9 June 2006

Bha01 **POP-Level and access-link-level traffic dynamics in a Tier-1 POP**
S.Bhattacharyya, C.Diot, J.Jetcheva, N.Taft, Proc. ACM SIGCOMM Internet Measurement Workshop, vol. 1 39-53, San Francisco, USA, November 2001

Bra06 **The missing link - Broadband access networks**
M.E.Bray, M.J.O'Mahony. Tech Digest of IET Access Technologies Conf., 21-22 June 2006 pp 85–88

Cav05 **Achievements of the European NOBEL project**
C.Cavazzoni, A.Di Giglio, G.Edwall, G.Eilenberger, G.Ferraris, H.Haunstein, S.Herbst, M.Jaeger, G.Lehmann, J.F.Lobo, A.Manzalini, S.Santoni, M.Schiano. Tech. Digest of European Conference on Optical Communication , 25-29 Sept. 2005 pp 37-40 vol.5

Cof02 **Growth of the Internet**
K.G.Coffman, A.M.Odlyzko, Optical Fibre Communication – vol. IV-B: Systems and Impairments, Academic Press, San Diego, 2002, pp.17-56

Col03 **Application, design, and evolution of DWDM in Pan-European Transport Networks**
D.Colle, P.Demeester, P.Lagasse, P.Falcao, P.Arijs, IEEE Communications Magazine, Vol. 41 (9), Sept. 2003 pp 48-50

Czy06 **Large-scale multimedia content delivery over optical networks for interactive TV services**
M. Czyrnek, E. Kuzmierek, C. Mazurek, M. Stroinski, Journal of Future Generation Computer Systems 22, pp 1018-1024, 2006

Des05 **Optical communications in 2025**
E.Desurvire.Tech. Digest of European Conference on Optical Communication, pp 5-6 vol.1,25-29 Sept. 2005

Des06 **Capacity Demand and Technology Challenges for Lightwave Systems in the Next Two Decades**
E.Desurvire, Journal of Lightwave Technology, Vol.24 (12), pp 4697-4710, Dec.2006

Dit03 **The European IST project DAVID: a viable approach toward optical packet switching**
L.Dittmann, C.Develder, D.Chiaroni, F.Neri, F.Callegati, W.Koerber, A.Stavdas, M.Renaud, A.Rafel, J.Sole-Pareta, W.Cerroni, N.Leligou, L.Dembeck, B.Mortensen, M.Pickavet, N.Le Sauze, M.Mahony, B.Berde, G.Eilenberger, IEEE Journal on Selected Areas in Communications, Vol. 21, (7), pp 1026-1040, Sept. 2003

Düs02a **Analysis of a dynamically wavelength-routed optical burst switched network architecture**
M. Düser, P. Bayvel, Journal of Lightwave Technology, Vol.20 (4), pp574-586, April 2002

Düs02b **Timescale analysis for wavelength-routed optical burst-switched (WR-OBS) networks**
M.Düser, I.de Miguel, P.Bayvel, D.Wischik. Tech. Digest of Optical Fibre Communication Conf. pp 222 – 224, 17-22 Mar 2002

Düs04 **Investigation of the scalability of dynamic wavelength-routed optical networks**
M. Düser, A. Zapata, P. Bayvel, OSA Journal of Optical Networking Vol. 6, pp667-686, special issue on "Optical Interconnection Networks", September 2004

Düs05 **Investigation of the impact of traffic growth and variability on future network architectures**
M. Düser.Tech. Digest of European Conference on Optical Communication, vol.5, 27-30, Glasgow, Scotland, September 2005

El-b02 **Optical Packet Switching in Core networks**
T.S EL-Bawab, J-D Shin. IEEE Comms magazine September 2002

Err02 **Self-similar traffic and network dynamics**
A.Erramilli, M.Roughan, D.Veitch, W.Willinger, Proceedings of the IEEE, Vol. 90 (5), pp800 – 819, May 2002

Fal02 **Deployment of next generation WDM networks in Europe**
P.Falcao, E.Mannie-Corbisier, M.Moelants P.Noel. Tech. Digest of Optical Fibre Communications Conference 2002, paper TuH4, 45-46

Fri02 **Transmission of 256 wavelength-division and polarization-division-multiplexed channels at 42.7Gb/s (10.2Tb/s capacity) over 3/spl times/100km of TeraLight/spl trade/ fibre**
Y.Frignac, G.Charlet, W.Idler, R.Dischler, P.Tran, S.Lanne, SBorne, C.Martinelli, G.Veith, A.Jourdan, J-P.Hamaide, S.Bigo. Tech. Digest of Optical Fibre Communication Conference pp FC5-1 - FC5-3, 17-22 March 2002

Fro06 **The Future of Transport - Evolution of Network Elements for Packet-oriented Transmission Backbone Networks**
W.Frohberg. Tech. Digest of Telecommunications Network Strategy and Planning Symposium, NETWORKS pp 1-6, Nov. 2006

Gau05 **The physical layer in the WONDER project: toward simplified solutions for packet-based optical networks**
R. Gaudino. Tech. Digest of European Conference on Networks and Optical Communications, vol.1, 194-200, London, UK, July 2005

Ger03 **On the synergy between electrical and optical switching**
O. Gerstel and H. Raza, IEEE Comms. Magazine, Vol. 41 (4), pp 98-104, 2003

Gna08 **25.6-Tb/s WDM Transmission of Polarization-Multiplexed RZ-DQPSK Signals**
A.H.Gnauck, G.Charlet, P.Tran, P.J.Winzer, C.R.Doerr, J.C.Centanni, E.C.Burrows, T.Kawanishi, T.Sakamoto, K.Higuma, Journal of Lightwave Technology, Vol. 26 (1), pp 79-84, Jan.1 2008

Gon05 **Traffic modelling and traffic engineering for next generation transport networks – results from the NOBEL project**
O.González, C.M.Gauger, D.Sass, M.L.García-Osma, A.J.Elizondo-Armengol, B. Puype, I.Lievens, P.Demeester, G.Rétvári, P.Fodor, J.Tapolcai, M.Düser. Tech. Digest of European Conference on Networks and Optical Communications, vol.1, pp 19-26, London, UK, July 2005

Gui00 **KEOPS optical packet switch demonstrator: architecture and testbed performance**
C.Guillemot, M.Henry, F.Clerot, A.Le Corre, J.Kervaree, A.Dupas, P.Gravey, Optical Fibre Communication Conference, Vol. 3, pp204-206, 7-10 March 2000

Hun00 **Approaches to optical Internet packet switching**
D.K. Hunter, I.Andonovic, IEEE Communications Magazine. Vol. 38 (9), pp 116-122, September 2000

Hun98 **Buffering in optical packet switches**
D.K.Hunter, M.C.Chia, I.Andonovic. Journal of Lightwave Technology, Vol. 16 (12), pp 2081-2094, December 1998

Hun99 **WASPNET: a wavelength switched packet network**
D.K.Hunter, M.H.Nizam, M.C.Chia, I.Andonovic. K.M.Guild, A.Tzanakaki, M.J O'Mahony, L.D.Bainbridge, M.F.C.Stephens, R.V.Penty, I.H.White, IEEE Communications Magazine, Vol. 37, (3,) pp 120 – 129, March 1999

IEE04 **IEEE Std 802.3ah: 'Part 3: Carrier Sense Multiple Access with Collision Detection (CSMA/CD) Access Method and Physical Layer Specifications** 2004

ITU03a **Broadband optical access systems based on Passive Optical Networks (PON)**
ITU-T Recommendation G.983.1 International Telecommunication Union 2003

ITU03a **Gigabit-capable Passive Optical Networks (GPON)**
ITU-T Recommendation G.984.1 General characteristics, International Telecommunication Union 2003

Jeo03 **Demonstration of all-optical packet switching routers with optical label swapping and 2R regeneration for scalable optical label switching network applications**
M.Y.Jeon, Z.Pan, J.Cao, Y.Bansal, J.Taylor, Z.Wang, V..Akella, K. Okamoto, S.Kamei, J.Pan, S.J.B. Yoo. Journal of Lightwave Technology, Vol. 21 (11) pp 2723 – 2733, November 2003

Jhu03 **Fibre access network for India as India poises for growth**
A. Jhunjhunwala, IEE Proceedings on Circuits Devices and Systems, Vol. 150, (6), pp 467-472, Dec. 2003

Koz03 **Link failure restoration in wavelength-routed optical burst switched (WR-OBS) networks**
E.Kozlovski, P.Bayvel. Tech. Digest of Optical Fibre Communications Conf., pp 222-223, 23-28 March 2003

Kun06 **Enabling technologies for next-generation optical packet-switching networks**
Chang Gee-Kung, Yu Jianjun, Yeo Yong-Kee, A.Chowdhury, Jia. Zhensheng

Proceedings of the IEEE, Vol. 94 (5), May 2006 pp 892-910

Lee06 **Fibre to the Home Using a PON Infrastructure**
C-H. Lee, W.V.Sorin, B.Y.Kim. Journal of Lightwave Technology, Vol. 24 (12), pp 4568-4583, Dec. 2006

Mar96 **Africa ONE: the Africa optical network**
W. Marra and J. Schesser, IEEE Communications Magazine, Vol.34, pp50-57, 1996

Muk00 **WDM optical communication networks: progress and challenges**
B. Mukherjee, IEEE Journal of Selected Areas in Communications, Vol. 18 (10), pp 1810-1824, 2000

Nak07 **Terabit OTDM transmission Key challenges**
M.Nakazawa, T.Hirooka, Digest of the IEEE/LEOS Summer Topical Meetings, pp 230-231, 23-25 July 2007

Nei05 **Ultra-high capacity optical IP routers for the netwrks of tomorrow: IRIS project**
D.T.Neilson, D.Stiliadis, P.Bernasconi. Tech. Digest of European Conference on Optical Communications, vol.5, 45-48, Glasgow, Scotland, September 2005

O'Ma01 **The application of optical packet switching in future communications networks**
M.J.O'Mahony, D.Simeonidou, D.K.Hunter, A.Tzanakaki, IEEE Communications Magazine, Vol. 39 (3), pp 128-135, March 2001

O'Ma06 **Future Optical Networks**
M.J.O'Mahony, C.Politi, D.Klonidis, R.Nejabati, D.Simeonidou. Journal of Lightwave Technology, Vol. 24, (12), pp 4684 – 4696, Dec. 2006

Par07 http://www.eurekalert.org/pub_releases/2005-12/dnal-hep120605.php

Pou06 **Burst-mode 10 Gbps optical header recovery and lookup processing for asynchronous variable-length 40 Gbps optical packet switching**
H.N.Poulsen, D.Wolfson, S.Rangarajan, D.J.Blumenthal. Tech. Digest of Optical Fibre Communication Conference, Anaheim, CA 2006

Qia99 **Optical Burst Switching (OBS) – a new paradigm for an optical internet**
C. Qiao, M. Yoo. Journal of High Speed Networks, Vol.8, pp 69-84, 1999

Ran06 **End-to-end layer-3 (IP) packet throughput and latency performance measurements in an all-optical label switched network with dynamic forwarding**
S.Rangarajan, H.N.Poulsen, P.G.Donner, R.Gyurek, V.Lal, M.L.Masanovic, D.J.Blumenthal. Tech. Digest of Optical Fibre Communication Conf. Vol. 3, 6-11 March 2005

San04 **Sandvine trend analysis**
Sandvine Intelligent Broadband Networks, December 2004, available at http://www.sandvine.com/solutions/gaming_trend.asp

Sen03 **Switched optical backbone for cost-effective scalable core IP networks**
S.Sengupta, V.Kumar, D.Saha. IEEE Communications Magazine, Vol. 41 (6), pp 60-70, June 2003

She04 **Lighting fibres in a dark network**
F.B.Shepherd, A. Vetta. IEEE Journal on Selected Areas on Communications, Vol. 22 (9), pp 1583-1588, September 2004

She07/a **A 10-Gb/s 1024-Way-Split 100-km Long-Reach Optical-Access Network**
D.P.Shea, J.E,Mitchell. Journal of Lightwave Technology, vol.25, (3), pp.685-693, March 2007

She07/b **Long-Reach Optical Access Technologies**
D.P.Shea, J.E,Mitchell, IEEE Network magazine, vol.21 (5), pp.5-11, Sept.-Oct. 2007

Shi00 **Fibre optic communication systems in Japan**
H. Shinohara. Tech. Digest of 13th Annual Meeting of IEEE Lasers and Electro-Optics Society, vol.1, pp 3-4, Puerto Rico, November 2000

Shi04 **Broadband Access in Japan – Rapidly growing FTTH Market**
Optical Fibre Communication Conf Market Watch, Atlanta Georgia 2004

Siv04 **Optical fibre networks and systems in India**
K.N.Sivarajan. Tech. Digest of Optical Fibre Communication Conf. Los Angeles, vol.1, pp 705-706, 2004

Smi00 **Data highway to the stars**
B.Smith. IEE Review, Vol. 46, (2), pp 15–18 March 2000

Spä00 **Dynamic routing and resource allocation in WDM transport networks,**
J. Späth. Computer Networks, Vol. 32, pp 519-538, 2000

Tar00 **Next generation DWDM networks: demands, capabilities and limitations**
S.Tariq, M.K.Dhodhi, J.C.Palais, R.E. Ahmed. Tech. Digest of Canadian Conference on Electrical and Computer Engineering, Vol, 2, pp1003 – 1007, 7-10 March 2000

Tel03 **Analysts see Internet traffic to explode**
TelecomWeb, March 2003, available at http://www.telecomweb.com

Tel06 www.telegeography.com

Ten05 **A detailed analysis and performance comparison of wavelength reservation schemes for optical burst switched networks**
J.Teng, G.N.Rouskas, Photonic Network Comms, Vol. 9 (3), pp311-335, 2005

Tuc05 **Slow-light optical buffers: capabilities and fundamental limitations**
R.S.Tucker, K.Pei-Cheng C.J.Chang-Hasnain. Journal of Lightwave Technology, Vol. 23,(12), pp4046 – 4066, Dec. 2005

Tuc06/b **Petabit-per-second routers: optical vs. electronic implementations**
R.S.Tucker. Tech. Digest of Optical Fibre Communication Conf, pp3, 5-10 March 2006

Tuc06a **The Role of Optics and Electronics in High-Capacity Routers**
R.S.Tucker, Journal of Lightwave Technology, Vol. 24 (12), Dec. 2006 pp4655-4673

Tur99 **Terabit burst switching**
J. Turner, Journal of High Speed Networks, Vol.8, pp 3-16, 1999

Var02 **Terabit transoceanic system assessment with industrial margins using 25 GHz channel spacing and NRZ format**
G.Vareille, O.Ait Sab, F.Pitel, J.F.Marcerou. Tech. Digest of Optical Fibre Communication Conf, pp295– 296, 17-22 March 2002,

Vok03 **Channel scheduling algorithms using burst segmentation and FDLs for optical burst-switched networks**
V.M.Vokkarane, G.P.V.Thodime, V.U.B.Challagulla, J.P.Jue. Tech. Digest of IEEE International Conference on Communications, Vol. 2, pp 1443-1447, 11-15May 2003

Wei03 **Networked multimedia: issues and perspectives**
S.Weinstein, A.D.Gelman. IEEE Communications Magazine, Vol. 41 (6), pp 138–143, June 2003

Wei99 **The evolution of China's optical fibre networks**
L.P. Wei, Y. Chen and G.G. Wong, Bell Labs Technical Journal, Vol.4 (1), pp125-144, Jan-Mar 1999

Wei99 **Just-in-time optical burst switching for multiwavelength networks**
J.Y.Wei, J.L.Pastor, R.S.Ramamurthy, Y.Tsai. Tech. Digest of International Federation of Information Processing Conference on Broadband Communications vol.1, pp 339-352, Hong Kong, November 1999

Whi03 **Demonstration and system analysis of the HORNET architecture**
I.M.White, Eric Shih-Tse Hu, Yu-Li Hsueh; K.Shrikhande, M.S.Rogge, L.G.Kazovsky, Journal of Lightwave Technology, Vol. 21, (11,) pp2489 – 2498, Nov. 2003

Wol06 **Synchronizing optical data and electrical control planes in asynchronous optical packet switches**
D.Wolfson, H.N.Poulsen, S.Rangarajan, Z.Hu, D.J.Blumenthal, G.Epps, D.Civello. Tech. Digest of Optical Fibre Communication Conf vol.1 Anaheim USA 2006

Won06 **Bandwidth and Buffer Tradeoffs in Optical Packet Switching**
E.Wong, M.Zukerman. Journal of Lightwave Technology Vol. 24 (12), pp4790 - 4798 Dec. 2006

Xue04 **Design and experimental demonstration of a variable-length optical packet routing system with unified contention resolution**
Fei Xue, Zhong Pan, Haijun Yang, Jinqiang Yang, Jing Cao, K.Okamoto, S.Kamei, V.Akella, S.J.B.Yoo. Lightwave Technology, Journal of Volume 22, Issue 11, Nov. 2004 Page(s):2570 – 2581

Yoo00 **QoS performance of optical burst switching in IP-over-WDM networks**
M. Yoo, C. Qiao, S. Dixit. IEEE Journal on Selected Areas in Communications, Vol.18 (10), 2062-2071, October 2000

Yoo06 **Optical Packet and Burst Switching Technologies for the Future Photonic Internet**
S.J.B.Yoo. Journal of Lightwave Technology, Vol. 24, (12), pp4468 - 4492 Dec. 2006

Yoo97 **Just-Enough-Time (JET): a high speed protocol for bursty traffic in optical networks**
Myungsik Yoo; Chunming Qiao, Digest of the IEEE/LEOS Summer Topical Meeting pp26 – 27, 11-15 Aug. 1997

Yoo99 **A novel switching paradigm for buffer-less WDM networks**
Myungsik Yoo, Chunming Qiao. Tech. Digest of Optical Fibre Communication Conf., Vol. 3, pp177–179, 21-26 Feb. 1999

Zan01 **Dynamic lightpath establishment in wavelength-routed WDM networks**
H.Zang, J.Jue, L.Sahasrabuddhe, R.Ramamurthy, B.Mukherjee. IEEE Communications Magazine, Vol. 39 (9), pp 100-108, September 2001

Zap03 **Dynamic Wavelength-Routed Optical Burst Switched Networks: Scalability Analysis and Comparison with Static Wavelength-Routed Optical Networks**
A. Zapata, P. Bayvel. Tech. Digest of Optical Fibre Communications Conf., Atlanta USA, 23-28 March 2003

Zap03a **Impact of burst aggregation schemes on delay in optical burst switched networks**
Zapata, P. Bayvel. Tech. Digest of IEEE LEOS Annual Meeting, vol.1, pp.57-58, Arizona USA, November 2003

Zap04 **Next generation 100-Gigabit Metro Ethernet (100GbME) using multi-wavelength optical rings**
A.Zapata, I.de Miguel, M.Düser, J.Spencer, P.Bayvel, D.Breuer, N.Hanik, A. Gladish. IEEE/OSA Journal of Lightwave Technology Vol. 22 (11), pp2420-2434, special issue on "Metro & Access Networks", November 2004

Zap05 **Dynamic vs. static lightpath allocation in WDM networks**
A.Zapata, P. Bayvel. Tech. Digest of European Conference on Optical Communications, Vol.2, pp. 273-274, Glasgow, Scotland, September 2005

Zap05a **Improving the scalability of lightpath assignment algorithms in dynamic networks**
A. Zapata, P. Bayvel. Tech. Digest of European Conference on Optical Communications, vol.1, pp 35-36, Glasgow, Scotland, September 2005

Chapter 2 Fast tunable lasers as burst transmitters

2.1 Tunable lasers as burst transmitters

A key component of all dynamic optical networks is the tunable transmitter used to transmit the payload data in packets or bursts. As described in chapter 1, the characteristics and the operation timescales of the transmitter, have a strong impact on the network performance and can influence the network design. In this chapter, the focus is not the fundamental laser switching time that has been the subject of many previous studies, but the impact of the laser switching process in WDM network environment across the full range of timescales. Firstly, at the shortest timescale, an interference effect arising directly from the switching process and occurring on a timescale shorter than the laser switching time is identified and its effect on the network performance quantified. Secondly, the impairment caused by long term thermal instability that is particularly important over the longer millisecond timescales of Type II OBS networks, is investigated and quantified in a network context. Both of these aspects are studied in detail for the first time. Prior to this, the tuning methods and main categories of tunable laser technology are investigated, described and compared experimentally. These results are then used as inputs to the development of a wavelength locked burst-mode transmitter described in chapter 3.

2.1.1 Review of laser tuning techniques

As outlined in chapter 1, the characteristics of an OBS transmitter define the limits of network performance. For example, the speed at which a lasing device is able to switch wavelength has a direct effect on key network parameters such as offset time in Type I OBS networks [Yoo07] and the edge delay in Type II OBS networks [Dus02]. Of importance to all network architectures is the number of stable ITU wavelengths the transmitter is able to operate at is also important to the network size and traffic carrying capability [Zap03]. Other important characteristics of potential transmitters are output power, side-mode suppression ratio (SMSR), wavelength stability, ageing drift and the degree of uniformity of these factors across all operating points. These factors will affect the achievable burst loss probability and hence may limit the network size. Realistically, potential devices should also perform well in terms of cost and

power consumption, being comparable to DFB laser currently used in WDM systems.

There are a number of possible candidates for such transmitters. Most are semiconductor-based devices and were originally developed to replace racks of single wavelength DFB lasers in WDM systems. Lasing dyes are available with high optical efficiency, but they are not convenient to handle outside of the laboratory. Doped crystal or fibre sources have been initially overlooked since the pump laser requirement increases the complexity, although some useful sources have been developed [Mas07,Qin03, Tim99, Bao96]. In contrast, devices based on semiconductor gain media may be efficiently pumped, rapidly tuned electrically and presented in a small butterfly packaged chip.

The semiconductor material used in the gain medium may be selected to provide gain over the desired operating range and combined with a wavelength selective feedback mechanism to provide the tunabliity. The simplest method tunable feedback mechanism is a mechanically tuned Fabry-Perot cavity with the periodic lasing wavelengths selected by the optical cavity length. An example of such a device is the mechanically tuned vertical cavity surface emitting laser (VCSEL) [Har00]. A second, mechanically tuned, approach is an external diffracting grating where the reflected light is tuned by rotation of the grating. Mechanical devices are not only be limited in terms of tuning range but cannot match the requirement for fast switching between wavelengths, generally able to tune in the ms regime [Ama98a].

Temperature effects may be used to alter the band gap of the semiconductor material to shift the laser gain spectrum and, in turn, the wavelength of peak gain. Temperature can also be used to alter the refractive index of the semiconductor material in the laser cavity to change the optical path length, and hence, the lasing modes. Typical values for InGaAsP material is of the order of 0.1nm/K [Ama98b] giving a tuning range, by this method alone, of around 10nm for a 100°K temperature range with the speed limited to the millisecond regime by the heating mechanism and thermal response of the device.

Potentially the fastest tuning mechanism uses the quantum confined Stark effect (QCSE) as a tuning mechanism [Ama98c]. The physical limit of this field induced effect is estimated to be around 10ps [Lam95] although little work has been done on developing wide tuning range devices in the communications band using this effect. Switching times of 10ns have been demonstrated at shorter wavelengths [Cai98, Cai94] and the best external cavity QCSE device has demonstrated 30*140GHz spaced channels around 1550nm over a 32nm tuning range [Son01]. Monolithic versions of these devices with smaller tuning ranges have been reported [Pan06, Pan07] but they are not yet close to meeting the tuning range, stability and cost requirements of dynamic optical networks (DONs).

An optical injection phase locked loop (OIPLL) and optical frequency comb generator (OFCG) [Ren03] was used in [Ren04a/b] to achieve tuning times of less than 12ns for 30 wavelength pairs using an SG-DBR laser (described below). The system uses the OFCG as a master laser source for a number of slave lasers stabilized in OIPLL blocks. In addition to rapid switching, the locking technique enabled wavelength stability of less than 1 kHz. With sufficient tuning range, such a system would be able to meet all the transmitter requirements for DONs of the type described in chapter 1 but at the cost of significant additional lasers, components and complexity.

Electronic tuning offers potentially fast and easy to implement tuning mechanism with the most common using carrier induced effects (CIE) to alter the refractive index of the semiconductor material [Ben90, Ama98d]. The most common electronic tuning technique is the free-carrier plasma effect where the refractive index caused by the injected electron-hole plasma is primarily due to polarization of the free carriers [Web94, Ben90, Sof86]. This process is described fully in [Ama98d].

For a single active section the carrier density reaches equilibrium above the lasing threshold and the predominant tuning mechanism from increasing the bias current becomes thermal effects. Hence, to achieve a wide tuning range it is necessary to include a specific tuning element or passive tuning section within the laser cavity. A good solution to provide a low cost, reliable, single

frequency tuning element is a Bragg grating. Indeed, 2 popular types of semiconductor lasers developed for telecommunication applications are based on variations of Bragg gratings. The first, based on a uniform grating is a distributed feedback (DFB) laser that gives generally a single wavelength output that may be tuned by up to 10nm with temperature [Ima01].

The second is a distributed-Bragg-reflector (DBR) laser that uses an embedded Bragg grating based on refractive index boundaries that may be tuned by current injection. The advantage of using these gratings over the mirrors used in Fabry-Perot Lasers, is that reflection back in to active gain medium takes place only at the Bragg frequency as determined by the grating pitch and this may be tuned by current injection to the grating section [Ama98d,e]. As with the gain section the refractive index of the grating material may be changed by current injection enabling tuning of the feedback mechanism. Also included in the device is a phase control section to shift the Fabry-Perot modes between the Bragg grating and the end facet for fine tuning as shown in schematic form in Figure 2-1. Such devices with tuning ranges of 17nm have been demonstrated [Del98].

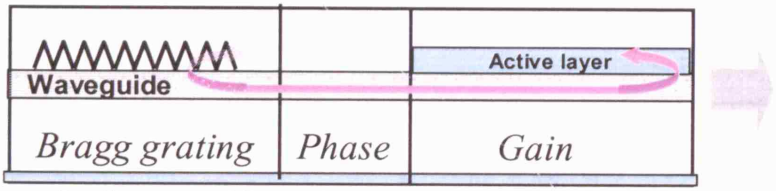

Figure 2-1 Schematic diagram of 3-section DBR tunable laser

2.1.2 Review of multisection tunable lasers

The tuning range can be extended further by adding a second grating section either side of the gain section to produce multi-section devices with the lasing wavelength determined by independent control of the bias currents in passive tuning sections. Although originally developed to replace racks of single wavelength DFB lasers in WDM systems the potential for fast switching also makes such devices the most promising technology for wavelength agile transmitters in dynamic optical networks (DONs). The simplest grating design suitable for widely tunable lasers is the sampled (Bragg) grating (SG) constructed from a series of small equally spaced gratings which reflect not only at the Bragg wavelength but also generate Fabry-Perot modes to provide a comb like response and sinc function envelope, characteristic of the Bragg

Grating [Mas98]. Indeed the most common tunable multisection tunable laser design is based on the combination of 2 such gratings with a gain section and phase section to provide fine control of the optical cavity length [Jay93, Mas98, Rob98a/b]. A detailed analysis of the grating response is included in section 7.3.1 of [Ama98e] and a schematic diagram is shown in Figure 2-2.

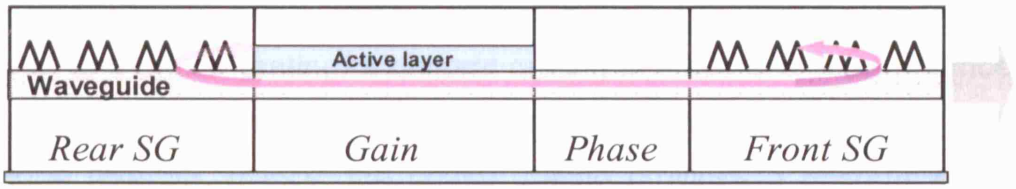

Figure 2-2 Schematic of SG-DBR tunable laser

The gratings are designed to ensure unequal comb spacing such that lasing only occurs when the pass-bands of both gratings overlap as in a Vernier [Jay93]. This combined with large bias currents and broad gain spectrum in the gain section increase the tuning range to over 70nm [Yu00], although the cost of this large tunabilty is the control complexity since the currents injected into each of the 4 sections (2 gratings, gain section and phase section to control the optical cavity length for precise control) are controlled independently. Figure 2-2 shows a schematic of a sampled Grating DBR laser (SG-DBR) and the tuning mechanism is demonstrated with the combined reflection spectra of the grating sections in Figure 2-3.

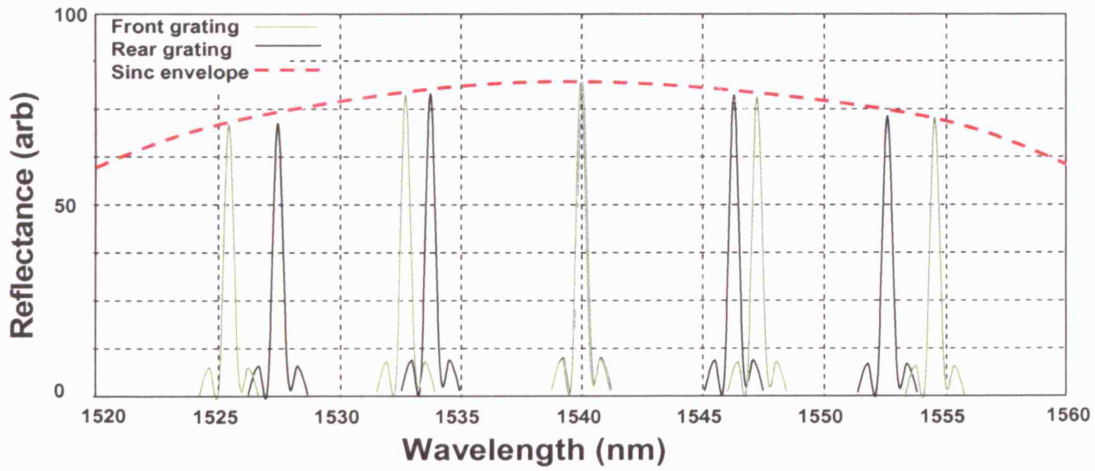

Figure 2-3 Reflection spectra from front and rear grating sections in SG-DBR laser design

The super structure grating DBR (SSG-DBR) uses a similar principle of unequally spaced gratings to provide wide quasi-continuous tuning by the Vernier effect but the gratings have an additional periodic phase modulation to increase the number of reflection peaks, extending the grating reflection combs and flatten the overall grating response [Ish93/1Ish96]. Such designs have

yielded devices with tuning ranges up to 105nm [Ish93/2] but the subtle variations in grating phase and pitch mean reliable production of such gratings is difficult [War04]

A further evolution based on DBR lasers is the "digital super-mode" DBR (DS-DBR) laser [Bus02, Rei02, War03, Rob04, War05, Pon05/06]. The rear section consists of a phase grating, a uniform grating interspersed with a number of π phase shifts optimized to provide an even comb response with a top hat envelope [War04]. Hence, the phase grating provides a uniform wavelength comb across the entire tuning range and has the advantage that the entire grating contains a uniform pitch significantly reducing complexity of the fabrication process. The front grating provides the quasi digital operation consisting of a number of broad phase gratings with individual contacts that may be operated in adjacent pairs to select a sub band of the entire tuning range. Without any current injection into the front section, the series of gratings reflects a broad wavelength range and the pitches are specifically chosen such that current injection to one or an adjacent pair of gratings causes tuning sub-bands to overlap around one of the wavelengths reflected from the rear section which is then used to provide intra sub-band tuning. A device schematic of the DS-DBR laser is shown in Figure 2-4 and the typical reflection spectra for both tuning sections are shown in Figure 2-5

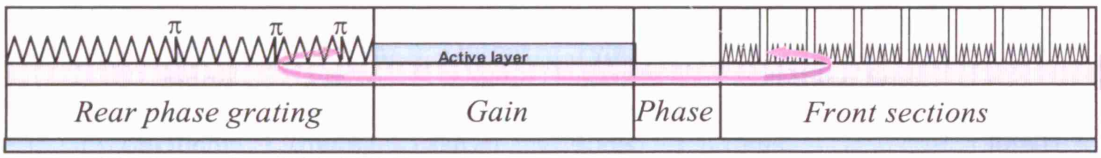

Figure 2-4 Schematic of DS-DBR tunable laser

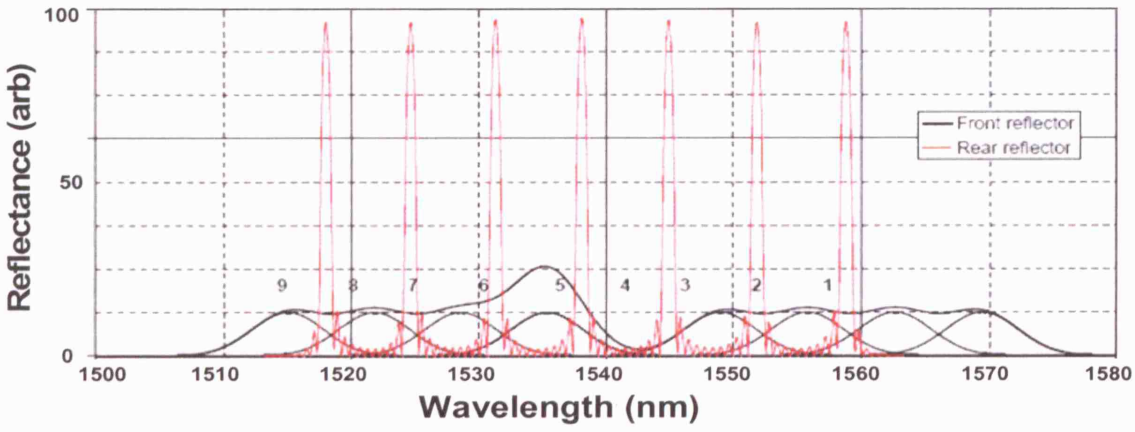

Figure 2-5 Reflection spectra for DS-DBR rear phase grating and front grating reflector

The advantages of the DS-DBR is that the tuning map is simplified to resemble a series of concatenated 3 section DBR devices that can offer a much simplified tuning current control algorithms than the SG or SSG-DBR devices for which adequate control algorithms require complex characterization in 3 or 4 dimensions. Characterization of all of these devices is discussed in section 2.2. The second key advantage discussed in sections 2.4 to 2.6 is the magnitude of the required tuning currents. Since current is injected into only a small section of the front grating the magnitude of the currents is smaller leading to a reduction in thermal instability from high tuning current switching. In addition to the devices described above, 2 further tunable laser designs, the grating-coupler with rear sampled-grating reflector (GCSR) and the modulated grating-Y-branch (MG-Y), were characterised and their operation is described in Appendix A.

2.1.3 Switching of multisection tunable lasers

The studies described thus far have all been based on monolithic devices with carrier-induced change in refractive index being the tuning mechanism. However, sub-nanosecond tuning has also been achieved with external cavity devices [Kau03] although problems of mechanical instability, the requirement for precise optical alignment and limited tuning range [Ber04] has made them less attractive devices for practical implementation than monolithic semiconductor lasers.

Table 2-1 Comparison of tunable transmitters for dynamic optical networking

Device	Tuning range	Tuning mech.	Output power	Typical SMSR	Typical switching time	Ref.
VCSEL	20nm	Mech/CIE	1dBm	30dB	1-10ms	Sun04
DFB	5-10nm	Thermal	0dBm	30dB	1-10ms	Ima01
DBR	10-30nm	CIE	0-5dBm	>30dB	<10ns	Del97/Fis01
GCSR	>70nm	CIE	0dBm	>35dB	<50ns	Sim03
SG-DBR	>70nm	CIE	5-10dBm	>35dB	<50ns	Yu00
SSG-DBR	>90nm	CIE	5-10dBm	>35dB	<50ns	Sar02
DS-DBR	50nm	CIE	8-9dBm	>40dB	not given	War03
MG-Y	30nm	CIE	13dBm	>40dB	<50ns	Wes04
SG-DBR	30nm	QCSE	-	-	<10ns	Son01
SG-DBR	40nm	OIL	5-10dBm	>50dB	<10ns	Ren04

Table 2-1 shows a summary of published switching performance based on the tunable laser technology described above. Nanosecond switching times and wide tuning ranges are possible with all of the devices described above using CIE or field effects. In general, the performance of these devices is not only determined by the design and fabrication of the device but by the speed and precision of the current control system. Indeed all the studies described so far

employ a similar method combining look up tables of operating points with digital to analogue converters and amplifiers to set the tuning currents. Fast switching between multiple channels was first studied in combination with large tuning range for GCSR lasers in [Rig96] and many more are shown in Table 2-2 for both GCSR and DBR devices.

Table 2-2 Summary of multi-channel/fast switching studies

Laser	Max. switch. time	No. channels	Tuning range	Packet Lengths	Ref
GCSR	50ns	32	25nm	1μs	Bha03
GCSR	50ns	32	25nm	2ms	Sim03
GCSR	10ns	100	70nm	100ns	Klo03
GCSR	100ns	100(non ITU)	44nm	Not given	Cha00
GCSR	5ns	40	60nm	10ns	Lav00
GCSR	15ns	6	30nm	250ns	Shr01
SG-DBR*	1μs	85	40nm	Not given	Mul02
SG-DBR	5ns	64	30nm	40ns	Sim06
SG-DBR	50ns	32	25nm	1μs	Bha03
SG-DBR†	5ns	30	6nm	>250ms	Ren04
DS-DBR	6ms	80	40nm	Not given	Pon05/06

† Using OIPLL and optical frequency comb generator * Uses active wavelength locking

The focus of many of these studies, particularly with the GCSR devices was minimizing the switching time and not the overall wavelength stability. In these studies, the lasers used in these were periodically switched on ns/μs timescales to avoid the destabilizing thermal effects that occur on the ms thermal time scale. Hence, whilst these demonstrations are applicable for OPS or Type I OBS schemes, they do not explore the detrimental thermal effects that become critical for Type II OBS networks, such as WR-OBS, where burst lengths are expected to be in millisecond regime [Düs02].

Despite widespread interest in their use there are relatively few detailed studies of the SG-DBR devices performing fast switching over a number of channels similar to those for GCSR devices. [Yu00] first examined fast switching and [O'Do01] showed experimentally 2000 operating points for a low SMSR of 25dB but only 124 stable operating points with an SMSR above 40dB. Fast switching of 4-8ns was shown in [Del98] for some channels for sub μs bursts and more recently [Sim06] showed sub 5ns switching between 64 channels for 40ns bursts and with a low wavelength accuracy ±12GHz. Other studies have focused on the wavelength switching transitions demonstrating the difficulty in efficiently accessing its large tuning range. [Yu02a] shows how mode

competition is present in the tuning sections of the SG-DBR devices can affect switching time and wavelength stability manifesting itself as hysteresis effect with different switching times between forward (increasing current) and backward (decreasing current) switching and [O'Do01] furthered this work dependency of switching time on the magnitude of the tuning current switch but again ignoring the slower thermal effects occurring on the μs/ms timescale. Equally, the published material on tunable lasers has paid little attention to the potential interference effect caused by the emission of spurious modes (switching crosstalk) during the switching process.

Hence, further to these studies, the aim of this chapter is to extend tunable laser measurements of wavelength stability to the millisecond timescales applicable to optical burst switching. For both wavelength stability and switching crosstalk the aim of the measurements presented was to identify and quantify potential impairment in a realistic network context in order to determine the performance requirements for the development of a burst-mode transmitter described in chapter 3.

2.1.4 Lasers used in measurements

A number of semiconductor tunable lasers from several manufactures were used in the experiments described in this and the following chapter. As can be seen in Table 2-4, these devices varied in performance since they range from early prototypes to state-of-the-art devices with integrated optical components and custom-built control electronics. Not all of the devices were available for the duration of the work and so the device code of the specific lasers used are included in all subsequent measurements. Indeed, since many of the devices used were research devices, their availability has shaped the direction of the work and, in some cases, limited the scope of the measurements. For example, only a single GCSR laser was used in these measurements due to scarcity of packaged chips in the absence of a commercial manufacturer of this laser design. Since the device was already several years old the performance of this device was not at the same standard as similar devices reported in literature as demonstrated in the device characterisation in Section 2.2. All the lasers were butterfly packaged at the manufacturers with the exception of integrated tunable

laser module which was packaged in a stand alone module with integrated drive electronics.

Table 2-3 Table of lasers used in switching (ch. 2) and λ-locking (ch. 3) measurements

Device ID /serial number	Device type	No, tuning sections	W'length range	Typical output pwr	Typical SMSR	Manufacturer/ Comments
TLS2078	SG-DBR	4	70nm	5dBm	40dB	Bookham
TLS2032	SG-DBR	4	70nm	5dBm	45dB	Bookham
TLS2048	SG-DBR	4	70nm	10dBm	50dB	Bookham
TLY1001	MG-Y	4	40nm	0dBm	40dB	Syntune
TLD1001	DS-DBR	13	60nm	13dBm	50dB	Bookham – Inc. SOA
TLD1002	DS-DBR	13	60nm	13dBm	50dB	Bookham – Inc. SOA
TLG1001	GCSR	4	50nm	-5dBm	45dB	Altitun
INT1140	DBR	3	10nm	8dBm	42dB	Intune Technologies

2.2 Laser characterisation

The first stage in adapting semiconductor tunable lasers for use in OBS transmitter is to carefully map their output characteristics as a function of their tuning parameters. For all the devices in Table 2-4, this means independent control of all tuning sections and the chip temperature. As described in more detail later in the chapter the ability to locate operating points with desirable characteristics and, more importantly for network operation, to identify sets of operating points with desirable switching characteristics, depends largely on the detail of the device characterization. However, the primary aim of the characterizations described here is to provide a comparison between the available devices and to identify operating points for subsequent switching measurements.

2.2.1 Device characterisation set-up

All characterization experiments were performed using the set up shown in Figure 2-6. Although temperature may be used as an additional control parameter the KHz thermal response means this is not appropriate for the requirements of DON transmitters. Hence, a constant temperature of 25°C was maintained for all laser characterizations.

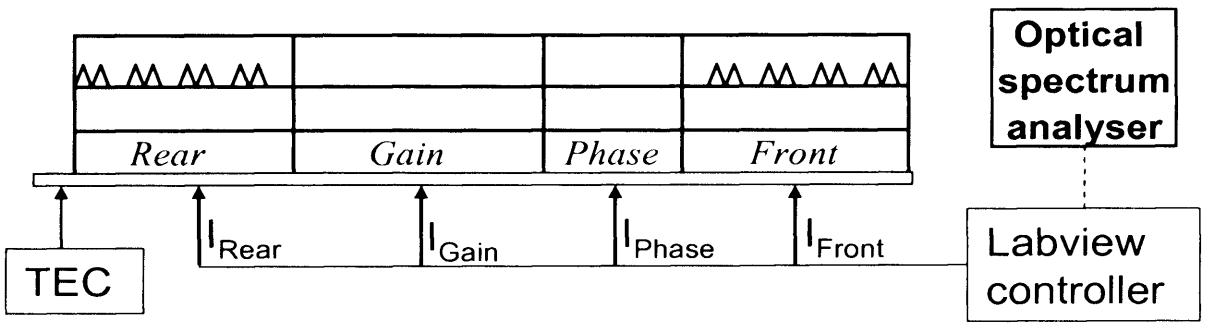

Figure 2-6 Experimental set-up for tunable laser characterization using SG-DBR

Each of the required tuning currents was driven by a GPIB controlled current driver whilst the laser output was monitored using an optical spectrum analyzer (OSA) which measured and stored the wavelength, output power and SMSR of the laser output for each tuning current increment. In general, characterizations were performed by varying each tuning current across its entire range in 0.2mA steps whilst the gain (power) and phase (fine tuning) section currents were maintained constant. The measurements were then repeated at new phase and gain tuning current values. The phase section provides control of the optical cavity length for fine tuning of the output wavelength with a wavelength-tuning current relationship that repeats with a period of approximately 1.5-2mA. Hence, smaller 0.1mA steps were used to cover 1 period of phase section tuning whilst the gain section was maintained constant well above the lasing threshold.

2.2.2 Device characterisation - SG-DBR

Figure 2-7 shows the tuning characteristics of the primary tuning sections, the front and rear gratings, of a SG-DBR laser. The plots show the output wavelength as a function of tuning current for constant gain and phase section tuning currents and, hence, are only subset of the total device tuning range and used to demonstrate the tuning properties of each device. The wavelength tuning maps of the SG-DBR, as also observed in the MG-Y device characterisation shown in Appendix A, shows the characteristic fan-like tuning caused by the Vernier tuning of 2 sampled gratings. Figure 2-7(a) shows regions of similar wavelength output denoted by coloured regions separated by thin and thicker black lines denoting current values that correspond to no wavelength output. The format of these lines is analyzed in more detail in [Yu02b] and shows that the thinner lines, perpendicular to the fan structure that represent small cavity mode jumps. The thicker back lines that separate each diagonal fan signify the super-mode boundaries corresponding to a change in which of the overlapping pass bands are responsible for the primary lasing mode. Together these lines frame the regions of high output power and high SMSR, both coloured in red in Figure 2-7(b) and Figure 2-7(c) where almost all useful operating points are located.

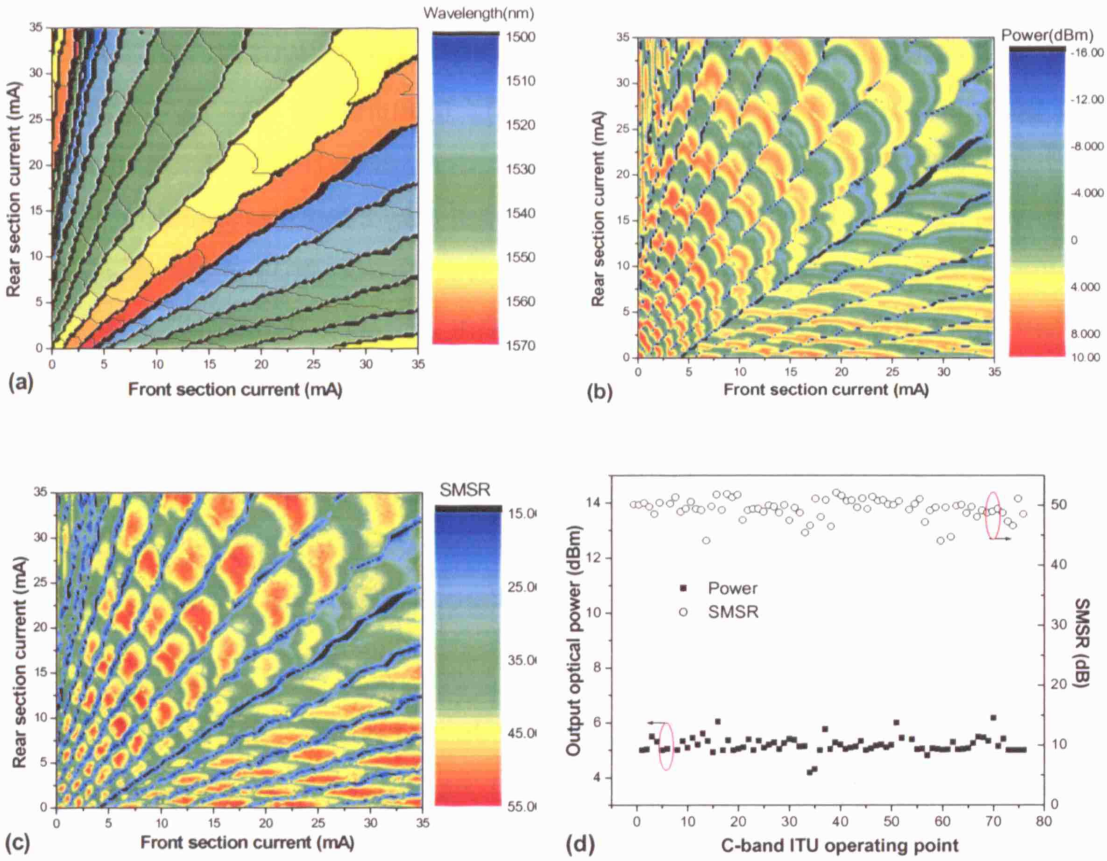

Figure 2-7 (a) Output wavelength, (b) output power, and (c) SMSR plots SG-DBR (TLS2078) with 0.2mA tuning current steps, 200mA gain, 5mA phase current, (d) distribution of C-band operating points

In addition to an appropriate wavelength, a suitable operating point should also have desirable output power and SMSR characteristics with the fine tuning of the competing-mode suppression best achieved by careful control of the phase section. Hence, although Figure 2-7(a-c) provide an indication of the tuning characteristics of the device a more appropriate measurement is the distribution of operating points over all wavelengths allowing for flexibility of both grating sections and the phase control.

Such a plot is shown in Figure 2-7(d) which shows the power and SMSR of operating points at each ITU wavelength across the most common operating range, the C-band, 1530 to 1560nm. Each operating point was considered valid if it was within 5GHz of the standardised ITU-T frequency grid [ITU06]. Where multiple operating points exist, the point with the most desirable power and SMSR characteristics was chosen according to a simple algorithm. Firstly, to ensure optimum power uniformity, the median average of all operating points was chosen as the target operating power for all wavelengths. For the SG-DBR,

this was chosen to be 5dBm. The best operating point was then determined by considering a narrow power range (0.2dB either side) around this target operating power and a minimum SMSR of 45dB. The optimum operating point with the highest SMSR was then chosen. If no suitable operating point was found the selection process was repeated with an increased range of power and then SMSR values. The power deviation from the target power was increased in steps of 0.1 dB and the SMSR increased in steps on 1dB with a minimum of 30dB. The wavelength resolution of the OSA for all characterisations was 0.01nm with the power measurements accurate to within 0.1dB. Using this method acceptable operating points were identified at 75 of the 76 C-band ITU wavelengths for the SG-DBR device. The standard deviation of output power and SMSR was 0.3 and 0.74 respectively.

2.2.3 DS-DBR

Figure 2-8 shows the characterization results of the DS-DBR tunable laser. As described previously the DS-DBR requires control of 8 separate front section gratings in adjacent pairs to select a sub-band matching a region of the wavelength comb reflected by the rear section phase grating. As a result the output wavelength plot shown in Figure 2-8(a) is divided into vertical strips, corresponding to each front grating pairing. Additionally, the device characterization here includes an integrated SOA for power boosting and additional control of power uniformity. The characterization data shown was provided with the device by the manufacturer, hence the output power and SMSR plots are not available for this device.

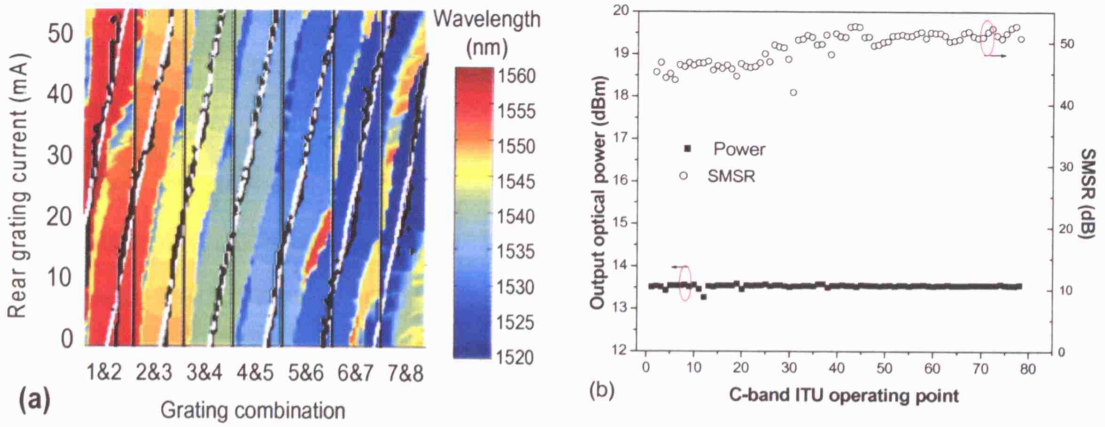

Figure 2-8 (a) Wavelength plot for DS-DBR laser (TLD1001) with 0.2mA tuning current steps, 200mA gain, 140mA SOA 5mA phase current and (b) distribution of C-band operating points from full characterization (provided by Bookham Technologies, UK)

As with the GCSR laser design, described in Appendix A, the technique for using a broad front reflector to select a tuning sub-band from the rear reflection comb results in near vertical super-mode boundaries. The integrated SOA provides the highest output power and power uniformity of all the devices studied showing a near constant power of 13.5dBm with a standard deviation (SD) of less than 0.04dB. The SD of the measured SMSR for the C-band operating points was 2.48. This is a little higher that that measured for the SG-DBR of 1.72 with an almost identical mean value of 49.3dB.

2.2.4 TL characterization summary

Sections 2.2.2 and 2.2.3 show the tuning characteristics of the two most common widely-tuneable fast-switching laser designs. Characterisation data of 2 further laser designs, the GCSR and MG-Y are shown in Appendix A. These results are intended to demonstrate the different tuning characteristics of each design rather than provide a quantitative comparison of their merits. Since only one of each of the GCSR and MG-Y devices were available it was impossible to perform a reliable comparison, particularly since the measured performance of these particular devices differed considerably from published studies. The best published studies of each laser together with a summary of the measurements described in previous sections are shown in Table 2-4 and are included to compare the device performance with the best currently reported in order to select devices for subsequent switching measurements.

Table 2-4 Summary of tuneable laser characterizations

	Measured characteristics					**Best published performance across entire C-band ITU Grid**		
Laser	**% 50GHZ ITU grid coverage**	**SMSR Mean (dB)**	**SMSR SD (dB)**	**Power Mean (dBm)**	**Power SD (dB)**	**Output Pwr (dBm)**	**SMSR (dB)**	**Ref**
SG-DBR	98.7	49.37	1.72	5.18	0.3	13*	38	Lil02
MG-Y	85.5	42.37	5.96	6.08	0.73	13*	40	Wes04
GCSR	100	40.86	3.26	-5.22	0.32	13	40	Gus03
DS-DBR	100	49.28	2.48	13.54*	0.04	13.5*	42	Pon05

* Includes integrated SOA

The list of published studies shows that a common feature of the best published performance of monolithic semiconductor tuneable lasers is the inclusion of an integrated SOA to both boost and equalize the output power. Due to its location within the laser cavity, tuning of the gain section of such lasers also changes the refractive index and subsequently output wavelength. Hence, an SOA outside of the laser cavity decouples control of the output power from the laser itself allowing for power equalization without affecting the

output wavelength. Minimizing changes of the gain section tuning currents also helps to reduce thermal effects from current switching. A good description of SOA power equalization in a DS-DBR laser can be found in [Pon05].

Both the SG-DBR and DS-DBR lasers compared favourably to the best published figures in terms of output power, SMSR and uniformity of C-band operating points although. With the exception of the output power for the SG-DBR which was less than the best published performance due to the lack of an integrated SOA, the measured performance of these devices was in line with the best published performance within the measurement accuracy limited by the OSA used. The GCSR laser also showed comparable performance to the published studies in most respects with only the output power significantly reduced and a degraded tuning map compared to studies reported in the literature. The MG-Y showed lower and less consistent SMSR than the best published figures and although the output power was comparable with the un-amplified SG-DBR device characterized it was well below the 13dBm obtained in [Wes04].

At the time this work was carried out, there was no existing manufacturer of GCSR lasers [Lig04] and almost all published work and all state of the art results regarding tuneable lasers in optical networks were based upon DBR designs. This fact, combined with the fact that the only GCSR device available showed less than ideal performance, it was decided to base further study of the switching transition on DBR based devices.

2.3 Switching of DBR lasers

This section describes work carried out to characterize the switching transition of DBR based tunable lasers. The aim was to characterize the switching transition and to identify the key control parameters applicable to DONs. After an investigation of the required tuning currents, a measurement system capable of pico-metre wavelength and sub-nanosecond time measurements is introduced and used to analyze the switching transition of DBR tunable lasers.

2.3.1 Magnitude of switching currents

An important consideration in the application of these tunable lasers to DONs is the thermal response of the device. Thermal effects are particularly problematic

in Type II OBS schemes since the thermal time constant of the laser and mount is of the same order of magnitude as the burst length. For multi-section tunable lasers, the wavelength switching dynamics are determined by both carrier density and temperature. Hence, after a step change in tuning current during a wavelength switching event, thermal transients can cause frequency shifts, proportional to the tuning current switch, in the output wavelength [Kos04, Mul03].

Hence, for application to DONs with millisecond burst lengths it is desirable to minimize these thermal transients by minimising the magnitude of tuning current switches whilst still covering the proposed tuning range. In order to ensure that subsequent measurement of switching times and thermal transients used realistic tuning currents, the tuning currents required to access as many wavelengths on the 50GHz C-band ITU grid as possible were determined for each device used in subsequent switching measurements. Figure 2-9 shows the relationship between the maximum tuning current and the percentage of 50GHz ITU grid channels covered for the 2 types of DBR based lasers used in switching measurements. This data was obtained from the characterisation data presented in section 2.2 and shows the maximum tuning currents required to access the entire tuning range.

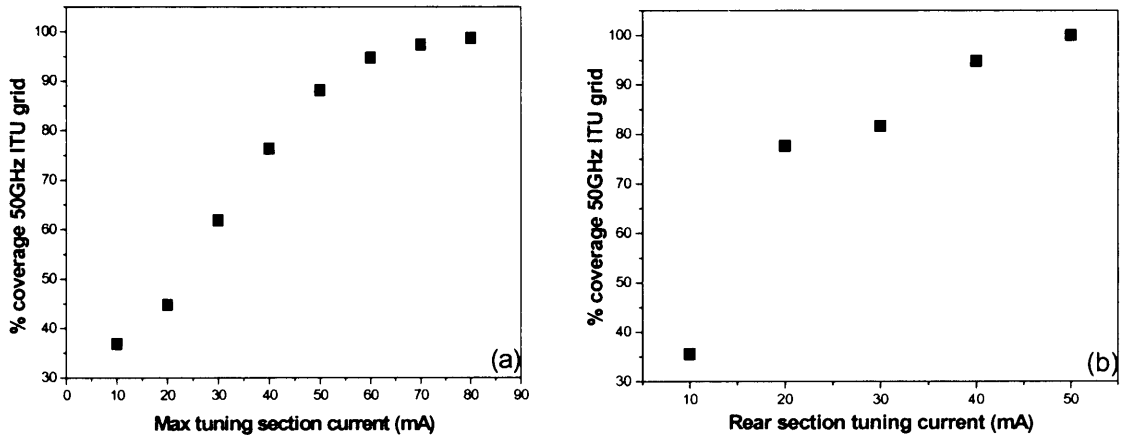

Figure 2-9 ITU grid coverage vs maximum required tuning current for (a) SG-DBR (TLS2078) front/rear tuning section and (b) DS-DBR (TLD1001) rear tuning section

Figure 2-9 provides an estimate of the upper bound for the tuning currents which may be used in subsequent switching measurements. In order to access all operating points on the ITU grid the maximum tuning current required is

50mA for the DS-DBR (rear section) and 80mA for the SG-DBR (both tuning sections) devices used.

2.3.2 Analysis of switching transition

Analysis of the switching transition and measurement of switching times was carried out by making measurements of both wavelength and time using a similar method to that described in [Mul99]. Wavelength measurements were performed using a mechanically-tuned fibre Fabry-Perot etalon (Micron optics FFP-100) with a 3dB bandwidth of 0.15nm. The time measurements were recorded using a Tektronix TDS210 digital oscilloscope. Measurement of the laser output as a function of both time and wavelength required the laser repeatedly switched between the start and finish wavelengths whilst the Fabry-Perot etalon was scanned through the wavelength range of interest at fixed intervals with an oscilloscope trace recorded at each wavelength increment. The etalon, oscilloscope and tunable laser drive current were computer controlled via a GPIB link. Custom built software was used to store the oscilloscope traces and determine and extract the output wavelength plots. Where required, a band-pass filter was used to select a single transmission peak from the periodic frequency response of the FP filter. The maximum wavelength accuracy of the measurement system was 5pm, limited by the stability of the mechanically tuned filter and oscilloscope noise with the maximum timing resolution of 200ps. The experimental set up used in all switching measurement is shown in Figure 2-10.

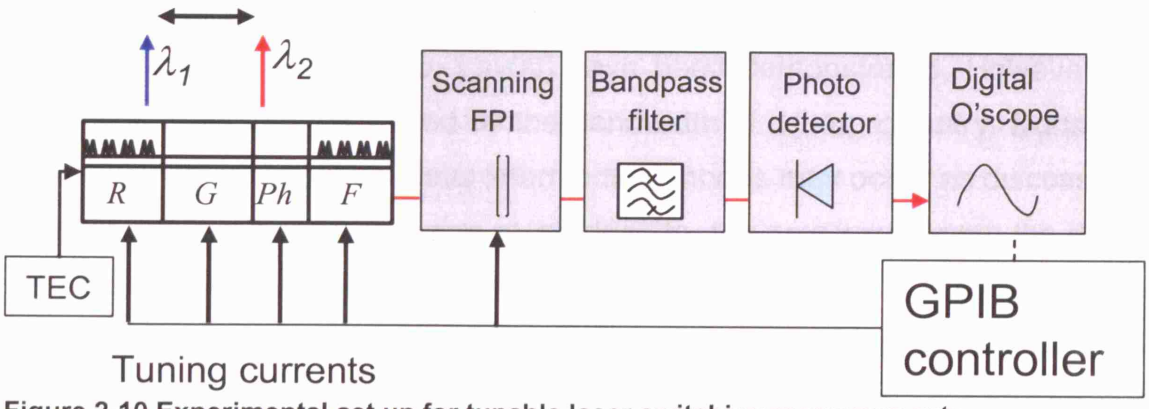

Figure 2-10 Experimental set up for tunable laser switching measurements

Once the FPI had been scanned over the wavelength range of interest, the oscilloscope traces could be combined to build a 3 dimensional picture of the laser output using an intensity plot of wavelength against time. An example of such a graph is shown in Figure 2-11 which also shows summary plots of the

wavelength of maximum power at each point in time and the output power recorded at this wavelength.

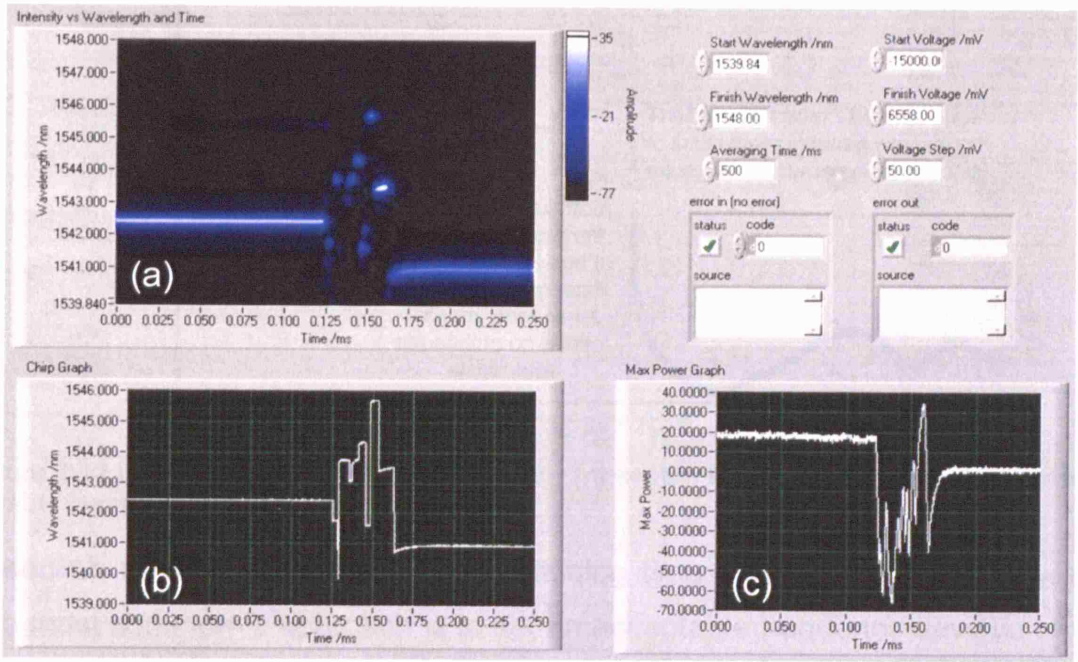

Figure 2-11 Screenshot of Labview software after measurement of an 80mA front tuning section switch showing (a) intensity of dominant lasing wavelength (b) wavelength of dominant lasing wavelength (Chirp) and (c) power of dominant lasing wavelength

2.3.2.1 Switching time definitions

Figure 2-12 shows the main features of the switching transition of DBR-based semiconductor lasers and it is the impact of these features in the context of a DON which is the focus of this chapter. After lasing on a stable wavelength, a step change of grating section tuning current causes the laser to begin lasing at a new wavelength. The time taken to tune to the new wavelength value is ultimately dependent on the device specific carrier dynamics and switching times as low as 5ns [Sim06, Lav00] have been demonstrated. However, the switching times may be limited by the bandwidth of driving circuitry. During the switching time lasing at spurious intermediate modes may occur as discussed in detail in section 2.4. Once lasing at, or close to, the new wavelength the device may then experience frequency deviation caused by thermal transients induced from the tuning current switch. The timescale of this frequency deviation is dependent on the thermal time constant of the device and any temperature stabilization scheme employed.

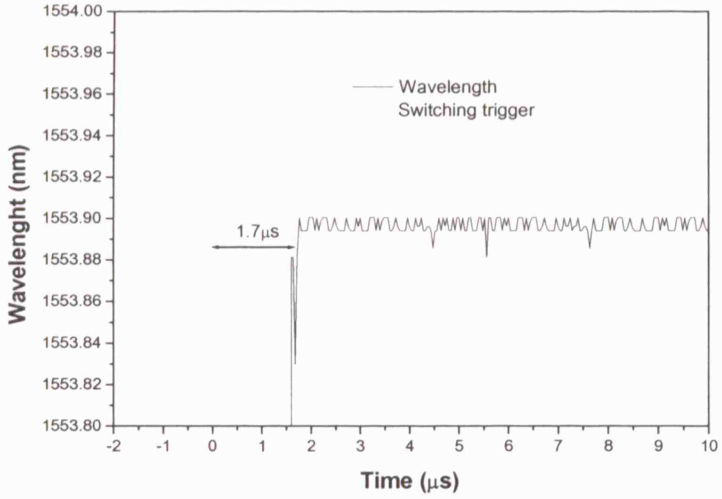

Figure 2-13 Measurement of current driver bandwidth limited switching time for 5mA switch on SG-DBR (TLS2078)

Although the driver bandwidth-limited switching time is broadly constant, the frequency deviation caused by switching-induced temperature variations is a function of the applied tuning current. As described above, this may be measured using the 90% to 10% fall time of the initial wavelength drift excursion. This fall time, together with the total wavelength drift, is shown as a function of the total tuning current switch in Figure 2-14. Measurements were performed using the experimental set-up shown in Figure 2-10 with the laser periodically switched across the transition being studied at a frequency of 1Hz to record scope traces at each wavelength increment. For all measurements the wavelength deviation is measured on the lowest total tuning current on both grating sections where the maximum thermal wavelength deviation occurs.

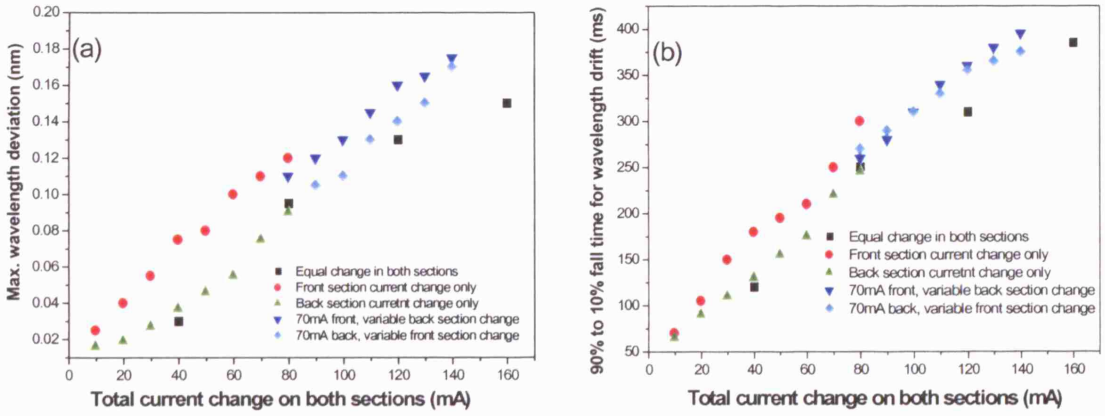

Figure 2-14 (a) Maximum wavelength excursion and (b) 90-10% Fall time of maximum wavelength excursion due to thermal drift for different tuning current switches –TLS2078

Figure 2-14 shows that in general, the thermal wavelength deviation and the time taken for the temperature control loop to respond to the wavelength excursion are proportional to the total tuning current switch. There is also some difference in the size of the wavelength excursion depending on which tuning section sees the largest current switch. In particular, equivalent current switches on the front section seem to cause larger wavelength excursions and it is thought this can be explained by asymmetry in the location of the thermistor. These measurements show that thermal wavelength drift occurs over the full range of timescales envisaged for Type II OBS networks burst lengths and illustrate the need to consider their impact for applications to such network architectures. This is described in sections 2.5 and 2.6.

2.4 Effects of finite switching time on BER - Inter-channel crosstalk

An undesirable feature of CIE tuned semiconductor lasers is the presence of crosstalk from the activation of intermediate modes during switching transitions that can cause BER penalties in WDM based systems [Kei99]. The aim of the experiments described in this section is to quantify the effect of this and to establish if such devices would require blocking of the device output during the switching transition to prevent interference in multi-wavelength networks. Additionally, the measurements described in this chapter aim to provide an indication of the duration of the required wavelength shielding (blanking) and assess any implication on network burst length.

2.4.1 Crosstalk in CIE semiconductor lasers

The presence of crosstalk in CIE tuned semiconductor lasers is evident from the output wavelength characterisation charts shown in section 2.2 and repeated again for a SG-DBR device in Figure 2-15. For this device, a switching transition from λ_1 to λ_2 can be induced by changing the front grating section from 8mA to 25mA. In doing so a number of modes around λ_3 and λ_4, corresponding to current injection levels at 12mA and 16mA are temporarily excited. The power of these spurious modes may reach that of the steady state device output power with the duration set by the driver bandwidth. Figure 2-15 shows a measurement of switching crosstalk made with a high resolution OSA for the 17mA switch with the switching time of 30μs due to current driver bandwidth limitation. Since the OSA averages over several ms the scan does not provide

accurate power measurements of the intermediate modes but does show how the spurious modes may be predicted from the device tuning map.

Table 2-5 Summary of wavelengths used for tunable laser crosstalk measurements

	Wavelength (nm)	Front section current (mA)	Rear section current (mA)	Gain section current (mA)	Phase section current (mA)
λ_1	1541.2	8	16	195	0.23
λ_3	1547.94	12	16	195	0.23
λ_4	1554.88	16.8	16	195	0.23
λ_2	1561.81	25	16	195	0.23

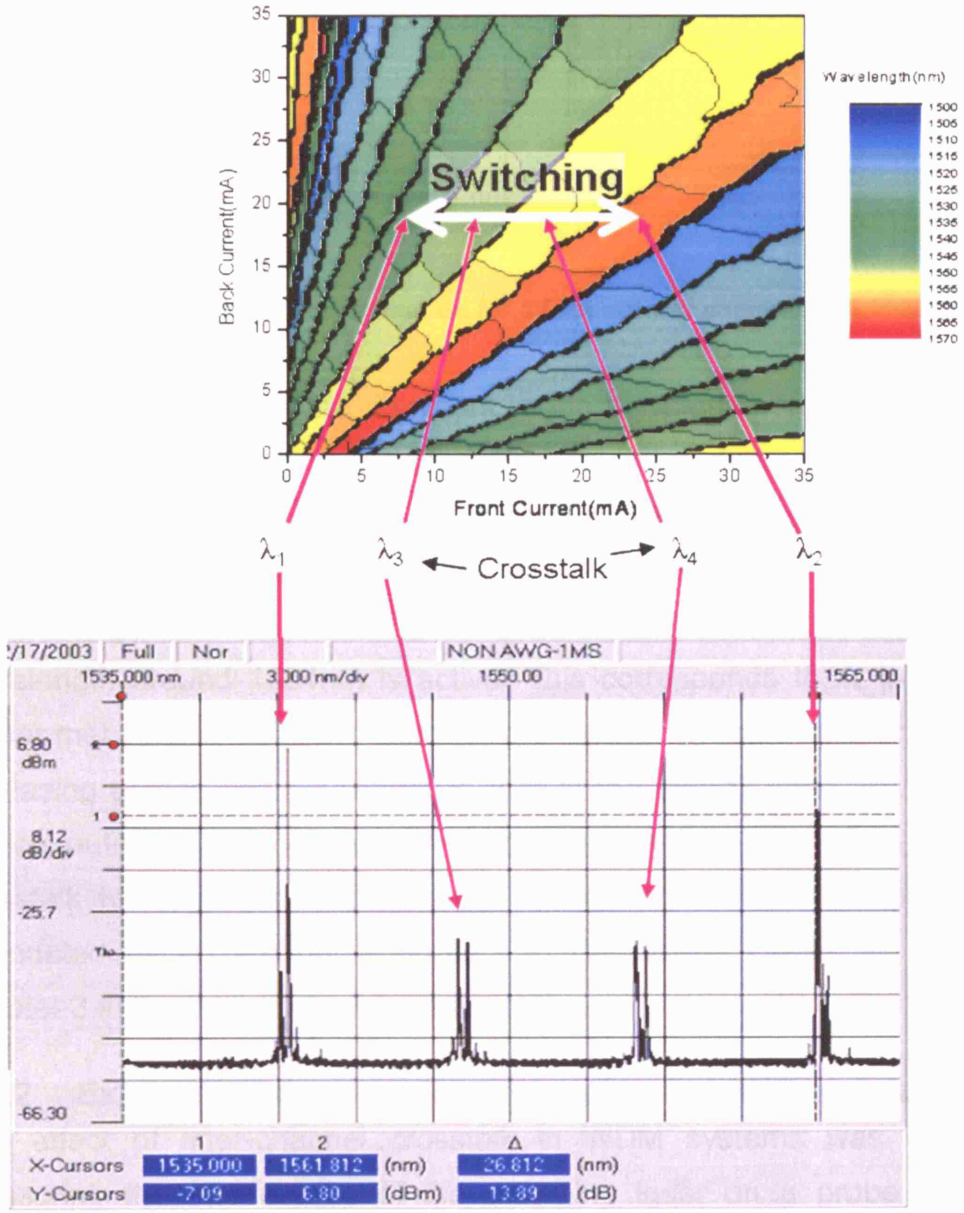

Figure 2-15 Identification of cross talk wavelengths in SG-DBR laser TLS2032 from characterisation chart (top) and OSA scan(bottom) –power values inaccurate

The duration and the power of the intermediate modes were studied using the set up in Figure 2-10. To capture the detail of the switching transition the bandwidth of the current drivers were limited to 50 kHz. Figure 2-16(a) shows

the same transition from λ_1 to λ_2 with Figure 2-16(b) showing the reverse transition from λ_2 and λ_1. Here, the output wavelength shown at any point in time is that with the highest power although competing modes may be lasing simultaneously.

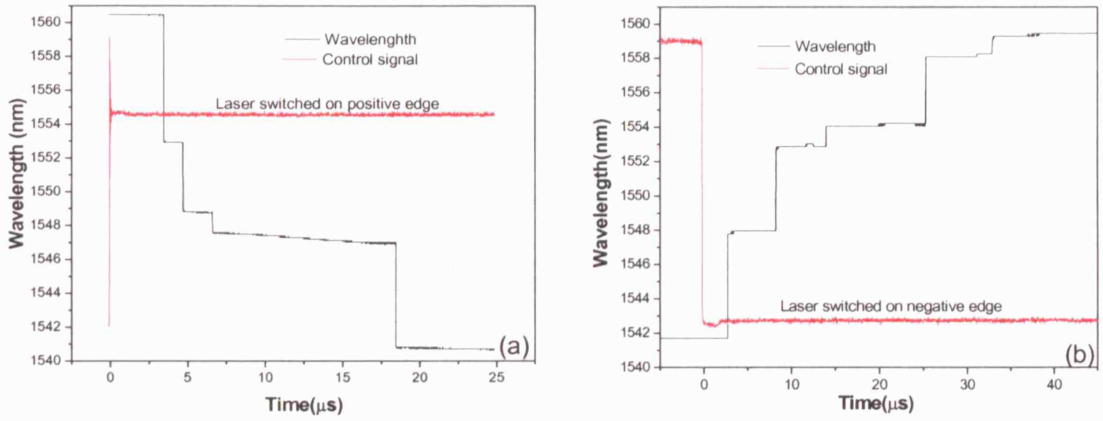

Figure 2-16 Detailed switching transition for 17mA current change in TL2032 (a) λ_1 to λ_2 and (b) λ_2 to λ_1

Figure 2-16 shows that the dominant lasing wavelength changes a number of times across the switching transition and that some degree of hysteresis exists since different excited modes are excited in the reverse transition. In Figure 2-16(a) the predominant intermediate mode is around 1547 nm, corresponding to λ_4 in Figure 2-15, but in Figure 2-16(b) for most of the switching time a wavelength around 1554nm is active. This corresponds to λ_4 in Figure 2-15. Power measurements of the intermediate modes revealed that for some modes the lasing power was equivalent to that of the steady state wavelengths and device output power. Hence, to completely remove the effect of switching crosstalk for application as an OBS transmitter, the laser output should be attenuated by an amount equivalent to the device OSNR as discussed in chapter 3 in the design of such a transmitter.

2.4.2 Experimental set-up for probe channel BER measurements

The effect of inter-channel crosstalk in WDM systems was quantified by measuring the interference of the switching laser on a probe signal in an experimental model of a dynamic OBS link. This was done by considering the bit-error-rate (BER) of a modulated probe channel. As shown schematically in Figure 2-17, a switching tunable laser represents an edge router transmitter in an OBS link continuously assigning bursts to λ_{B1} and λ_{B2} set to match λ_1 and λ_2 shown in Figure 2-15. This signal is then combined with a continuous signal

from a second edge router at λ_P representing a WDM signal sharing the same fibre and subject to switching crosstalk interference.

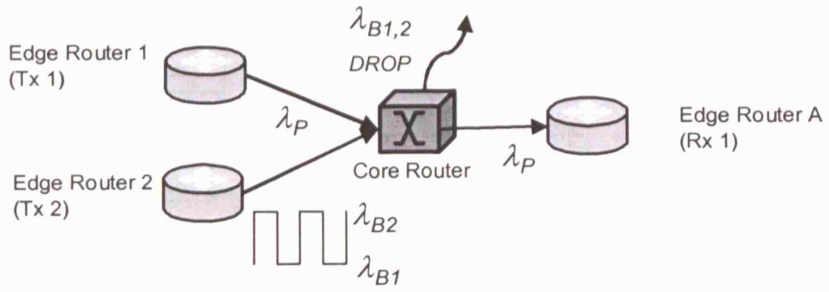

Figure 2-17 Schematic of OBS model for measurement of switching crosstalk impairment

The experimental implementation shown in Figure 2-18(a) was based on a scheme where a single core router was used to combine signals from two edge routers. Tunable wavelength transmitters were used to generate both the probe channel and the switching burst channel. The probe channel wavelength (λ_P), generated from Tx_1, was set to match the region of switching crosstalk identified at λ_4 ($\approx$1554nm) and modulated with a 10Gbit/s non-return-to-zero (NRZ) pseudo-random-binary-sequence (PRBS) of length 2^{15}-1. This was transmitted through an arrayed waveguide grating (AWG) which performed the wavelength routing functionality and received at a third edge router. The switching crosstalk was generated from burst-mode operation of Tx_2 which was switched with a 50% duty cycle between λ_1 (λ_{B1}) and λ_2 (λ_{B2}) and the switching period was varied to investigate the impact of burst length in a network context.

The interference effects caused by switching crosstalk were sufficiently high so as to allow direct measurement of the BER of the modulated probe channel as a function of receiver power using the pulse pattern generator (PPG) and BER test-set (BERT). The receiver used a high-Q filter based clock recovery and this is shown in more detail in Figure 2-18(b). For such a clock recovery scheme, since an NRZ intensity modulated signal does not usually contain a strong clock signal, [Raz96], it is necessary to use a frequency multiplier to double the RF frequency of the data signal. Once doubled, a narrow band amplifier centred at the clock frequency is used to ensure strong tones around the clock frequency which may then be extracted using a high-Q filter. The bandwidth of the high Q filter sets the locking time of the burst-mode clock recovery and was chosen to be 10 MHz for this receiver as a trade-off between locking performance and noise on the clock of the signal.

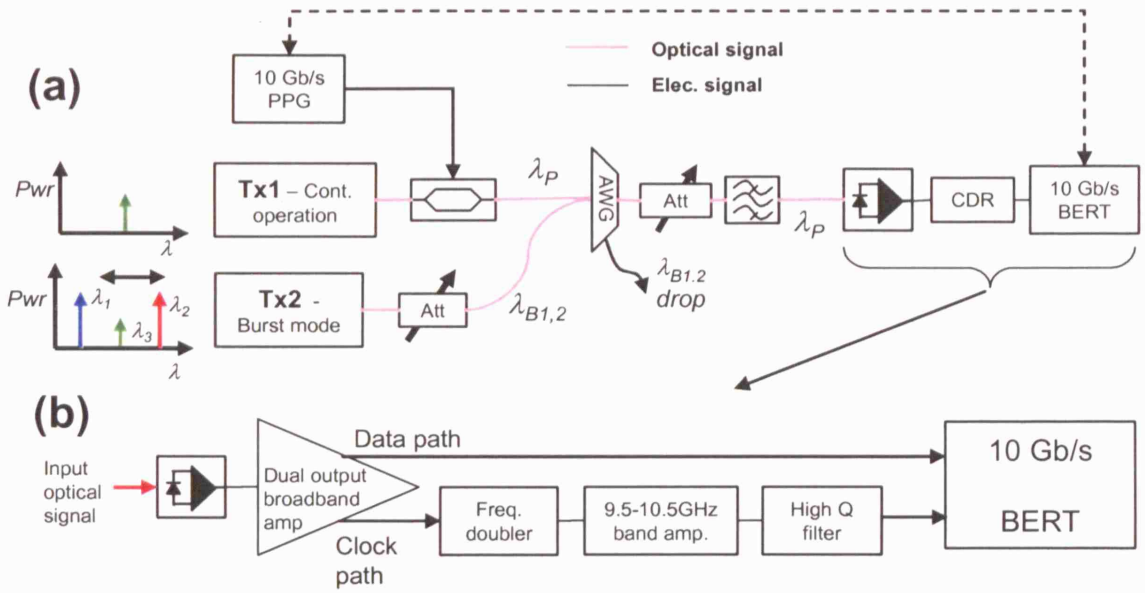

Figure 2-18 Experimental set-up for switching crosstalk measurements

2.4.3 Scanning probe channel measurements

The initial experiment used the same laser and switching transition identified in section 2.4.1. The OSA scan used to identify switching crosstalk in Figure 2-15 showed the presence multiple closely spaced modes around 1554nm excited during switching. To investigate the impact this cluster of modes will have in a multi-wavelength network environment the probe channel was scanned across a 1nm wavelength range. To determine the effect of burst length on any measured impairment this measurement was repeated for 2 switching intervals typical of Type II OBS networks, 1ms and 10ms.

For both burst lengths, the interference from the switching cross talk caused an error floor on the probe channel. The value of the error floor varied as a function of the probe channel wavelength and was observed across the band of wavelengths for which switching crosstalk was observed in Figure 2-15. Figure 2-19 shows the value of the measured error floor for each wavelength and burst length.

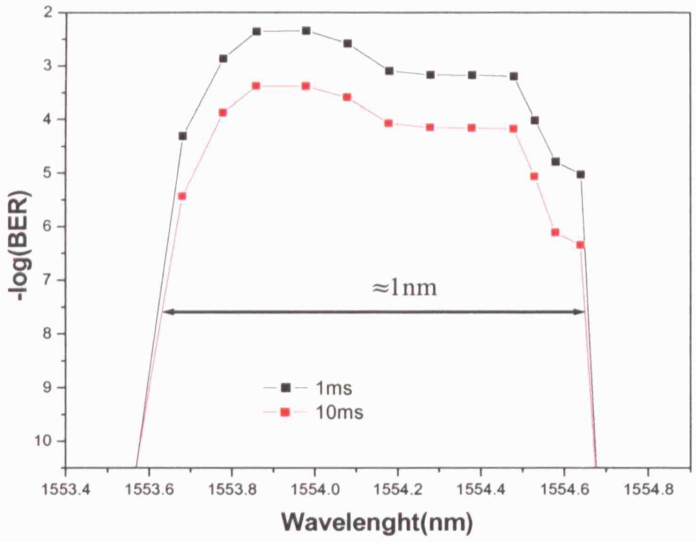

Figure 2-19 BER error floor value vs wavelength for 1 and 10ms bursts with TL2032 switching between 1541.2 to 1562.8 with 17mA change in front tuning current

Figure 2-19 shows the wavelength profile of the potential disruption a single switching transition could have in a WDM system. As could be expected, reducing the burst length and increasing the rate at which the switching transitions occur increases the frequency of errors caused by switching crosstalk. Hence, increasing the burst length by an order of magnitude from 1 to 10ms also reduced the BER by an order of magnitude in the centre of the cross talk band.

Figure 2-19 shows the impact switching crosstalk has on a WDM based network. The region studied corresponds to one of the 2 regions of crosstalk identified in the OSA scan of Figure 2-15 and shows a significant BER penalty across a region of over 1nm. Assuming the second region (λ_4 in Figure 2-15) causes disruption across a similar wavelength range, it means that a single wavelength transition based on 17mA tuning current could potentially cause BER penalties across a 2nm wavelength band or up to 6 channels from the 50GHz ITU grid. Considering that a real network would consist of many lasers switching across many different wavelengths pairs such results show that blanking of the laser output during switching is imperative for their application to WDM based optical network architectures.

The effect of varying the burst duration was then studied further with a fixed probe channel at 1554.18nm for burst lengths between 5ms and 5 seconds

using the same 17mA current switch. In addition to this, the experiments were repeated using the same wavelengths for λ_{B1} and λ_P but with 80mA current change to λ_{B5} to investigate the effect of larger current changes. These current changes and wavelengths are shown in Table 2-6 and the value of the measured error floor is shown in Figure 2-20.

Table 2-6 Operating point for 80mA switching crosstalk experiments

Name	Wavelength (nm)	Front section Current (mA)	Back Section Current (mA)	Gain Section Current (mA)	Phase Section Current (mA)
λ_{B1}	1541.20	8	16	195	0.23
λ_{B2}	1562.80	25	16	195	0.23
λ_{B5}	1533.84	88	16	195	0.23
λ_P (probe)	1554.18	16.8	16	195	0.23

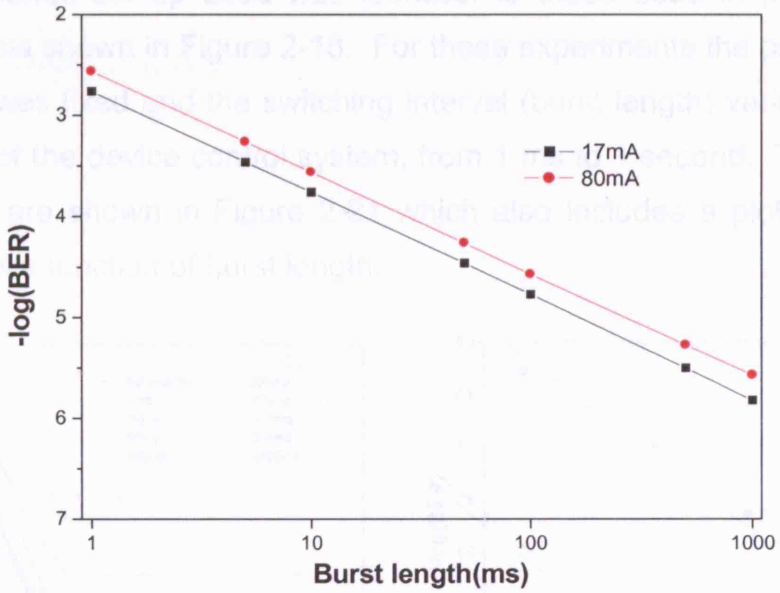

Figure 2-20 Error floor values for different burst lengths for 17mA and 80mA front tuning current switches - TLS2032

Figure 2-20 shows that the burst length is proportional to the value of the error floor for both tuning current switches. As in the previous figure, increasing the frequency of switching transitions increases the impairment caused by switching crosstalk. However, the measured error floor values are higher for the smaller 17mA current change. This is because the switching time is the same for both transitions, as set by the current driver bandwidth. Hence, as evident from Figure 2-15, many more potential lazing modes exist for the 80mA switch mean that amount of time the laser output is matched the probe wavelength is reduced and this is reflected in the frequency of probe channel errors.

2.4.4 Crosstalk in fast switching lasers

All the BER measurements described thus far have been carried out using current drivers with a bandwidth of around 500 kHz. To determine whether the measured impairment caused by switching crosstalk in WDM based networks is still an issue for nanosecond switching transmitters, probe channel experiments were repeated using a fast-tunable laser module. The module was based on a 3-section DBR laser (INT1140) integrated with drive electronics and a microprocessor used to store the operating points. The switching time of this device was measured to be between 20ns and 80ns for all wavelength combinations using the experimental set-up shown in Figure 2-10.

The experimental set up used was identical to those used in previous BER measurements shown in Figure 2-18. For these experiments the probe channel wavelength was fixed and the switching interval (burst length) varied according to the limits of the device control system, from 1 ms to 1 second. The resultant BER curves are shown in Figure 2-21 which also includes a plot of the error floor value as a function of burst length.

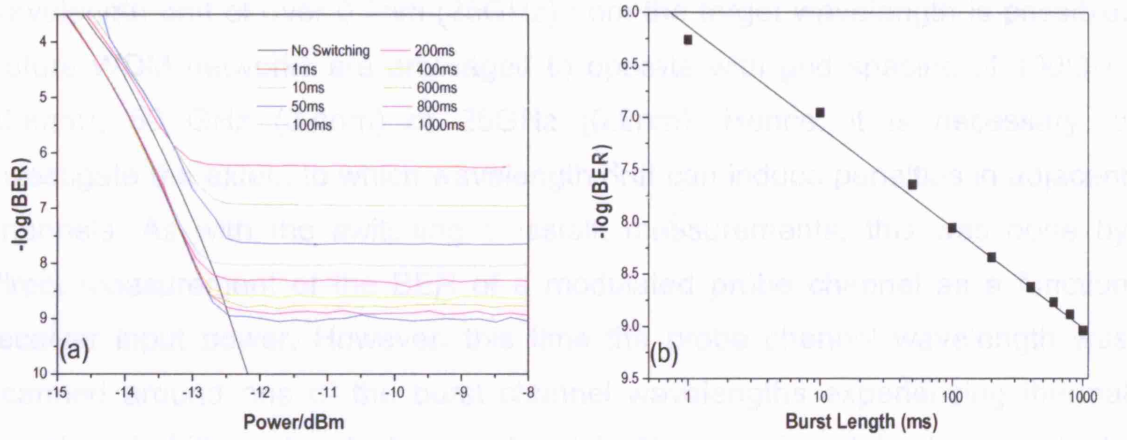

Figure 2-21 (a) BER vs received power showing error floors due to crosstalk from fast switching tunable laser for burst lengths from 1 to 1000ms and (b) value of error floor at each burst length – INT1140

Figure 2-21 shows that despite wavelength tuning times of less than 80ns, crosstalk on the probe channel wavelength was significant enough to produce an error floor for all burst lengths from 1ms to 1second. Since the burst length affects the frequency of switching transitions, the BER value of this error floor decreases linearly with burst size. For 1ms bursts, this error rate corresponds to approximately 10 bits per burst and shows that switching crosstalk also causes

widespread disruption with nanosecond transmitter tuning times. The error floor values for the tunable laser module with nanosecond tuning were approximately 3 orders of magnitude lower than those for the microsecond tuning laser. This can be expected since switching crosstalk is emitted for the duration of the switching transition. These results show the impairment switching crosstalk can have on specific probe channel wavelengths. Since switching crosstalk may be emitted over the entire device tuning range, it is possible to state that the average BER of all channels is proportional to the laser switching time (t_{switch}) and inversely proportional to the average burst length (t_{burst}). Hence,

$$BER \alpha \frac{t_{switch}}{t_{burst}} \qquad (2.1)$$

2.5 Impact of thermal wavelength drift on adjacent channels in a WDM system

Section 2.4 showed that switching crosstalk has the potential to cause severe disruption in a multi-wavelength network. In this section, the focus is interference in adjacent WDM channels from thermally induced wavelength drift on the switched (burst) channel. The measurements in section 2.3 showed that wavelength drift of over 0.2nm (25GHz) from the target wavelength is possible. Future WDM networks are envisaged to operate with grid spacing of 100GHz (0.8nm), 50 GHz (0.4nm) or 25GHz (0.2nm). Hence, it is necessary to investigate the extent to which wavelength drift can induce penalties in adjacent channels. As with the switching crosstalk measurements, this was done by direct measurement of the BER of a modulated probe channel as a function receiver input power. However, this time the probe channel wavelength was scanned around one of the burst channel wavelengths experiencing thermal wavelength drift due to a high current switch. The experimental set-up, similar to that shown in Figure 2-18 and using the same clock recovery scheme, is shown in Figure 2-22.

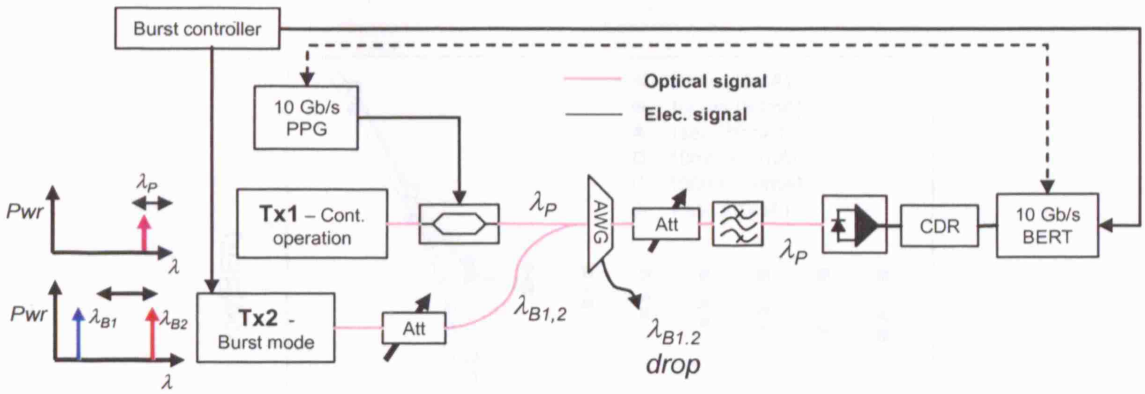

Figure 2-22 Experimental set-up for adjacent WDM probe channel measurement

Measurements of adjacent channel interference caused by thermally induced wavelength drift were made for the worse case scenario of an 80mA tuning current switch with an SG-DBR laser exhibiting wavelength drift of up to 0.1nm. In order to isolate the interference impairment caused by wavelength drift from the spurious modes that arise during the switching transition the measurement of the probe channel BER was gated such that the measurement started after the SG-DBR laser had switched to λ_{B1}. Additionally, to ensure any measured interference was due to wavelength drift and not just from the close proximity of probe and burst channels each measurement was performed for tuning current switch of 80mA (high wavelength drift) and 10mA (negligible thermal drift) to the same 1541.4nm wavelength to allow a comparison. To minimise the interference of the burst channel, a narrow optical filter of 0.28nm 3dB-bandwidth was centred at the probe channel wavelength. The probe channel was scanned up to 0.45nm (>60GHz) either side of λ_{B1}. For comparison with the measured wavelength drift, the BER measurements were carried out for burst lengths (switching frequencies) covering a range of thermal timescales from 10ms to 1 second. The measured plots of BER against receiver power are shown for the case where the probe channel is 50GHz away from the burst channel in Figure 2-23 which includes curve for both 10mA and 80mA tuning current switches.

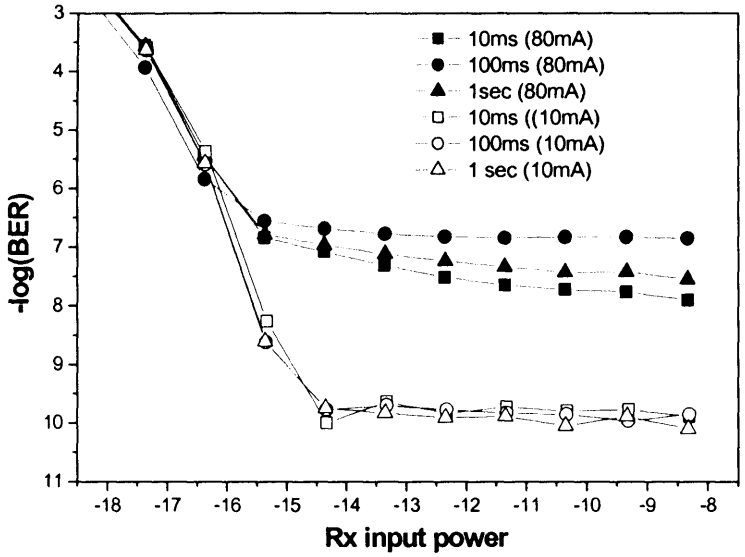

Figure 2-23 Probe channel BER vs receiver power at 50GHz spacing from final wavelength for high and low drift switching – TLS2048

Figure 2-23 shows that at 50GHz spacing the band-pass filter is not able to prevent probe channel interference for either switching transition, however, it does show that the wavelength drift from the high tuning current switch results in error floor values 2-3 orders of magnitude higher than the 10mA switch. With low wavelength drift the error floor occurs for error rates around 10^{-10} and there is no discernible effect caused by changing burst length. However, with high wavelength drift, the error floor values are separated by the burst length. The splitting of these lines can be understood from study of the wavelength drift plot shown in Figure 2-24. The highest error floor occurs for 100ms bursts where wavelength drift shifts the burst channel further into the probe channel filter bandwidth for a larger proportion of the burst length. Hence the burst length dependence of the measured impairment is determined by the thermal response of the device to step changes in tuning current and the response of the temperature control loop.

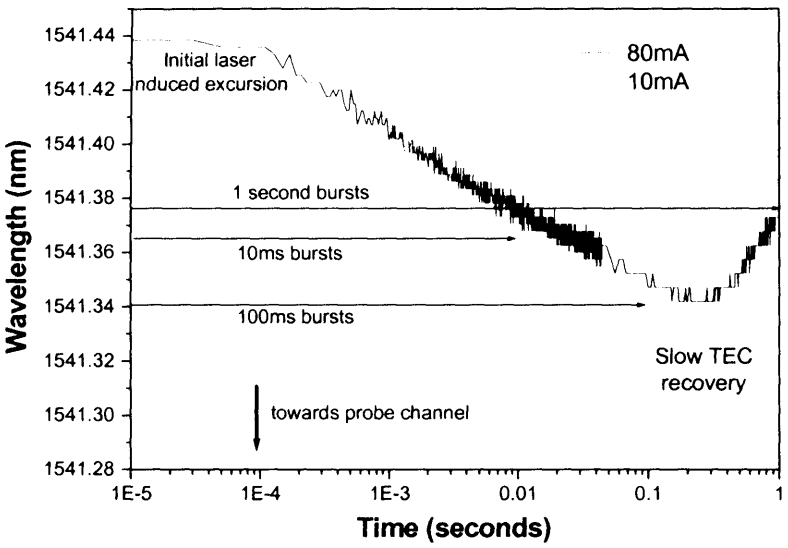

Figure 2-24 Wavelength drift for 80mA and 10mA tuning current switches (TLS2048) as a function of burst length for adjacent channel interference measurements

The wavelength deviation for the 2 switching transitions is also evident in the summary of error floor values for the scanned probe channel. Figure 2-25 shows the error floor values of the measured BER curves for both high and low tuning current switches for 100ms bursts as the probe channel was scanned from -0.4 nm to -0.1 nm and from 0.1 to 0.2 nm away from the burst channel. In Figure 2-24 the majority of the 100ms burst sees wavelength deviation at wavelengths shorter than the final burst channel wavelength. This is also the case for interference measured for the scanning probe channel in Figure 2-25. Again, the presence of interference is inferred by comparing a low current (low wavelength drift) switch with a high current switch (high thermal wavelength drift). For wavelengths longer than the final burst channel wavelength, where the laser output spends less than 1ms in each switching cycle, a difference between the switching current is only observed for probe channel deviations up to of 0.15nm.

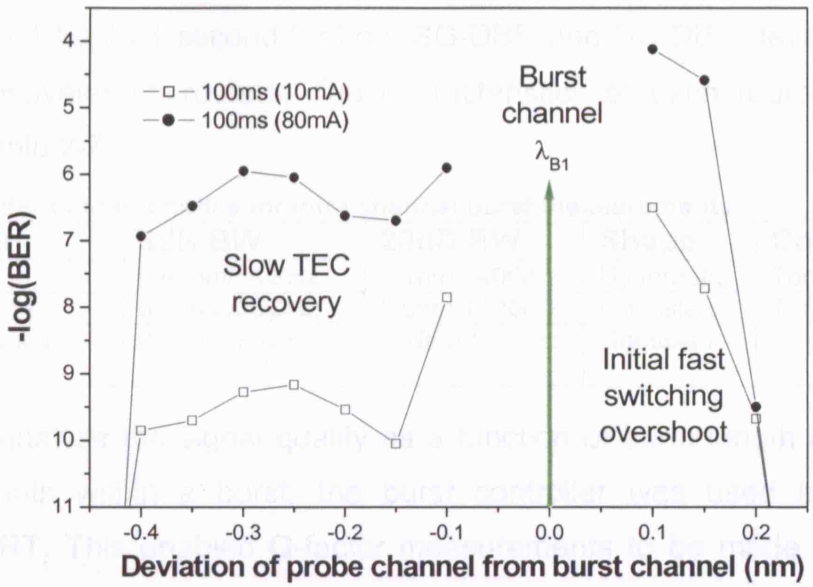

Figure 2-25 BER error floors values for probe channel scanned across switched burst channel (TLS2048) for low and high drift current switching

2.6 Switching optical bursts through finite bandwidth wavelength routers

The measurements in sections 2.4 and 2.5 show that the switching of DBR tunable lasers can interfere and cause bit errors in other WDM channels both from spurious emission during switching and long term wavelength drift after switching. In this section the effect of these impairments on the burst channel itself is investigated. Narrow wavelength routers, with bandwidths approaching that of the measured wavelength drift have the potential to transform wavelength fluctuations such those caused by wavelength drift into amplitude fluctuations that result in transmission penalties. In this work, this penalty is investigated using BER measurements as a function of burst length, router bandwidth and total wavelength drift.

2.6.1 Experimental set-up for Q-factor measurements

The effect that thermally induced wavelength deviation has on the signal passing through a filtering element was investigated using the setup shown in Figure 2-26. The output of a tunable laser (Tx_1) was modulated at 10Gb/s with a NRZ PRBS pattern of length of 2^{31}-1 and its power adjusted using a variable optical attenuator (VOA) at the input of an erbium doped fibre amplifier (EDFA) to give a fixed optical signal-to-noise ratio (OSNR). The EDFA was gain-clamped with an optical feedback loop (described in more detail in chapter 5) to prevent gain transients arising from burst-mode operation. The output of the

laser was switched periodically between two wavelengths for burst lengths ranging from 10μs to 1 second for both SG-DBR and DS-DBR devices and for 3 different wavelength routers. The characteristics of each router used are shown in Table 2-7.

Table 2-7 Router characteristics for intra channel burst measurements

Router type	3dB BW	20dB BW	Shape	Comment
100GHz AWG	0.43nm/54GHz	1.1nm/140GHz	Hyperbolic	Temp. controlled
50 GHz AWG	0.28nm/35GHz	0.9nm/110GHz	Gaussian	Tunable filter
25GHz free-space grating router	0.16nm/20GHz	0.28nm/35GHz	Gaussian	

In order to analyze the signal quality as a function of burst length or rather at different points within a burst, the burst controller was used to gate the receiver/BERT. This enabled Q-factor measurements to be made with gating windows, varied between 1μs and 200ms, and synchronized with the burst. The gating window offset from the start of the burst and the gating window duration was logarithmically increased as it was swept across the entire length of the optical burst, as shown in Figure 2-26(b). This complex gating window allowed for a comparison of the signal quality for different burst lengths. Q-factor measurements were calculated from BER measurements made as the decision-threshold voltage was swept across the 1 and 0 voltage levels as described fully in [Ber93]. All BER measurements were compiled from a number of switching transitions with the measurement time varied to ensure that measurements for each timing window were made using the same total number of bits.

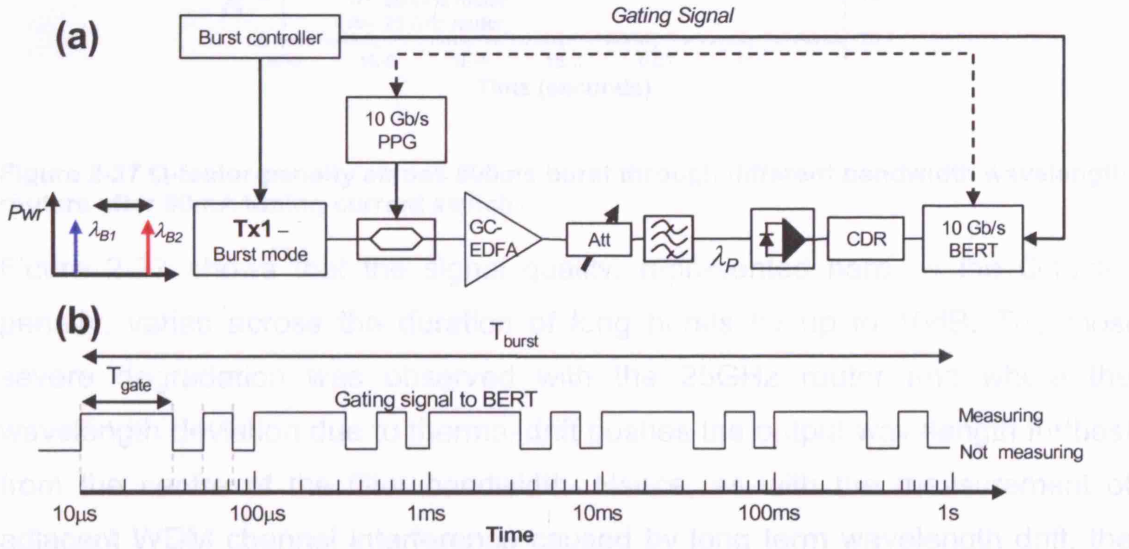

Figure 2-26 (a) Experimental set-up for gated BER measurements to study signal quality across long bursts and (b) timing windows used for Q-factor measurements across 1 second burst.

2.6.2 BER measurements of bursts with wavelength drift through different router bandwidths

Initial measurements of burst signal quality were carried out using the logarithmic sliding timing window for the maximum single tuning current switch (80mA) on an SG-DBR laser for each of the 3 routers. The target wavelength λ_1 for all measurements was 1550.92nm (193.3THz) with the second wavelength λ_2 was a dependent on the tuning current change studied. The signal was then passed through each of the routers and the Q-factor measurement performed for each of the timing windows shown in Figure 2-26(b). In each case the centre of the router pass-band was aligned with the final wavelength for the switching transition used. The OSNR, measured at 0.1nm bandwidth, was maintained at 35dB for all measurements. The results for all 3 router bandwidths together with the measured wavelength drift for the particular tuning current switch is shown in Figure 2-27.

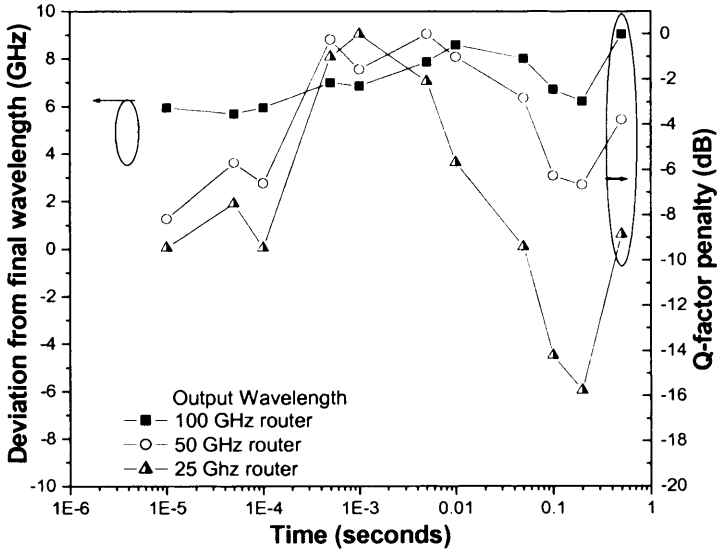

Figure 2-27 Q-factor-penalty across 500ms burst through different bandwidth wavelength routers after 80mA tuning current switch

Figure 2-27 shows that the signal quality, represented here by the Q-factor penalty, varies across the duration of long bursts by up to 16dB. The most severe degradation was observed with the 25GHz router and where the wavelength deviation due to thermal drift pushes the output wavelength furthest from the centre of the filter bandwidth. Hence, as with the measurement of adjacent WDM channel interference caused by long term wavelength drift, the magnitude of the signal degradation becomes a function of burst length.

2.6.3 Q-factor penalty vs tuning current

The Q-factor penalty, and wavelength deviation, was plotted as a function of the tuning current switch for both SG-DBR and DS-DBR devices. The same experiment described in the previous section was carried out for both lasers using a number of tuning currents for a single router bandwidth. For the DS-DBR the 50GHz router was used with tuning current switches from 10 to 50mA. For the SG-DBR laser, the 100GHz router was used with tuning current switched up to 80mA used. Both sets of results are shown in Figure 2-28.

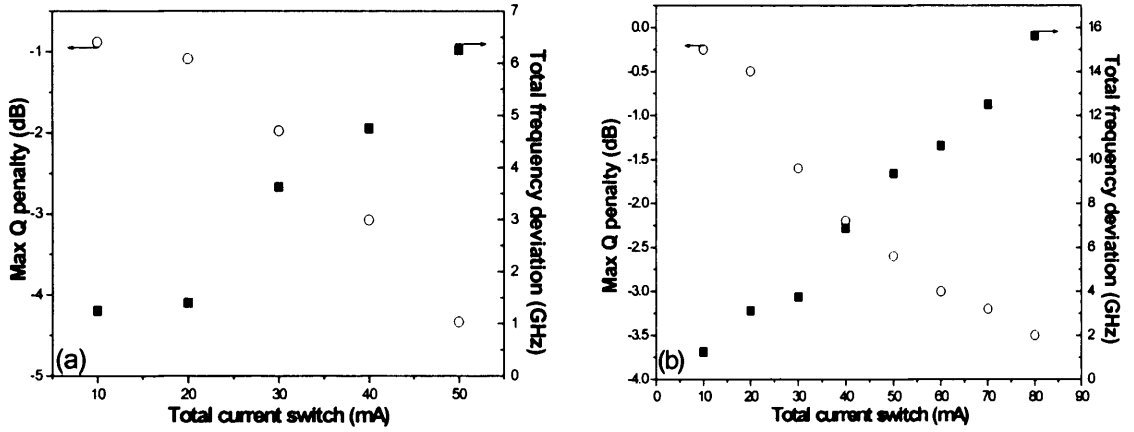

Figure 2-28 Total Q-factor variation and wavelength drift versus tuning current for (a)DS-DBR (TLD1002) and 50GHz router and (b) SG-DBR (TLS2048) with 100Ghz AWG

The relationship with tuning current shown in Figure 2-28 for both lasers confirms that the measured Q-factor penalty is a result of wavelength drift induced from high current switching and shows that the performance characteristics of the transmitter required for optimum performance are set by the design of the core network routers.

2.6.4 Switching laser through finite bandwidth routers-simulation

The magnitude of the measured Q-factor penalty was verified by a simple simulation of the experimental set-up by calculating the Q-factor/BER of a 10 Gb/s NRZ signal, passing through an optical filter as a function of wavelength deviation for a fixed wavelength transmitter. The filter bandwidth and offset from the centre of the pass-band and level of added noise were chosen to replicate the measurements described in section 2.6.2.

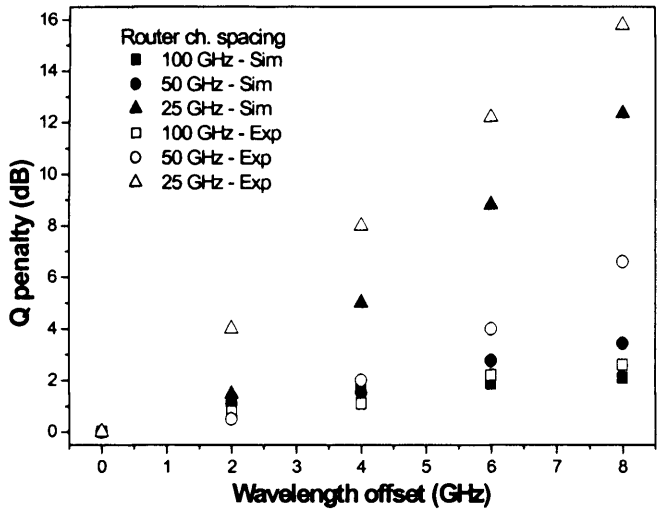

Figure 2-29 Comparison of measured and simulated Q-factor penalty for wavelength offsets through different bandwidth filters – TLS2048

Figure 2-29 shows reasonable agreement between the predicted and measured Q-factor penalty for all filter bandwidths. However, in almost all cases, particularly at the highest measured wavelength deviation of up to 8GHz, the measured Q-factor penalty exceeds the predicted value. The additional penalty is thought to be caused by the additional noise added by the current drivers. Since the response of each of the tuning section is dependent on the level of current injection, noise in the current drivers causes small fast timescale wavelength deviations which are translated into amplitude and subsequently Q-factor fluctuations in the presence of a narrow filter. Indeed, subsequent analysis revealed that the current drivers used in these measurements were susceptible to interference from noise in the mains power supply which was then detectable in the current output.

Despite this, the results of these measurements and the simulation results show that thermal wavelength drift alone is also responsible for significant signal degradation of the burst channel itself. This signal degradation, quantified by considering the Q-factor penalty, is dependent on the magnitude of the wavelength drift but more crucially on the bandwidth of the optical routers used. Based on both measured and simulated data, Figure 2-29 shows that wavelength drift of up to ±2GHz caused a minimal Q-factor penalty of around 1dB for both the 100GHz and 50GHz spaced routers or 1GHz for the 25GHz router. These results, together with those in 2.6.3 show that for both DBR laser types, for the wavelength drift caused by tuning currents required to access

operating points across the C-band, an additional wavelength stabilization scheme is required and the wavelength stability required depends on the core router bandwidth.

2.7 Summary

This chapter described and investigated the operation of monolithic semiconductor tunable lasers and their application to DONs. The work used a series of experimental measurements to investigate and quantify the impact of switching crosstalk and long term wavelength drift in WDM network environment for the first time. The thermal drift measurements extended the study of these devices from the previously studied μs timescales, to the ms timescale applicable to Type II OBS networks. The results obtained, show the performance requirements of a burst-mode transmitter and are used in the design of such a transmitter described in Chapter 3.

The characterization data in section 2.2 revealed how detailed device specific characterization is crucial for identification of sets of operating points with desirable switching characteristics across the desired tuning range. In section 2.3, sub-ns time and pico-metre wavelength measurements were used to identify possible sources of impairment in the context of DONs. Sections 2.4 to 2.6 provided quantitative measurements of the impairment caused by these features using experimental model of a Type II OBS networks.

Section 2.4 showed that emission of spurious lasing modes the switching transition generates background crosstalk that interference to other WDM channels across the network. A single switching transition was shown to corrupt up to 1 bit in 1000 across a 1nm wavelength range and similar impairment was observed with the fast switching tunable laser module which showed that the BER is proportional to the laser switching time and inversely proportional to the number of switching transitions (average burst length) of the network scheme in operation. Hence, blanking of the laser output during the switching transition is essential for the application of such devices to DONs to prevent widespread impairment due to background crosstalk. The power of these spurious modes was measured to match the steady state output power of the device showing that any blanking mechanism should provide attenuation of the laser output

equivalent to OSNR of the transmitted bursts. Techniques for implementing this blanking are discussed in chapter 3.

Finally, the impact that long term wavelength drift caused by high current switching can have in WDM networks was investigated in terms of adjacent channel interference and on the burst channel. The typical thermal time constants in the ms regime mean that this effect is particularly critical over the Type II OBS network timescales and can be ignored in shorter burst length schemes. Section 2.5 showed that wavelength drift due to high current switching in SG-DBR lasers can interfere with adjacent WDM channels separated by 50GHz with a scanned probe channel identifying the key switching features of initial laser excursion and overcompensation by TEC. Subsequently, wavelength drift was shown to interfere with neighbouring channels in an optical label switching system [Con07] and in 25GHz and 12.5GHz DWDM systems. For the DWDM system it was observed that the interference could be reduced by increasing the blanking time of the tunable laser at the cost of network efficiency.

Section 2.6 looked at the impairment caused by thermal wavelength drift on the burst channel itself as it passes through narrow wavelength routers. Q-factor penalties of up to 3dB were observed with a standard AWG router with 100GHz channel spacing due to thermal wavelength drift. For the 25GHz router, a Q-factor penalty of 16dB was observed. For a 1dB Q-factor penalty, it was found that wavelength drift of up to 2GHz was possible for 50GHz and 100GHz spaced WDM system compared to 1GHz for a 25GHz spaced system.

The results in this chapter show that for DBR based laser designs, where high current switching is required to access the desired tuning range, an additional control system is needed to reduce thermal wavelength excursions for schemes with millisecond burst lengths. Several techniques are possible to implement wavelength locking or stabilization of the output wavelength of semiconductor tunable lasers and these are discussed in Chapter 3 which looks at the design of a burst-mode transmitter based on the tunable laser technology investigated in this chapter. In addition to a wavelength locking control loop, the proposed

transmitter makes use of fast control of integrated SOAs to provide blanking of the laser output during the switching transition.

2.8 References

Ama98 **Tunable laser diodes**
M.C Amann and J. Buus published Artech House (1998)
(a) Ext cavity mechanically tuned lasers pg 207-211
(b)Thermal tuning pg91-92 QCSE pg 90-91
(c) QCSE pg 90-91
(d) Free carrier plasma Effect Pg 86-90
(e) SG-DBR response pg 167-177
(f) Y-Brach laser Pg178-181

Bag90 **242 nm continuous tuning from a GRIN-SC-MQW-BH InGaAsP laser in an extended cavity**
M.Bagley, R.Wyatt, D.J.Elton, H.J.Wickes, P.C.Spurdens, C.PSeltzer, D.M.Cooper, W.J.Devlin. Electronics Letters, Vol. 26, (4), 15 pp267-269 Feb. 1990

Ben90 **Carrier-induced change in refractive index of InP, GaAs and InGaAsP**
B.R.Bennett, R.A.Soref, J.A.Del Alamo. IEEE Journal of Quantum Electronics, Vol. 26 (1), pp 113-122, Jan. 1990

Ber04 **Fast wavelength switching using digitally tunable external cavity laser** A. A.Bergonzo, R.Brenot, M.Picq, O.Legouezigou, J.Landreau, H.Sillard, J.Jacquet, Electronics Letters , Vol. 40 (10) , pp:617 – 618, 13 May 2004

Ber93 **Margin measurements in optical amplifier system**
N.S.Bergano, F.W.Kerfoot, C.R.Davidsion. IEEE Photonics Technology Letters, Vol. 5 (3), pp 304-306, March 1993

Bha03 **Demonstration of stable wavelength switching on a fast tunable laser transmitter**
A.Bhardwaj, J.Gripp, J.E.Simsarian, M.Zirngibl. Photonics Technology Letters, IEEE, Vol. 15, (7), pp 1014 – 1016 July 2003

Bus02 **A widely tunable Digital Supermode DBR laser with high SMSR**
G.Busico, N.D.Whitbread, P.J.Williams, D.J.Robbins, A.J.Ward, D.C.J.Reid. Tech. Digest of European Conference on Optical Communication Vol. 2, pp1-2, 2002

Cai94 **MQW tuned semiconductor lasers with uniform frequency response**
B.Cai, A.J. Seeds and J.S Roberts. IEEE Photonics Technology Letters, Vol. 6, (4), pp 496 – 498, April 1994

Cai98 **MQW tuned semiconductors lasers**
B.Cai and A.J.Seeds. Electronic Letters, no,25, pp145-146, 1998

Con07 **Cross-Channel Interference Due to Wavelength Drift of Tunable Lasers in DWDM Networks**
E.Connolly, F.Smyth, A.K.Mishra, A Kaszubowska-Anandarajah, L.P.Barry. IEEE Photonics Technology Letters, Vol. 19, (8), pp616-618, April15 2007

Del98 **Widely tunable 1.55-μm lasers for wavelength-division-multiplexed ptical fibre communications**
F.Delorme. IEEE Journal of Quantum Electronics,Vol.34 (9) pp1706-1716, Sept. 1998

Duc05 **Design and analysis of DS-DBR lasers for C- and L-band, achieving a combined count of over 200 consecutive 50 GHz spaced channels**
J.P.Duck, L.Ponnampalam, A.J.Ward, D.J.Robbins, G.Busico, N.D.Whitbread, D.C.J.Reid. Tech. Digest of European Conference on Optical Communication, Vol. 4, pp 895-896, 25-29 Sept. 2005

Dus02 **Analysis of a dynamically wavelength-routed optical burst switched network architecture**
M. Düser, P. Bayvel. Journal of Lightwave Technology, Vol.20 (4), pp574-586, April 2002

Far99 **Complete wavelength control of GCSR lasers over EDFA band**
T.Farrell, J.Dunne, R.O'Dowd. Tech. Digest of Lasers and Electro-Optics Society Vol. 1, 8-11 pp 329 – 330, Nov. 1999

Fis01 **Monolithic widely-tunable DBR lasers**
G.A.Fish. Tech. Digest of Optical Fibre Communication Conf., Vol. 2, ppTuB1-1 - TuB1-4, 2001

Gus03 **Record output power (25 mW) across C-band from widely tunable GCSR lasers without additional SOA**
Y.Gustafsson, S.Hammerfeldt, JHammersberg, M.Hassler, T.Horman, M.Isaksson, J.Karlsson, D.E.Larsson, O.D.Larsson, L.Lundqvist, T.Lundstrom, M.Rask, P.J.Rigole, E.Runeland, A.Saavedra, G.Sarlet, R.Siljan, P.Szabo, L.Tjernlund,O.Traskman, H.de Vries, J.O.Wesstrom, C.Ogren. Electronics Letters, Vol. 39 (3), pp 292-293, Feb. 2003

Har00 **Tunable long-wavelength vertical-cavity lasers: the engine of next generation optical networks?**
J.S.Harris. IEEE Journal of Selected Topics in Quantum Electronics, Vol. 6 (6), pp 1145 – 1160, Nov.-Dec. 2000

Har07 **Design, Fabrication and Application of Integrated VCSELs**
J.S.Harris, Nano-Optoelectronics Workshop, 2007, pp85 – 86, Aug. 11 2007

Ima01 **Wideband athermal wavelength monitor integrated wavelength temperature-tunable DFB-LD module**
M.Imaki, S.Yamamoto, M.Sato, Y.Nishimura, K.Masuda, S.Takagi, A.Adachi, J.Yamashita, Y.Hirano. Electronics Letters Vol. 37, (16), pp1035-1036, 2 Aug. 2001

Ish93 **Multiple-phase shift super structure grating DBR lasers for broad wavelength tuning**
H.Ishii, Y.Tohmori, Y.Yoshikuni, T.Tamamura, Y.Kondo. IEEE Photonics Technology Letters, Vol. 5,(6), pp 613 – 615, June 1993

Ish93/2 **Super-structure-grating (SSG) for broadly tunable DBR lasers**
H.Ishii, Y.Tohmori, Y.Yoshikuni, T.Tamamura. IEEE Photonics Technology Letters, Vol. 5 (4) pp 393 – 395, April 1993

Ish96 **Quasicontinuous wavelength tuning in super-structure-grating (SSG) DBR lasers**
H.Ishii, H.Tanobe, F.Kano, Y.Tohmori, Y.Kondo, Y.Yoshikuni. IEEE Journal of Quantum Electronics, Vol. 32 (3), pp433-441 March 1996

ITU06 http://www.itu.int/rec/T-REC-G.694.1-200206-I/en

Jay93 **Extended tuning range in sampled grating DBR lasers**
V.Jayaraman, A.Mathur, L.A.Coldren, P.D.Dapkus. IEEE Photonics Technology Letters, Vol. 5 (5), pp 489 - 491 May 1993

Kau03 **16-channel digitally tunable external-cavity laser with nanosecond switching time**
M.Kauer, M.Girault,J.Leuthold, J.Honthaas, O.Pellegri, C.Goullancourt, M. Zirngibl. IEEE Photonics Technology Letters,Vol. 15 (3), pp 371-373 March 2003

Kei99 **A review of WDM Technology and Applications**
G.E Keiser, Optical Fibre Tech., Vol. 5, pp3-39, Jan. 1999,

Klo03 **Fast control circuit for a GCSR tunable Laser for Applications in Optical Packet Switching**
D. Klondis, G. Zervas, C. Politi, M. Simeonidou, M. O'Mahoney. Tech. Digest of European Conference on Networks and Optical Communications 2003.

Kos04 **Thermal effects in monolithically integrated tunable laser transmitters**
P.Kozodoy, T.A.Strand, Y.A.Akulova, G.Fish, C.Schow, Ping-Chiek Koh; Zhixi Bian; J. Christofferson, A.Shakouri. IEEE Transactions on Components and Packaging Technologies, Vol. 28, (4), pp 651 – 657, Dec. 2005

Kus93 **Dynamics of frequency switching in tunable asymmetric Y-branch lasers**
M.Kuznetsov, N.K.Shankaranarayanan, P.Verlangieri, A.G.Dentai. IEEE Photonics Technology Letters, Vol. 5, (6), pp 625 - 627 June 1993

Lam95 **Carrier thermalization by phonon absorption in quantum-well modulators and detectors**
Y.L Lam and J. Singh Journal of Quantum Electronics Vol 31, no. 5 pp 923-926

Lav00 **Rapid Tunable Transmitter with Large Number of ITU channels Accessible in less than 5ns**
O. A. Lavrova, G. Rossi and D. J Blumenthal. Tech. Digest of European Conference on Optical Communications Vol.2, pp169-170 Sept. 2000

Lig04 http://www.lightreading.com/document.asp?site=ofc&doc_id=47567

Mas07 **Tunable Erbium Doped Fibre Laser Using a Silicon Micro-Electro-Mechanical Fabry-Perot Cavity**
J.Masson, S.Bergeron, A.Poulin, N.Godbout, Y-A,Peter. IEEE/LEOS International Conference on Optical MEMS and Nanophotonics, pp171-172, July 16-Aug.12 2007

Mas98 **Tunable sampled-grating DBR lasers with integrated wavelength monitors**

B.Mason, S.P.DenBaars, L.A.Coldren. IEEE Photonics Technology Letters, Vol. 10, (8), pp 1085 – 1087, Aug. 1998

Mul02 **Full-coverage microsecond wavelength switching of a monolithic widely tunable laser, from any channel to any channel, over the entire C band on the ITU G.682 ITU grid**
T. Mullane, D. McDonald, T. Farrell, and J. Dunne. Proc SPIE Conf. Opto-Ireland Optics and Photonics Technologies and Applications, pp. 260-265, 2002

Mul03 **Thermal contribution to wavelength switching characteristics of widely tunable lasers**
G. Mulvihill, Y.Yu, S.O'Duill,R.O'Dowd. Tech. Digest of The 16th Annual Meeting of the IEEE Lasers and Electro-Optics Society, LEOS 2003. Vol. 2, pp640 - 641,2003

Mul99 **Ultrafast measurements of an SG-DBR laser with picosecond time and nanometre wavelength resolution using a Fabry-Perot interferometer**
T.Mullane,T.Farrell, J.Dunne, Yonglin Yu, R.O'Dowd. Tech. Digest of 12th Annual Meeting.IEEE Lasers and Electro-Optics Society Vol 2, pp 894 – 895, 8-11 Nov. 1999

O-Do01 **Frequency Plan and Wavelength Switching limits for Widely Tunable Semiconductor Transmitters**
R.O'Dowd, S.O'Duill, N.O'Gorman, G.Mulvihill, and Y.Yonglin. Journal of Quantum Electronics, Vol. 7, No. 2, March/April 2001

Pan06 **Monolithically integrated QCSE-tuned InGaAsP MQW ridge waveguide DBR laser**
M.Pantouvaki, C.P.Liu, C.C.Renaud, S.Cole, M.Robertson, R.Gwilliam, A.J.Seeds. Tech. Digest of Conf. on InP and Related Materials, pp:72-74, 7-11 May 2006

Pan07 **Fast Tuneable InGaAsP DBR Laser Using Quantum-Confined Stark-Effect-Induced Refractive Index Change**
M.Pantouvaki, C.C.Renaud, P.Cannard, M.J.Robertson, R.Gwilliam, A.J.Seeds. IEEE Journal of Selected Topics in Quantum Electronics, Vol. 13, Part 1, pp 1112 - 1121 Sept/Oct. 2007

Pon05 **Dynamic control of wavelength switching and shuttering operations in a broadband tunable DS-DBR laser module**
L.Ponnampalam, R.Barlow, N.D.Whitbread, D.J.Robbins, G.Busico, J.P.Duck,,A.J.Ward, D.C.J.Reid, P.J.Williams. Tech. Digest of Optical Fibre Communication Conf., Vol. 2, 6-11 March 2005

Pon06 **Dynamically controlled channel-to-channel switching in a full-band DS-DBR laser**
L.Ponnampalam, R.Barlow, N.D.Whitbread, G.Busico, J.P.Duck, A.J.Ward, D.J. Robbins. IEEE Journal of Quantum Electronics, Vol. 42 (3), pp223-230, March 2006

Qin03 **Multiwavelength erbium-doped fibre lasers with active overlapping linear cavities**
M.Qinghe, J.W.YLit. Journal of Lightwave Technology, Vol.2 (1), pp160-169, Jan 2003

Raz96 **Monolithic Phase-Locked Loops and Clock Recovery circuits**
B.Razadi. John Wiley and Son (1996) ISBN-0-7803-1149-3 pg33-35

Rei02 **A novel broadband DBR laser for DWDM networks with simplified quasi-digital wavelength selection**
D.C.J.Reid ,D.J.Robbins, A.J.Ward, N.D.Whitbread, P.J.Williams, G.Busico, A.C.Carter, A.K.Wood, N.Carr, J.C.Asplin, M.Q.Kearley, W.J.Hunt, D.R.Brambley, J.R.Rawsthorne. Tech. Digest of Optical Fibre Communication Conf. pp 541-543, 17-22 Mar 2002

Ren03 **Exact, agile, optical frequency synthesis using an optical comb generator and optical injection phase lock loop**
CC.Renaud, C.F.C.Silva, M.Düser, P.Bayvel, A.J.Seeds. Digest of the LEOS Summer Topical Meetings Vo.16, (3) pp 903 – 905 14-16 July 2003

Ren04a **Nanosecond channel-switching exact optical frequency synthesizer using an optical injection phase-locked loop (OIPLL)**
C.C. Renaud; M. Düser; C.F.C. Silva; B. Puttnam; T. Lovell; P. Bayvel; A.J. Seeds; IEEE Photonics Technology Letters, Vol. 16 (3), pp 903 – 905, March 2004

Ren04b **Nanosecond switching time, uncooled, zero frequency DWDM source**
C.C. Renaud; M. Düser, B. Puttnam; T. Lovell; P. Bayvel; A.J. Seeds. Tech. Digest of Optical Fibre Communication Conf., Vol. 1, 23-27 Feb. 2004

Rig96 **Wavelength coverage over 67 nm with a GCSR laser: tuning characteristics**

and switching speed
P-J.Rigole, S.Nilsson, L.Backbom, B.Stalnacke, T.Klinga, E.Berglind, B.Stoltz, D.J.Blumenthal, M.Shell, IEEE Semiconductor Laser Conf. pp125-126, 13-18 Oct 1996

Rob04 **A high power, broadband tunable laser module based on a DS-DBR laser with integrated SOA**
D.J.Robbins, G.Busico, L.Ponnampalam, J.P.Duck, A.J.Ward, D.C.J.Reid, P.J. Williams, N.D.Whitbread, R.A Griffin, E.Barton,B.Reid, K.Kasunic. Tech. Digest of Optical Fibre Communication Conf..Vol. 1, 23-27 Feb. 2004

Rob98a **Design and optimisation of sampled grating DBR lasers for dense WDM networks**
D.J.Robbins, N.D.Whitbread, P.J. Williams, J.R.Rawsthorne. Tech. Digest of European Conference on Optical Communication, Vol.1, pp 221-222, 20-24 Sept. 1998

Rob98b **Sampled grating DBR lasers for WDM systems**
D.J.Robbins, N.D.Whitbread, P.J. Williams, J.R.Rawsthorne. Tech. Digest of IEE Colloquium on Multiwavelength Optical Networks: Devices, Systems and Network Implementations pp9/1-9/4 18 June 1998

Shr01 **Performance demonstration of a fast-tunable transmitter and burst-mode packet receiver for HORNET**
K.Shrikhande,.I.M.White, Eric Shih-Tse Hu, M.S.Rogge, L.G.Kazovsky. Tech. Digest of Optical Fibre Communication Conf., Vol. 4, Pages:ThG2-1 - ThG2-3, 2001

Sim03 **Fast switching characteristics of a widely tunable laser transmitter**
J.E. Simsarian. A.Bhardwaj, J.Gripp, K.Sherman, S.Yikai, C.Webb, Liming Zhang, M.Zirngibl. IEEE Photonics Technology Letters, Vol. 15 (8), pp 1038-1040 Aug. 2003

Sim06 **Less than 5-ns wavelength switching with an SG-DBR laser**
J.E. Simsarian, M.C. Larson, H.E. Garrett, Hong Xu, T.A. Strand. IEEE Photonics Technology Letters Vol. 18 (4), pp 565 – 567, Feb. 15, 2006

Sof86 **All-silicon active and passive guided-wave components for λ = 1.3 and 1.6 μm**
R.Soref, J.Larenzo. IEEE Journal of Quantum Electronics, Vol 22, pp 873-879, June 1986

Son01 **1.55 μm multichannel DWDM source using quaternary/quaternary MQW InGaAsP/InP QCSE tuning**
J. B.Song, C. C. Button, A.J Seeds. IEE Elecronics. Letters, Vol. 37, No.7, pp 426-427, 29th March 2001

Sun04 **Long wavelength-tunable VCSELs with optimized MEMS bridge tuning structure**
D.Sun, W.Fan, P.Kner, J.Boucart, T.Kageyama, D.Zhang, R.Pathak, R.F.Nabiev, W.Yuen. IEEE Photonics Technology Letters, Vol.16 (3), pp 714-716, March 2004

Tim99 **10 Gbit/s directly modulated, high temperature-stability external fibre grating laser for dense WDM networks**
F.N.Timofeev, I.A.Kostko, P.Bayvel, O.Berger, R.Wyatt, R.Kashyap, I.F.Lealman, G.D.Maxwell. Electronics Letters Vol. 35, (20), pp 1737-1739, 30 Sept. 1999

War03 **Modelling of phase-grating based wideband tuneable lasers with simplified quasi-digital wavelength selection**
A.J.Ward, D.J.Robbins, G.Busico, N.D.Whitbread, P.J. Williams L.Ponnampalam, D.C.J.Reid, J.R.Rawsthorne. IEE Proceedings in Optoelectronics, Vol. 150, (2) pp 199 – 204, 18 April 2003

War04 **Realization of phase grating comb reflectors and their application to widely tunable DBR lasers**
A.J.Ward, D.J.Robbins, D.C.J., Reid, N.D.Whitbread, G.Busico; P.J.Williams, J.P. Duck, D.Childs, A.C.Carter, IEEE Photonics Technology Letters, Vol. 16, (11) pp 2427-2429, Nov. 2004

War05 **Widely tunable DS-DBR laser with monolithically integrated SOA: design and performance**
A.J.Ward, D.J.Robbins, G.Busico, N.D.Whitbread, P.J. Williams L.Ponnampalam, D.C.J.Reid, J.R.Rawsthorne , E.Barton, A.C.Carter, M.J.Wale. IEEE Journal of Selected Topics in Quantum Electronics, Vol.11 (1), pp 149-156, Jan-Feb 2005

Web94 **Optimization of the carrier-induced effective index change in InGaAsP waveguides-application to tunable Bragg filters**
J-P.Weber. IEEE Journal of Quantum Electronics, Vol.30 (8), pp1801-1816, Aug

1994

Wes01 **GCSRs and other widely tunable lasers**
J.O.Wesstrom, J.Bergerengen, G.Sarlet, Y.Gustafsson, P.Szabo, B.Broberg
Digest of the LEOS Summer Topical Meetings, pp. 2, 30 July-1 Aug. 2001

Wes02a **On the frequency stability of widely tunable GSCR lasers**
Y.Gustafsson, J.O.Wesstrom, P.Szabo. Tech. Digest of Optical Fibre Communication Conf., pp 727-728, 17-22 Mar 2002

Wes02b **Design of a widely tunable modulated grating Y-branch laser using the additive Vernier effect for improved super-mode selection**
J.O.Wesstrom , S.Hammerfeldt, J.Buus, R.Siljan, R.Laroy, H. de Vries, IEEE semiconductor Laser Conference, pp 99 – 100, 29 Sept.-3 Oct. 2002

Wes04 **State-of-the-art performance of widely tunable modulated grating Y-branch lasers**
J.O.Wesstrom, G.Sarlet, S.Hammerfeldt, L.Lundqvist, P.Szabo, P-J.Rigole, Optical Fibre Communication Conf., Vol. 1, 23-27 Feb. 2004

Yu00 **Fast wavelength switching of a high-speed SG-DBR laser for dynamic wavelength routing Lasers**
Y. Yu, S.O'Duill, N. O'Gorman, G. Mulvihill, R.O'Dowd, IEEE Lasers and Electro-Optics SocietyAnnual Meeting, Vol. 2, pp 583 – 584, 13-16 Nov. 2000

Yu02/1 **Interpretation of wavelength Switching Effects of Widely Tunable Lasers**
Y. Yu and R. O'Dowd. IEEE Photonics Technology Letter, Vol.14, No 10, Oct 2002

Yu02/2 **Influence of mode competition on the fast wavelength switching of an SG-DBR**
Y. Yu and R. O'Dowd, Journal of Lightwave Technology, Vol, 20 (4), pp:700-704, April 2002

Zap03 **Dynamic Wavelength-Routed Optical Burst Switched Networks: Scalability Analysis and Comparison with Static Wavelength-Routed Optical Networks**
A. Zapata, P. Bayvel. Tech. Digest of Optical Fibre Communications Conf., Atlanta USA, 23-28 March 2003

Chapter 3 Burst-mode transmitter implementation

As outlined in chapter 1, a burst-mode transmitter, capable of rapid, nanosecond, tuning to stable ITU wavelengths across the C-band is crucial for future dynamic optical networks (DONs). The previous chapter showed that the fast-tunable lasers, envisaged as the core transmitter technology, require 2 additional control features for application to DONs, particularly over the longer timescales applicable to Type II OBS networks. Firstly, to prevent switching crosstalk causing background interference on all channels the laser output should be attenuated (blanked) as the laser is switched to each new wavelength. Secondly, once switched the wavelength output requires a control system to ensure wavelength stability over the desired range of burst lengths. Chapter 2 revealed that for burst lengths applicable to Type II OBS schemes, wavelength stability of 1 GHz is required to obtain minimal Q-factor penalty for transmission through narrow routers with 25GHz channel spacing with the requirement for blanking set by the signal-to-noise ratio of the device. Hence, this chapter examines the techniques for meeting these requirements and describes the implementation of fully operational burst-mode transmitter complete with blanking functionality and wavelength locking control loop.

3.1 Review of wavelength locking for tunable lasers

Wavelength stabilization or locking has been a requirement for optical transmitters in a broad range of WDM based networking applications and a number of schemes exist. Fixed wavelength applications have used notch filters but these are unable to respond to dynamic wavelength deviations caused by wavelength switching in tunable lasers. Accurate control of temperature has also been used to stabilize the wavelength output. Typical wavelength-temperature sensitivity is about 0.2-0.5nm/°C depending on the laser design [Ren06]. Whilst this may meet the 5% accuracy target of ±5 GHz for 100GHz spaced systems and quasi-continuous laser operation, it is likely to prove more difficult to maintain the required wavelength stability with a smaller channel spacing and with the addition of dynamic thermal transients caused by high current switching and long term wavelength deviation caused by aging.

The most common locking configuration for WDM sources uses the multiple transmission peaks of a Fabry-Perot Etalon to provide a periodic wavelength

reference that may be matched to the desired grid spacing. Typically, a small percentage of the signal is tapped from the laser output to generate a correcting signal to be applied to the laser with a feedback loop. The standard arrangement is a further split of the tapped power with one arm passed through the etalon before photo-detection to provide a wavelength dependent photocurrent that may be used to generate an error signal by comparison with the wavelength independent photocurrent from the reference photodiode. For standard implementation, such as commercially available external wavelength lockers [JDS07a], the locker is designed to give an ITU grid spaced locking point at the intersection between the flat reference photocurrent and the periodic Airy function etalon transmission peak as shown in Figure 3-1

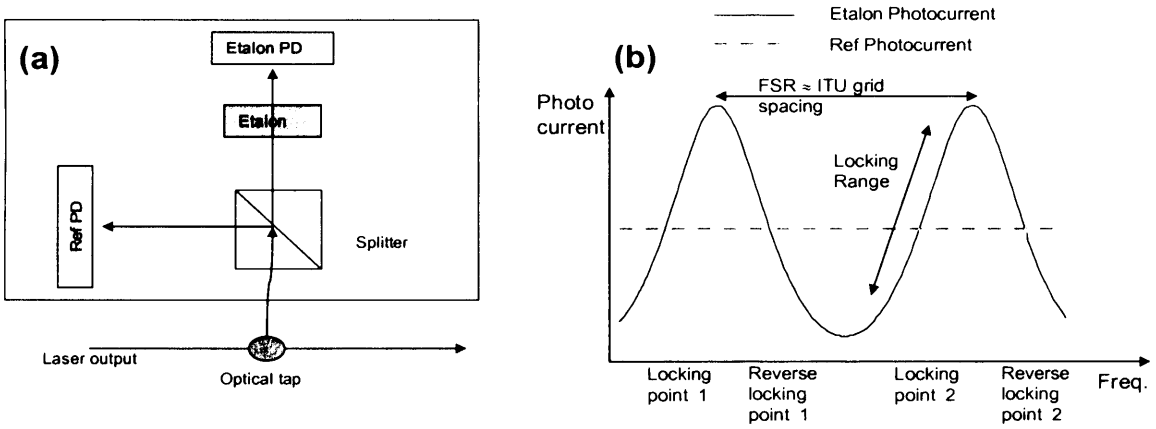

Figure 3-1 (a) Schematic of external wavelength locker and (b) location of locking points by comparison of reference and Etalon photocurrents

Etalon based lockers have been demonstrated outside the laser package [DeM05, Sim03] but Industry trends of reducing package size have led to development of internal wavelength lockers. With multisection tunable lasers the most common approach is to split the beam between the front facet and collimating optics [Pon06, Ham02] but etalon based lockers receiving light from the back facet have also been implemented [Han03].

The error signal is calculated from the difference between the 2 photocurrents and wavelength stability is achieved by using the magnitude and sign of the error signal to adjust the laser wavelength accordingly. For semiconductor tunable lasers, this is generally done by tuning of the laser phase section. This has been achieved both using an analogue control circuit [Pon06] and using digital signal processing [Sim04]. A summary of etalon based wavelength locking schemes is shown in Table 3-1. Alternatives to the use of etalons as the

wavelength selective element in locking schemes have included Fibre Bragg Gratings (FBGs) [Ich02], thin film filters [Car00] and a diffractive interferometer [Sos04].

Table 3-1 Summary of published studies Using Etalon based lockers

Ref	Laser Type	Locker type	Control circuit	Lock time	W'length Stability	Comments
DeM05	ECL	Etalon	N/A	N/A	± 1GHz	
Ich02	N/A	FBG Etalon	Analogue	N/A	N/A	Athermal operation over 70°C
Hea03	DFB array	Etalon	Analogue	N/A	± 1GHz	
Sim03	GCSR	Etalon	DSP	50ns	± 3GHz	Short bursts to remove thermal transients
Pon06	DS-DBR	Etalon	Analogue	6ms	± 2.5GHz	Integrated etalon locker and SOA used for blanking
Kim04	SG-DBR	Etalon	N/A	N/A	± 0.5GHz	Etalon temp control by thin film resistor for athermal operation

Some of the best wavelength stability results with tunable lasers have been demonstrated using optical injection locking with an optical phase locked loop. With injection locking provided by an optical frequency comb generator as a master laser source for a number of slave lasers stabilized in OIPLL blocks, wavelength stability below 1 KHz was observed in combination with nanosecond switching time for an SG-DBR with the tuning range limited by the size of the reference comb [Ren04]. For OBS applications multiple lasers in the same edge router would be able to use the same reference comb but the stability improvement is unlikely to be outweighed by additional cost and complexity.

Control of the laser tuning currents is not restricted only to the phase section. Algorithms enabling operation of tunable lasers without temperature controller by careful control of all tuning sections have been shown to provide wavelength stability of ± 6GHz for DBR laser with a 100GHz spacing [Ren06] and 5GHz stability for a DS-DBR laser in a 50GHz system [Liu06]. However, both schemes fall short of the frequency stability targets for 50GHz and 25GHz wavelength routers determined in chapter 2.

Tunable lasers have been shown to degrade over time due to the development and migration of defects within the semiconductor material. Combined with environmental changes this degradation can cause long-term frequency drift

that has been estimated to be up to ±10GHz per year [Woo93, Del97, Del99, Lav99, Lav00]. Addressing of this problem has led to a number of alternative wavelength stabilization schemes intended to maintain both a stable output wavelength and maximum SMSR. The correlation between active (Gain) section voltage and the DBR reflection peaks denoting the centre of a cavity mode can be exploited to ensure wavelength stability [Sar00, Sar99]. Since the perfect alignment of reflector peaks causes a local minimum in threshold gain and carrier density that determines the active section voltage [Ish98], a voltage sensor may be used to provide an error signal that is, in turn, used to control the reflector currents of an MG-Y device. Combined with a wavelength feedback loop control of the phase section similar to those described above, wavelength stability of ±1GHz for continuous operation with temperature varied over 10°C [Lar07] has been reported with this technique. A similar technique was also used to identify saddle points corresponding to local minima in SSG and SG-DBR devices by measurement of the output power [Ish98] but found problems due to carrier induced losses in the DBR section absorbing the output light. The design of the MG-Y device allows direct monitoring of the reflector sections independently allowing for adjustment of the tuning sections currents to maintain maximum SMSR due to environmental changes such as long term temperature changes, ageing or fabrication tolerances. Such algorithms can reduce the requirement for detailed characterization or compensate for ageing or environmental changes but wavelength stability comparable with wavelength lockers is only achieved in conjunction with conventional wavelength lockers with phase sections control. Although it is likely that burst-mode transmitters intended for commercial use over many years will include such control loops to compliment a phase control based wavelength locker, it is unlikely that these schemes can provide the necessary speed and accuracy to correct for short timescale effects and have yet to be demonstrated under dynamic operation.

These facts, combined with the availability of etalon based lockers that now appear integrated with photodiodes in commercial tunable laser packaged products [Boo07, jDS07/2], make etalon based lockers the most likely technique for achieving the desired wavelength stability outlined in chapter 2. Currently, the best performance of such a locker with a switching tunable laser with blanking [Pon6] showed a wavelength stability of ±2.5GHz but with the

wavelength locked switching time of 6ms. As determined in the chapter 2, wavelength routers for 50GHz and 25GHz require wavelength stability of 2GHz and 1GHz respectively and the timing requirements of DONs mean that the wavelength stabilisation scheme must operate on the timescale required for switching.

Hence, the aim of this chapter is to investigate the limits of such a control scheme and improve the wavelength locking performance to ns-μs regime required by DONs [Bay04]. This is done by introducing a linearised theoretical model of a wavelength locking loop and applying standard control theory to determine the optimum control coefficients as a function of key loop parameters. This model is then used to construct a wavelength locking control board for a DS-DBR laser that also employs blanking of the laser output during switching using an integrated SOA.

3.2 Optimizing etalon-based locking system

This section describes the design and optimization of etalon based wavelength locking loop (WLL) for DBR tunable lasers. Due to its advanced design, comprising both an integrated wavelength locker (etalon and photo-detectors) and SOA which can be used for shielding of the laser output, the design of the burst-mode transmitter was based around the DS-DBR module described in chapter 2. Although locking measurements with SG-DBR devices using an external locker and SOA were also performed the modelling and optimization of the wavelength locking loop is performed using the characteristics of the DS-DBR device. For clarity, the full mathematical model of the wavelength locking loop is contained in the Appendix B with the key steps outlined in this section.

3.2.2 Structure of wavelength-locking-loop

The integrated wavelength locker design, shown in Figure 3-2(a), uses a transflective etalon to split the signal between 2 photodiodes (PD), one each for the transmitted and reflected signals. This improves the locking performance since the signal from both detectors has the characteristic etalon spectral response, shown in Figure 3-2(b). Hence, the rate of change of the error signal with wavelength is twice that of the configuration shown in Figure 3-1 enabling faster convergence to the locking point.

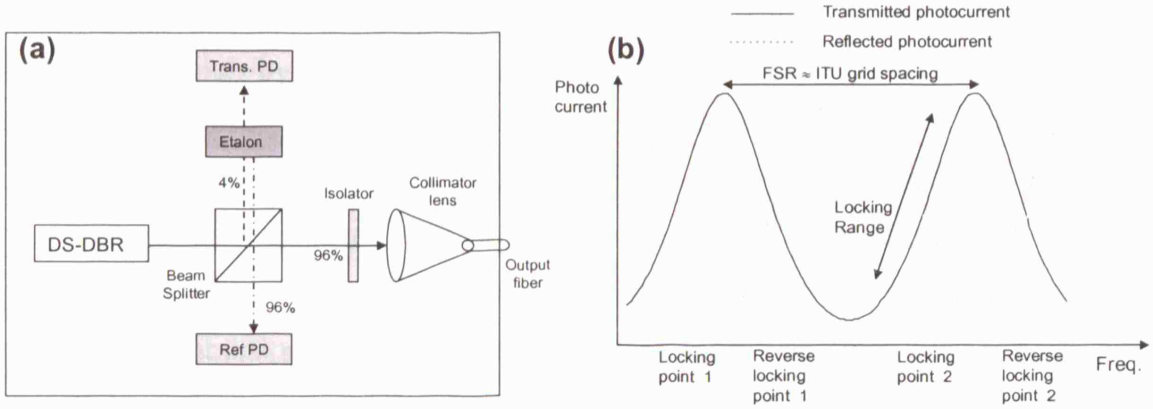

Figure 3-2 (a) Schematic of DS-DBR laser package containing DS-DBR and internal wavelength locker and (b) transmission spectra for transmitted and reflected photodiodes

At the laser output, a beam splitter is used to direct 4% of the optical signal generated by the laser sections to the etalon which further splits the signal into transmitted and reflected components. The etalon is designed to generate 2 photocurrents at the photo-detectors which are approximately equal at the locking points which are periodic and equally spaced in frequency. The free spectral range (FSR) of the etalon is 100GHz, again matched to the standard ITU-T, which as shown in Figure 3-2(b) allows locking at frequency intervals at half the FSR (50GHz) assuming any control circuit is able adjust the sign of the phase section correction signal according to the slope of the etalon spectral response.

The next stage is to develop the input to the wavelength locking circuitry. The structure of the proposed feedback loop is shown in Figure 3-3.

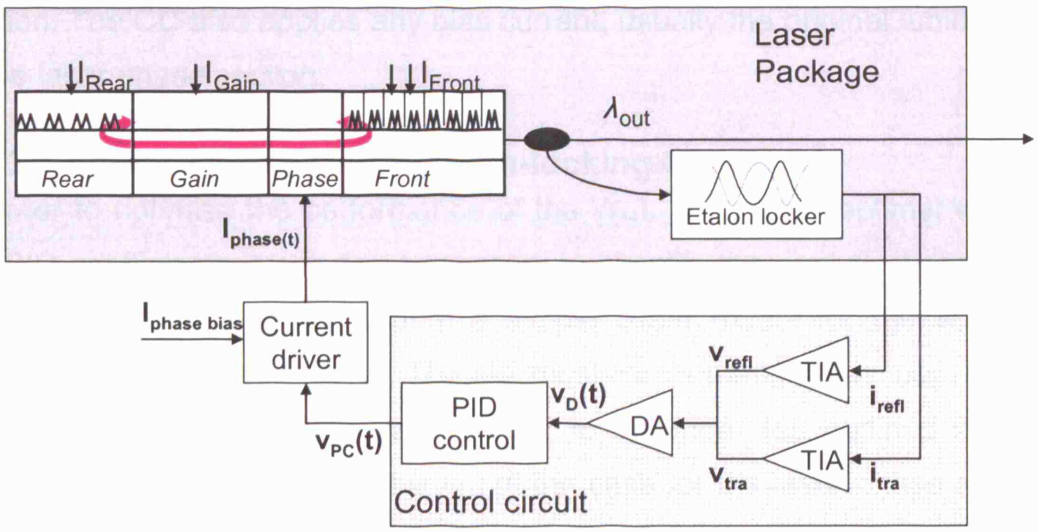

Figure 3-3 Structure of wavelength locking loop comprising integrated wavelength locker and proposed control circuit

With the loop enabled the photocurrents are a function of the laser output frequency which by the compensating action of the loop become a function of time. The first stage is the transimpedance amplifier (TIA) stage that converts the currents to time dependent voltage signals. The differential amplifier (DA) then calculates a voltage, $v_D(t)$, which is proportional to the difference between the 2 TIA voltages, v_{ref} and v_{tra} from the wavelength locker. The control circuit is the active stabilising element in the feedback loop and calculates a correcting signal from the output of the DA, the error signal voltage $v_D(t)$. As defined in standard control theory [Bro91]. The correction signal voltage, $V_{pc}(t)$, is used to drive the laser phase section and correct the laser wavelength according to the following relation. For a proportional-integral and differential (PID) control the correction voltage is:

$$v_{PC}(t) = \left[k_P v_D(t) + k_I \int_{t_{RST}}^{t} v_D(t) d\tau + k_D \frac{\partial v_D(t)}{\partial t} \right] k_f \qquad (3.1)$$

Where k_P, k_I and k_D are the coefficients for proportional, integral and differential controls and weight the contribution of each control to the final phase section tuning correction and k_F is a general loop coefficient covering all other loop components. Similarly, expressions for alternative control schemes, such as proportional-integral (PI) or integral (I) only may be written by setting of the appropriate coefficients to zero. The phase correction voltage V_{PC} is then passed through the current driver (CD) which coverts the signal and applies the appropriate conversion to match it to tuning characteristics of the laser phase section. The CD also applies any bias current, usually the original tuning current to the laser phase section.

3.2.3 Linearising the wavelength-locking-loop

In order to optimise the performance of the WLL and derive optimal values for the PID coefficients it was first necessary to simplify the analytical model. The first stage of this was to assume a simple linear model for the wavelength locking loop described thus far. The electrical components of the loop, the TIAs, DA and current driver may be assumed to be linear (as outlined in the full derivation in Appendix B) but this is not the case for the laser phase section or the etalon response. However, these loop elements only need to operate linearly in specified operating range around the locking point. This locking

range was determined experimentally using DS-DBR laser (TLD1001) by studying the phase section tuning characteristics and the measured response of the etalon locker as shown in Figure 3-4.

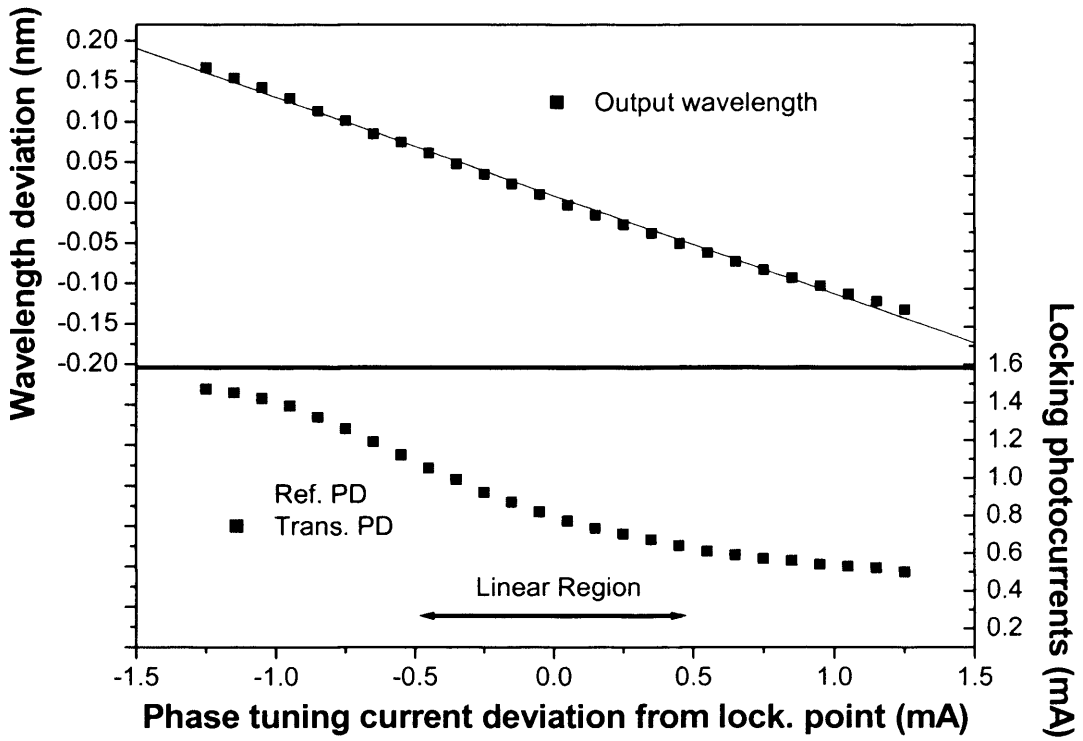

Figure 3-4 Linearization of phase section and etalon response with phase tuning current

Figure 3-4 shows the measured wavelength deviation locker photocurrents as a function of phase section current around an ITU locking point. The wavelength deviation as a function of tuning current is approximately linear across the entire measured range which is limited at the extremes by degraded SMSR and ultimately by a cavity mode hop.

The etalon response may also be assumed linear over smaller range corresponding to 1mA tuning current range or a wavelength deviation of almost 0.2nm (25GHz) which is almost twice the largest measured wavelength deviation for the same device in chapter 2. Hence, the etalon response can be considered linear around the ITU wavelength in question with the slope calculated from the derivative of the etalon spectral response. Assuming linear performance of all of the elements of the feedback loop allows treatment of the feedback loop as a standard negative feedback scheme with system and control blocks. The periodic nature of the etalon locker allows modelling of a

general case in which all wavelengths in this model are expressed as deviations from the nearest ITU wavelength with the wavelength correction induced by phase section tuning current correction, $\Delta\lambda_P$, being an adjustment to the initial lasing wavelength $\Delta\lambda_L$ to give the instantaneous lasing wavelength $\Delta\lambda_{Out}$. For this model, the instantaneous lasing wavelength $\Delta\lambda_{Out}$ may be considered the input to the system block comprising etalon, TIAs and DA using standard control theory [Bro91]. The differential signal voltage in turn may be considered the input to the control block comprising the PID control and current driver.

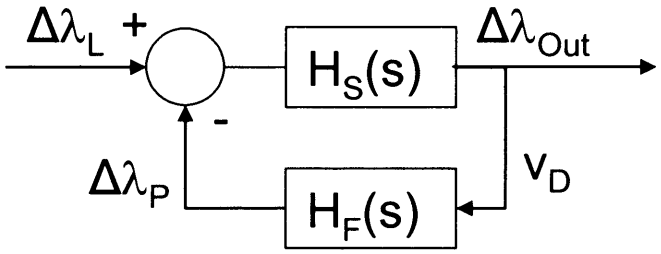

Figure 3-5 Linearised model of wavelength locking control loop

Once linearised, with all key parameters expressed as a function of time the variables described thus far may be written in the Laplace domain and ultimately formulated in to a single loop transfer function from which the optimum control coefficients may be derived. Such as expression, derived in full in Appendix B, is shown in equation (3.2).

$$\Delta\lambda_{out} = \frac{\Delta\lambda_0 s(s+\omega_L)^2}{s(s+\omega_L)^2 + k_F\omega_L{}^2(k_D s^2 + k_P s + k_I)} \qquad (3.2)$$

Where, k_P, k_I and k_D are the control coefficients, k_F is a general loop coefficient covering all other loop components and ω_L is the loop bandwidth.

3.2.4 Optimal control coefficients

Equation (3.2) is important since it contains the control coefficients to be optimised and its equivalent in the time domain may be used to define the wavelength locking time as shown in Figure 3-6. The objective of the wavelength locking loop is to lock to the output wavelength in the shortest possible time. Hence, as with the definition of switching time defined in chapter 2, the locking time, t_L, may be defined such that the output wavelength falls and remains within a specified wavelength range, $\Delta\lambda_T$.

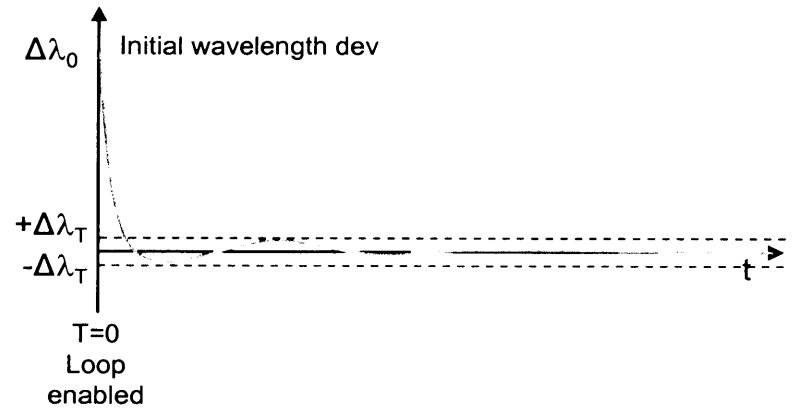

Figure 3-6 Typical loop response to step wavelength deviation

Hence, at the instant the output wavelength is first within the locking range equation (3.2) may be set equal to this wavelength deviation ($\Delta\lambda_{OutT}(t_L) = \Delta\lambda_T$) and the optimal control coefficients, (and locking time) may be derived by comparison with a optimal target response to represent desirable locking characteristics. As shown in more detail in Appendix B, using an exponential target function of the form $\Delta\lambda_{OutT}(t) = \Delta\lambda_0 e^{-\omega_N t}$,where ω_N is the natural angular frequency of the target low pass response, this approach and the theoretical analysis of the WLL lead to expressions for the optimal control coefficients as function of the loop bandwidth, ω_L, as given in equations (3.3), (3.4) and (3.5) for a PID control.

$$k_P k_F = 2 \tag{3.3}$$

$$k_I k_F = \omega_L \tag{3.4}$$

$$k_D k_F = 1/\omega_L \tag{3.5}$$

As can be deduced from equation (3.5) and is shown by numerical simulation in section 3.3, the differential coefficient in a PID control can become almost negligible for this application, being inversely proportional to the loop bandwidth. As a result, it was also necessary to consider the optimal control coefficients of a PI control. As also shown in full in Appendix B, assuming a PI control loop in the same theoretical analysis gives the following expressions for the control coefficients.

$$k_P = 1/4k_F \tag{3.6}$$

$$k_I = \omega_L/4k_F \tag{3.7}$$

3.3 Comparison of control schemes

The feasibility of implementing a WLL based on the linearised model was investigated using a numerical simulation of the wavelength locking loop developed in the MATLAB/Simulink environment by Alessandro Bianciotto of the Politecnico di Torino. The simulator included the non-linear characteristics of the etalon and phase section and allowed time-domain monitoring of all the key quantities. The Simulink model was used to find the optimal value of the wavelength locking coefficients based on an iterative process from initial guesses and predict the wavelength locking performance for both the PID and PI based models described. In addition to the PID and PI models described, a 3rd purely integral model was also examined. The numerical optimisation of the control coefficients used the MATLAB function *fminsearch*, based on the Nelder-Mead simplex method [Lag98] with the values of the initial guesses were based on the theoretical model described. These values and all the physical parameters used to model the remaining loop components are shown in Table 3-2. In order to provide an experimental verifiable model, the parameters of all loop components were based on the measured characteristics of the DS-DBR laser, integrated locker and current drivers.

Table 3-2 Parameters used in WLL simulation

Parameter	Description	Value/Unit
$k_{p,\ initial\ (PID)}$	Initial guess for proportional coefficient – PID case	0.9182
$k_{i,\ initial\ (PID)}$	Initial guess for integral coefficient – PID case	2.88E6
$k_{d,\ initial\ (PID)}$	Initial guess for coefficient – PID case	7.3E-8
$k_{p,\ initial\ (PI)}$	Initial guess for proportional coefficient – PI case	0.1147
$k_{i,\ initial\ (PI)}$	Initial guess for integral coefficient – PI case	7.21E5
$k_{i,\ initial\ (I)}$	Initial guess for integral coefficient – I case	4.27E5
$\Delta\lambda_0$	Initial wavelength deviation	0.1nm
G_c	Conductance gain of current driver	0.005 Ω^{-1}
$R_{T1,2}$	TIA resistor value	1 kΩ
ω_c, ω_s	Low pass cut off frequency for system/control	2π*1E6
K_{ph}	Slope of wavelength vs phase section current	-113.9 nm/A
G_{DA}	Gain of differential amplifier	1
G_P	Gain of proportional control amplifier	5
Δf_{FSR}	Etalon free-spectral range	100 GHz
f_{ref}	ITU reference optical frequency	191 THz
β_E	Etalon extinction ratio	3.3
I_{eta}	Maximum etalon photocurrent	1 mA
k_{eta}	Etalon characteristic coefficient	1

The results of the numerical simulation for the 3 control scenarios are shown in Table 3-3 and Figure 3-7. Table 3-3 displays the calculated optimum values for each coefficient and the desired locking time for each of the 3 control scenarios investigated.

Table 3-3 Optimum coefficients derived from WLL simulation

Scenario	K_i	K_p	K_d	Lock time
PID	2.641E6	0.9143	1.107E-7	0.365μs
PI	1.1129E6	0.4367	-	0.5968μs
I	4.6405	-	-	1.6439μs

For the PID case, Table 3-3 shows that the optimized differential coefficient is many orders of magnitude smaller than the other coefficients, as predicted from the theoretical model in equations (3.3), (3.4) and (3.5).To determine whether this value was negligible to the loop response Figure 3-7 also shows the locking performance for the coefficients obtained for the PID control case with the differential coefficient artificially set to zero. In order to test the validity of the theoretical model, locking traces derived from the ideal theoretical values of the optimal PID coefficients are also included in Figure 3-7. These results were not obtained by simulation but by using the MATLAB *step* function which calculated the step response directly from theoretical model which assumed linear etalon and phase section characteristics.

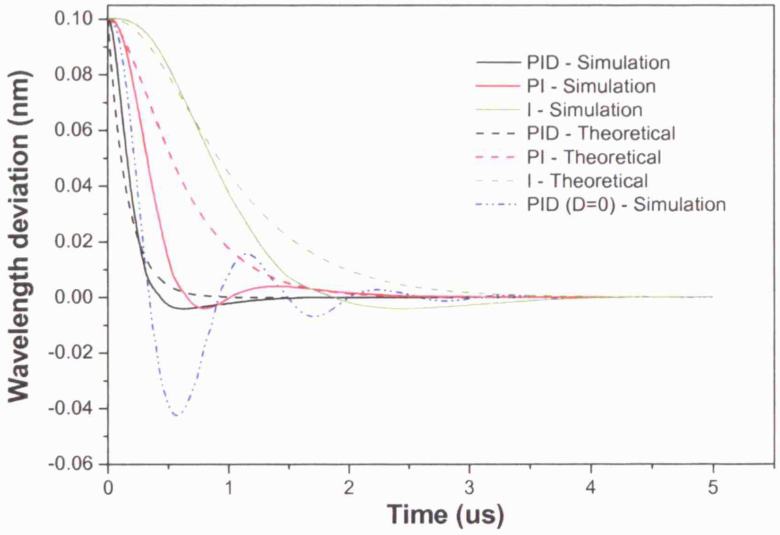

Figure 3-7 Numerically and theoretically derived output wavelength deviation curves for different control scenarios

Figure 3-7 shows that there is reasonable correlation between the locking performance for the theoretical and simulated cases for all 3 control scenarios supporting the validity of the proposed model. The discrepancy between the theoretical and simulated is thought to derive from the assumptions of linear performance in the theoretical case. The simulated results show that fastest locking performance is obtained by using a full PID control with a small but not negligible differential coefficient. With the differential coefficient set to zero, the

resulting step response, shows large oscillations and differs strongly from the optimal response. Hence, as shown in the control coefficient derivation in Appendix B, the proportional and integral coefficients must be re-optimised to achieve sufficient locking performance for a PI control in order to obtain stable, fast locking should practical implementation of a PID control not prove possible.

3.4 Experimental verification of PID control

Section 3.2 presents a model of the WLL and shows that such a model can be used to derive the optimal PID coefficients based on the desired locking performance. However, the success of this model also showed that the optimal differential coefficient is approximately proportional to the inverse of the loop angular frequency and for the MHz frequencies envisaged for the loop operation, beyond the capability of analogue electronics. This presents problems for the physical implementation of the WLL since it may not be practically possible to implement such a small coefficient with available electrical components in either the digital or analogue domain [Bro91]. For this reason, the experimental verification of the loop model with a PID control was performed using an offline PID controller. The offline PID control was based on optimally calculated coefficients from the MATLAB/Simulink model which was used to calculate the desired locking trace. This locking trace was then applied to the laser phase section with an arbitrary waveform generator (AWG) via the external modulation input of the current driver. As described above, the phase section, photodiode characteristics and electrical parameters were based on experimentally measured values. Using the offline PID control it was therefore possible to investigate the performance of the PID control for a specific high tuning current switch and compare the performance with both the unlocked and theoretically predicted cases.

In each case the wavelength deviation due to the switching was measured using the technique described in chapter 2 based on a scanning Fabry-Perot Interferometer with the burst controller used to synchronise wavelength switching, locking and measurement. The full experimental set-up is shown in Figure 3-8.

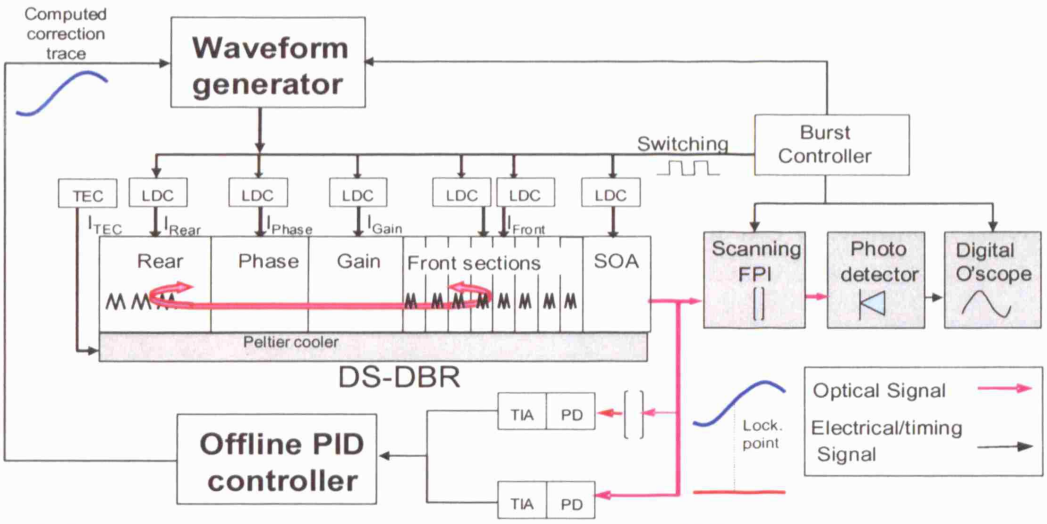

Figure 3-8 Set-up for experimental validation of optimized PID coefficients using offline PID controller

The operation of the offline PID control was tested with a worst case wavelength deviation caused by high tuning current switching. This was a large tuning current switch of 50mA on the rear tuning section (low to high) and simultaneous 140mA switch on the SOA (low to high), as could occur after a long period of blanking in an OBS transmitter. The total wavelength drift for this transition was measured to be 0.11nm and the operation of the PID control is shown over the initial few microseconds where the laser output is furthest from the final target wavelength, as shown in Figure 3-9. For this measurement the length of the locked burst was minimized to ensure maximum wavelength deviation from the steady state condition.

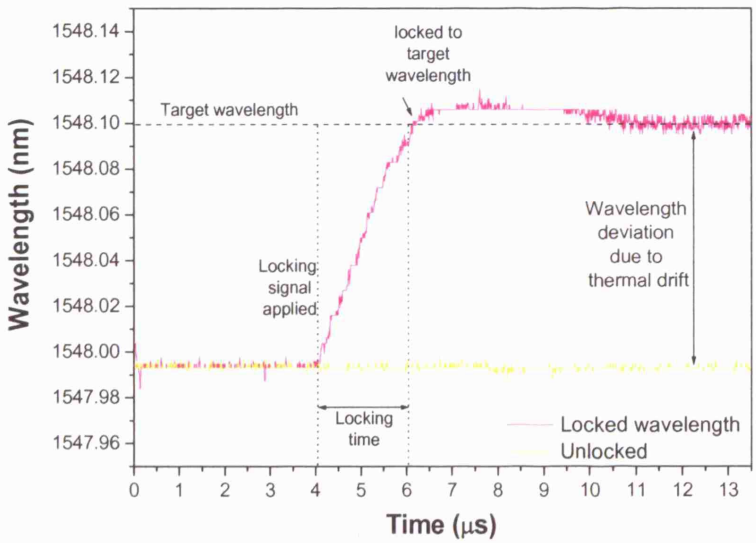

Figure 3-9 Experimental verification of offline PID control under high tuning current switching

Figure 3-9 shows that the offline PID controller is able to correct for the initial wavelength deviation of 0.11nm with a locking time of around 2μs set by the 500KHz bandwidth limitation applied to the simulated PID control. Figure 3-9 shows that the PID control, with coefficients calculated with knowledge of the initial wavelength deviation, is able to compensate for the wavelength deviation caused by high tuning current switching.

3.5 Experimental verification of PI control – Building a BMTx

Without the differential control, the experimental verification of the PI control was not hindered by the same implementation issues as the PID control loop and was based on construction of control board constructed from custom built analogue electronics. The PI control board was used to perform real time locking measurements under high tuning current switching and combined with precise timing control to form the basis of the burst-mode transmitter able to meet the requirements outlined in chapter 2.

3.5.1 Wavelength locking loop implementation

The operation of the loop and components both inside and outside the laser package were as those shown in Figure 3-2 and Figure 3-3. The TIA, differential amplifier and control circuit were implemented on a custom built printed circuit board which also contained additional timing control to enable time synchronization with the tunable laser timing controller and experimental hardware. As shown in the circuit diagram in Figure 3-10, a TIA and gain adjustment stage was used for each of the transmitted and reflected signals from the etalon. The first stage was used to convert the photocurrents i_T and i_R to approximately equal voltages v_{t1} and v_{r1} with lasing occurring at an ITU-U frequency. The second amplifier stage was used for high precision calibration of the voltages with before the differential amplifier used to generate the error signal from the difference between the 2 voltages.

Once generated, the error signal or differential voltage $V_{D,}$ which should be zero at the locking point, is fed simultaneously to the proportional and integral control. At the output of each control arm are the variable resistors which enabled control of the weighting of each control arm before a final output summing stage. Control of these resistors enabled investigation of the control coefficients calculated in section 3.2.

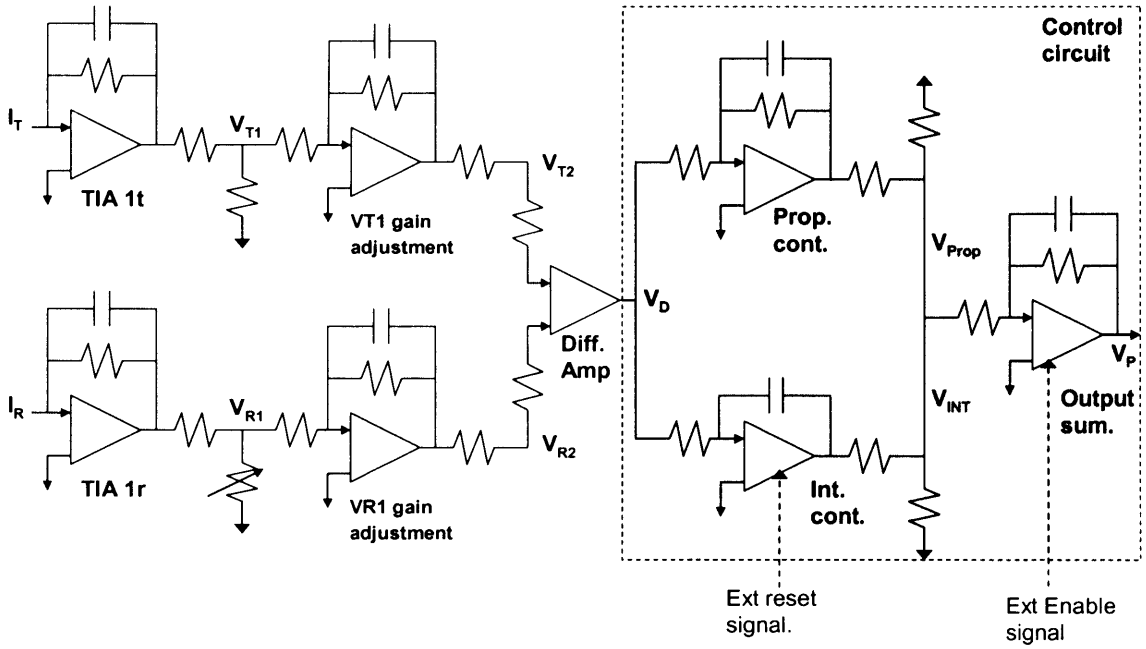

Figure 3-10 Circuit diagram of wavelength locking control board

For practical implementation, to reduce the impact of high frequency noise, feedback resistors and capacitors were chosen to limit the bandwidth of each stage to the chosen loop bandwidth, which was set by the 500KHz bandwidth of the current driver used to deliver the phase section current. This was with the exception of the integrator where the capacitance value was chosen to provide the desired integration time based on the value of the integral coefficient. An additional reset signal was applied to the integrator to block spurious signals during the period of mode competition before the locker is activated. Similarly, the board output was controlled by a control voltage applied to the final output summer to ensure correction voltages are only applied to the current driver and in turn to the laser phase section when the wavelength control is required. During measurements, both control signals are provided externally by the burst timing controller and synchronized with the tuning current switch allowing for a period of mode competition during switching.

3.5.2 Locking measurements

To test the performance of the wavelength locking board measurements of both the wavelength stability and the BER/Q-factor of transmitted bursts were made. The experimental set-up for the wavelength stability measurements, shown in Figure 3-11, was the same as that used in the PID control experimental verification and that described in chapter 2. Also shown in Figure 3-11 is the

additional timing control required by the wavelength control loop and synchronized with the tuning current switch.

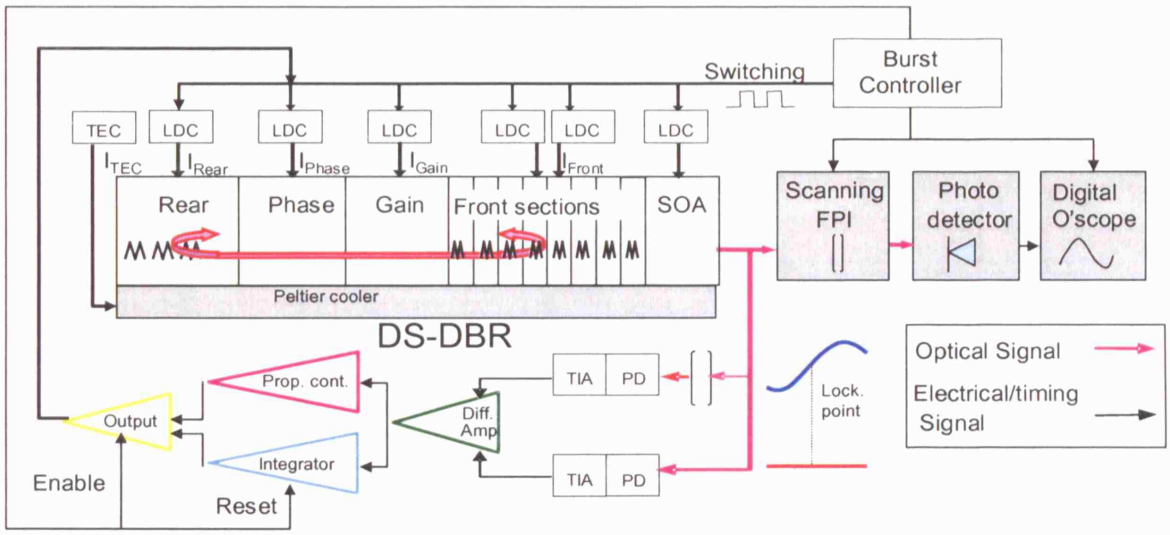

Figure 3-11 Set-up for measurement of wavelength stability and timing control for BMTx

Wavelength stability measurements were carried out for burst lengths in the range of 10μs to 500ms for the DS-DBR for a high tuning current switch with the optimal control coefficients visually optimized to obtain the fastest non-oscillating response. The burst controller, a Sony DG2300 delay generator, was used as the central timing control for both the laser and the measurement equipment. In addition to providing the tuning currents and switching signal for the laser sections the burst controller also gated the SOA current to shield the laser output during switching.

3.5.3 Wavelength locking of DS-DBR

The bandwidth limited switching and locking times are shown in Figure 3-12 which shows the timing diagram for the first 20μs of a wavelength switching event with and without the activation of the WLL. Initially, the SOA current is switched to zero to prevent the emission of switching crosstalk before the tuning current switch is initiated and the SOA is reactivated. After the period of mode competition, the lasing wavelength is within the locking range, set by the linear approximation of the etalon response, shown in Figure 3-4, and the locking circuit is activated.

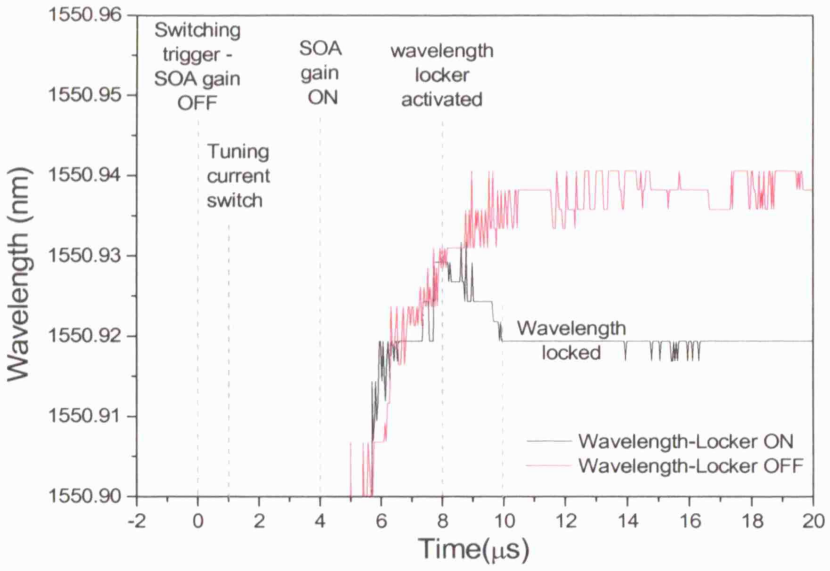

Figure 3-12 Timing diagram for wavelength switching transition with and without active wavelength locking and with SOA blanking for 50mA rear section switch (TLD1001)

Once activated, the wavelength locking loop takes approximately 2μs to lock the output wavelength to the ITU-T wavelength at 1550.92nm. The locking time is the same as the laser switching time and set by the 500 KHz current driver bandwidth. To provide a comparison with the locking performance, the wavelength drift characteristic of the unlocked switching is also shown. The timing of the wavelength switching event may also be observed by considering the action of the individual loop elements. Figure 3-13 shows a set of oscilloscope traces taken directly from the control board during a wavelength switching event. Most notable is the voltage output of the differential amplifier, indicating the wavelength deviation from the nearest ITU-T operating point. During the period of mode competition the DA and the proportional control oscillate as the spurious competing modes are generated. Meanwhile, the integrator and output stage return and remain approximately at zero whilst disabled. Once, activated, the locking loop sends the differential amplifier to zero in approximately 2μs by the combined action of both the integrator and proportional control. As in the previous figure, the locking time is consistent with the modulation bandwidth of the LDC measured to be 500KHz.

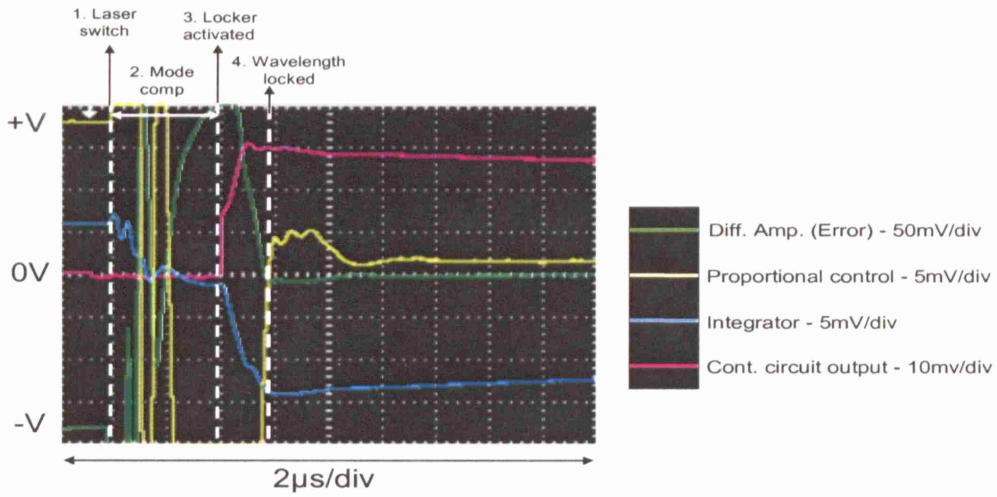

Figure 3-13 Oscilloscope trace showing control circuit element during wavelength

The long term wavelength stability of the control board was investigated using switching measurements with burst lengths up to 500ms. Figure 3-14 shows the measured wavelength stability for 2 switching transitions. The first, in Figure 3-14(a), is for a 50mA tuning current switch (high to low) on the rear section whilst the second, Figure 3-14(b), is the wavelength drift resulting in a simultaneous switch of the rear tuning section (low to high) and 140mA switch on the SOA (low to high) as would occur after a period of blanking.

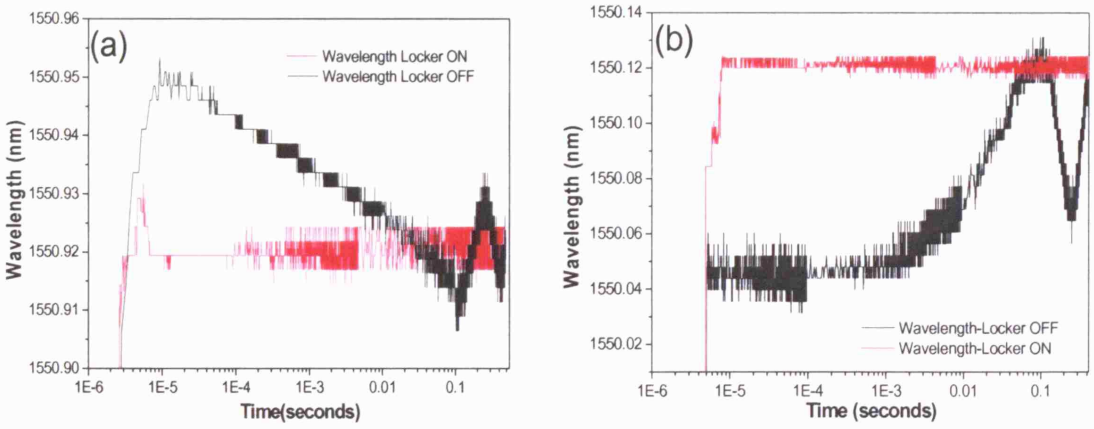

Figure 3-14 Comparison of switching transition with/without wavelength locking control loop for (a) 50mA rear current switch and (b) 150mA SOA current switch - TLD1002

The wavelength stability for both of the worst case switching scenarios for the DS-DBR shown in Figure 3-14 is maintained below 1GHz by the action of the wavelength locking loop compared to over 6GHz for the unlocked switching transitions. This is comparable with the highest reported stability for etalon based wavelength lockers and is a 5-fold improvement on previous wavelength locking measurements for DS-DBR. Similarly, despite the bandwidth limitation of the LDCs, the measured switching times represent an improvement of 3

orders of magnitude from previous measurements of wavelength locked switching transitions. Figure 3-15 again shows the outputs of the control loop elements, but, during a longer 1 second wavelength switch. Figure 3-15 shows that over the longer timescale the integrator closely matches the shape of the wavelength deviation caused by the thermal transients and dominates the control circuit output whilst the proportional control provides only a fixed contribution throughout the burst duration. Additionally, the differential amplifier output remains constantly at zero showing the burst wavelength remains locked for the duration of the burst as in Figure 3-14.

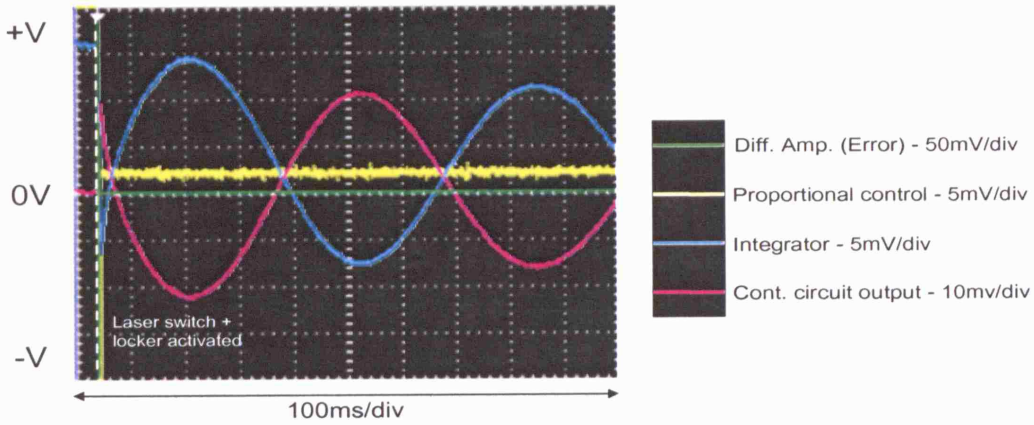

Figure 3-15 Oscilloscope trace showing control circuit elements during 1 second wavelength switch

The locking range and operation of the locking circuit was further tested by the measurement of the locking performance in the presence of a number of initial wavelength deviations set by an offset on the phase section current between two super-mode boundaries. The wavelength deviation plots are shown in Figure 3-16 and show the wavelength locking board shows good locking performance for all locking conditions investigated with no discernible difference in locking time.

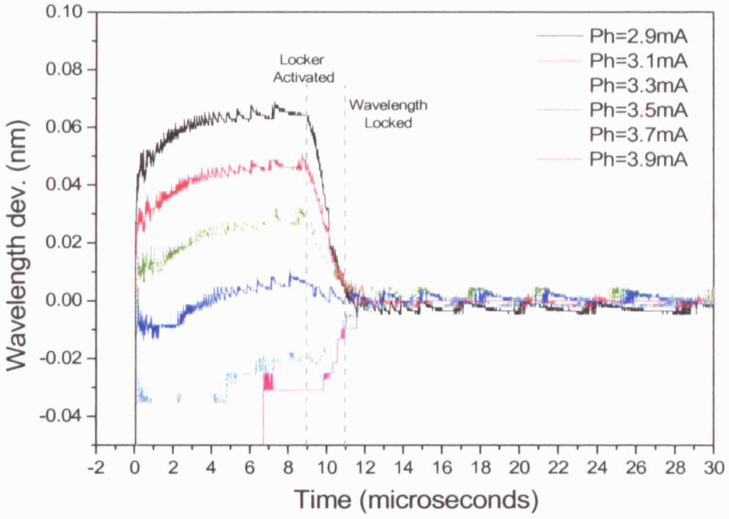

Figure 3-16 Locking operation for different initial wavelength deviations - TLD1002

3.5.4 Wavelength locking of SG-DBR

The performance of the wavelength locking board was further investigated for the SG-DBR laser using large current switching using an external wavelength locker based on a single etalon path and reference photodiode as shown in Figure 3-1. As with the DS-DBR, the performance of the wavelength locker was tested using a high current switch to an arbitrary ITU-T wavelength. The etalon response and constant reference photocurrents together with the output wavelength are shown as a function of phase current in Figure 3-17(a), based on a 5% tap of the total laser output power. The measured wavelength stability across a 1-second burst, after an 80mA tuning current switch is shown with and without the wavelength locking control loop in Figure 3-17.

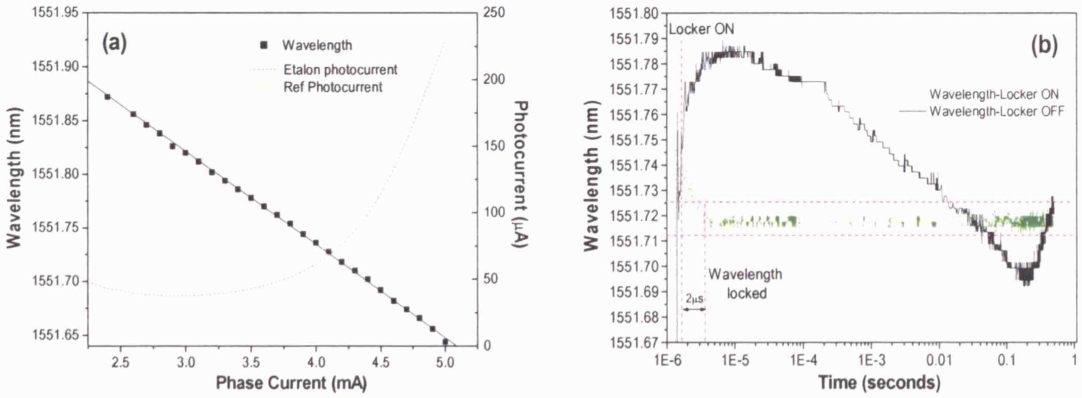

Figure 3-17 (a) Locking point characterization and (b) wavelength stability measurements for locked and unlocked 80mA rear section tuning current switch - TLS2078

Figure 3-17 shows that the measured wavelength stability of the locked wavelength after a high tuning current switch is again less than 1GHz, similar to the value measured with the integrated wavelength locker. Interestingly, the same locked wavelength stability and 2μs locking time were measured for the externally locked SG-DBR as with the integrated locker in the DS-DBR. As shown in Figure 3-17(a) this is despite the order of magnitude reduction in the measured photocurrents due to low responsivity of photodiodes in the external locker, the 100% reduction of the error signal/wavelength slope compared to the transflective etalon design and more than double the total wavelength drift for the equivalent uncontrolled switch compared to the DS-DBR. As with the DS-DBR measurements, the locked wavelength stability is limited by the electrical noise arising from the on-board components with the locking speed limited by the bandwidth of the LDC.

3.6 Q-factor/BER measurements of quality of locked signal through finite BW filter

Final experimental confirmation of the implemented wavelength locker was obtained with BER-derived Q-factor measurements for bursts transmitted through narrow (20GHz to 50GHz) wavelength routers as described previously in section 2.5. The measurement set up is shown in Figure 3-18.

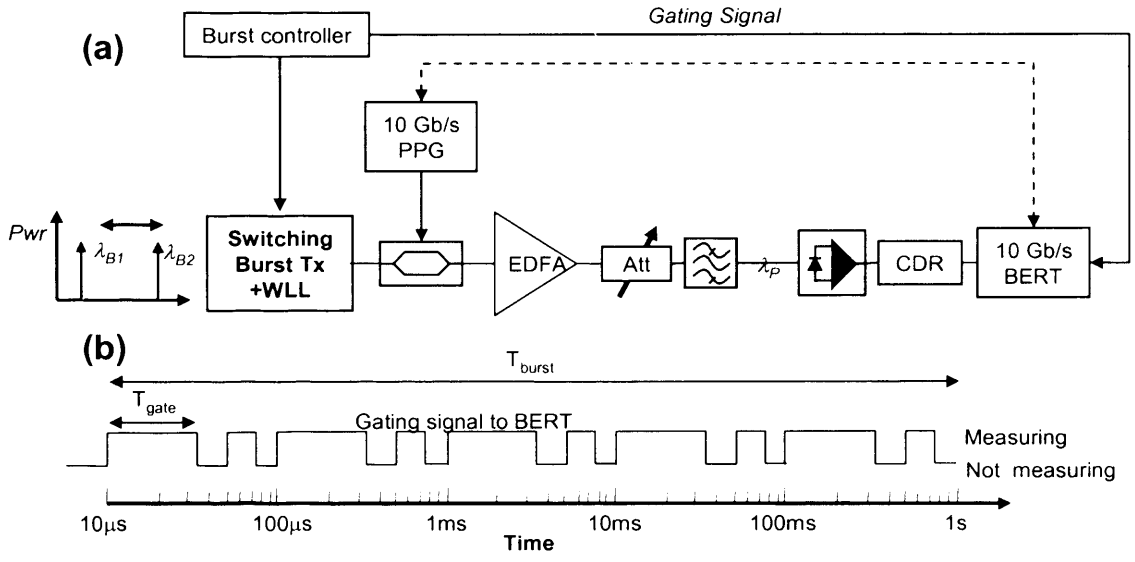

Figure 3-18 Experimental set-up for gated BER measurements to study signal quality across long bursts and (b) timing windows used for Q-factor measurements across 1 second burst

In order to analyze the signal quality as a function of burst length or at different points within a long burst, the burst controller, used to control both the switching and wavelength locking of the laser was also used to gate the receiver. As

before, Q-factor measurements were made within short gating windows, the size of which were logarithmically increased and scanned across the length of the wavelength locked optical bursts, as shown in Figure 3-18(b), to allow for direct comparison with the unlocked measurements described in chapter 2.

The study of lasers transmitted through wavelength routers described in section 2.6 showed that the largest penalty was observed with an SG-DBR laser exhibiting high thermal drift from an 80mA tuning current switch and the free space grating router with a 3dB bandwidth of 0.008nm. The measured Q-factor penalty at an OSNR of 35dB is shown for both the locked and unlocked burst following an 80mA tuning current switch in Figure 3-19.

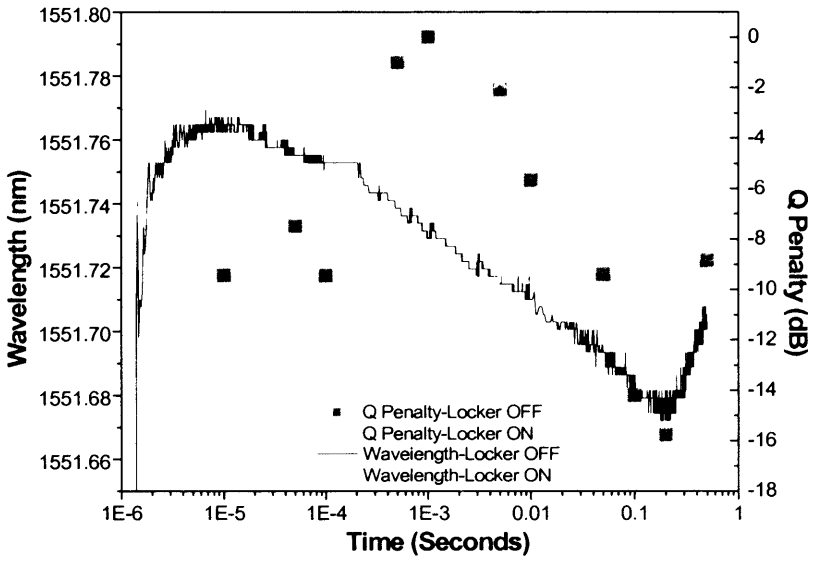

Figure 3-19 80mA tuning current switch through free space grating router with and without wavelength locking – TLS2078

For this extreme case, the use of the wavelength locking control circuit results in a large Q-factor gain at all points across the burst. In order to provide a measurable comparison between the locked and unlocked cases, it was necessary to perform all measurements without any noise loading. Hence, the variation of measured Q-factor values for the locked signal is thought to be due to extrapolation errors since measurements with high Q-factor values, up to 20dB were based on relatively few errors. Without the locker active, the Q-factor penalty varies across the burst according the wavelength deviation as previously shown in figure 2-31.

The comparison of the measured Q-factor was then repeated for the case of a high tuning current switch for the DS-DBR and 50GHz spaced wavelength router. The measured Q-factor values for both a 50mA rear section tuning current switch and 140mA current switch on the SOA, with and without the wavelength locking control loop are shown in Figure 3-20 with all Q-factor measurements performed at a fixed OSNR of 25dB.

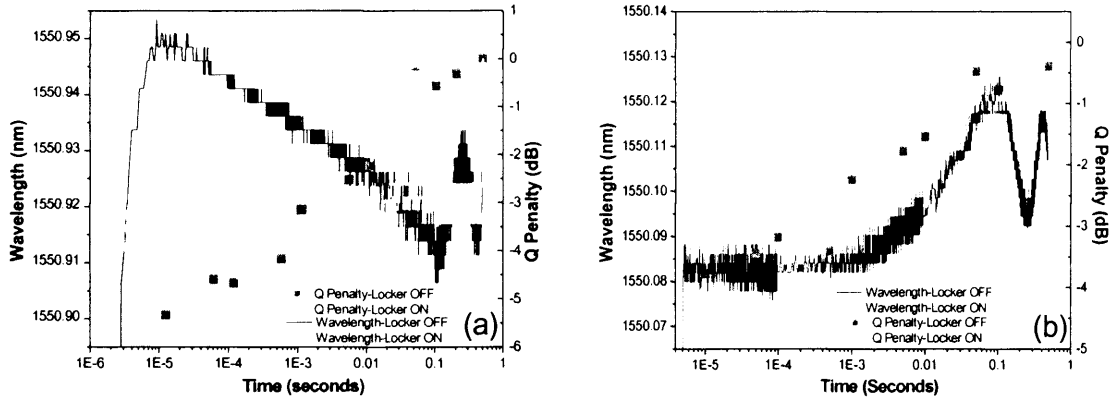

Figure 3-20 Q-factor measurements of signal quality across 500ms burst after transmission through 0.03nm filter for unlocked and wavelength locked wavelength switches for (a) 50mA tuning current switch on rear section (high to low) and (b) 140mA tuning current modulation (low to high) on SOA section – TLD1002

For both switching transitions the Q-factor penalty for the unlocked burst increased with the deviation from the final wavelength, as expected from section 2.6, with a maximum Q-factor penalty of 5dB. With the wavelength locking control loop active, the Q-factor penalty is reduced 1dB for across the entire 500ms burst again demonstrating the improvement of signal quality gained with use of the wavelength locking control loop.

3.7 Extrapolation of loop bandwidth

To investigate the performance of the WLL at higher speeds, the numerical simulator described in section 3.2 was used to calculate the optimal control coefficients and the loop locking time for each control scenario at higher loop bandwidths ranging from 1 to 100MHz. For this, the bandwidth limitation imposed on all loop components was raised to the new loop bandwidth and the simulator was used to calculate the optimum coefficients and locking time in each case. These results are shown in Figure 3-21.

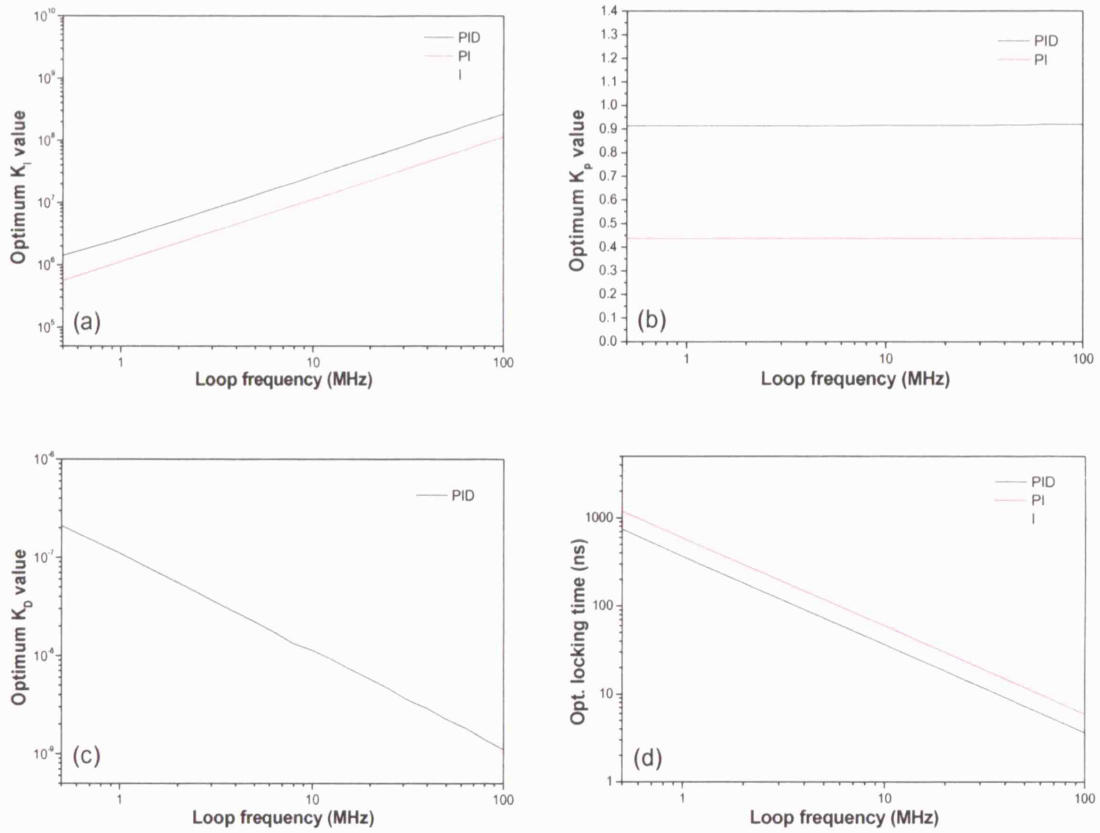

Figure 3-21 Optimized control loop coefficients as a function of loop bandwidth showing (a) integral, (b) proportional and (c) differential coefficients and (d) optimal wavelength locking time

As revealed by equations (3.3) to (3.5) and equations to (3.6) to (3.7), the integral coefficient increases proportionally with the loop bandwidth in all cases whilst the proportional coefficient in independent of the loop bandwidth. For the PID case the optimal value of the differential coefficient is inversely proportional to the loop bandwidth as predicted in equation (3.5). Hence, for systems requiring the faster nanosecond locking performance, the implementation of a full PID control becomes even more difficult.

The locking time improves linearly with increased loop bandwidth in all 3 cases with locking times for the 100MHz loop bandwidth being in the nanosecond regime for both the PID and PI control scenarios with the integral control roughly 3 times slower. Hence, the operation of the board at higher speeds support the construction of the PI control board as a trade-off between locking performance and the feasibility of practical implementation.

The discrepancy between the measured loop locking time for the implemented wavelength control board and the equivalent simulated case for PI control at a loop bandwidth of 500KHz (900ns) is believed to be a result of the non-ideal characteristics of the control board and loop components.

3.8 Summary

In this chapter, wavelength switching schemes were discussed, with particular attention paid to phase section control schemes suitable for fast wavelength stabilization of multi-section semiconductor tunable lasers. Based on this, a theoretical analysis of a linearised etalon-based wavelength locking loop was presented and used to derive optimal coefficients for different control scenarios. As a result of a trade-off between locking speed and practical implementation, a wavelength locking control board, based on a PI control was built and used in wavelength control scheme for high-current switching in DBR tunable lasers. The locking time was measured to be 2μs, limited by the bandwidth of laser current drivers with numerical simulations of the WLL demonstrating operation 2 orders of magnitude faster. The wavelength locked transmitter was then used in a demonstration of a burst-mode transmitter with SOA blanking of the laser output during switching events to prevent interference from switching crosstalk. Modulation of the SOA drive current, which also leads to thermally induced wavelength transients, was used in combination with the maximum tuning current switch to provide a worst case thermal wavelength drift of 0.11nm. For this case, with the locker activated, the wavelength stability was measured to be under 1GHz with a locking time including SOA blanking of 5μs for all the switching events measured. These results represented a three order of magnitude improvement in locking speed and five-fold increase in wavelength stability over previous experimental demonstrations with DS-DBR lasers [Pon06].

3.9 References

Bay04 **Optical burst switching: research and applications**
P.Bayvel, M.Düser. Tech. Digest of Optical Fibre Communication conf., Vol. 2, 23-27 Feb. 2004

Boo07 http://www.bookham.com/datasheets/transmitters/TL-5000.cfm

Bro91 **Modern control theory**
William L. Brogan. Third edition (1991), pub Prentice Hall, ISBN:0-13-589763-7

Car00 **Design of thin-film interference filters for telecommunications applications**
C.K.Carniglia. Tech. Digest of Optical Fibre Communication Conf., Vol. 2, pp93, 7-10 March 2000

Del97 **Widely tunable DBR lasers with wavelength drift lower than 0.009 nm/yr over all**

addressable wavelength channels
F.Delorme, G.Alibert, M.Robinet, P.Boulet, G.Terol, P.Devoldere. Tech. Digest of European Conference on Optical Communications, Vol. 1, pp34-37, 22-25 Sept. 1997

Del99 **Wavelength aging analysis of DBR lasers using tuning section IM frequency response measurements**
F.Delorme, B.Pierre, H.de Baillliencourt, G.Terol, P.Devoldere. IEEE Photonics Technology Letters, Vol. 11 (3), pp 310 - 312 March 1999

DeM05 **High wavelength accuracy of a full C-band external cavity tunable laser using an intracavity wavelength reference etalon**
J.De Merlier, K.Mizutani, S.Sudo, S.Watanabe, K.Sato, K.Kudo. Tech. Digest of European Conference on Optical Communication, Vol. 3, pp:567-568, 25-29 Sept. 2005

Ham02 **Integrated wavelength locker for tunable laser applications**
B.Hammond, S.Bingzhi, J.Mathews, E.Chen, E.Schwartz. Tech. Digest of IEEE Lasers and Electro-Optics Society Annual Meeting, Vol. 2, 479 – 480, 10-14 Nov. 2002

Han03 **Development of internal wavelength lockers for tunable laser applications**
H.Han, B.Hammond, R.Boye, S.Bingzhi, J.Mathews, B.TeKolste, A.Cruz, D.Knight, B.Padgett, D.Aichele, Electronic Components and Technology Conf. pp 805-808, May 27-30, 2003

Hea03 **Widely tunable laser module using DFB array and MEMs selection with internal wavelength locker**
J.Heanue, E.Vail, M.Sherback, B.Pezeshki. Tech. Digest of Optical Fibre Communications Conf., Vol.1, pp 82-83, 23-28 March 2003

Ich02 **Athermal wavelength lockers using fibre Bragg gratings**
M.Ichioka, J.Ichikawa, Y.Kinpara, T.Sakai, H.Oguri, K.Kubodera. Tech. Digest of IEEE/LEOS Workshop on Fibre and Optical Passive Components pp 208-212, 5-6 June 2002

Ish98 **Mode stabilization method for superstructure-grating DBR lasers**
H.Ishii, F.Kano,Y.Yoshikuni,H.Yasaka. Journal of Lightwave Technology, Vol. 16, (3), pp 433-442, March 1998

JDS07/1 http://www.jdsu.com/index.cfm?productid=7&pagepath=Products/Optical_Communications/Products/Passive_Components_Modules/Wavelength_Lockers&id=5411

JDS07/2 http://www.jdsu.com/index.cfm?productid=606&pagepath=Products/Optical_Communications/Products/Tunable_Transmission_Modules&id=4832

Kim04 **Thermally controlled wavelength locker integrated in widely tunable SGDBR-LD module**
Jongdeog Kim, Byung Seok Choi, Hogyeong Yun, Su Hwan Oh, Jong-Hyun Lee, Hyunsung Ko, Kwang-Seong Choi, Sahnggi Park, Jong Tae Moon, Moon-Ho Park. IEEE Photonics Technology Letters, Vol. 16 (11), pp 2430-2432, Nov. 2004

Lar07 **Stabilisation and control of widely tunable MG-Y lasers with integrated photodetectors**
R.Laroy, G.Morthier, T.Mullane, M.Todd, R.Baets. IET Optoelectronics Vol. 1 (1), pp:35-38, February 2007

Lag98 **Convergnece properties of the Nelder-Mead simplex methos in low dimensions**
J.C.Lagarias, J.A.Reeds, M.H.Wright, P.E.Wright. SIAM Journal of Optimization, Vol. 9 (1), pp 112-147, 1998

Lav00 **Accelerated aging studies of multi-section tunable GCSR lasers for dense WDM applications**
O.A.Lavrova, D.J.Blumenthal, Journal of Lightwave Technology. Vol. 18 (12), pp2196-2199, Dec 2000

Lav99 **Tuning and aging characteristics of multisection tunable GCSR lasers for dense WDM applications**
O.A.Lavrova, D.J.Blumenthal. Tech. Digest of IEEE Lasers and Electro-Optics Society 1999 12th Annual Meeting Vol. 1, pp 200 – 201, 8-11 Nov. 1999

Liu06 **Directly-modulated DS-DBR tunable laser for uncooled C-band WDM system**
Y.Liu, J.D.Ingham, R.G.S.Plumb, R.V.Penty, I.H.White, D.J. Robbins, N.D. Whitbread, A.J.Ward. Tech. Digest of Optical Fibre Communication Conf., pp 3, 5-10 March 2006

Pon06 **Dynamically controlled channel-to-channel switching in a full-band DS-DBR laser**
L.Ponnampalam, R.Barlow, N.D.Whitbread, G.Busico, J.P.Duck, A.J.Ward, D.J. Robbins. IEEE Journal of Quantum Electronics, Vol. 42 (3), pp223 – 230 March 2006

Ren04 **Nanosecond channel-switching exact optical frequency synthesizer using an optical injection phase-locked loop (OIPLL)**
C.C. Renaud, M. Düser, C.F.C. Silva, B. Puttnam, T. Lovell, P. Bayvel, A.J. Seeds. IEEE Photonics Technology Letters, Vol. 16 (3), pp 903 – 905, March 2004

Ren05 **Coolerless tunable semiconductor laser operated over 32, 100 GHz-spaced, channels with less than 0.1 nm thermal drift**
C.C. Renaud, A.J. Seeds. IEE Electronics Letters, Vol. 41 (3), pp127-128 3 Feb 2005

Ren06 **100 GHz spaced 10 Gbit/s WDM over 10 /spl deg/C to 70 /spl deg/C using an uncooled DBR laser**
C.C.Renaud, M.J.Fice, L.Lealman, P.Cannard, L.Rivers, A.J.Seeds. Tech. Digest of Optical Fibre Communication Conf., pp3, 5-10 March 2006

Sar00 **Control of widely tunable SSG-DBR lasers for dense wavelength division multiplexing**
G.Sarlet, G.Morthier, R.Baets. Journal of Lightwave Technology, Vol. 18 (8), pp1128-1138, Aug. 2000

Sar99 **Wavelength and mode stabilization of widely tunable SG-DBR and SSG-DBR lasers**
G.Sarlet, G.Morthier, R.Baets. IEEE Photonics Technology Letters, Vol.11, pp 1351-1353, Nov. 1999

Sim03 **Fast switching characteristics of a widely tunable laser transmitter**
J.E. Simsarian. A.Bhardwaj, J.Gripp, K.Sherman, S.Yikai, C.Webb, Liming Zhang, M.Zirngibl. IEEE Photonics Technology Letters, Vol. 15 (8), pp 1038-1040, Aug. 2003

Sim04 **Wavelength locking a fast-switching tunable laser**
J.E. Simsarian, Liming Zhang, IEEE Photonics Technology Letters, Vol. 16, (7), pp 1745-1747, July 2004

Sos04 **Integrated Wavelength Locker for CostýEffective Laser Packaging**
Y.Soskind, J.Perkins, T.Wall. Tech. Digest of Electronic Components and Technology Conference, pp :234 – 238, 31 May-3 June 2005

Woo93 **The effects of aging on the Bragg section of a DBR laser**
S.L.Woodward, P.Parayanthal, U.Koren. IEEE Photonics Technology Letters, Vol. 5 (7), pp 750-752, July 1993

Chapter 4 Burst-Mode Reception

4.1 Burst-mode receivers in optical networks

The second crucial sub-system required for implementation of an optical burst switched network is the optical receiver that must be able to respond to large power, timing and phase fluctuations of the incoming signal, on a burst-by-burst basis. For most OBS architectures, including WR-OBS, the burst-mode receivers (BMRx) are located in edge routers, alongside the tunable lasers, and act as the outgoing interface between the optical and electrical domain. Since the BMRx in an OBS network must be capable of recovering burst data originating from any node in the network there exist a number of additional design constraints compared to conventional optical receiver.

In addition to being able to cope with idle periods inherent in burst traffic, the BMRx must be able to accurately recover the timing and data information from optical bursts arriving asynchronously. It must also be able to compensate for path dependent power fluctuations between bursts transmitted through different lengths of fibre or varying numbers of routing or amplification stages. These power fluctuations have been estimated to exceed 10dB and in some cases be as high as 20dB [Cha01, Cha97]. In order to achieve these aims any required header, guard band or preamble should be as short as possible to maximize network efficiency with the currently tolerated framed data overhead of 5% to 10% being considered as the upper limit. The receiver should be able to operate equally well for bursts of varying length as for fixed length and place no restriction on the frequency content of transmitted data.

In this chapter, existing receiver designs for burst-mode optical networks are reviewed and assessed in terms of their ability to meet these requirements. Based on this assessment, potential schemes for the ideal BMRx are discussed along with the key design issues centred on the receiver coupling and burst power equalisation. Finally, a new approach for BMRx using conventional AC-coupled photodiode, asynchronous 20Gb/s digital sampling and digital signal processing is described and experimentally verified.

4.1.1 Figures of merit for BMRx studies

BMRx's appear in a wide range of system and network contexts and subsequently have been studied from a number of different perspectives. As a result, a number of different figures of merit have been used in published studies on burst-mode reception for comparison of BMRx performance. It is, therefore, necessary to define the following parameters that are used to assess burst-mode receiver performance in the subsequent analysis of experimental data.

- Receiver sensitivity
- Operating range (Max. input power - Receiver sensitivity)
- Burst-to-burst dynamic range
- Burst efficiency

The receiver sensitivity is defined as the minimum input signal power for a specified performance criterion and may apply to continuous or burst-mode signals. Similarly, the receiver operating range may be defined as the difference between the receiver sensitivity and the maximum input power for the specified performance criteria. This is not necessarily the same as the burst-to-burst dynamic range of a burst-mode receiver which is defined as the maximum allowable power difference between adjacent bursts for which specified performance criteria is met for all bursts. The sensitivity, operating range and burst-to-burst dynamic range may be expressed as a Q-factor or OSNR penalty or as a specified bit error rate or burst header error rate.

The burst efficiency is defined as the ratio of the burst overhead to the total burst length. The burst overhead consists of all sections of the transmitted burst that are not used for transmission of data signal and is generally the sum of 2 parts. The first part is any additional transmitted bits required to facilitate burst reception by providing management data used in burst data recovery. These can be burst preambles or tails used to signify the start and end of burst or provide information about the power or phase of the incoming burst but also includes any additional bits used in line coding schemes such as 8B/10B that may be required to overcome physical impairments. The second contribution to burst overhead comes from the required separation or guard band required between bursts. The length of the guard band may be set by physical parameters such as the reset time of electronic control circuits, the switching

time of transmitters at the start of the link or dictated by the signalling protocol employed.

4.1.2 Review of published BMRx designs

A number of different approaches have been taken in the design of burst-mode receivers depending on the specific use required and the available components. The key component of any optical receiver is the photodiode (PD) but for burst-mode receivers, how this is coupled to the decision-circuit is an important design consideration. The most common configuration for a conventional high bit rate optical receiver is to use a PD capacitively coupled to the decision-circuit [Agr02a], commonly referred to as AC-coupling. This simplifies the design of the electrical circuit by allowing the decision voltage to be fixed at zero but is not ideal for a BMRx because variations in the average input optical power from idle periods, guard bands or path dependent losses leads to a large DC-offset, known as baseline wander, across bursts. These DC-offsets originate from the charging and discharging of the coupling capacitors and the time constant of the DC-offset decay is set by the value of the capacitor. Whilst the time constant may be chosen in the design of the decision-circuit the initial over/under shoot depends upon the power variation between the previous input signal (burst or guard band) and the current burst and thus varies dynamically depending on the input data stream. Figure 4-1 shows the baseline wander (BLW) across an isolated 1ms optical burst received with a conventional AC-coupled receiver, with an RC time constant of around 100kHz, and illustrates the problem of optimum decision-threshold setting.

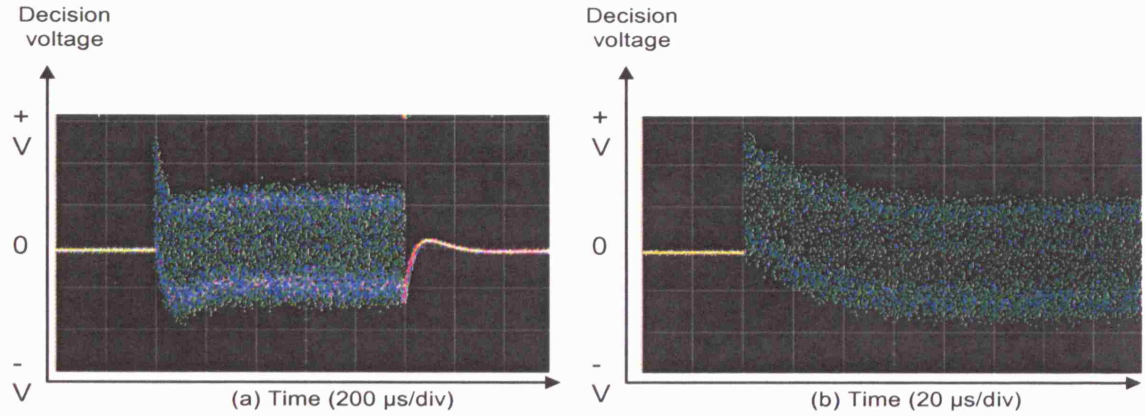

Figure 4-1 Baseline wander from (a) 1ms and (b) first 160us, of burst received with AC-coupled Rx

A second key difference between conventional receivers and those optimised for bursts is the clock recovery scheme. Fast clock recovery is imperative for

BMRxs since it must be performed after the arrival of each burst, with any delay contributing to network overhead. A common approach for fast clock recovery in NRZ systems uses a frequency doubler to ensure significant spectral power at the bit rate and a high-Q filter centred at the bit rate to extract the clock signal [Agr02b]. In this scheme the clock acquisition time depends on the bandwidth of the high-Q filter, increasing the bandwidth will decrease the acquisition time however this is at the expense of increased noise on the recovered clock. Typical schemes use a bandwidth of 10-100MHz which results in an acquisition time of 10-100ns. Recently, high bit-rate systems based on phase locked loops [Li06, Geo02, Rei01] and all-optical systems using optical gates [Kan03, Sta05] have also been used for burst-mode clock recovery.

4.1.2.1 DC-coupled BMRx

Solutions to the problem of BLW arising from an AC-coupled receiver can be grouped in to 2 broad categories. The first approach, as has been demonstrated at bit rates up to 1.25Gb/s, is simply to use a DC-coupled photodiode and ensure all subsequent electrical amplifiers are also DC-coupled. Ota et al. [Ota92] reported the first Gb/s BMRx using an avalanche photodiode DC-coupled to a transimpedance amplifier (TIA) to obtain a dynamic range of 23dB and a reset time of 100ns for 1Gb/s data transmission. Subsequently, [Bak01] proposed an additional dynamic offset compensation circuit to improve the performance of such receivers. More recently, driven by the requirement for burst-mode reception in the upstream path of passive optical networks (PONs), [Le04] describes an integrated circuit (IC) BMRx with a 300ns guard band and preamble for a 1.25Gb/s Ethernet PON and [Oss05] obtained a reset time of 25ns using limiting amplifiers and a DC-coupled avalanche photodiode (APD) for 1.25Gb/s gigabit PON application. [Le04] used a feed-forward technique and TIA with automatic gain control (AGC) to equalize the incoming burst power before the decision-circuit with a fixed threshold whilst [Oss05] used limiting amplifiers after the PD for the same effect.

Table 4-1 Comparison of DC-coupled burst-mode receiver performance

Ref	Bit rate (Gb/s)	Req'd guard band/ reset time	Pre-amble	Sens (dBm)	Dyn. range (dB)	Comments
Ota92	1	100ns	--	-37.5	23	
Le04	1.25	250ns	50ns	-26.4	21	AGC
Oss05	1.25	25.6ns	18ns	-32.8	23.8	

-- Value not appropriate or not obtainable from reference

The primary design challenge for DC-coupled burst-mode receivers, and in some AC-coupled designs, is how to dynamically set the decision-threshold to an appropriate value for the incoming burst. A DC-coupled BMRx requiring a data preamble to extract its decision-threshold will exhibit sensitivity penalties compared to continuous-mode receivers and the impact of preamble length on the sensitivity has been studied extensively [Eld93, Cha94, Men95, Cha97]. More recently an additional problem of random DC offsets originating from imperfection in the fabrication process [Oss06] was described. The largest hurdle for the widespread adoption of DC-coupled BMRx designs, as evident in the low bit-rate demonstrations listed in Table 4-1, is their scalability to higher bit rates. Whilst DC-coupled photodiodes with appropriate bandwidth are commercially available, it is the availability of DC-coupled AGC and limiting amplifiers that make this approach difficult at higher bit rates. Indeed a DC-coupled BMRx at 10Gb/s has yet to be reported and no DC-coupled AGC or limiting amplifiers with a bandwidth suitable for 10Gb/s transmission are commercially available.

4.1.2.2 AC-coupled BMRx

Despite the inherent difficulties described there does exist a number of BMRxs designed around PDs AC-coupled to the decision-circuit. The most common approach is to select values of the coupling capacitor and resistor in order to reduce the time constant of the decay and allow a guard band between transmission of meaningful data. Whilst this technique simplifies the problem of DC-offset removal and decision-threshold setting it introduces additional operating complexities in addition to reduced network efficiency from the unusable portion of each transmitted burst.

Whilst conventional AC-coupled receivers designed for continuous operation require a large capacitor to reduce the cut-off frequency and maintain as much of the frequency spectrum of the received data as possible, BMRxs require smaller values of capacitance if they are to be able to respond rapidly to the power variation caused by incoming bursts. For typical OBS burst lengths, on a µs-ms timescale, acceptable overheads would require the removal of the initial DC offset on a ns- µs timescale. Reducing the time taken to respond to input power changes to this level reduces the required overhead required per burst

but also means the receiver may start to respond to power level changes originating from the data itself. Since reducing the time constant of the decay is equivalent to increasing the high pass cut-off of the AC-coupled circuit, this rejects the low frequency content of the received data giving rise to signal distortion during transmission of long strings of ones or zeros [Max04].

It is for this reason that many published AC-coupled BMRx designs use additional line coding to remove the low frequency content of the transmitted data. For example, in 8B/10B line coding scheme each 8 bit sequence of source data is converted into a 10bit code block with higher transition density to reduce the low frequency content. Such a receiver is theoretically described in [Bui04]. At 1.25Gb/s this approach was pioneered by Han and Lee who used 8B/10B line coding to remove the low frequency content allowing a low frequency cut off of 14.5MHz requiring a guard band of 74ns [Han03]. In [Han04] numerical analysis was used to compare an optimized version of the line coded receiver to a continuous receiver with a 2^9-1 PRBS for different cut-off frequencies and shows a minimal penalty burst-mode operation. For 1.25Gb/s Ethernet PON applications [Woo05] showed an AC-coupled BMRx in a small form-factor pluggable (SFP) package transceiver card and [Bae05] showed a low cost receiver using commercially available AGC TIA and APD.

Similar line coding schemes have also been demonstrated at higher bit rates. The performance of a receiver similar to that proposed in [Bui04] was analyzed in [Rot05] for other line coding schemes and showed a locking time of 30ns for a 10dB dynamic range with a 2dB penalty due to AC-coupling at 12.5Gb/s.

In addition to the published studies on BMRxs, there exists a large body of published work on optical burst/packet switching systems and networks that have required the implementation of high speed burst-mode receivers. An AC-coupled BMRx design appears in a number of studies of high-capacity optical switch fabrics using fast tunable lasers and arrayed waveguide routers at bit rates up to 40Gb/s [Gri01], [Due03] and [Gri03]. The BMRx used in these experiments use fast CDR chips [Rei01] to extract clock and data information after a fast AC-coupled receiver with a low pass frequency cut off of 10MHz [Due03]. Whilst these studies do not use specific line coding the effect of BLW

due to the low frequency cut-off is removed by limiting the burst length to 10μs and using a short PRBS (2^7-1) containing limited runs of consecutive matching symbols. The receiver input power of arriving bursts is also maintained broadly constant during these measurements further reducing the potential disruption caused by BLW from the AC-coupled PD. Similarly, a BMRx for a packet ring network [Shr00] demonstrated a BMRx with fast clock recovery in 40ns using an RF mixer with the frequency content of bursts limited by using a PRBS of length 2^7-1 and using equal power 1μs bursts.

Alternative AC-coupled BMRx designs have been reported for high bit- rate PON systems. In [Kim03] the first step towards directly addressing the BLW problem with the design of an equalizing amplifier for AC-coupled BMRxs together with 10Gb/s CDR unit [Kim 02]. The scheme used high speed mean value detectors to track the real time signal baseline changes and used these as the threshold voltage for 2 limiting amplifiers with a required 40 bit preamble sequence. A dynamic range of 9.2 dB was reported for this receiver although this is thought to be the operating range of the receiver under continuous operation and not the power difference between adjacent bursts. All AC-coupled receiver configurations are summarised in Table 4-2 in section 4.2.

4.1.2.3 Alternative BMRx schemes

A newly emerging category of BMRx for NRZ data is based on differential data edge detection with limiting amplifiers. These receivers [Kim04, Nog05, Nog06] use an AC-coupled PD followed by an electrical delay after a differential limiting amplifier to track the edges (symbol transitions) of an NRZ signal. A hysteresis comparator is then used to recover the original data. [Kim04] demonstrated a 10Gb/s BMRx requiring a 16bit preamble for 128 bit bursts. In [Nog05] an improved design showed error free burst recovery with 0.5ns locking time for bursts varying by a factor of 3 in electrical peak-to-peak voltage. In [Nog06], the noise sensitivity of the design was improved by using a limiting amplifier with variable gain set by input burst power. This improved the operating range to 28dB (electrical) but the ability to deal with adjacent burst power variations and the length and separation of bursts is not described, and so how this problem is addressed is unclear. Differential detection is also used to recover Manchester coded data signals in [Nis02] and a digital ring oscillator to carry out clock

recovery [Yam99]. However this complicated scheme required Manchester coded input data and a thermal error correction circuit. The first burst-mode receiver using differential phase shift keying (DPSK) by the same author in [Nis99] and [Su04] showed how linear optical amplifiers can be used to improve the dynamic range of such receivers.

4.1.2.4 All-optical BMRx

Another method employed to overcome the problem of BLW wander from an AC-coupled photodiode is to perform the power equalization tasks in the optical domain. [Pet06] used a series of SOA based Mach Zender Interferometers (MZI) to implement all-optical BMRx for 40GB/s RZ pulses. Here MZI's were used for power equalization [Shi98], wavelength conversion and clock and data recovery [Sat05]. However, the function of OBS edge router is to convert to the electrical domain and although optical processing of this kind can be used to reduce the demand on the receiver by power equalizing/regenerating bursts along transmission links or as a receiver front end the problem of converting to the electrical domain with burst data containing large idle periods still remains.

4.1.2.5 Digital BMRx

One area that been sparsely researched in relation to high bit rate optical burst-mode receivers yet has the potential to solve many of the problems described is digital signal processing. Indeed many of the problems described in the analogue implantations may be solved simply if the means exist to process bursts digitally. The development of fast analogue to digital conversion (ADC) and high power programmable digital signal processing (DSP) chips and field programmable gate arrays FPGA [Alt05] have enabled many enhancements to high speed optical networking previously thought beyond the electronic domain.

In 2003 20GS/s ADC chips with on-board memory to capture resulting data-streams operating at 20GS/s opened the door for sampling above the Nyquist frequency for 10 Gb/s analogue data streams [Pou03]. Subsequently, further research has pushed the boundaries to higher bit rates and better performance [Sch06, Far04, Lee04]. Additionally, high bandwidth real time data storage oscilloscopes capable of 40GS/s ADC have become commercially available [Tek05] enabling the study of applying DSP principles to high bit optical

communication. The potential of DSP to solve the problems faced by the BMRx designs described thus far are discussed in the next section.

4.1.2.6 Summary of published BMRx schemes

Section 4.1 and Table 4-2 show that although many techniques exist for the development of multi Gb/s burst-mode receivers for a variety of optical networking areas there is not currently one solution that meets the requirements of the ideal WR-OBS or even OBS network. As outlined at the start of the chapter, the receiver should be able to recover data and timing information from asynchronous optical bursts displaying large power fluctuations. The receiver should also be able to receive bursts of variable length between idle periods with minimal required preamble to maximize network efficiency and without placing a restriction on the frequency content of transmitted data.

Table 4-2 Summary of published BMRx Studies

Ref	Sig. C'ling	Bit rate (Gb/s)	Req'd guard band/ reset time	Pre-amble	Sens (dBm)	Dyn. range (dB)	Op. range (dB)	Comments
Ota92	DC	1	100ns	--	-37.5	23	23	
Le04	DC	1.25	250ns	50ns	-26.4	21	21	AGC
Oss05	DC	1.25	25.6ns	18ns	-32.8	23.8	23.8	
Rot05	AC	10	30ns	30ns	--	--	--	8B/10B line coded
Kim03	AC	10	--	None	--	--	9.2	Only attempted BLW correction
Nog06	AC	10	--	0.8ns	--	--	28	BLW not addressed
Nis03	AC	10	--	4ns	-24.8	9	9	Manchester code
Su04	AC	10	--	3.2ns	--	25	25	Requires DPSK, uses LOAs to increase DR
Gri03	AC	40	--	40ns	--	--	--	Short PRBS limiting CID, equal pwr bursts

-- Value not appropriate or not obtainable from reference

In entirely DC-coupled BMRx designs, the circuitry for the fast threshold control and the problem of random DC offsets in have so far proved expensive and difficult to scale to higher bit rates [Oss06, Han03 Bri02]. Meanwhile, AC-coupled designs for µs-ms burst length schemes are limited by the trade-off between slow locking times or signal degradation arising from consecutive identical digits (CID). Line coding can be used to limit the BLW problem for fast locking receivers, however, the cost is a further reduction in network efficiency in addition to the loss at the start of the burst for the initial offset. Line coding schemes such as 8B/10B introduce a 20% overhead in the number of transmitted bits necessary and whilst more efficient schemes, such as 64B/66B

used in 10Gb Ethernet links exist, additional line coding also adds additional complexity to the receiver.

A preferable solution to the BLW problem is to correct for it as attempted in [Kim03], where mean value detectors were used to track BLW across transmitted bursts. If instead of tracking the changes caused by BLW, the effect of it was removed by applying the inverse electrical filter then it becomes possible cancel out the effect BLW before the decision-circuit. In order to construct such a filter and apply it on a burst by burst basis it is necessary only to extract the initial burst amplitude from each arriving burst since the time constant of the originating DC-offset is known from the chosen value of the coupling capacitor and resistances. The arrangement of such an analogue BMRx is described in section 4.2.1.

4.2 Designing a 10Gb/s BMRx

The aim of this section is to examine the options for designing and building a BMRx receiver in order to choose the optimum scheme to meet all the requirements of an OBS network.

4.2.1 Analogue BMRx with BLW correction

There are a number of ways to potentially implement an analogue burst-mode receiver depending on the coupling of the photodiode and available components. One implementation considered is based upon a DC-coupled photodiode and AC-coupled variable gain amplifier and is shown in Figure 4-2.

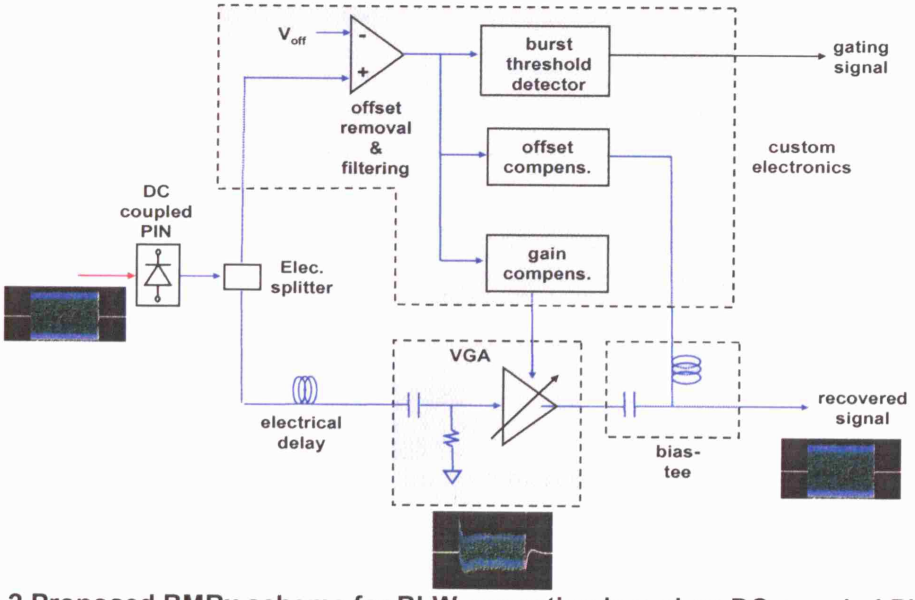

Figure 4-2 Proposed BMRx scheme for BLW correction based on DC-coupled PIN

The DC-coupled PIN enables the signal to be split in the electrical domain before BLW offsets are introduced by the AC-coupled variable gain amplifier (VGA). This allows for the signal path to be electronically buffered whilst the incoming burst is processed by the control path. The control path consists of 3 function blocks and a low pass filter to remove the high frequency data components. The first is simply a threshold detector that is activated upon the arrival of a new burst. The second function block of the control path is to apply the opposite BLW offset to the AC-coupled signal path via the bias tee. Since in this case, the PD is DC-coupled, the offset compensation is for the BLW arising from the VGA which is used to compensate for burst-to-burst power fluctuations and to AC-couple the signal path in order to allow for a constant zero decision-threshold. The final block of the control electronics controls the gain of the VGA to equalize burst power fluctuations.

A second method for an analogue BMRx implementing a BLW correction is shown in Figure 4-3, where, an optical split is used with the signal path based on a conventional AC-coupled continuous mode receiver. The control arm in this case is very similar to that described in Figure 4-2 with the addition of a slow monitor photodiode to recover the power envelope of the incoming burst at the input to the control arm.

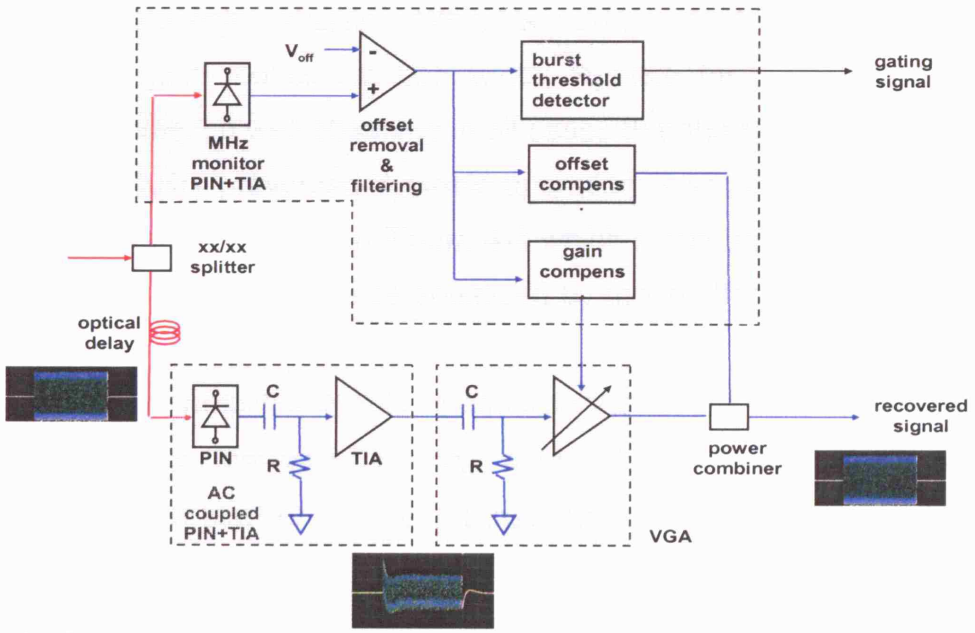

Figure 4-3 Proposed BMRx control architecture based on an optical split and slow PD control path

Once the BLW and burst power corrections have been applied, the schemes shown in Figure 4-2 and Figure 4-3 also require fast clock recovery and a

decision-circuit implemented with one of the techniques discussed in section 4.1. However, although numerical simulations demonstrated theoretical operation of these schemes, practical implementation of the scheme presented a number of difficulties before consideration of the problem of fast clock recovery was addressed.

As with almost all BMRx schemes, obtaining accurate estimations of the received burst amplitude for both BLW and burst power corrections is the primary control problem. Since the mark-to-space ratio of the transmitted data is unknown, a known data sequence or preamble is required at the start of each burst to detect the burst amplitude. The length of this preamble is set by the speed at which the control electronics are able to detect burst arrival and average power. Due to component availability and bandwidth limitation of interconnection, practical laboratory implementation would realistically be based on MHz electronics with a similar bandwidth monitor photodiode for the optically split scheme. Hence, such a scheme would require a preamble of several microseconds. A long preamble was also required since detection of burst amplitude in both cases was subject to the same sources of error from noise corrupted threshold and random offsets as the DC receivers described in section 4.1.2.1. However, a more serious shortcoming was the absence of a suitable variable gain amplifier. Whilst a number of 10Gb/s VGAs with the required MHz gain modulation bandwidth, suitable for equalization of μs-ms bursts, were tested, it was observed in all cases that the response (group delay) of the gain circuitry prevented dynamic operation over the required timescales. An example of this is shown in Figure 4-4 which is the amplitude envelope of 2 bursts with 8dB power difference equalised by modulating the gain of a 10Gb/s VGA. The yellow signal shows the timing of the gain voltage signal and shows that although the amplifier is able to equalise the amplitude of the 2 bursts, the response time of the gain circuitry, approximately 5μs, causes amplitude fluctuations at the start of each burst that may not only increase the BER but prevent correct identification of crucial header information, leading to loss of entire bursts.

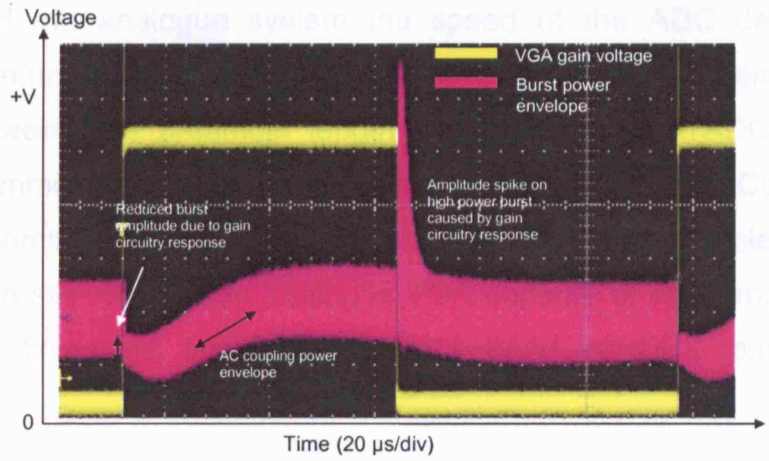

Figure 4-4 Amplitude fluctuations of received bursts equalised with variable gain electrical amplifier due to response of gain circuitry

Furthermore, the expense of an optical split and second PD for the AC-coupled approach and the availability of DC-coupled PDs for bit rates beyond 10 Gb/s make implementation of such analogue receivers impractical with current technology.

4.2.2 Analogue BMRx with digital BLW correction

For both the analogue receiver schemes shown it should also be possible to implement the control path with digital signal processing. This would require digital sampling of the analogue waveform from the 10Gb/s waveform for electrical split in Figure 4-2 or from the monitor PD in Figure 4-3. Once sampled, the data can be used to extract the burst power and calculate the appropriate BLW correction before being converted back to an analogue voltage driver to apply the corrected signal back onto the received burst. A possible arrangement is shown in Figure 4-5 that also shows a threshold detector to signal burst arrival.

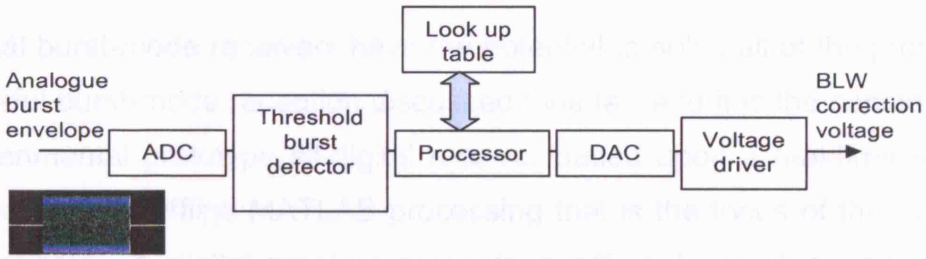

Figure 4-5 Potential digital control path for analogue burst-mode receiver with BLW correction

As with the analogue control the speed of the ADC needs to be fast enough to make an accurate estimate of the average burst power from the burst preamble over a number of bits at the start of each burst. As with the speed of the control

electronics in the analogue system the speed of the ADC determines the number of preamble bits required for an accurate power measurement and so a trade-off between the preamble length and speed of the ADC also exists. Although commercially available FPGAs with integrated ADCs and DACs capable of sampling at hundreds of MHz exist [Alt05] the implementation of such a design still requires an analogue VGA capable of adjustment on a sub-microsecond timescale suitable for guard band of OBS burst switching schemes.

4.2.3 All-digital BMRx

The absence of suitable electrical amplifier for burst power compensation can be overcome if the entire receiver processing is implemented in the digital domain as enabled by the recent improvements in high speed analogue to digital conversion. Applying baseline wander and burst power corrections in the digital domain is possible without such component issues as those described for analogue systems, provided sufficient sampling speed and computing resources are available. Whilst not widely available as commercial products, the technology required to implement burst-mode reception of multi-Gb/s optical signals in the digital domain are beginning to be reported in research forums [Sch06, Far04, Lee04, Pou03] and the tools to investigate these concepts are already available in research laboratories. Real time sampling scopes are able to digitally sample analogue waveforms at up to 40Gb/s in real time by using random access memory to compile multiple acquisitions of real time data [Tek05]. Once stored, digital signal processing concepts, applicable to burst-mode receivers, can be explored with offline processing.

All-digital burst-mode receivers have the potential to solve all of the problems of successful burst-mode reception discussed thus far, and it is the construction of an experimental prototype all-digital receiver based upon a real-time sampling oscilloscope with offline MATLAB processing that is the focus of the remainder of the chapter. A digital receiver presents a different set of issues, many of which have previously been addressed at lower bit rates, which need to be solved before a successful implementation is possible. These issues are discussed below with the experimental set-up and digital receiver characterisation described in sections 4.3 and 4.4.

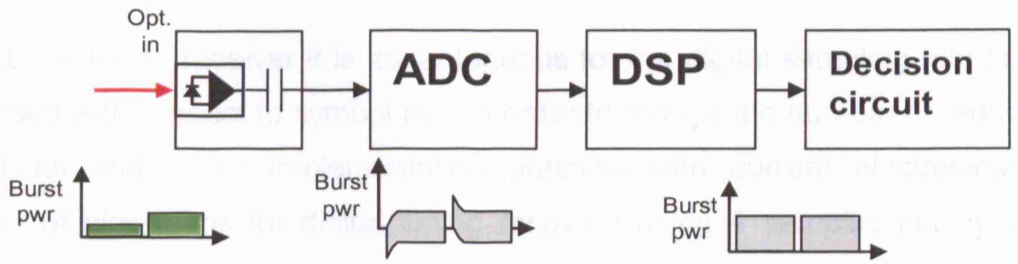

Figure 4-6 Block diagram of proposed digital BMRX

The block level diagram of the proposed digital BMRX (DBMRx) is shown in Figure 4-6. The first key stage is that of converting the analogue received optical signal to digital form. As is well known, to maintain the entire waveform and completely eliminate aliasing the sample rate must be at least twice the symbol rate. However, the avoidance of aliasing does not guarantee optimum representation of the analogue waveform as shown in Figure 4-7. This shows that sampling at twice the bit rate can still lead to eye closure during quantisation if not optimally synchronised with signal.

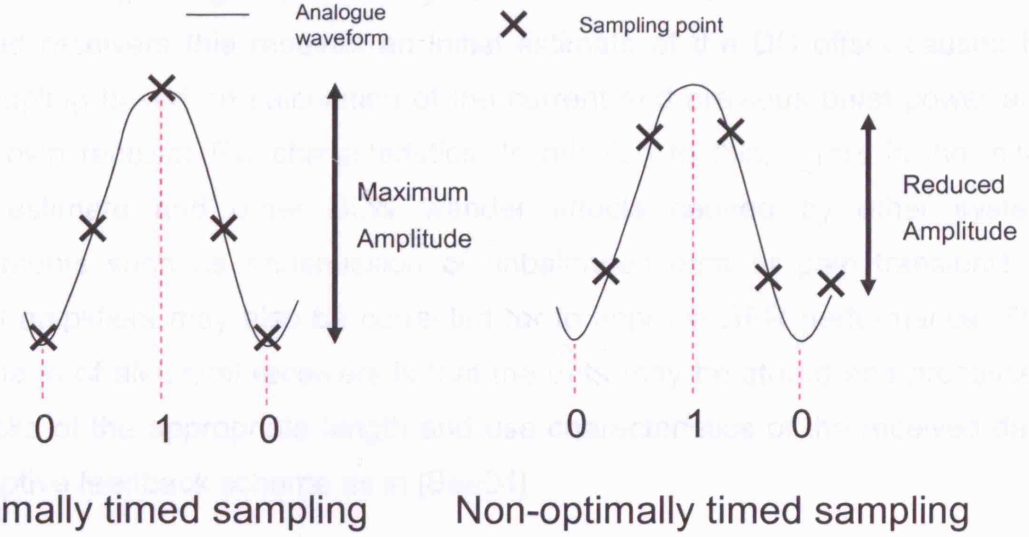

Figure 4-7 Digital eye closure due to non optimal sampling

In general for digital systems where analogue input signals are converted to digital form by a sampler followed by a digital processor, timing adjustment is performed by feedback from the digital processor, or via a feed forward technique from an analogue processor, before the sampler. In cases where it is not possible adjust the sampling clock, or where data is arriving asynchronously (as in a BMRx) then it may be possible to recover an optimal digital waveform from the non optimal samples by interpolation in the digital processor [Gar93], where interpolation in this case refers to correcting both the timing and amplitude of digital samples to optimally represent the analogue waveform.

For a burst-mode receiver it is advantageous for the digital sampling rate to be minimised with respect to symbol rate in order to reduce the number of required operations and make implementation practical with current electronics. A number of algorithms for digital timing recovery using 4 samples per symbol have been reported [Oer88, Pan96] but subsequent work on digital modems and other digital communication systems generated algorithms using only 2 samples per symbol [Zhu01, Ver94, Men97]. Of these, the feed-forward approach has been mostly adopted for burst-mode transmission applications for its faster acquisition time since no feedback loop is required [Zhu03] and the most computationally efficient technique for symbol timing recovery is described in [Lee02].

In addition to interpolating the sampled waveform to recover the maximum eye-opening the digital signal processing must also make BLW corrections. For AC-coupled receivers this requires an initial estimate of the DC offset caused by AC-coupling based on calculation of the current and previous burst power and the known receiver RC characteristics. In addition to this, errors in the initial BLW estimate and other BLW wander effects caused by other system impairments such as transmission of unbalanced data or gain transients in optical amplifiers may also be corrected for to improve BER performance. The advantage of all-digital receivers is that the data may be stored and processed in blocks of the appropriate length and use characteristics of the received data in adaptive feedback scheme as in [Bae04].

These 2 processing functions form the basis of the signal processing implemented for the prototype digital burst-mode receiver (DBMRx). All processing was performed offline in MATLAB with code written by Dr Benn Thomsen and described in [Tho06]. Figure 4-8 shows the schematic of the digital signal processing used in the experimental receiver measurements described in chapter 4.3.

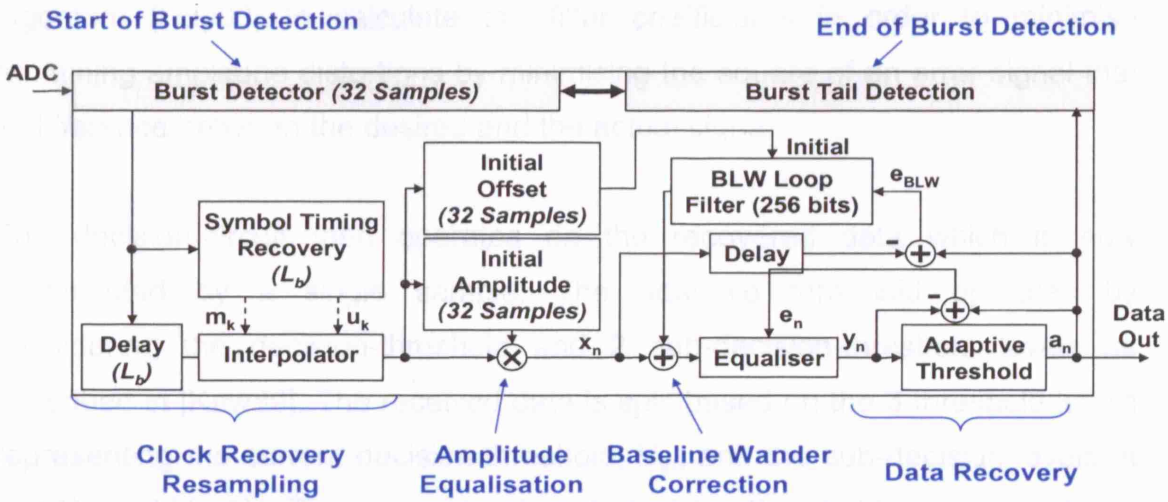

Figure 4-8 Schematic of digital signal processing for DBMRx

Prior to the arrival of a burst, the burst detector, a 32-sample FIR digital correlator is set to identify the burst preamble above background noise. The correlator multiplies the known preamble sequence with the incoming data providing an output maximum when the burst preamble is identified. Once the incoming burst is detected, the rest of the system is enabled for the 2-stage recovery process. The first stage is the feed-forward timing recovery, implemented with the algorithm of [Lee02] which processes the incoming data in blocks of length L_b, set to 512 samples as a trade-off between operating frequency range and noise susceptibility. The signal is delayed at the input to the interpolator for the duration of the block whilst the required timing interval, given in terms of a base-point sample (m_k) and fractional interval (u_k) as described in [Gar93], is calculated. A simple linear interpolator, implemented as a two tap FIR filter with variable coefficients, is used to produce 2 samples per symbol.

The initial BLW correction and amplitude rescaling is calculated using the last 32 samples of a known preamble sequence. Once initialised the adaptive BLW compensator uses the error signal (e_{BLW}) between the recovered data A_n and the uncompensated signal (X_n). The BLW loop filter was set to average over 256 bits as a trade-off between a suitably fast response time and susceptibility to power fluctuations caused by random noise. Next, a 3-bit fractionally spaced feed-forward adaptive equaliser is used to compensate any remaining amplitude variations and convert the digitised, interpolated waveform to a single sample per symbol. The adaptive equaliser uses a least mean squares

algorithm [Hay00] to calculate the filter coefficients in order to minimise remaining amplitude distortions by minimising the square of an error signal that is difference between the desired and the actual signal.

The decision-circuit then operates on the recovered data which is now represented by a single sample. The adaptive threshold operates by considering the decision-threshold and 2 sub-decision-threshold levels as described in [Kaw89]. The received data is split based on the 3 threshold levels representing the current decision-threshold, V_{th}, and the sub-decision levels at $V_{th}+\Delta V$ and $V_{th}-\Delta V$. The error rate at each decision-threshold is compared and the levels adjusted to ensure that the error rates at each sub-decision are equal and ensuring the threshold of the decision-circuit is set to the centre of the eye opening.

Finally, the end of a burst is signified by either a digital correlator detecting a known burst tail sequence for variable length bursts or by timeout for fixed length bursts.

The preamble in this implementation serves 2 purposes. The first is to allow burst detection by filtering at the clock frequency associated with the known sequence and the second to determine the burst amplitude to set an appropriate initial threshold. However, the possibility also exists to perform these 2 functions without the use of a preamble. Recently, Zhao et al proposed a clustering based algorithm for burst-mode optical receivers [Zha06] that was able to eliminate noise corruption errors in the preamble by making burst amplitude measurements over the entire burst based on a 2 step clustering process with an initial estimate used for the 1st partition. However, the initial partition is based on the average of the received data and leads to significant errors for unbalanced data, placing a restriction on the data content. This limitation of the data content contradicts the initial BMRx objectives outlined in section 4.2 and so made alternative preamble less schemes impossible. Furthermore, a preamble free system still requires a burst detections scheme and how this is achieved in unclear.

4.3 Experimental set-up for digital BMRx characterisation

4.3.1 Burst transmitter

In order carry out experimental validation and characterisation of the proposed digital receiver it was first necessary to construct a transmitter capable of replicating the condition a BMRx would face in an OBS network environment. The burst transmitter for the experimental investigation was based on the design in chapter 3 but using 2 independently driven SG-DBR tunable lasers, and modulated by external Mach Zender modulators. Two transmitters were required to provide adjacent bursts with asynchronous phase, but also enabled greater flexibility of burst timing within the constraints of driver-limited switching times, described in previous chapters. The layout of the transmitter is shown in Figure 4-9.

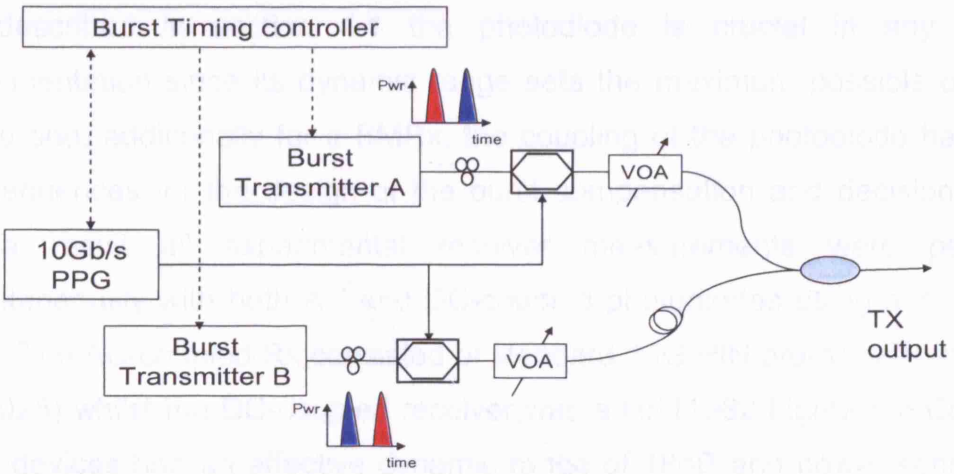

Figure 4-9 Burst transmitter comprising 2 SG-DBR tunable lasers

A repeating data pattern of 2 bursts separated by 100ns guard band with 32 bit preamble and tail was programmed into an Anritsu AZ7792 10Gb/s pulse pattern generator (PPG). As a trade-off between improving the error statistics of BER measurements and reducing the offline MATLAB processing time, a fixed burst length of 52 μs was chosen for each burst of the repeating 2 burst pattern. A data generator (DG) Sony DG2030, was used as the burst timing controller and synchronized with the PPG to control both the laser switching and data pattern. Since, an ASE removing filter was used in the receiver configuration a single wavelength was used for time interleaved burst generation from each transmitter. Whilst not transmitting on the received wavelength the laser was switched to a second out-of-band wavelength with a minimal (5mA) tuning current switch in order to minimize thermal transients and remove the requirement for wavelength locking.

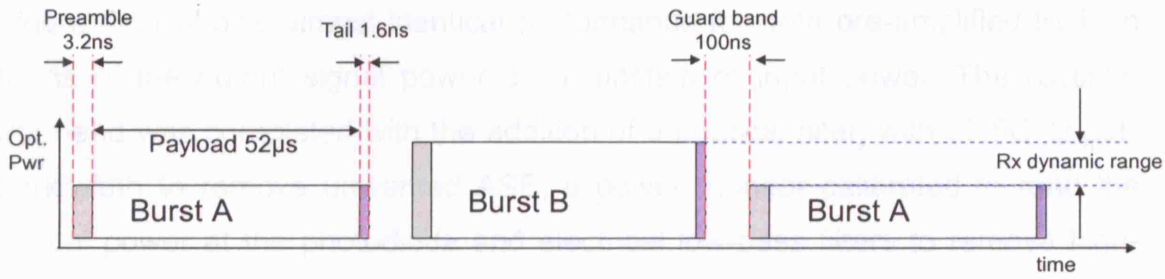

Figure 4-10 Burst structure showing preamble, payload, tail and guard band

4.3.2 Receiver characterisation set-up

As described in section 4.2.3, the digital receiver design was based around the fast ADC of a Tektronix TDS6154C real time oscilloscope capable of capturing digital waveforms from 4 input channels simultaneously. The sampling rate for all measurements was 20GS/s with an effective resolution of 5 bits.

As described in section 4.1 the photodiode is crucial in any receiver implementation since its dynamic range sets the maximum possible operating range and, additionally for a BMRx, the coupling of the photodiode has strong consequences for the design of the burst compensation and decision-circuits. As a result all experimental receiver measurements were performed simultaneously with both AC and DC-coupled photodiodes using a 3dB-optical split. The AC-coupled Rx consisted of standard 10G PIN pre-amp (Hamamatsu GS2025) whilst the DC-coupled receiver was a HP11982 Lightwave Converter. Both devices had an effective dynamic range of 18dB and power sensitivity of -18dBm at a BER of 10^{-9}. The peak-to-peak amplitude of the output signal as a function of input power for both photodiodes is show in Figure 4-11.

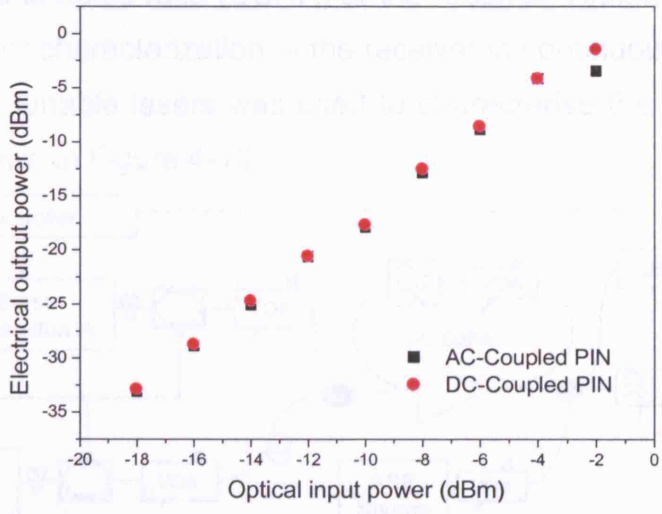

Figure 4-11 Measured output power for pre-ADC receiver configurations as function of optical input power

Figure 4-11 shows almost identical performance for both pre-amplified PINs in terms of the output signal power as a function of input power. The receiver front-end was completed with the addition of an optical filter, with 37.5GHz 3dB bandwidth to remove unwanted ASE, a power monitor calibrated to read the optical power at the photodiode and electrical low-pass filters to remove high-frequency noise before the ADC. The trigger signal was required to synchronise measurements due to the limited storage capacity of the oscilloscope but was not used for burst detection in the digital signal processing. The experimental set-up used for all BMRx characterization measurements is shown in Figure 4-12.

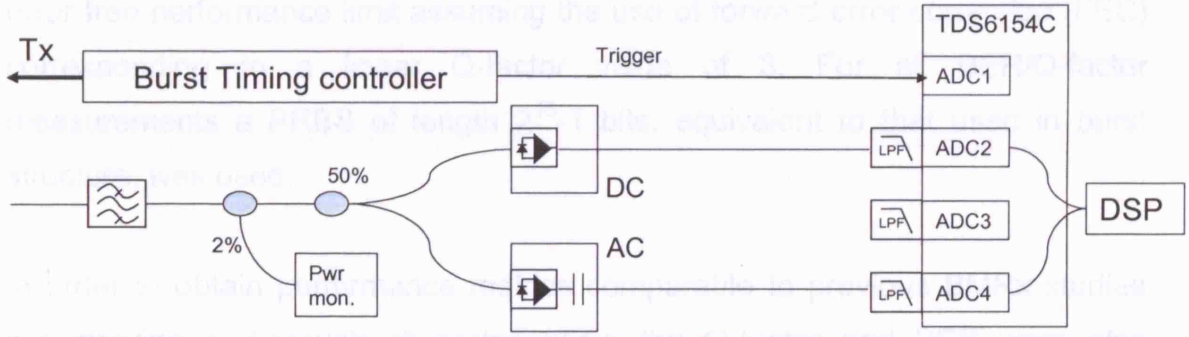

Figure 4-12 Experimental implementation of digital BMRx receiver characterisation set-up

All receiver characterisations described in the subsequent sections were carried out by combining the burst transmitter (Figure 4-9) performed with the receiver set-up, shown in Figure 4-12, in a back to back configuration. A gain-clamped EDFA (see chapter 5) was required to boost the transmitter power to cover the system losses and provide optical power across the entire receiver operating range. An additional ASE source and power monitor was also added to control the optical signal to noise ratio (OSNR) at the receiver. Although only 1 tunable laser was used for characterization of the receiver in continuous mode the same set-up with both tunable lasers was used to characterise the receiver in burst-mode and is shown in Figure 4-13.

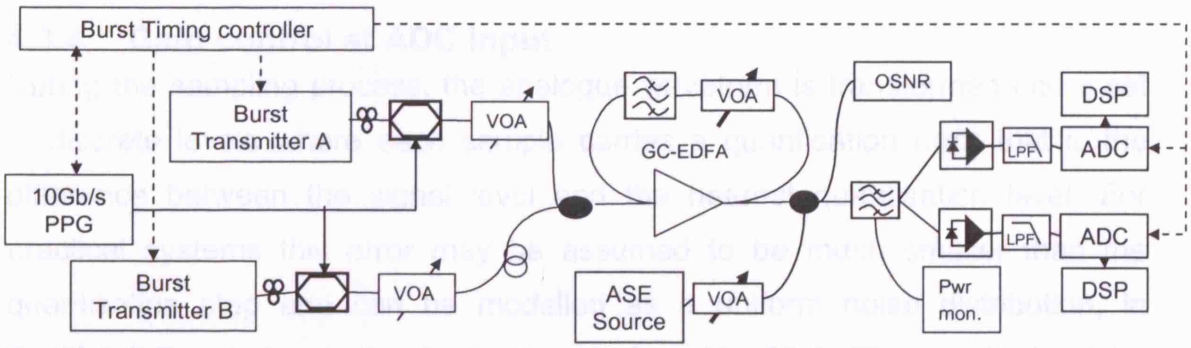

Figure 4-13 Experimental set-up for receiver characterization measurements

4.3.3 Q-factor/BER measurements

In order to characterize receiver performance, Q-factor/BER measurements were performed by error counting for different receiver input powers and OSNRs. Since the lengths of the optical bursts used when operating in burst-mode were limited by reasonable processing time and storage capacity, it was necessary to increase the BER to measurable levels by OSNR degradation. At low OSNR the BER is derived directly from the number of bit errors between the transmitted and received bit streams. In particular, in order to compare performance based primarily on error counting the key figure of merit for receiver performance comparison is the required OSNR for a BER of $1*10^{-3}$, the error free performance limit assuming the use of forward error correction (FEC) corresponding to a linear Q-factor value of 3. For all BER/Q-factor measurements a PRBS of length 2^{15}-1 bits, equivalent to that used in burst structure, was used.

In order to obtain performance metrics comparable to previous BMRx studies and provide a thorough characterisation, the Q-factor and BER were also estimated for OSNRs up to 30dB. Where few or no errors were counted in the received burst, this was done by considering the distribution of noise around the one and zero levels using the method described in [Ber93]. However, the accuracy of BER measurement required for this technique is dependent on the length of the data sequence used [Jer84]. Since, the number of bits over which measurements were made were limited by the size of the saved waveform an initial characterisation of the receiver performance showed that the expected trend was observed up to linear Q-factor values of 11, corresponding to BER=$1*10^{-31}$. Hence only measurements up to this value, equivalent to a Q-factor of 20.8 on a log scale are shown in subsequent results.

4.3.4 Gain control at ADC input

During the sampling process, the analogue waveform is transformed into a set of discrete levels where each sample carries a quantisation error that is the difference between the signal level and the nearest quantisation level. For practical systems this error may be assumed to be much smaller than the quantisation step and can be modelled as a uniform noise distribution, in addition to any noise on the analogue waveform [Agr02c]. The amplitude of the

noise source is proportional to the number of quantisation levels used to represent the analogue waveform [She05] and can be critical in digital systems where the ADC input voltage may vary as in the case of an optical receiver operating at a range of optical powers.

Hence, the requirement of automatic gain control (AGC) in the receiver was also studied. In this context, gain control (GC) describes the adjustment of the analogue voltage output of the TIA before the analogue to digital conversion. AGC is an important step for a digital receiver designed to adjust to large fluctuations of input signal voltage since the effective resolution of ADC is fixed. In this case the effective 5 bit resolution of the oscilloscope limited all measurements to 32 discrete levels across the input voltage range of the ADC. In order to maintain maximum detail in the digitized waveform a DC-coupled amplifier at the input to the AGC was used to match the input analogue signal to the input voltage range of the AGC. Whilst for receiver characterization this was performed manually at course settings for known power ranges during the characterisation, this would need to be carried out dynamically on burst by burst basis in a network environment.

Under continuous operation the receiver was characterized over the input power range of the photodiodes with the highest power limited to -2dBm by the maximum transmitter power. An initial measurement representing a scenario when AGC is used was made by optimising the gain of the ADC pre-amplifier to match each input signal power to the dynamic range of the ADC. The receiver was then also characterized with two fixed gains before the ADC. In separate measurements the ADC pre-amplifier gain was fixed to be appropriate for input signal powers of -2dBm and -6dBm as the input power was varied down to -18dBm to investigate if the receiver performance without GC varies over different input power ranges. Techniques to implement AGC are addressed in section 4.6.

4.4 Receiver characterisations results

4.4.1 Characterisation of receiver in continuous mode

Before operating the receiver in burst-mode its performance was first characterised under continuous operation to provide a performance benchmark.

Figure 4-14 shows the measured Q-factor values for the receiver calculation for an input optical power of -2dBm, the maximum receiver input power used for all characterisation measurements.

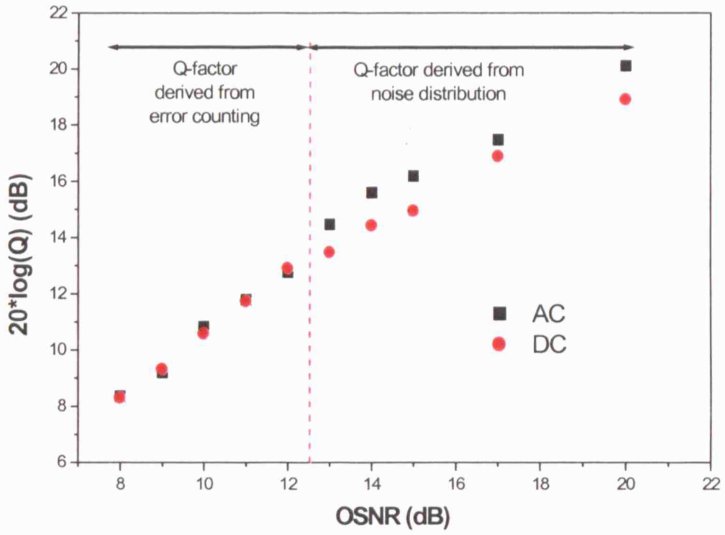

Figure 4-14 OSNR receiver characterization for -2dBm input power

The first 5 data points at the lowest OSNR, those derived from error counting of the received signal show very little variation of measured Q-factor between the 2 receiver configurations varying linearly with OSNR. The small variation in Q-factor derived from the noise distribution at higher OSNRs is believed to be due to the marginally superior noise performance of the AC-coupled photodiode.

Figure 4-15 shows the same characterisation for a receiver input power of -18dBm. Here the range of the ADC was initially adjusted to allow for the reception of bursts with the average powers of -2dBm and -6dBm as shown in Figure 4-15 respectively. The receiver was also characterised with and without manual gain control. For the characterization without GC, neither receiver configuration was able to retrieve the data pattern well enough to measure Q-factor above 9.5dB equivalent to a BER of 10^{-3}. With gain control applied (identical data shown on both plots) each receiver configuration performs equally well and achieves a BER below 10^{-3} between 11dB and 12dB OSNR.

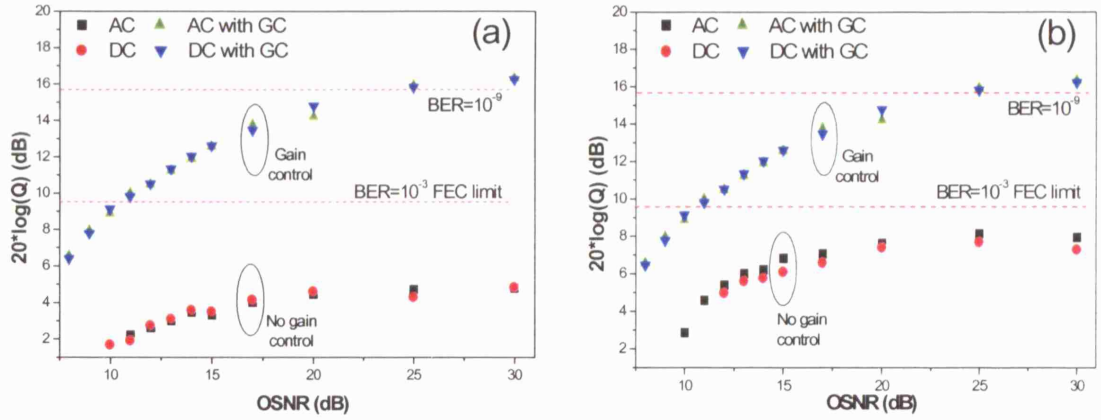

Figure 4-15 OSNR receiver characterization for -18dBm input power with (a) fixed gain control setting from -2dBm and (b) fixed gain control from -6dBm

Figure 4-14 and Figure 4-15 show the detail of receiver characterisations performed at -2dBm and -6dBm for all receiver configurations over a range of OSNRs from 8 to 30dB. The receiver characterisation results for all input power ranges are shown in Figure 4-16 to Figure 4-18.

Figure 4-16 shows the maximum measured Q-factor without noise loading, for each input optical power where the pre-ADC amplifier was optimised for both -2dBm and -6dBm optical input power. This measurement is presented to provide a comparison with the standard receiver sensitivity metric. However, as the Q-factor measurement is based on interpolation from a relatively small data set determined by the burst length, the accuracy of this measurement is limited. Therefore, in addition to this, we use the more reliable metric of the required OSNR at a BER of 10^{-3} based on direct error counting and these plots are included in Figure 4-17 and Figure 4-18.

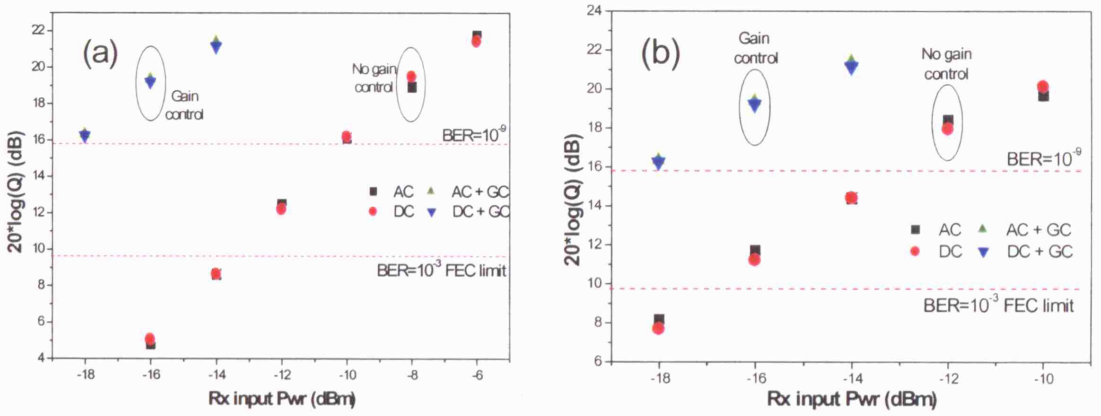

Figure 4-16 Q-factor at maximum OSNR vs receiver input power for CW receiver with automatic gain control and (a) non GC receiver with -2dBm max input power and (b) non-GC receiver with -6dBm max input power

Figure 4-16 shows that without gain control the optimisation of the pre ADC amplifier is crucial in setting the quantisation noise limited operating range of the receiver. With the amplifier optimised at the highest input optical power the receiver achieves a BER<10^{-3} at approximately -13dBm optical input power and a BER<10^{-9} at approximately -10dBm. With the receiver optimised for an optical input power of -6dBm the receiver input power for which the FEC performance metric is met is also reduced by 4dB giving the same quantisation noise-limited dynamic range. Figure 4-16 also shows the significant performance improvement obtained by optimisation of the pre-ADC amplifier. With gain control employed, the receiver becomes limited by photodiode sensitivity with a BER>10^{-9} measurable down to -18dBm in agreement with the published sensitivity values of both photodiodes.

As described in 4.3.3, the error statistics set by the burst lengths of interest require noise loading at the receiver in order to reduce the BER to levels measurable with error counting across the entire receiver operating range. To ensure reliable error statistics for continuous and subsequent burst measurements a BER of 10^{-3} was chosen as the performance metric for a receiver characterisation in terms of required OSNR. Figure 4-17 and Figure 4-18 show the required OSNR to achieve a linear Q-factor of 3, equivalent to the minimum BER of $1*10^{-3}$ required for FEC, with and without the ADC amplifier optimised for the input optical powers (denoted with or without gain control (GC) as before. The values of required OSNR for BER of $1*10^{-3}$ shown are calculated from a linear interpolation of neighbouring points derived from error counting and the dynamic range is defined as the input power range over which the OSNR penalty for BER of 10^{-3} is under 1dB.

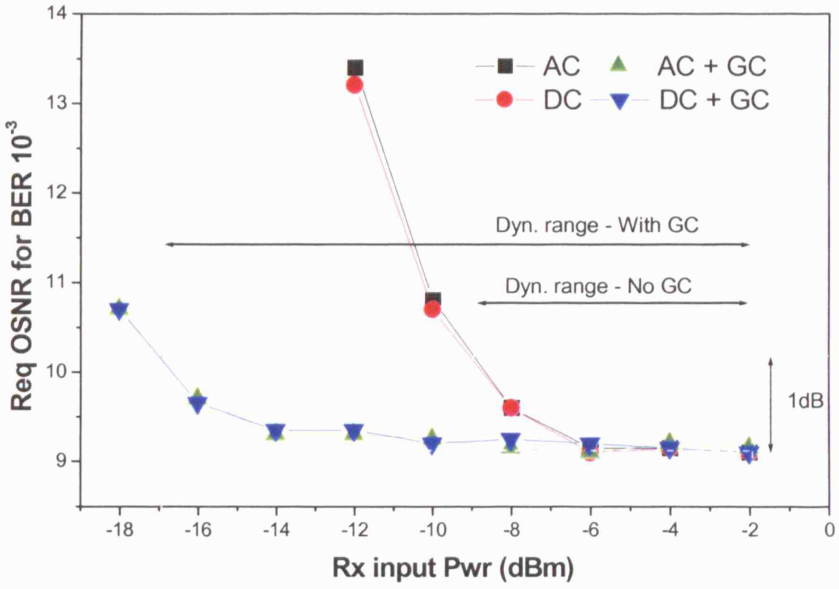

Figure 4-17 Required OSNR for BER=10^{-3} for all receiver configurations with GC and without gain control from -2dBm

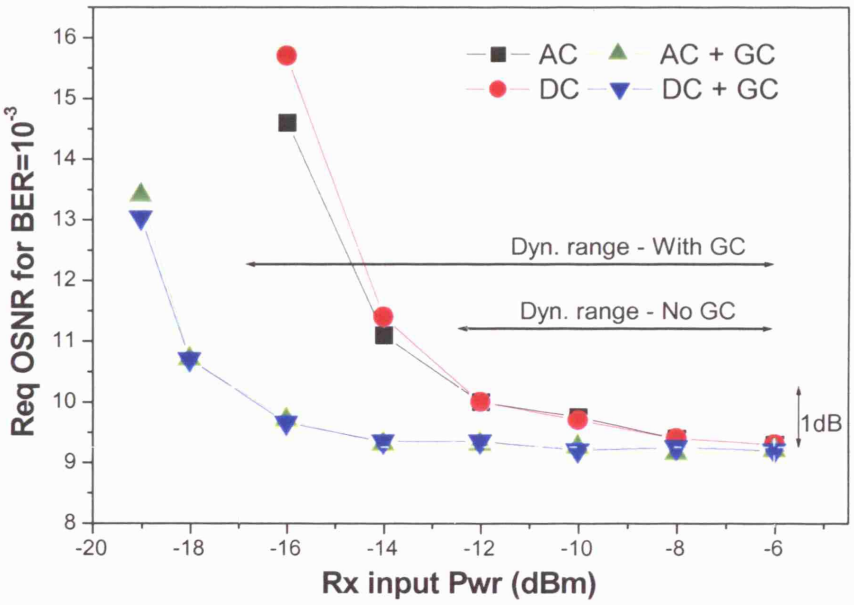

Figure 4-18 Required OSNR for BER=10^{-3} for all receiver configurations with and without gain control from -6dBm

Figure 4-17 and Figure 4-18 show similar trends to those described in Figure 4-16 but the improved error statistics provided by error counting allow for more accurate measurement of dynamic range across the whole receiver operating range. For the AC and DC-coupled receivers without GC almost identical performance is observed at low OSNRs with the dynamic range of 6-7dB limited by quantization noise arising from the ADC. With GC employed the full dynamic

range of 15dB is apparent in the characterisation from -2dBm but reduced to 11dB for the characterisation from -6dBm since the lower bound dynamic range of GC receivers is limited by photodiode sensitivity and fixed for both characterizations. With GC, less than a 1dB OSNR penalty was observed for values as low as -17dBm.

In the large body of published work on burst-mode receivers, a number of different figures of merit have been used for comparison of BMRx performance. Table 4-3 is a summary of the continuous mode characterisations described thus far to provide easier comparison with the receiver in burst-mode and with alternative BMRx schemes in later discussion. The dynamic range is defined both as the input power range for which a 1dB OSNR penalty for BER=10^{-3} is maintained and also, as defined for non-FEC systems, as the input power range for which a BER of $<1x10^{-9}$ is obtained. The sensitivity quoted in the lower bound of the dynamic range measurement in each case.

Table 4-3 Summary of receiver characterisation in continuous mode

	Non GC characterisation from -2dBm		**Non GC characterisation from -6dBm**	
Receiver configuration	**Dyn range-1dB OSNR penalty (Sensitivity)**	**Dyn. Range – BER 10^{-9} (Sensitivity)**	**Dyn range-1dB OSNR penalty (Sensitivity)**	**Dyn. Range – BER 10^{-9} (Sensitivity)**
AC	7dB (-8dBm)	8.5dB(-10.5dBm)	6.5dB (-12dBm)	8.5dB (-13.5dBm)
DC	7dB (-8dBm)	8.5dB(-10.5dBm)	6.5dB (-12dBm)	8.5dB (-13.5dBm)
AC+GC	15dB (-17dBm)	17dB(-19dBm)	11dB* (-17dBm)	13dB*(-19dBm)
DC+GC	15dB (-17dBm)	17dB(-19dBm)	11dB* (-17dBm)	13dB*(-19dBm)

*** Assuming upper bound of dynamic range to be -6dBm**

Table 4-3 shows that the quantisation error limited dynamic range of receivers without gain control is similar for both of the input power ranges studied with the only difference being a 1dB increase in dynamic range for a 1dB OSNR penalty for the characterisation performed from -2dBm. Table 4-3 also shows that the addition of gain control is able to completely remove the quantisation noise limitation to receiver dynamic range. Where the input signal voltage at the ADC input is fixed the dynamic range of both AC and DC-coupled receipt was limited to 6-7dB as the signal voltage at the input to the ADC diminishes with input power. As shown in Figure 4-17 and Figure 4-18, with the ADC input voltage optimised for each optical input power the receiver dynamic range becomes limited by the photodiode sensitivity.

4.4.2 Characterisation of receiver in burst-mode

Characterisation of the receiver under burst-mode operation was performed for input ranges from -6dBm to -18dBm using the experimental set-up shown in Figure 4-13 and the burst transmitter shown in Figure 4-9. The maximum optical input power was limited to -6dBm by limitations in the maximum output power supplied by the burst-mode transmitter. However, it was shown in the previous CW characterisation that the quantisation noise-limited dynamic range was similar for both measurements irrespective of whether the maximum power was -2dBm or -6dBm. For burst characterisation the output power of each transmitter was controlled independently to adjust the optical power of bursts from each transmitter to explore the effect of power differences between adjacent bursts on receiver performance.

4.4.2.1 Receiver performance with equal power bursts

For the initial characterisation, bursts of equal power were generated as the receiver input power and OSNR were scanned as carried out previously in continuous mode characterisation. The purpose of using equal power bursts is to reduce the distortion of the received waveform caused by AC-coupling to help isolate the cause of any receiver penalty. For adjacent bursts of equal power a small BLW error is observed for the AC-coupled photodiode due to the drop in average power caused by the guard band between bursts. However, since the guard band is shorter than the time constant of the AC-coupled PD used the effect is minimal and easily compensated for by the adaptive equaliser during digital processing.

Characterising the receiver performance with equal power bursts can provide a number of useful measurements to assess the receiver performance in burst-mode. The removal of large BLW swings caused by adjacent bursts with large optical power differences allows for measurement of any penalty due to burst-mode operation. As described in [Eld93], this can occur from the setting of the decision-threshold from a noise corrupted preamble in a standard BMRx but it is unclear whether the BLW correction and adaptive equaliser used here may eliminate this penalty. More importantly, the use of equal power bursts allows the removal additional quantisation error on the lower power burst and allows for analysis of the improvement gain control may have on a digital burst-mode

receiver by allowing optimal setting of the pre ADC amplifier. For comparison, the performance of equal power bursts are shown together with unequal power bursts in the next section.

4.4.2.2 Receiver performance with unequal power bursts

In addition to constant power bursts it is also essential to characterise the receiver performance for the more demanding case of variable power bursts where the power difference is between adjacent bursts as defined by dynamic range. For this, the power of each laser in the burst transmitter was independently controlled to produce a repeating pattern of 2 different amplitude bursts, as shown in the burst structure diagram in Figure 4-10. For all measurements the power of burst transmitter B was set to be -6dBm at the input to the receiver whilst the power of transmitter A was varied at the receiver input from -6dBm to -19dBm. Since, from the previous measurements, there was little perceived difference in the performance of AC and DC-coupled receivers, only results for the AC-coupled receiver are shown in the following section, although a summary of both receivers is given in section 4.4.3.

Figure 4-19(a) shows the Q-factor without noise loading for each receiver input power for both equal and varying power bursts. For the unequal power burst the value on the axis corresponds to the lower power burst following a burst of -6dBm input power. In contrast to the similar measurement under continuous operation it was not possible to make Q-factor measurements at low optical input power where the digital signal processing is not able to detect the presence of a burst or correctly identify the preamble sequence due to noise. Figure 4-19(b) shows the required OSNR for a BER of 10^{-3}. The required OSNR measured is that of the weak burst, with the OSNR of the higher power burst increased by the burst power difference. As in the continuous case, Figure 4-19 shows the minimum input power for which the estimated Q-factor values are below the 10^{-9} BER level and Figure 4-19(b) shows the dynamic range of each receiver configuration based on a 1dB OSNR penalty with the measured values based directly on error counting.

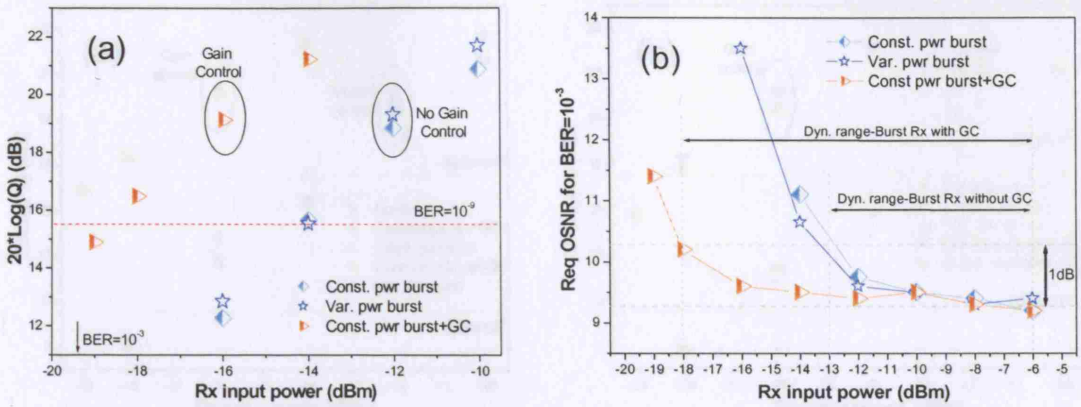

Figure 4-19 (a) Q-factor vs received input power and (b) required OSNR for BER=10^{-3} for variable burst power following burst of -6dBm

The strong correlation between the constant power bursts (diamonds) compared to burst with varying adjacent power (stars) in Figure 4-19 shows that no penalty is observed for reception of adjacent bursts with different powers compared to constant power bursts. This result is important for full receiver characterisation since it allows a comparison of constant burst power results with gain control with those of the receiver under continuous mode. Additionally, as also observed under continuous operation, there is a significant improvement gained by the use of gain control before the ADC. This improvement is approximately 6dB in Q-factor without noise loading or an additional 5dB dynamic range for a 1dB penalty in required OSNR similar to that observed under continuous operation.

4.4.3 Summary of receiver characterisation results

Sections 4.4.1 and 4.4.2 describe a number of detailed characterisations of receiver performance over a wide range of input powers and OSNRs for both continuous and burst input signals. In order to summarise these results Figure 4-20 and Figure 4-21 show a comparison of continuous and burst-mode data with both varying and constant power adjacent bursts and for both AC and DC coupled receivers. As in previous characterisations, both measured Q-factor without noise loading (Figure 4-20) and the required OSNR for a BER of 10^{-3} (Figure 4-21) were used to assess receiver performance.

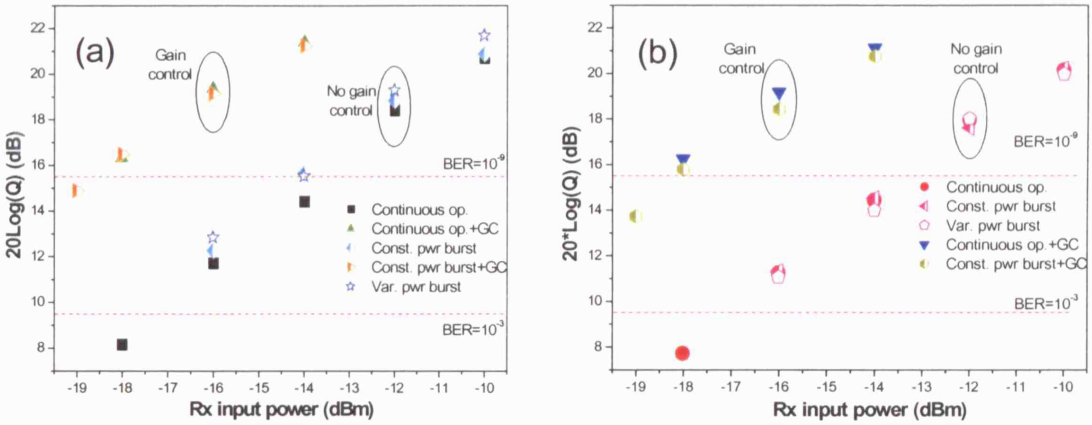

Figure 4-20 Measured Q-factor without noise loading for (a) AC coupled Rx and (b) DC coupled receiver

The Q-factor vs Rx input power plots displayed in Figure 4-20 show very similar performance for both the AC and DC-coupled receivers with the results grouped according to whether pre-ADC gain control is employed. With gain control there is little difference between the maximum measured Q-factor values for any of the receiver configurations and, hence, no penalty for burst-mode compared to continuous operation.

The situation is less clear for the receiver configurations without gain control which shows some variation between the measured Q-factor values particular for the AC-coupled PD where the measured Q-factor for the burst-mode exceeds that for continuous operation over the whole power range by up to 0.5dB. However, since these values are estimates from short data sequences and correspond to very low BERs ($<1*10^{-12}$) such a spread is within the accuracy limits of the measurement. Crucially, there is no perceivable penalty for burst-mode compared to continuous operation for either receiver coupling and similarly no perceivable penalty for variable power bursts compared to constant power bursts. A similar picture is shown in Figure 4-21 which shows the required OSNR plot for all receiver configurations.

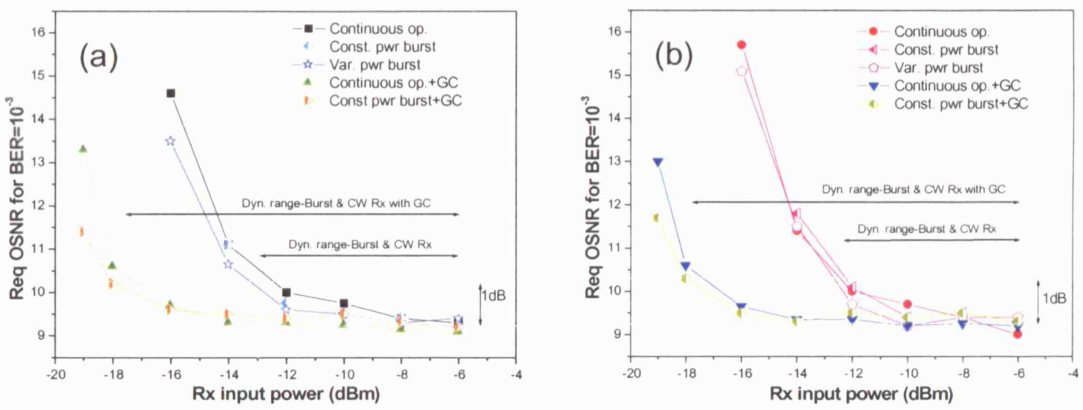

Figure 4-21 Required OSNR for BER=10-3 for (a) AC-coupled and (b) DC-coupled receivers

The OSNR characterisation of both receivers also shows that there is no significant or appreciable penalty for burst-mode operation compared to continuous operation, or for variable power burst compared to constant power bursts. However, as with the Q-factor measurements there is a detectable improvement in performance for the AC-coupled receiver for variable power adjacent bursts compared to both constant power bursts and continuous operation. For the required OSNR, the improvement translates to an improvement in dynamic range of around 0.5dB and is also discussed below.

Table 4-4 shows a summary of all receiver characterisations from -6dBm in terms of dynamic range and minimum required Rx input power for both a 1dB OSNR penalty and a BER below $1*10^{-9}$. The data for burst-mode operation is based on measurements of variable power bursts with adjacent burst power of -6dBm.

Table 4-4 Comparison of receiver performance for continuous and burst operation

	Dynamic range (min req'd Rx input power)-for 1dB OSNR penalty		**Dynamic range (min req'd Rx input power) -for BER<$1*10^{-9}$**	
Rx config.	Continuous	Burst	Continuous	Burst
AC	6.5dB (-12dBm)	7dB (-12dBm)	8.5dB (13.5dBm)	9dB (-14dBm)
DC	6.5dB (-12dBm)	6.5dB (-12dBm)	8.5dB (13.5dBm)	8.5dB (-13.5dBm)
AC+GC	11dB (-17dBm)	12dB (-18dBm)	12dB (-18dBm)	13dB(19dBm)
DC+GC	11dB (-17dBm)	12dB (-18dBm)	12dB (-18dBm)	13dB(19dBm)

Table 4-4 shows that despite some discrepancies in performance of the receiver in burst-mode operation compared to continuous, the fundamental figures of merit for the receiver are almost unchanged for operation in burst or continuous mode. These results show that digital signal processing is capable of

completely recovering the BLW error for standard AC-coupled photo-detectors (in addition to DC-coupled) with the only overhead being the 32bit preamble used in all measurements. The length of the preamble and techniques for reducing it are discussed in section 4.7.

The detailed characterisation results for the receiver in continuous and burst operation, described in sections 4.4.1 and 4.4.2 respectively, show a number of trends. Most striking is the increase in receiver performance in terms of achievable range of input signal power fluctuations, by up to 5.5dB, for both burst and continuous signals obtained by adjusting the signal amplitude at the input to the ADC. The results of both burst and continuous operation show that gain control could eliminate the quantisation errors that otherwise limit the dynamic range of all receiver configurations. Techniques for implementing analogue gain control are discussed in section 4.6.

The results of all receiver characterisations show that the AC-coupled receiver gave marginally better performance in terms of both the required OSNR to reach the BER=10^{-3} limit and measured higher Q-factor values for the same input powers with both continuous and burst signals. For continuous-mode these results equate to basic receiver characterisation and can be attributed to superior noise performance of the AC-coupled PD and TIA compared to the DC coupled PD.

The small improvement observed for burst-mode operation may be in part due to the accuracy of receiver power and noise measurements which each carried a potential error of up 0.25 dB and were performed as separate measurements with modification to the experimental set up in each case. However, the increased difference in the required OSNR between the AC and DC-coupled burst-mode receivers without gain control implies that the digital signal processing employed leads to better measured performance for the AC-coupled case although it is not currently clear how.

4.5 Impact of sampling frequency

The tolerance of the DBMRx to variations in the asynchronous sampling rate around 20GS/s was also investigated. For the receiver the tolerance to variation

in data signal rate is inversely proportional to the block length used in symbol timing recovery since this ultimately determines how quickly the receiver is able to adapt to input data frequency changes. However, as with analogue clock recovery, a decreasing the response time increases the susceptibility of the timing recovery to degradation caused by random noise. The block length for the timing recovery was chosen to be 512 samples (equivalent to a refresh rate of 39MHz) to ensure that an acceptable BER performance of $1*10^{-3}$ was obtained for OSNR levels as low as 10dB. Figure 4-22 shows the Q-factor penalty for bursts with an OSNR fixed at 17dB as the sampling frequency was detuned from 20GS/s by +-20MHz. The Q-factor penalty was found to be less than 1dB over a sampling detuning of 28MHz. There was an additional penalty of 0.1 to 0.3dB for the over-sampled frequency (>2 samples per symbol) compared to under-sampling (>2 samples per symbol).

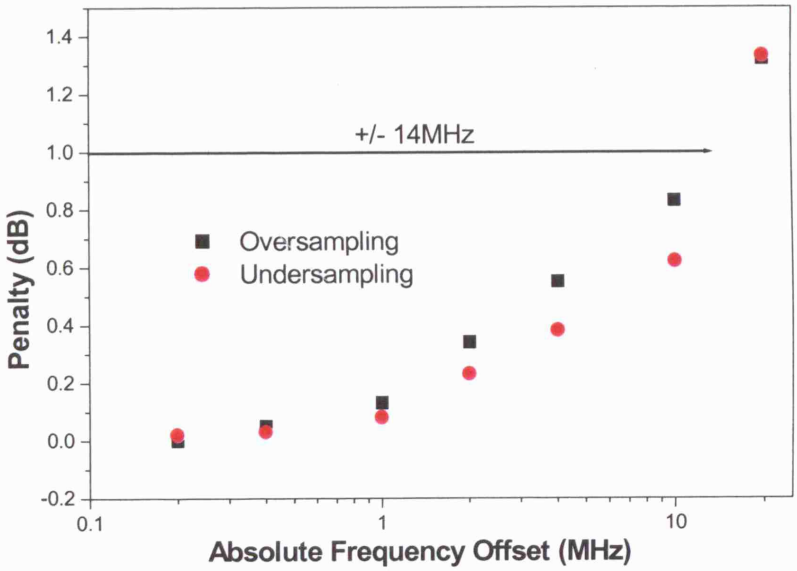

Figure 4-22 Q-factor penalty as function of sampling frequency offset from 20GS/s for AC-coupled DBRX

4.6 Increasing dynamic range – overcoming quantisation

The results in sections 4.3 and 4.4 show that without gain control the operating range of digital receiver is limited by quantisation errors after analogue to digital conversion. Without gain control, the dynamic range of the receiver does not reach the burst-to-burst power variation estimated for DONs. Hence, overcoming the quantisation noise limit is imperative to meet the fundamental receiver requirements outlined in section 4.1 Errors introduced by poor representation of the analogue waveform in the digital domain may not be easily

corrected once the information is lost. Instead, as shown in the receiver characterisations taken where manual gain control was used to improve the receiver performance, the solution to this problem lies in processing the received waveforms in the analogue domain. Pre-ADC amplification may be carried out with electrical amplification between the photodiode and ADC or with optical amplification before the photodiode as performed in conventional optical receivers where an EDFA is used as an optical pre-amplifier [Agr02d]. However, unlike conventional receivers, for a burst receiver the amplification gain needs to be adjusted on a burst by burst basis and presents further complications which are addressed in this section.

4.6.1 Electrical analogue burst power compensation

The characterisation of the digital burst-mode receiver shown in section 4.4 showed that with appropriate setting of the pre-ADC amplifier the 5-bit ADC resolution was capable of recovering burst-mode data with the presence of BLW amplitude swings of greater than 12dB resulting from the AC-coupling of the photodiode and a second AC-coupling amplifier. This section investigates the implementation of a real-time pre-ADC amplifier for burst equalisation based on a variable gain amplifier (VGA), controlled with an external voltage, or limiting amplifier (LA). Figure 4-23 shows two possible receiver configurations where analogue burst power equalisation is performed before digital sampling.

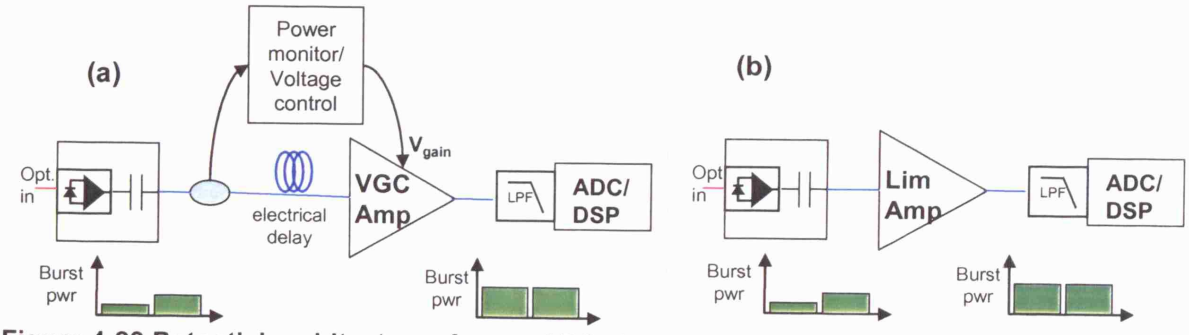

Figure 4-23 Potential architectures for pre ADC electrical burst power equalisation

Figure 4-23(a) is analogous to the analogue BMRx design based on electrical splitting and power monitoring shown in Figure 4-2 where an analogue control circuit comprising power envelope detector and converter to measure the power of each incoming burst and apply a suitable control voltage to the VGA. For such a scheme, the power of the burst is required to set the amplifier gain in advance of the burst payload arrival and is naturally suited to a feed-forward scheme of the type shown allowing bursts to be delayed during processing. As

with the receiver design in Figure 4-2, a similar implementation with an optical split and slow monitor photodiode may also be used as the power monitoring path but the success of such a scheme hinges on whether the high performance demands placed on the VGA and associated control circuitry can be met.

Not only do such schemes require a VGA with high enough signal bandwidth for the bit rate but they also require high enough gain modulation bandwidth to be able to correct to burst power variations. For a receiver of this kind the minimum required bandwidth is set by the minimum required guard band between arriving bursts. For the 100ns guard band used in this scheme this would require a modulation bandwidth in excess of 10MHz with no additional delay. As shown, a fixed offset for additional processing time could be provided by electrical or optical delay. The amount of delay required is dependent on the processing time of the control circuitry and although ultimately limited by the minimum system burst length it is likely to be of the same MHz timescale as the amplifier modulation bandwidth and more easily achieved electrically.

Figure 4-23(b) shows a simpler burst power equalisation scheme where a limiting amplifier is used to equalise burst power fluctuations before the ADC input. Limiting amplifiers are also often used in continuous receiver set ups to compensate for power fluctuations of incoming data signals prior to the decision-circuit. However, as with VGAs required in the previous scheme, such amplifiers are rarely DC-coupled at high signal bandwidths and so will also produce the characteristic AC-coupled power envelope under burst–mode operation. This results in additional problems for electrical burst equalisation since the AC-coupled envelope may already occupy the entire ADC input voltage range before amplification and subsequently be pushed data outside of its range after amplification as shown in Figure 4-24.

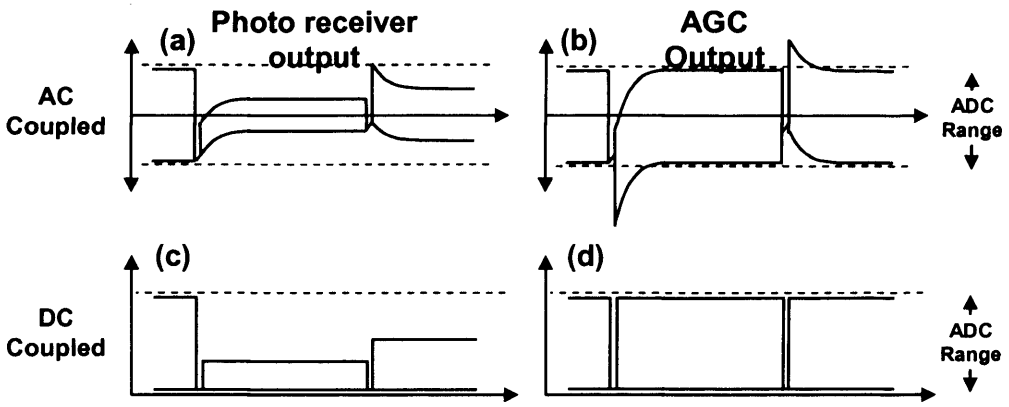

Figure 4-24 Clipping of AC-coupled bursts by electrical amplifier based pre-ADC equalizer

As with BMRx designs, the time constant of the AC-coupling envelope may be reduced by selection of appropriate coupling capacitor but at the cost of the low frequency data content and a limitation on the number of consecutive identical digits. As a result, no obvious scheme for electrical burst equalisation for an AC-coupled receiver exists without developing specific components but this is not the case for burst equalisation in the optical domain.

4.6.2 Optical analogue burst power compensation

In the optical domain, continuous receivers use an EDFA as an optical pre-amplifier to boost weak signals into the operating range of the photodiode before detection. The problem of gain transients arising from bursty input signals in EDFAs, discussed in detail in Chapter 5, together with slow gain dynamics [Des02] make them unsuitable for dynamic burst power adjustment on the time scales required for OBS. More suited to this task are semiconductor optical amplifiers (SOAs). The nanosecond gain dynamics of SOAs have already been utilised for burst/packet equalisation during optical regeneration in a number of schemes [Chi01, Wes04, Tra05] which may be grouped in to 2 approaches.

The first approach is to exploit the gain saturation of SOAs to boost a range of input powers to the saturated output power level. Such techniques requires the SOA saturation power to be less than the lowest expected burst power and operating in the saturated regime can also cause patterning distortion on the data signal since the gain dynamics are fast enough to respond to the modulated data pattern. Despite these difficulties such a scheme has been used as a receiver input pre amplifier for a 10Gb/s differential receiver [Yam97,

Shi98]. Here, a saturated SOA was able to reduce 10dB power fluctuations to 4dB but Manchester coding was required to overcome waveform distortion for standard NRZ signals. The second approach is to monitor the power fluctuations of incoming bursts and convert this into an electronic control signal. [Wes04] used a monitor PD and digital control circuit to adjust the power of a saturating laser probe signal whilst [Tra05] used a monitor photodiode and control circuit to adjust the amount of gain clamping from optical feedback to equalise burst powers in a 3R regenerator.

Whilst an SOA in the saturated regime may not be suitable for burst equalisation due to signal distortion, the possibility of exploiting the relationship between small signal gain and drive current exists. In conjunction with a monitor PD and control circuit that may be digital as in [Wes04] or analogue as in [Tra05] and a small delay of the signal path, the power of incoming bursts may be detected and used to set the gain of an SOA operating as a dynamic optical pre-amplifier. The most plausible configuration for such a scheme is a feed-forward scheme with a low speed photodiode similar to the analogue optical receiver shown in Figure 4-3. The photodiode bandwidth only needs to exceed the maximum burst rate and the control circuit could equally be implemented digitally. This approach may indeed prove more successful at mapping the non linear relationship between drive current and signal gain via a device specific look up table than the analogue approach although both approaches could potentially be used.

Figure 4-25 shows a proposed architecture for a digital burst-mode receiver with SOA pre-amplifier for pre ADC burst equalisation. Also shown, Figure 4-25(b) is a proposed scheme for implementing digital control comprising slow ADC, threshold detector to indicate burst arrival, control current processor based on preloaded look-up table and device current driver following digital to analogue conversion.

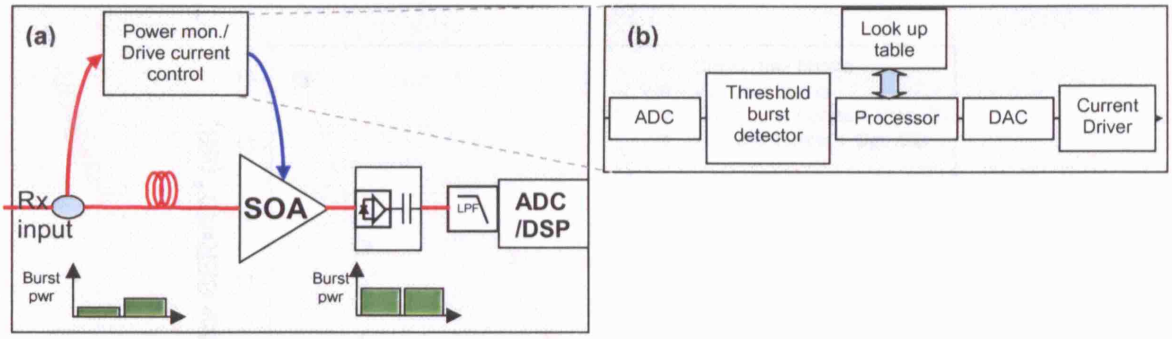

Figure 4-25 (a) Digital burst-mode receiver with SOA based burst equalizing pre-amplifier and (b) schematic of digital burst equalizer control

An experiment to determine the improvement in dynamic range provided by burst equalisation in an SOA optical pre-amplifier was carried out using the digital burst-mode receiver and standard linear SOA with a small signal gain of 10.5dB at 1550nm.

As with the previous burst-mode characterisations, 52µs bursts were generated from the burst transmitter, Figure 4-9, with the output from the strong burst (Tx B) maintained at constant power level of -6dBm whilst the weak burst (TxA) varied over a range of 20dB at the SOA input. For this demonstration the feed forward control loop was not implemented and the SOA current was adjusted using *a priori* knowledge of the burst power difference. Thus, the SOA drive current control was driven with a step function manually adjusted to give the best possible burst equalisation for each input burst power combination.

Figure 4-26 shows the required OSNR for a BER>10^{-3} for the burst receiver with optical burst equalisation. Also included for comparison are the curves for the stand alone digital receiver (4.4.2.2) and the digital receiver with electrical gain control (4.4.2.1). For clarity only the AC-coupled receiver results are shown with the DC-coupled receiver giving similar performance as described in previous measurements. In order to isolate the dynamic range improvement of each gain control techniques no electrical gain control or amplification was used with the optical pre-amplification.

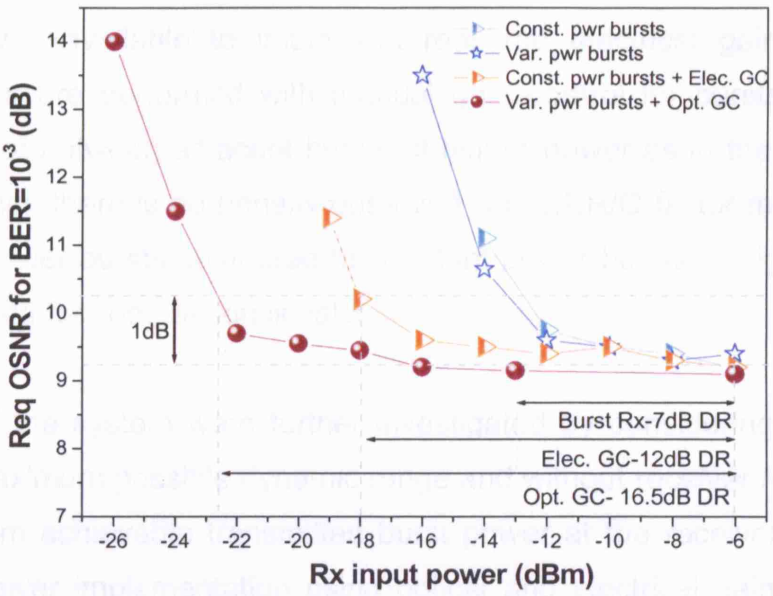

Figure 4-26 Required OSNR for BER=10^{-3} adjacent burst power of -6dBm

Figure 4-26 shows that both electrical and optical burst equalisation have the potential to significantly improve the dynamic range of a digital burst-mode receiver of this kind if performed before analogue to digital conversion. Without any gain control a dynamic range of 7dB is observed for a 1dB OSNR penalty under burst-mode operation with both constant and variable power adjacent bursts. This is extended to 12dB using electrical gain control and 16.5dB with optical burst equalisation employed. As described in 4.4.1 and 4.4.2, the addition of gain control at the ADC input removes the quantisation noise that limits the receiver performance with the receiver sensitivity and dynamic range then limited by the operating range of the photo-detector. Electrical gain control is able to match the electrical signal at the output of the photodiode to the ADC input range whilst optical gain control used the gain of the optical amplifier to boost much lower input signal powers into the operating range of the photo-detector. The addition of the optical amplifier for optical burst equalisation improved the dynamic range for adjacent burst power differences by 9.5dB, almost matching the measured small signal gain for the device in the same wavelength range. Hence, since many SOAs are able to provide up to 30dB gain, there is large potential for significant further improvement in burst-to-burst dynamic range using optical gain control.

It should be noted that because no electrical amplifier with sufficient modulation bandwidth was available to implement real-time electrical gain control the results shown are performed with manual gain control for bursts of constant power and not between adjacent bursts of higher power as in the other cases. However, since there is no penalty observed with BER/Q-factor measurements of variable power bursts compared to constant power bursts in Figure 4-21 the use of this data for comparison is valid.

The limits of the system were further investigated by considering an adjacent burst with maximum possible dynamic range and without receiver noise loading. The maximum achievable transmitted burst power at the receiver was -4dBm and the receiver implementation using optical and electrical gain control was used. Using this configuration the maximum dynamic range for the minimum specified BER performance of $1*10^{-3}$ was achieved with bursts of -32dBm input power giving a dynamic range for the minimum performance criterion of 28dB for the AC-coupled receiver and 26dB for the DC-coupled.

4.6.3 Summary of gain control techniques

The previous section shows that increasing the dynamic range of a digital burst-mode receiver required burst equalisation to be implemented before the conversion of the analogue waveform to the digital domain and that this equalisation may potentially be performed in either the electrical or optical domains. However, the experiments described serve only to demonstrate the principle of burst equalisation in such a digital receiver and a number of problems still need to be solved to realise a fully functioning system in either the electrical or optical domains. Most obviously lacking is the control electronics required to implement such a scheme. Using the optical approach the SOA switching times needs to be shorter than the minimum guard band. This is 100ns for the system described but has been set as low as 25ns in some proposed PON systems [She07].

The second problem is detecting the arrival of bursts. Without gain control this is performed in the digital signal processing phase after ADC by detecting the clock tone in the burst preamble. Such a technique, as has been demonstrated by the recovery of bursts at low OSNRs, is very robust to degradation by

random noise. Implementing this technique for the control signal would require duplication of much of the receiver and may reduce the practicality of such a receiver design. Alternatively, a burst detector could be implemented in analogue or low speed digital electronics by detecting signals above a given threshold but at the cost of noise susceptibility. However, with sufficient delay on the signal path to allow for averaging on the control path the effect of noise could be reduced at the cost of additional receiver and the physical size of a receiver able to accommodate sufficient fibre delay.

4.7 Summary

The review of published work on high bit-rate optical burst-mode reception revealed shortcomings in existing designs. Hence, this chapter presented the design and characterisation of a new all-digital burst-mode receiver complexity based on asynchronous digital sampling at twice the bit rate and digital signal processing to implement an adaptive equaliser to correct for base line wander caused by AC-coupling in the receiver signal path.

Experimental characterisation of the digital burst-mode receiver shows that no measurable penalty was observed when operating the receiver in burst-mode compared to continuous operation at the expense of only a 32bit preamble. Additionally, the receiver was tolerant to fluctuations of ±14MHz in the asynchronous sampling rate. Without any burst equalisation before the ADC the dynamic range of the receiver in burst-mode was measured to be 7dB for a 1dB penalty in required OSNR for a BER>10^{-3} limited by quantisation noise at the ADC. Initially electrical burst equalisation was investigated using bursts of equal power to remove the clipping effect caused by AC-coupling in adjacent bursts with power variations exceeding 7dB. This technique eliminated the limitation of quantisation noise and made the receiver sensitivity the limiting factor receiver dynamic range. Next, optical burst equalisation, based on drive current control of an SOA, was shown to increase the dynamic range for burst-to-burst power variations to 16.5dB. Finally, both electrical and optical gain control were employed to recover adjacent bursts with up to 28dB power variation. The limitation to further dynamic range improvement in this case was both the photodiode sensitivity and the optical and electrical amplifier gain, all of which have the potential for further improvement.

Table 4-5 shows a comparison of basic performance of the digital burst-mode receiver (DBMRx) with the published BMRx studies previously show in Table 4-3. Included is both the performance of the standalone receiver and that with optical burst equalisation.

Table 4-5 Comparison of DBMRx performance and published BMRx studies

Ref	Signal C'ling	Bit rate (Gb/s)	Req'd guard band/ reset time	Pre-amble	BER=10^{-9} Sens (dBm)	Dyn. range (dB)	Comments
Ota92	DC	1	100ns	n/a	-37.5	23	
Le04	DC	1.25	250ns	50ns	-26.4	21	AGC
Oss05	DC	1.25	25.6ns	18ns	-32.8	23.8	
Rot05	AC	10	30ns	30ns	n/a		8B/10B line coded
Kim03	AC	10	n/a	None	n/a	9.2*	Only attempted BLW correction
Nog06	AC	10	n/a	0.8ns	n/a	28*	BLW not addressed
Nis03	AC	10	n/a	4ns	-24.8	9	Manchester code
Su04	AC	10	n/a	3.2ns	n/a	25	Requires DPSK, uses LOAs to increase DR
Gri03	AC	40	n/a	40ns	n/a	n/a	Short PRBS limiting CID, equal pwr bursts
DBMRX	**AC/DC**	**10**	**100ns**	**3.2ns**	**-13**	**7**	**No data restriction**
DBMRx +SOA	**AC/DC**	**10**	**100ns**	**3.2ns**	**-22.5**	**16.5**	**Includes SOA pre-amp**

The studies listed in Table 4-5 encompass a wide range of approaches and BMRx's designed to meet a large diverse set of requirements. As a result there is no single metric that may serve as a comparison for ranking purposes and instead each system must be judged on its merits. For example, one comparable metric could be the burst efficiency defined in Section 4.1.1 as the ration of burst overhead to useful transmitted data. However many of the BMRx designs are able to work with variable burst lengths with others fixed and so the suitable burst length is not typically addressed. Similarly, a network efficiency figure can be derived for schemes requiring line coding by considering the number of additional coding bits required (e.g. 80% for 8B/10B) but it is not so easy to compare this with schemes where the data frequency content is controlled by limiting the burst length as in [Gri03].

What is possible to say is that the digital burst-mode receiver described meets all the requirements of a receiver for application in an OBS, or specifically a WR-OBS, edge router. The key requirement being that the receiver is able to deal with burst-to-burst power fluctuations without placing a restriction on the data content, burst length and with minimal overhead. The overhead of the

system described was the 32 bit preamble sequence at the start of each burst, 16 bits of which is used in burst detection and 16 for the initial AC-coupling BLW correction. The tail required for variable burst length system was an additional 16 bit sequence. Assuming the guard band and burst length as those in the measurements described gives a burst efficiency of 99.8% although there is some potential to reduce the guard band. The 100ns guard time used was set by the driver limited switching time of the transmitter and has potential for reduction as described in the previous chapters.

Similarly the length of the required preamble determines the maximum transmission efficiency once the guard band has been minimised and so worthy of some discussion. The measurements described in section 4.4 showed zero penalty for burst-mode compared to continuous operation. This result is not consistent with the theoretical work by Eldering [Eld93]. This study calculated the penalty for burst-mode operation as a function of the number of bits used to determine the initial threshold setting and predicted a 0.28dB penalty for a 16bit sequence. Eldering analysed the case where the BER of the analysed bursts was calculated using a fixed threshold, determined entirely from the preamble. For the receiver described here, the preamble was used to calculate the initial BLW correction but an adaptive equaliser was able to correct for errors in the initial threshold setting due to noise corruption or other signal distortion across the duration of the burst. Eldering's model could be adapted to include the adaptive threshold and is an avenue of potential future study since it could be experimentally verified using the experimental set-up described in this chapter.

4.8 References

Agr02 **Fibre-Optic communication systems third edition**
G.P. Agrawal, John Wiley and sons, 2002ISBN 0-471-21571-6
(a) Receiver coupling pg 149-150
(b) Receiver clock recover pg 159-180
(c) Quantisation noise pg 8-10
(d) Receiver pre-amp pg 261-264

Alt05 **http://www.altera.com/literature/ds/ds_stratixII_dsp_dev_board.pdf**

Bae04 **Efficient digital baseline wander algorithm and its architecture for fast Ethernet**
J.H.Baek, J.H.Hong, M.H.Sunwoo, K.U Kim. Tech. Digest of IEEE Workshop on Signal Processing Systems, pp 136-141, 2004

Bae05 **Low-cost and high-performance APD burst-mode receiver employing commercial TIA for 1.25-gb/s EPON**
J.M.Baek, J.W.Kwon, J.W.Park,D.Y.Rhee, E.H.Lee, J.H.Lee, Y.K.Oh, D.H.Jang. IEEE Photonics Technology Letters, Vol. 17 (10), pp 2170-2172, Oct. 2005

Bak01 **Decision-threshold based on dynamic offset compensation for burst-mode receiver**
T.Den Bakker, T.Kun-Yii, Y.K.Park. Tech. Digest of European Conference on Optical Communication, Vol. 2, pp 222 - 223, 30 Sept.-4 Oct. 2001

Ber93 **Margin measurements in optical amplifier system**
N.S.Bergano, F.W.Kerfoot, C.R.Davidsion. IEEE Photonics Technology Letters, Vol. 5 (3), pp 304 – 306, March 1993

Bri02 **A SiGe BiCMOS burst-mode 155-Mb/s receiver for PON**
S.Brigati, P.Colombara, L.D'Ascoli, U.Gatti, T.Kerekes, P.Malcovati. IEEE Journal of Solid-State Circuits, Vol. 37 (7), pp 887-894 July 2002

Buc04 **Impact of SOA gain saturation and dynamics on the throughput of optical burst switching nodes**
H.Buchta, E.Patzak, J.Saniter, S.F.Raub. Tech. Digest of Optical Fibre Communication Conf. Vol. 2, pp3, 23-27 Feb. 2004

Bui04 **Theoretical design and optimization analysis of AC-coupled fibre optic burst-mode receiver**
E.Buimovich, D.Sadot. Tech. Digest of Lasers and Electro-Optics Conf., Vol. 1, pp 3, 2004

Cha94/1 **Inherent transmission capacity penalty of burst-mode receiver for optical multiaccess networks**
S.Chao, L.K.Chen, K.W.Cheung. IEEE Photonics Technology Letters, Vol. 6 (5), pp 664-667, May 1994

Cha94/2 **BER penalty of burst-mode receiver in optical multiaccess network**
S.Chao, L.K.Chen, K.W.Cheung. Tech. Digest of Lasers and Electro-Optics Society Annual Meeting, Vol. 1, pp 198-199, 31 Oct.-3 Nov. 1994

Cha95 **BER performance of digital optical burst-mode receiver in TDMA all-optical multiaccess network**
S.Chao, L.K.Chen, K.W.Cheung. IEEE Photonics Technology Letters, Vol. 7 (1), pp 132 – 134, Jan. 1995

Cha97 **Theory of burst-mode receiver and its applications in optical multiaccess networks**
S.Chao, L.K.Chen, K.W.Cheung. Journal of Lightwave Technology, Vol. 15 (4), pp 590 – 606, April 1997

Chi01 **Semiconductor optical amplifiers: a key technology to control the packet power variation**
D.Chiaroni, N.Le Sauze, T.Zami, J-Y.Emery. Tech. Digest of European Conference on Optical Communication, Vol. 3, pp 314-315, 30 Sept.-4 Oct. 2001

Des02 **Erbium-Doped Fibre Amplifiers**
E.Desurvire, Published 1994 John Wiley and Sons ISBN 0-471-58977-2, Pg 16

Due03 **Fast packet routing in a 2.5 Tb/s optical switch fabric with 40 Gb/s duobinary signals at 0.8 b/s/Hz spectral efficiency**
M.Duelk, J.Gripp, J.Simsarian, A.Bhardwaj, P.Bernasconi, MZirngibl, O.Laznicka. Tech. Digest of Optical Fibre Communications Conference, 2003

Eld93 **Theoretical determination of sensitivity penalty for burst-mode: fibre optic receivers**
C.A Eldering. Journal of Lightwave Technology, Vol.11 (12), pp 2145-2149, Dec.1993

Far04 **Performance of a 10.7Gb/s receiver with Digital Equaliiser using Maximum Likelihood Sequence Estimation**
A.Farbert, S.Langenbach, N.stojanovic, C.Dorschky, T.Kupfer, C.Schulien, J-P.Elbers, H.Wernz, H.Griesser, H.Glingener. Tech. Digest of European Conference on Optical Communication post deadline 2004

Gar93 **Interpolation in digital modems. I. Fundamentals**
F.M.Gardner. IEEE Transactions on Communications, Vol. 41 (3), pp 501-507, March 1993

Geo02 **Clock and data recovery IC for 40-Gb/s fibre-optic receiver**
G.Georgiou, Y.Baeyens, C.Young-Kai, A.H.Gnauck, C.Gropper, P.Paschke, R. Pullela, M.Reinhold, C.Dorschky, J-P.Mattia, T.W.von Mohrenfels, C.Schulien. IEEE Journal of Solid-State Circuits Vol. 37, (9), pp 1120-1125, Sep 2002

Gri01 **Demonstration of a 1.2 Tb/s optical packet switch fabric (32/spl times/40 Gb/s) based on 40 Gb/s burst-mode clock-data-recovery, fast tunable lasers, and a high-performance N/spl times/N AWG**

J.Gripp, M.Duelk, J.Simsarian, S.Chandrasekhar, P.Bernasconi, A.Bhardwaj, Y.Su, K.Sherman, L..Buhl, E.Laskowski, M.Cappuzzo, L.Stulz, M.Zirngibl, O.Laznicka, T.Link, R.Seitz, P.Mayer, M.Berger. Tech. Digest of European Conference on Optical Cmmunication, Vol. 6, pp 58 – 59, 30 Sept.-4 Oct. 2001

Gri03 **Optical switch fabrics for ultra-high-capacity IP routers**
J.Gripp, M.Duelk, J.Simsarian, A.Bhardwaj, P.Bernasconi, O.Laznicka, M.Zirngibl. Journal of Lightwave Technology, Vol. 21 (11), pp 2839 – 2850, Nov. 2003

Han03 **AC-coupled burst-mode optical receiver employing 8B/10B coding**
S.Han, M.S.Lee. Electronics Letters Vol. 39 (21), pp 1527-1528, 16 Oct. 2003

Han04 **Burst-mode penalty of AC-coupled optical receivers optimized for 8B/10B line code**
S.Han, M.S.Lee. IEEE Photonics Technology Letters, Vol.16(7), pp 1724-1726, July 2004

Hay00 **Communications Systems**
S.Haykin, 4th edition, Pub. Wiley, Chap 6.

Jer84 **Techniques for Estimating the Bit Error Rate in the Simulation of Digital Communication Systems**
M.Jeruchim, IEEE Journal on Selected Areas in Communications, Vol. 2 (1), pp153-170, Jan 1984

Kaw89 **Smart optical receiver with automatic decision-threshold setting and retiming phase alignment**
M.Kawai, H.Watanabe, T.Ohtsuka, K.Yamaguchi. Journal of Lightwave Technology, Vol. 7 (11), pp 1634-1640, Nov. 1989

Kan03 **Clock and data recovery circuit for 10-Gb/s asynchronous optical packets**
G.T.Kanellos, L.Stampoulidis, N.Pleros, T.Houbavlis, D.Tsiokos, E.Kehayas, H. Avramopoulos, G.Guekos. IEEE Photonics Technology Letters, Vol. 15 (11), pp 1666-1668, Nov. 2003

Kim04 **A 10-Gbit/s CMOS-burst-mode clock and data recovery IC for a WDM/TDM-PON access network**
S.Kimura, M.Nogawa, K.Nishimura, T.Yoshida, K.Kumozaki, S.Nishihara, Y.Ohtomo. Tech. Digest of The 17th Annual Meeting of the IEEE Lasers and Electro-Optics Society, Vol, 1, pp 310 - 311, 7-11 Nov. 2004

Lee02 **A new non-data-aided feedforward symbol timing estimator using two samples per symbol**
Seung Joon Lee. IEEE Communications Letters, Vol. 6 (5), pp 205-207, May 2002

Le04 **A burst-mode receiver for 1.25-Gb/s ethernet PON with AGC and internally created reset signal**
Quan Le, Sang-Gug Lee, Yong-Hun Oh, Ho-Yong Kang, Tae-Hwan Yoo. IEEE Journal of Solid-State Circuits, Vol. 39 (12), pp 2379-2388 ,Dec. 2004

Lee04 **A 5-b 10-GSample/s a/D converter for 10-gb/s optical receivers**
Jaesik Lee, P.Roux, Ut-Va Koc, T.Link, Y.Baeyens, C.Young-Kai. IEEE journal of Solid-State Circuits, Vol. 39, (10), pp 1671-1679, Oct. 2004

Li06 **Burst-mode clock and data recovery in optical multiaccess networks using broad-band PLLs**
A.Li, J.Faucher, D.V.Plant. IEEE Photonics Technology Letters, Vol. 18 (1), pp 73-75, Jan. 1 2006

Max01 **NRZ Bandwidth – LF cutoff and baseline"**
Maxim Inc Application note HFAN-09.04.
http://www/maxim-ic.com/appnotes.cfm/appnote_number/1738/in/en

Men97 **Synchronization techniques for digital receivers**
U. Mengali and A.N.D'Andrea. New york Plenum press 1997

Men95 **Performance of optical direct receivers using noise corrupted decision-threshold**
P.Menendez-Valdes. Journal of Lightwave Technology, Vol.13 (11), pp2202-2214, Nov. 1995

Nis99 **10-Gb/s optical DPSK packet receiver proof against large power fluctuations**
H.Nishizawa, Y.Yamada, Y.Shibata, K.Habara. IEEE Photonics Technology Letters, Vol.11 (6), pp 733- 735, June 1999

Nis02 **Design of a 10-Gb/s burst-mode optical packet receiver module and its demonstration in a WDM optical switching network**
H.Nishizawa, Y.Yamada, K.Habara, T.Ohyama. Journal of Lightwave Technology, Vol. 20 (7) pp 1078-1083, July 2002

Nog05 **A 10 Gb/s burst-mode CDR IC in 0.13 /spl mu/m CMOS**
M.Nogawa, K.Nishimura, S.Kimura, T.Yoshida, T.Kawamura, M.Togashi, K. Kumozaki, Y.Ohtomo. Tech. Digest of IEEE Solid-State Circuits Conference, Vol.1, pp 228-595, 6-10 Feb. 2005

Nog06 **A 10Gb/s burst-mode adaptive gain select limiting amplifier in 0.13/spl mu/m CMOS**
M.Nogawa, Y.Ohtomo, S.Kimura, K.Nishimura, T.Kawamura, M.Togashi. Tech. Digest of IEEE Conference on Solid-State Circuits, pp 940-949, Feb. 6-9, 2006

Oer88 **Digital filter and square timing recovery**
M.Oerder, H.Meyr. IEEE Transactions on Communications, Vol. 36 (5), pp 605-612, May 1988

Oss05 **A 1.25-gb/s burst-mode receiver for GPON applications**
P.Ossieur, D.Verhulst, Y.Martens, C.Wei, J.Bauwelinck, Q.Xing-Zhi, J..Vandewege. IEEE Journal of Solid-State Circuits Vol.40, (5), pp 1180-1189, May 2005

Oss06 **Influence of random DC offsets on burst-mode receiver sensitivity**
P.Ossieur, T.De Ridder, Q.Xing-Zhi, J.Vandewege. Journal of Lightwave Technology, Vol. 24 (3), pp 1543-1550, March 2006

Ota92 **DC-1 Gb/s burst-mode compatible receiver for optical bus applications**
Y.Ota, R.G.Swartz, V.D.Archer. Journal of Lightwave Technology, Vol. 10 (2), pp 244-249, Feb. 1992

Pan96 **A new approach for evaluating the performance of a symbol timing recovery system employing a general type of nonlinearity**
E.Panayirci, E.K.Bar-Ness. IEEE Transactions on Communications, Vol. 44 (1), pp 29-33, Jan. 1996

Pet05 **A 40 Gb/s 3R Burst-mode Receiver with 4 integrated MZI switches**
D.Petrantonakis, G.T.Kanellos, P.Zakynthinos, N.Pleros, D.Apostolopoulos, H.Avramopoulos. Tech. Digest of Optical Fibre Communication Conf. 5-10 March 2006

Pou03 **A 20 GS/s 8 b ADC with a 1 MB memory in 0.18 /spl mu/m CMOS**
K.Poulton, R.Neff, B.Setterberg, B.Wuppermann, T.Kopley, R.Jewett, J.Pernillo, C. Tan, A.Montijo. Tech. Digest of IEEE Solid-State Circuits Conf, pp 318-496 vol.1, 2003

Rei01 **A fully integrated 40-Gb/s clock and data recovery IC with 1:4 DEMUX in SiGe technology**
M.Reinhold, C.Dorschky, E.Rose, R.Pullela, P.Mayer, G.Kunz, Y.Baeyens, T.Link, J-P.Mattia. IEEE Journal of Solid-State Circuits, Vol.36 (12), Dec 2001, pp1937-1945

Rot05 **Performance analysis of AC-coupled burst-mode receiver for fibre-optic burst switching networks**
E.Rotem, D.Sadot. IEEE Transactions on Communications, Vol.53 (5), pp 899-904 May 2005

Sat05 **40-gb/s burst-mode optical 2R regenerator**
R.Sato, T.Ito, Y.Shibata, A.Ohki, Y.Akatsu. IEEE Photonics Technology Letters, Vol. 17 (10), pp 2194 – 2196, Oct. 2005

Sch06 **A 22GS/s 5b adc in 0.13/spl mu/m SiGe BiCMOS**
P.Schvan, D.Pollex, W.Shing-Ch, C.Falt, N.Ben-Hamida. Tech. Digest of IEEE International Conference on Solid-State Circuits, pp 2340 – 2349, Feb. 6-9, 2006

She05 **ADC limitations on the dynamic range of a digital receiver**
Zheng Shenghua, Xu Dazhuan, Jin Xueming. Tech. Digest of IEEE International Symposium on Microwave, Antenna, Propagation and EMC Technologies for Wireless Communications,Vol. 1, pp 79-82, 8-12 Aug. 2005

She07 **A 10-Gb/s 1024-Way-Split 100-km Long-Reach Optical-Access Network**
D.P.Shea, J.E,Mitchell. Journal of Lightwave Technology, vol.25, (3), pp.685-693, March 2007

Shi98 **Semiconductor laser diode optical amplifiers/gates in photonic packet switching**
Y.Shibata, Y.Yamada, K.Habara, K., N.Yoshimoto. Journal of Lightwave Technology, Vol. 16, (12), pp 2228-2235, Dec. 1998

Sta05 **40 Gb/s fast-locking all-optical packet clock recovery**
L.Stampoulidis, E.Kehayas, H.Avramopoulos, Y.Liu, E.Tangdiongga, H.J.S.Dorren. Tech. Digest of Optical Fibre Communication Conf. Vol. 4, 6-11 March 2005

Su04 **Wide dynamic range 10-Gb/s DPSK packet receiver using optical-limiting amplifiers**
Yikai Su, Xiang Liu, J. Leuthold. IEEE Photonics Technology Letters, Vol. 16 (1), pp296 – 298, Jan. 2004

Tek04 **TDS6000 and TDS6000B series,TDS7000 and TDS7000B series & CSA7000 series Memory Erasure and Nonvolatile Memory Parts List (WebID: 3561):**
http://www2.tek.com/cmswpt/pifinder.lotr?cn=tds6000bc&lc=EN
http://www.tek.com/products/oscilloscopes/tds6000/
http://www.tek.com/site/mn/mnfinder_detail/1,1096,,00.html?id=3826&pn=071122801

Tra05 **Optical packet power equalization with large dynamic range using controlled gain-clamped SOA**
A.V.Tran, C-J.Chae,R.S.Tucker. Tech. Digest of Optical Fibre Communication Conf. Vol 1, 6-11 March 2005

Ver94 **Symbol timing recovery scheme tolerant to carrier phase error**
D.Verdin, T.C.Tozer. Electronics Letters Vol. 30, (2) , pp 116-117, 20 Jan 1994

Wes04 **Combining control electronics with SOA to equalize packet- to-packet power variations for optical 3R regeneration in optical networks at 10 Gbit/s**
H.Wessing, B.Sorensen, B.Lavigne, E.Balmefrezol, O.Leclerc. Tech. Digest of Optical Fibre Communication Conference, Vol. 1, 23-27 Feb. 2004

Woo05 **AC-coupled burst-mode OLT SFP transceiver for gigabit ethernet PON systems**
Jin-Wook Kwon; Joong-Hee Lee; Jae-Myung Baek; Joo-Chul Cho; Ja-Won Seo; Sung-Soo Park; Jung-Kee Lee; Yun-Kyung Oh; Dong-Hoon Jang. IEEE Photonics Technology Letters, Vol.17 (7) pp 1519 – 1521, July 2005

Yam97 **10 Gbit/s differential receiver for large optical power fluctuation**
Y.Yamada, Y.Shibata, K.Habara. Electronics Letters, Vol. 33 (19) pp 1642-1644, Sept. 1997

Yam99 **Ultra-fast clock recovery for burst-mode optical packet communication**
Y.Yamada, S.Mino, K.Habara. Tech. Digest of Optical Fibre Communication Conf. Vol. 1, pp 114-116, 21-26 Feb. 1999

Zha06 **K-means clustering-based data detection and symbol-timing recovery for burst-mode optical receiver**
Tong Zhao, A.Nehorai, B.Porat. IEEE Transactions on Communications, Vol. 54, (8), pp 1492 – 1501, Aug. 2006

Zhu01 **A fully digital timing recovery scheme using two samples per symbol**
W.P.Zhu, M.O.Ahmad, M.N.S.Swamy. Tech. Digest of IEEE International Symposium on Circuits and Systems, Vol. 2, pp 421-424, 6-9 May 2001

Zhu03 **A feedforward symbol synchronization scheme for digital receiver**
W.P.Zhu, Yupeng Yan M.O.Ahmad, M.N.S.Swamy. Tech. Digest of International Conference on Neural Networks and Signal Processing, Vol.1, pp 587-590, 14-17 Dec. 2003

Chapter 5 Burst Amplification

5.1 Introduction

For Type II OBS networks, the key subsystems of burst-mode transmitter and receiver discussed in previous chapters would be co-located in the edge nodes at the interface between optical and electrical domain. Between these edge routers lies the optical core, across which the generated optical bursts are transmitted, comprising optical routers, connecting fibre and optical amplifiers, which must be capable of amplifying bursty traffic with minimal impairment.

The focus of this chapter is optical amplification and in particular techniques for burst-mode operation of erbium-doped-fibre-amplifiers (EDFAs). The slow gain dynamics of conventional EDFAs leads to gain transients in response to input power variation typical of burst networks. The aim of the work described in this chapter was to use a realistic network scenario based on the subsystems described in the previous chapters to investigate the impact of the key parameters on the BER of bursts transmitted through dynamic burst switched networks. This new approach allows determination of the optimal configuration and the relative impact of the primary impairments. The results presented show that the feedback cavity loss (FCL) is the key control parameter and that the optimum FCL is not in the region of high gain compression that was the focus of much of the previous work.

5.1.1 Review of technologies for burst-mode amplification

For most dynamic optical networks, an optical amplifier is required to provide gain across the entire range of transmitted wavelengths with minimum spectral variation and without adding an additional penalty for burst traffic [Agr02a]. The transmission window is generally considered to be the C-band and gain variation ideally limited to 1-2dB. These requirements generally rule out semiconductor optical amplifiers (SOAs) due to fast cross-gain effects and there has not been widespread deployment of Raman and Brilliouin fibre amplifiers due to limited amplifier gain and the high power optical pumping requirement in the most common part of the optical spectrum [Agr02a]. Instead, doped fibre amplification using stimulated emission is the most common mechanism to meet the amplification requirement in optical networks. Indeed, with its broad

gain spectrum, polarisation insensitivity and relatively slow gain dynamics, the erbium doped fibre amplifier (EDFA) has been used to provide optical amplification in almost all WDM based point to point transmission systems deployed to date [Agr02, Siv04, Fal02, Shi00, Muk00, Wei99].

However, fluctuations of input power resulting from the adding or dropping of WDM channels, network faults or directly from transmission of long (µs-ms) bursts of data can cause gain fluctuations resulting in transmission penalties. Since the total output power of a saturated EDFA is broadly constant, input power fluctuations, caused by adding and dropping bursts, induce gain transients on surviving channels that lead to transmission penalties. The power variations across a burst arising from EDFA gain transients are particularly problematic in standard burst-mode receivers which employ a fixed decision-threshold (see Chap. 4) and can also lead to potentially catastrophic failure of downstream components.

These negative effects occur on two timescales which determine the success of compensation schemes. The most problematic and widely studied is cross-gain modulation which occurs on surviving channels which occurs on the scale of the EDFA response time, set by the lifetime of the meta-stable excited erbium lifetime and of the order of hundreds of microseconds [Des02a, Ali94]. An example of cross gain modulation on continuous signals due to input power fluctuations is shown in Figure 5-9 below. A number of techniques using optical feedback and electronic control have been proposed to ensure constant gain after adding and dropping of channels in WDM systems and dynamic burst switched networks. Electronic feed-forward techniques use a photodiode to detect incoming power variations followed by a control circuit to adjust the power of an additional input channel [Tra05, Bia03, Xia00, Yoo99/00] or by varying the power of the pump to control the gain of the remaining signals [Sri97a]. Feed-forward electronic control of the pump power has also been demonstrated in conjunction with feedback control [Lie06, Yos06] and in a hybrid scheme with optical control [Chu97].

Electronic control schemes can minimize the transmission penalties from burst-mode EDFA operation but at the expense of additional components and

complexity and high speed electronics for full control. As demonstrated in [Bia03], the slow (millisecond) EDFA gain dynamics mean that relatively slow electronic control loops (MHz) are sufficient to compensate for cross gain modulation effects, even in dynamic burst switched networks where power fluctuations may occur at intervals much smaller then the burst length. However, the slow gain recovery causes additional transients on single bursts or on burst channels of varying power, as shown in Figure 5-1, that requires a response time shorter than that of the power variation [Oik07, Oka05, DeO05].

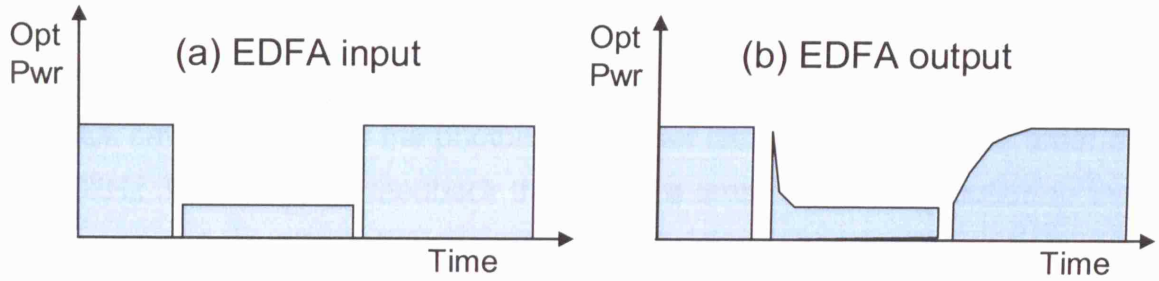

Figure 5-1 Gain transients on signals with varying input power requiring fast electronic control

A simpler technique that eliminates the requirement for high speed electronics or additional lasers and photodiodes is all-optical gain-clamping (AOGC) where a portion of ASE from the EDFA output is coupled back to the input to form a laser cavity. This clamps the gain of each channel as the power of the lasing channel is able to adjust according to input power fluctuations with a response time set by the loop round trip time. In the most common configuration, first described in [Zir91] and shown in Figure 5-2, gain control is achieved by using a band-pass filter to select the lasing wavelength in a ring laser structure with an attenuator to allow adjustment of the feedback cavity loss (FCL) providing flexibility in the amount of gain-clamping depending on required performance and conditions [Des02b]. Fibre-Bragg- Gratings [Enn05, Yi04, Poo04, Cho01] or wavelength selective mirror [Ahm04] may also be used to select the lasing wavelength and block transmission of the feedback wavelength with output signal channels.

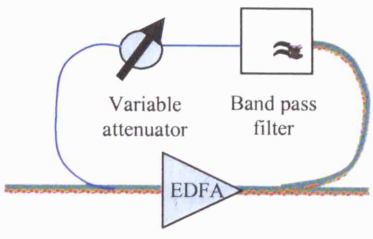

Figure 5-2 Layout of simple gain-clamped EDFA

The gain dynamics of EDFAs lead to two wavelength dependent effects that may degrade performance in WDM based networks after channels are added or dropped in optical feedback loops. With insufficient power in the feedback channel to ensure lasing for maximum input signal power, power transients at the input to an EDFA arising from burst add/drop results in cross gain modulation on the remaining channels, which appear as a steady state power fluctuation (SSPF) with a magnitude dependent on the proportion of output power coupled back to the input. Additionally, the use of optical feedback also introduces amplitude fluctuations due relaxation oscillations (RO) associated with the laser cavity [Bah03, Luo97/98]. The RO frequency depends on the feedback cavity length and the photon and carrier lifetimes and is of the order of 10-100kHz. Under optical feedback there also a small static contribution to the output power fluctuations from spectral hole burning (SHB), arising from the inhomogeneity in the erbium gain spectrum, that varies with the optical feedback wavelength [Luo98, Kro98].

Whilst these effects may not be catastrophic for short burst length OPS/Type I OBS schemes or quasi-static wavelength-routed networks where reconfiguration occurs over slower timescales they become critical in Type II burst networks where burst lengths are expected to be similar to the EDFA response times [Bay04, Dus02, Agr02, Muk00]. Subsequent work on all-optical gain clamping has focused on reducing the magnitude of these gain transients. Electronic feed-forward techniques have also been applied in conjunction with optical feedback to reduce the magnitude of RO and SSPF [Chu02, Has02], but not on the timescales required for dynamic OBS networks. Additionally, a number of all-optical techniques have also been proposed to improve the performance of optically gain-clamped amplifiers. [Liu99a] showed that the use of 2 feedback loops at different wavelengths act to cancel the RO induced by the other to stabilize the gain of surviving signal channels whilst [Liu99b] compensated for ROs by introducing an oscillation of an opposite sign with an RF driven acousto-optic modulator. A variation that completely eliminates RO provides optical feedback with an ASE reflecting mirror and coarse WDM coupler [Ahn04]. However, the surviving channels are still subject to SSPF and reduced gain. Table 5-1 is a summary of the main studies of EDFA gain clamping, showing both electronic and optical techniques.

Table 5-1 Summary of gain transient control schemes for EDFAs with varying input power

Ref	Control Scheme	Burst length	Max.no channels add/drop	Max Trans. (dB)	Comment
Zir91	Opt. FB	10ms	--	--	Optical feedback loop
Luo97/98	Opt. FB	500μs	7 out of 8	0.5	Characterizes SHB SSPF and RO
Choi01	Opt. FB	--		1.2	2 stage EDFA + FBGs used to clamp only 1st stage
Liu99/1	Opt. FB	1ms	31 out of 32	0.3	2 F'back wavelengths
Ahn04	Opt. FB	n/a	16 out of 17	0.5	No opt. cavity to remove ROs
Chu02 (Has02)	Opt. FB+ Elec FF	2ms	39 out of 40	1.4	Uses AOGC with additional FF Elec control for RO- Sim. only
Liu99b	Opt. FB+ Elec FF	1ms	7 out of 8	0.075	Uses AOGC with additional FF Elec control for RO compensation
Xia00	Elec FF	Not given	Not given	1	Improved light injection config-no circuit implemented
Bia03	Elec FF	1ms	16 out of 17	0.7	16 burst step change
Tra05	Elec FF	500μs	1 out of 2	1	Envelop detection demonstrated
Yos06	Elec.FF+FB	1.6ms	3 out of 4	1	After 5 EDFAs in recirculating loop experiment
Lie06	Elec.FF+FB	7ms	20 out of 21	0.5	At 2nd of 6 amp link

Although, it is possible that electronic control techniques will be feasible either entirely or in a hybrid solution they offer no performance advantage in terms of resource savings compared to AOGC. This fact, the possible restriction on burst length shown in Tables 5.1 and 5.2 and the elegance and resource savings of an entirely optical solution mean that optical gain clamping is considered for the rest of this chapter. Much of the existing work on optical gain-clamping has focused on reducing the magnitude of the gain transients by electronic control or characterising RO and SSPF without considering the effect these two effects have on the BER of transmitted bursts or considering the full range of gain clamping scenarios governed by the key design parameter, the feedback cavity loss (FCL). For example Luo et al [Luo97] provides a detailed analysis for a single feedback cavity loss at high gain compression and only [Ric97] explains the role of FCL in a theoretical model. Additionally, few studies [Tho05a, Zho00] have considered the BER of bursts transmitted through amplifiers experiencing cross gain modulation due to burst add/drop and none have attempted to use the quality of transmitted signals to characterize and optimize performance parameters.

The aim of the work described here was to use a realistic network scenario based on the subsystems described in the previous chapters to investigate the impact of the key parameters on the BER of bursts transmitted through dynamic

burst switched networks. Subsequently, the measurements allow determination of the optimal configuration and the relative impact of the primary impairments. The results presented show that the feedback cavity loss (FCL) is the key control parameter in minimizing the BER of transmitted bursts. In particular, the optimum level of feedback for different input power fluctuations is considered and it is shown that the optimum feedback level, determined from the signal quality of transmitted bursts, is not in the region of high gain compression that was the focus of much of the previous work. The same approach is then employed to determine the optimum feedback wavelength.

5.2 Theory of optical gain clamping

The role of optical gain clamping in DONs was formalized in early work on the subject, most notably in [Des91, Zir91 and Sal90], and although originally derived for steady state conditions requires only little adaptation for application to DONs .

The relationship between the input and output signal power in an N-channel system was derived in [Sal90] for steady state conditions and assuming homogeneous broadening. This equation, shown as equation (5.1), shows that the gain of any wavelength is independent of total optical input power.

$$P_k^{out} = P_k^{in} \exp\left[-\alpha_k L + \frac{1}{P_k^{IS}} \sum_{J=1}^{N} (P_j^{in} - P_j^{out}) \right] \qquad \textbf{(5.1)}$$

P_k^{IS} is the intrinsic saturation power and α_k is the absorption coefficient at wavelength λ_k and L is the doped fibre length. Thus, considering the feedback channel at λ_f and rearranging to make the sum of all channels the subject of the equation and writing the ratio P_f^{out} / P_f^{in} as the loss of the feedback loop, yields:

$$\sum_{J=1}^{N} (P_j^{in} - P_j^{out}) = P_f^{IS} (\ln \beta + \alpha_k L) \qquad \textbf{(5.2)}$$

Equation (5.2) may be substituted back into equation (5.1) to give the equation presented in [Zir91] which may be written in terms of the channel output power, equation (5.3), or the signal gain as in equation (5.4).

$$P_k^{out} = P_k^{in} \exp\left[-\alpha_k L + \frac{P_f^{IS}}{P_k^{IS}} (\ln \beta + \alpha_f L) \right] \qquad \textbf{(5.3)}$$

$$G_k = \exp\left[-\alpha_k L + \frac{P_f^{IS}}{P_k^{IS}}(\ln\beta + \alpha_f L)\right] \quad \textbf{(5.4)}$$

β=1/FCL, P_f^{IS} and P_k^{IS} are the intrinsic saturation powers and α_f and α_k are the absorption coefficients of the feedback and k-th channel, respectively.

Thus, since all the quantities in the exponent are constant, this equation shows that, for the range of input powers for which lasing is possible, the gain of each signal channel is set through the FCL. From equations (5.3) and (5.4), it becomes possible to determine the power and gain of all of the channels under gain clamping conditions. Additionally, these equations show that the origin of the wavelength dependence is controlled through the coefficients α_f and α_k and the saturated gain ratio P_f^{IS} / P_k^{IS}. The same trends are observed in a dynamic rate equation based models [Na99, Son99, Gil91].

5.3 Experimental Investigation of GC-EDFA performance

5.3.1 Experimental set up

The first stage of the experimental investigation was to characterize the performance of a single gain-clamped EDFA in terms of the key gain clamping parameters. This required an experimental network model to make direct measurements of the magnitude of gain transients (both SSPF and RO) induced on surviving channels as well as BER/Q-factor measurements to determine the quality of transmitted bursts as a function of the FCL. All measurements for single amplifier operation were performed with the experimental set-up, shown schematically in Figure 5-3, based on a model of a single OBS link between two core routers containing a single GC-EDFA. A continuous signal, generated at λ_P from edge router 1, was used as a probe channel transmitted across the link and received at edge router 3. Meanwhile, the transmitter in edge router 2 generated an ON-OFF burst sequence at λ_B that simulated the adding and dropping of multiple simultaneous bursts before the GC-EDFA before being dropped at a second core router after the GC-EDFA.

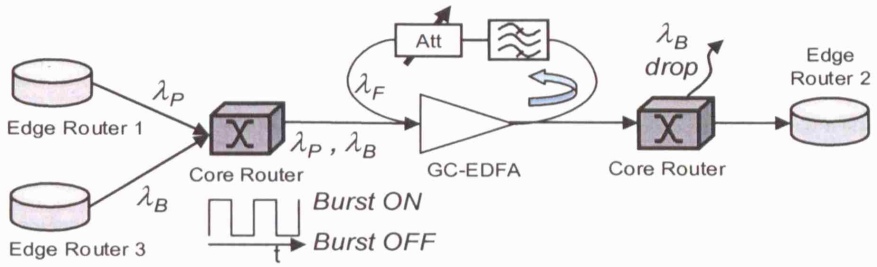

Figure 5-3 OBS link schematic for single GC-EDFA analysis

The experimental implementation was based on the sub-systems described in the proceeding chapters. The edge router transmitters comprised two SG-DBR tunable lasers labelled as Tx_1 and Tx_2 in the experimental set-up shown in Figure 5-5. Tx_1 was operated in continuous mode and used as the probe channel to measure the effect of burst add/drop on surviving channels. Tx_2 was operated in burst-mode with a switching time below 20ns. Tx_2 was switched between 2 wavelengths with a period of 400μs and 50% duty cycle and the output coupled into the link amplifier via a wavelength routing node which only passed λ_B. The wavelengths used in all experiments are shown in Table 5-2.

Table 5-2 Channel wavelengths used in GC-EDFA experiments

Channel	Wavelength (nm)
λ_B Filtered burst channel	1535.9
λ_P Signal channel	1542.6
λ_F Feedback channel	1528, 1538, 1551

Three feedback wavelengths were chosen to cover the range of the EDFA gain spectrum to investigate the effect of changing the gain of the lasing cavity. The ASE spectrum, of the amplifier used for all single GC-EDFA measurements is shown in Figure 5-4(a) showing the gain variation across the transmission window. Figure 5-4(b) shows the OSA spectrum showing burst, signal and feedback channel with a feedback wavelength of 1552nm.

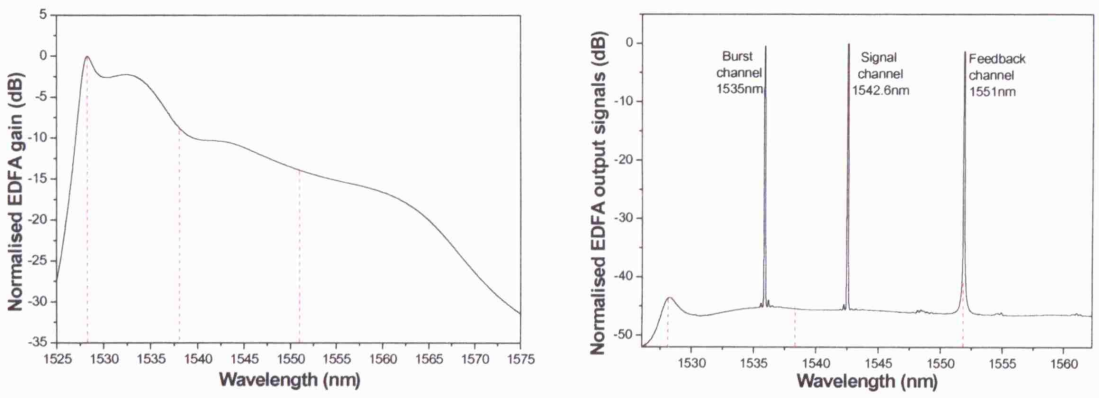

Figure 5-4 (a) EDFA gain spectrum (no signal input) and (b) EDFA output with burst and signal and feedback channel. Red lines show feedback wavelength investigated

The time period chosen for the burst channel modulation is of the order of that envisaged for OBS based DONs [Bay04, Dus02, Muk00] and also matched to the timescale of the EDFA transient effects. The power of the Tx_2 burst channel was varied to replicate the impact of different numbers of added/dropped bursts up to a maximum of 16 bursts corresponding to a power difference of 12dB at the input of the EDFA. The transmitter set up and timing was designed to replicate the worst case scenario with a single surviving channel and multiple bursts added and dropped simultaneously. The channel powers used in all measurements are shown in Table 5-3.

Table 5-3 Burst channel powers at EDFA input and equivalent no. of added dropped channels

Burst channel EDFA input power	Power relative to signal channel	Equivalent number of added/dropped bursts
-17 dBm	0 dB	1
-11 dBm	+ 6 dB	3
-5 dBm	+ 12 dB	16

To eliminate additional BLW caused by AC-coupling, the signals were received by the DC-coupled digital receiver described in chapter 4 and operated in continuous mode. For these measurements 2 receiver configurations were used. The first used a fully adaptive threshold, correcting for amplitude and BLW fluctuations. The second receiver configuration used a fixed threshold to investigate the impact of EDFA gain transients on a standard optical receiver and provide a performance comparison for the adaptive threshold receiver. For all measurements the receiver timing was set up to capture at least 1 full cycle of the burst add/drop sequence and the fixed decision-threshold was optimized to minimise the BER across the entire data sequence. In order to allow for error counting over the limited sequence length noise was added at the receiver to obtain a fixed OSNR of 11dB (0.1nm resolution). The complete experimental set-up is shown in Figure 5-5.

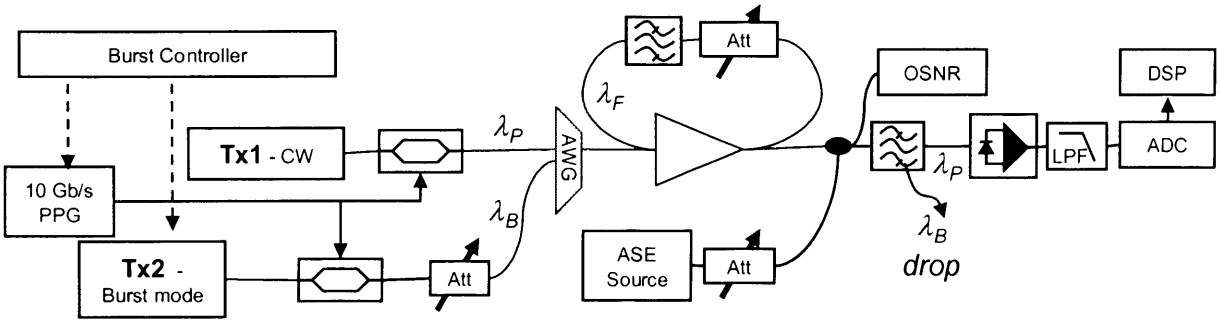

Figure 5-5 Experimental for characterization of single GC-EDFA

The EDFA was gain-clamped using a feedback loop based on a 2% tap at the EDFA output, an optical band-pass filter (0.4nm 3dB BW) to select the feedback wavelength, a variable optical attenuator (VOA) to control the feedback cavity losses (FCL) and a 3dB coupler to couple the feedback channel and signal together at the EDFA input. In practice, it would be desirable for the input coupler to have an unequal split ratio in order to minimize loss on the signal path. However, in order to obtain as wide a range of FCL for the subsequent measurements a 3dB coupler was chosen. The minimum FCL was 20dB determined by the insertion loss of the couplers and components in the feedback loop.

5.3.2 GC-EDFA performance as a function of feedback cavity loss

The FCL is the most important control parameter for network operation since its value will set the balance between maximizing the gain transient suppression and the gain seen by the propagating signals. Reducing the power in the feedback channel by increasing feedback cavity losses increases the amount of gain available to signal channels but limits the magnitude of input power variations for which transient suppression is achieved. Thus, there is an optimum point at which effective transient suppression is achieved whilst maintaining a large gain and hence, control of the optical feedback level is crucial in DONs. The aim of this section is to show that for a single amplifier an optimum value of FCL exists and that this value is dependent on both the magnitude of the input power fluctuations (no. of added/dropped bursts) and the feedback cavity wavelength.

The results described in this section are presented as follows. Firstly, measurements of channel powers, SSPF and RO and Q-factor/BER are presented as a function of FCL and the burst channel power. Since measurements were made at 3 feedback wavelengths, each result is given for a single feedback wavelength and then, where appropriate, the wavelength dependence of each effect is then addressed separately.

5.3.3 Channel power under steady state operation

Before considering the adding and dropping of bursts under dynamic conditions the relationship of channel powers was investigated under continuous operation

as a function of FCL to determine the range of FCL over which the feedback channel is able to lase. Figure 5-6(b), (c) and (d) shows the power of the feedback and probe channels as a function of FCL for burst channel powers equivalent to 1, 3, and 16 bursts. Figure 5-6 (a) shows the same plot with no burst channel present.

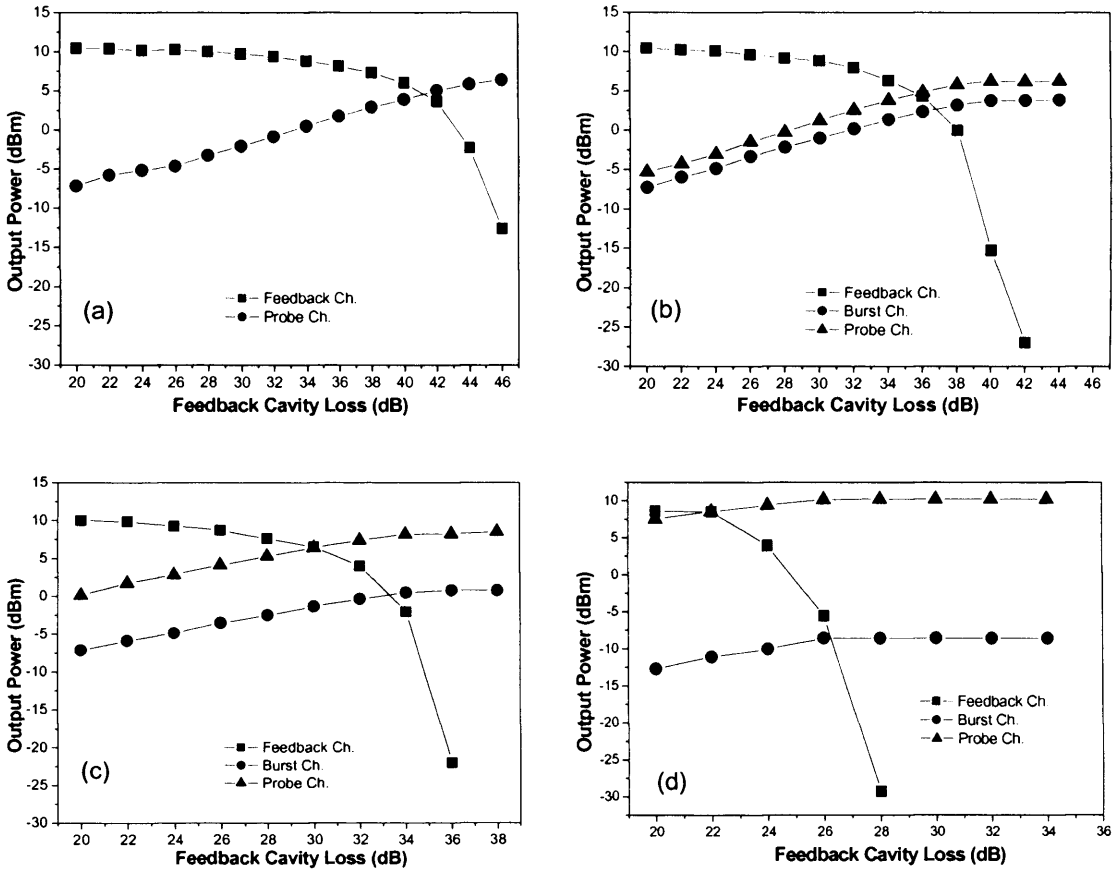

Figure 5-6 Channel powers at EDFA output for range of FCL and 1528nm feedback channel for (a) no burst channel and with burst channel powers equivalent to (b) 1, (c) 3 and (d) 16 bursts

Figure 5-6 shows how the gain of the individual channels changes under steady-state conditions. With only the signal channel present, Figure 5-6(a), lasing of the feedback channel occurs for FCL values of up to 46dB and the signal channel gain increases steadily with FCL before beginning to saturate. Figure 5-6(b) to Figure 5-6(d) show that the introduction and power increase of the burst channel shifts the range of cavity losses over which lasing is possible. Also evident from Figure 5-6(b), where burst and probe channels are equal at the EDFA input, is the difference in the intrinsic saturation power of burst and signal channel wavelengths and change of relative power between the 2 channels due to the strength of the feedback channel defined as gain tilt [Des02c]. For the channel powers investigated in Figure 5-6, the maximum

change in gain between the probe and burst channels was 0.9dB, equivalent to change in gain tilt of 0.12dB/nm, and following the trend outlined in [Ric98].

In order for the optical feedback to successfully clamp the gain of the input signals it is necessary for the feedback channel to lase (i.e. the feedback channel is present in the output spectrum) over the entire range of input power fluctuations. As shown in section 5.3 the feedback channel power is controlled by the FCL. Figure 5-7 shows a summary of the results shown in Figure 5-6 by considering a 20dB decay in the power of the feedback channel as the point where the feedback channel is no longer able to lase. Hence Figure 5-7 shows the maximum FCL required for gain clamping for each input burst channel power (or input power fluctuation in the dynamic case) and demonstrates how input power fluctuations are absorbed by the lasing feedback channel. As expected from equations (5.3) and (5.4), the relationship between the FCL and input power fluctuation is linear with the slope determined by the ratio of the intrinsic saturation power of the feedback and signal powers.

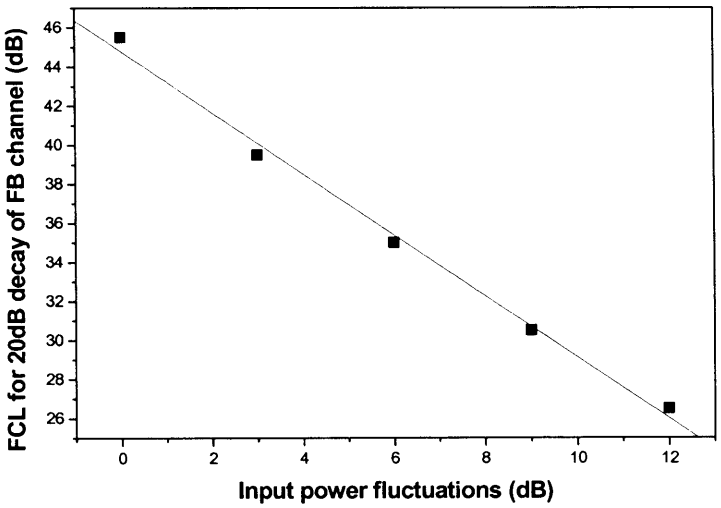

Figure 5-7 FCL required for lasing (20dB below max FC channel power) for different input power fluctuations

The clamping of the amplifier gain with optical feedback also has an effect on the amplifier noise figure [Des02c] and is also a function of the FCL as investigated in [Ric98]. The amplifier noise figure is defined as the ratio of input to output OSNR and increases at high gain compression as the signal gain reduces. Figure 5-8 shows the measured noise figure for the probe channel with an input power of -17dBm and 35dB OSNR and equivalent power burst

channel. The same noise figure increase was measured for all other burst channel powers.

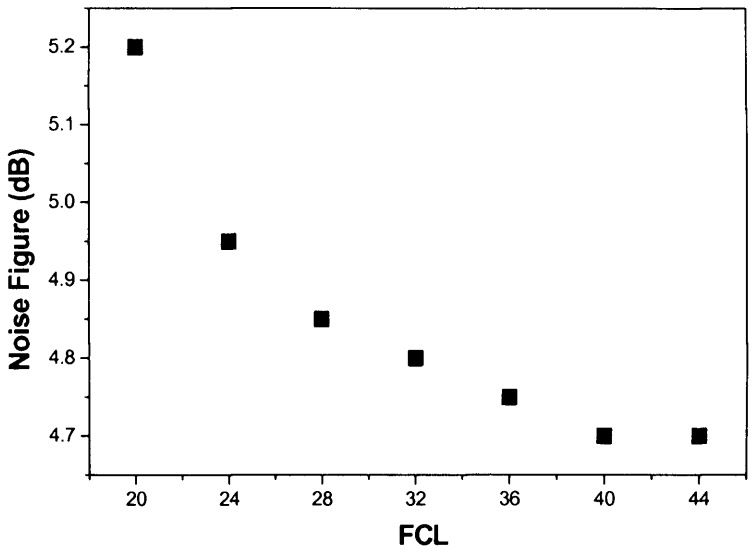

Figure 5-8 Noise figure of probe channel as a function of FCL with probe and burst channel input power -17dBm and 35dB OSNR

5.3.4 Measurements of transmission impairments

To identify how each of the degradation mechanisms affect the signal quality of the surviving channel with bursty input traffic, measurements of both SSPF and RO were made on the burst envelope as a function of FCL for each feedback wavelength and number of dropped channels using a low-speed digital oscilloscope and photodiode and the results are shown in Figure 5-9. Figure 5-9 shows the received waveforms for FCL ranging from 20-42dB. The feedback wavelength used was 1528nm and the burst channel power variation of 12dB was equivalent to 16 simultaneously added and dropped bursts. Over this range of FCL the corresponding gain compression at the probe channel wavelength of 1542.6nm ranged from 0 to 12dB when there is no burst present. With the burst present, the corresponding gain compression ranged from 0 to 3dB. The difference in signal channel gain between the clamped and unclamped condition is defined in [Luo97/98] as the gain compression. Since a realistic network would be dimensioned for the case of all channels present, the gain compression value with all channels present (up to 3dB) represents the maximum gain reduction for each FCL for a system of up to 17 channels.

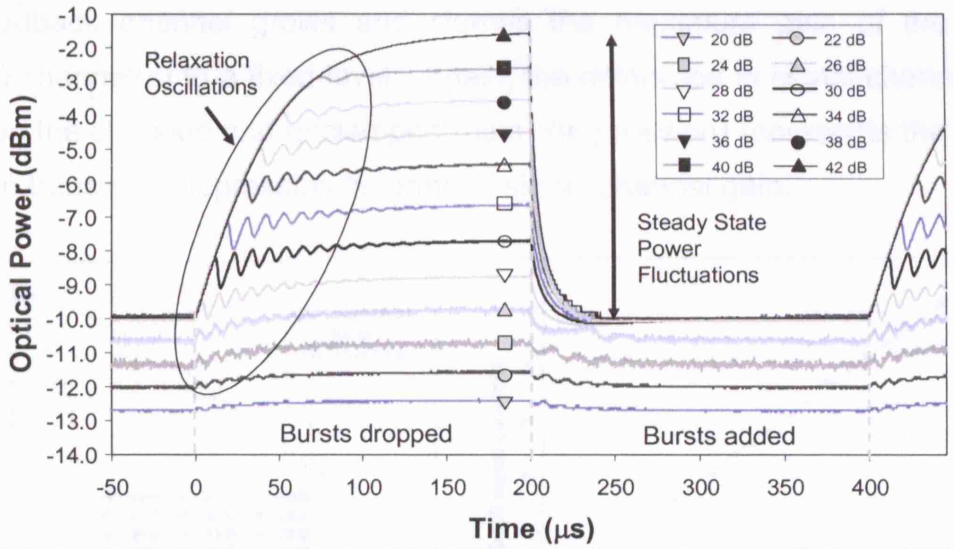

Figure 5-9 Steady state power fluctuations (SSPF) and relaxation oscillations (RO) on probe channel as a function of feedback cavity loss caused by burst add/drop (16 simultaneous bursts)

With the FCL minimized to the component insertion loss the feedback channel is able to maintain enough power to almost completely suppress both SSPF and RO on the probe channel caused by the simultaneous adding and dropping of 16 bursts. However, this is at the expense of reduced small-signal gain for the probe channel which suffers a gain compression of 3dB compared to unclamped operation with all channels present. As the power in the feedback channel reduces with increasing FCL, the small signal gain increases and both impairments begin to appear on the probe channel. When the FCL exceeds 26dB there is insufficient gain in the feedback channel for the lasing condition to be satisfied when the burst channel is present and this results in the sharp increase of SSPF. Further increase in FCL results in additional SSPF until the feedback channel is unable to lase for both burst add and drop events and the EDFA gain is no longer clamped. This occurs for a FCL of 42dB in Figure 3. Relaxation oscillations reach a peak in both amplitude and frequency between these last two stages.

Figure 5-9 also shows the trade-off between the gain transient suppression and the gain available to signal channels that is controlled by the FCL. This point is further illustrated by the amplifier gain curve for the probe channel for the same feedback wavelength and range of FCL shown in Figure 5-10. In agreement with Figure 5-9, a FCL of 42dB is enough to completely remove the feedback channel and equivalent to unclamped operation. At lower FCLs, the power of

the feedback channel grows and clamps the maximum gain of the probe (signal) channel(s) to a fixed level. Again, the difference in signal channel gain between the clamped and unclamped (gain compression) represents the cost of the gain transient suppression in terms of signal channel gain.

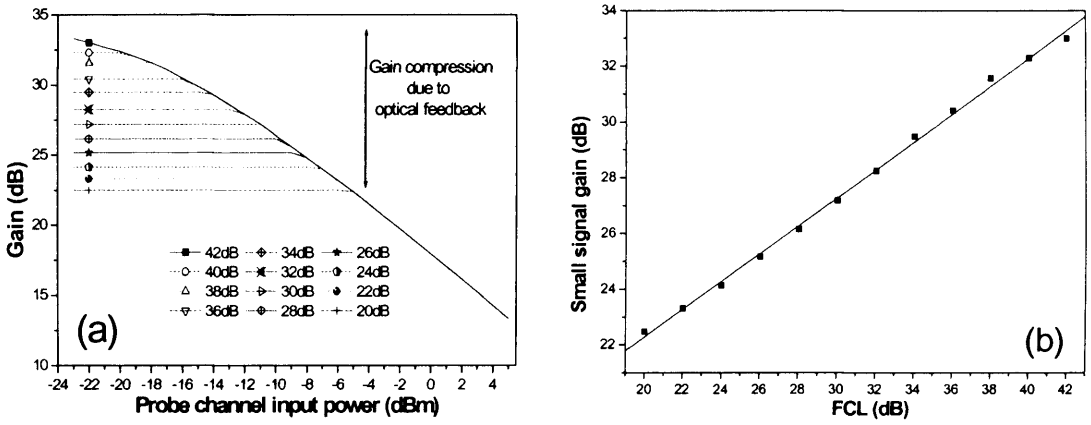

Figure 5-10 (a) Gain vs amplifier input power for range of FCL and (b) amplifier gain vs FCL or 1542.6nm probe channel with feedback channel at 1528nm

Figure 5-10(a) shows the essence of how optical feedback is able to suppress input power fluctuations by providing a fixed gain signal channels across a range of input powers. The graph also shows how the range of input power determined by the amount of optical feedback. Figure 5-10(b) is based on the data in Figure 5-10(a) and shows the small signal gain as a function of FCL. The slope of the line is approximately 0.5 resulting from the relative gain difference of the 1528nm feedback channel and the 1542.6nm probe channel measured to be approximately 3dB.

5.3.5 Relaxation oscillations

Figure 5-9 also shows that the magnitude of the gain transients caused by relaxation oscillations of the lasing cavity are small in comparison to the steady state power fluctuations that occur when there is insufficient power in the lasing channel to compensate for input power fluctuations. Despite this, as discussed in section 5.1.1, the characterization, reduction and elimination of RO has been the focus of widespread research [Chu02, Na99, Kim99, Liu99a, Liu99b, Luo98/97]. This is because all previous studies have assumed that the feedback cavity design operates in the high gain suppression regime such that SSPF caused by insufficient power in the lasing channel does not occur, and thus, RO become the significant source of amplitude fluctuations on surviving channels. As with the subsequent measurements of SSPF and bit error rate of

the surviving channels, here the study of RO is extended across a broader range of FCL and input power fluctuations. The aim of this is to show that the impact of RO on the signal quality of surviving channels can be dwarfed by the associated loss of gain when the FCL is decreased in order to optimally suppress the RO.

The measurement of both the magnitude and where possible the frequency of the RO is shown in Figure 5-11. The oscillation frequency was obtained by fitting a damped sinusoidal function to the received waveform. The RO frequency could only be determined when the amplitude was greater than the photodiode noise limited measurement error but the trend is evident in each case and shows frequencies of 50 to 100 KHz for all FCL in line with the published measurements of [Luo97a/b].

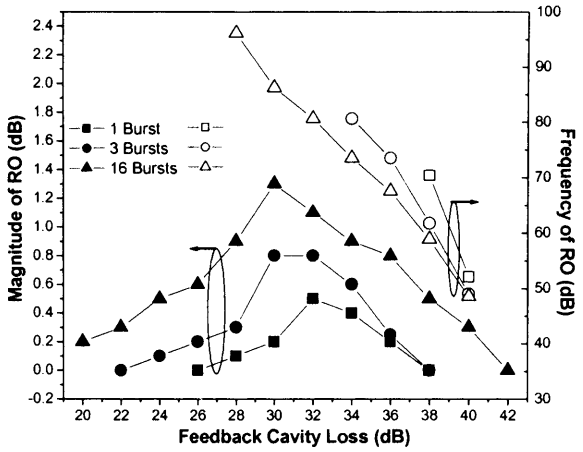

Figure 5-11 Magnitude and frequency of relaxation oscillations for 1, 4, and 16 dropped bursts for a feedback wavelength of 1528nm

The wavelength dependence of the RO is shown in Figure 5-12 which shows the magnitude of RO as a function of FCL for 16 added/dropped bursts for 3 different feedback wavelengths.

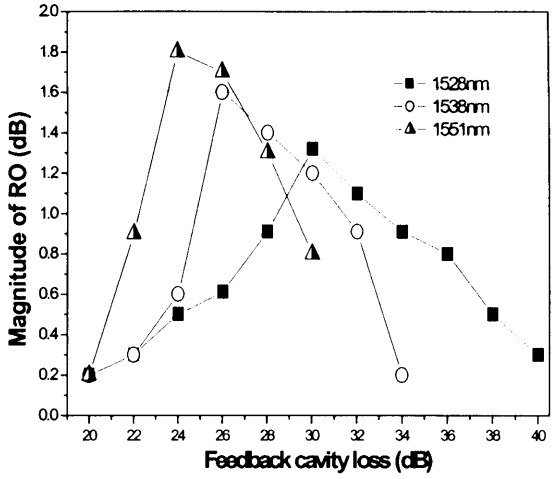

Figure 5-12 Amplitude of relaxation oscillations vs feedback channel attenuation for different feedback channel wavelengths after 16 bursts dropped

The dependence of the RO amplitude on feedback channel wavelength shown in Figure 5-12 can be explained by considering the ratio of differential gains of the surviving and feedback channels for changes in the average inversion [Luo98, Gil91]. This ratio becomes smaller for feedback wavelengths approaching the 1530nm gain peak, causing smaller power excursions that result in lower frequency oscillations. This was confirmed by theoretical results of gain recovery time in [Ric98] that showed that for a fixed cavity loss, the number of added/dropped channels causes variations in the rate of gain change on the surviving channel. Hence, adding/dropping of more channels causes larger initial transients and resulting oscillations.

5.3.6 Steady state power fluctuations

Across the range of FCL studied so far 2 separate effects contribute to power transients in surviving channels after input power fluctuations caused by burst add/drop. For high gain compression, where the lasing channel maintains enough power to continue lasing for all input power fluctuations steady-state power fluctuations occur due to spectral hole burning arising from inhomogeneity in the erbium gain spectrum. This effect and its wavelength dependence has been studied in detail [Ric98, Luo98/97] since it occurs in the region of operation envisaged for optically gain-clamped amplifiers. The effect has been shown to be affected by both the lasing feedback channel and signal channel wavelength and contributes to amplitude fluctuations on the same order of magnitude as the measured relaxation oscillations. The second cause of

SSPF is caused by insufficient power in the lasing channel to cover the range of input power fluctuations. In this case input power fluctuations in the region where the feedback channel is unable to lase affect the gain of surviving channels. This results in the sharp rise of SSPF shown in Figure 5-9 and as shown in subsequent section, occurs in the range of FCL where optimum BER performance is also obtained and is, therefore, important in determining the optimum feedback cavity design.

In this work, as with RO, the magnitude of the SSPFs were measured across the entire range of FCLs in order to provide a comparison with BER measurements and determine the impact of each effect on the signal quality of surviving channels in realistic burst switched network environment. Figure 5-13 shows the measured SSPF for burst channel powers equivalent to 1, 3 and 16 bursts for feedback wavelengths at 1528, 1538 and 1551nm.

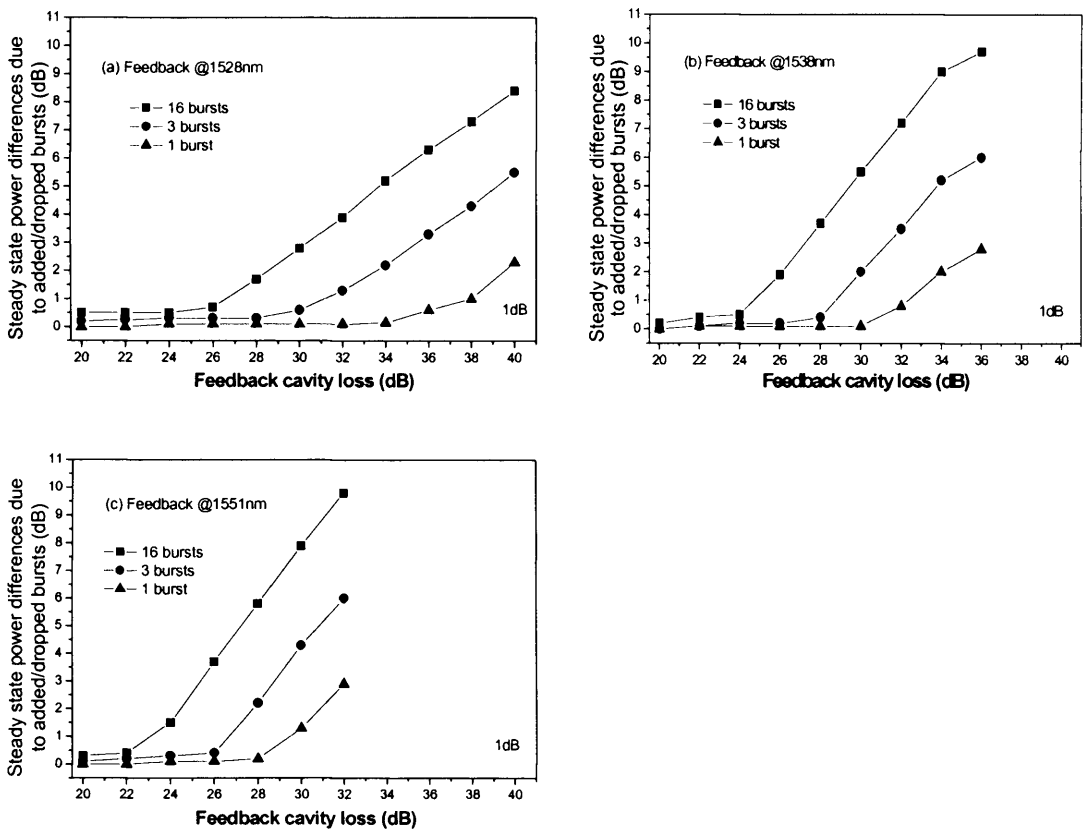

Figure 5-13 Steady state power fluctuations due to 1, 3 and 16 added/dropped bursts as function of feedback channel attenuation for feedback channels at (a) 1528nm, (b) 1538nm and (c) 1551nm

Each combination of burst channel power and feedback wavelength, plotted in Figure 5-13, shows the same trend. In each case, at lower FCLs there is a flat

region where the feedback channel contains enough power to suppress transients on the surviving to below the 1dB line shown. As the feedback channel power diminishes with higher FCL the point where the feedback channel is no longer able to lase with the burst channel on is reached and the SSPFs grow more rapidly until the lasing channel disappears completely. The FCL for which these events occur depends on both the magnitude of the input power fluctuations and the feedback wavelength.

Increasing the power of the burst channel means that more optical feedback (lower FCL) is required to prevent gain transients on the probe channel. For a 1528nm feedback channel, the FCL required for a 1dB SSPF for 1 added or dropped burst varies by 12dB compared to the 16 burst case. Since it is advantageous to reduce the amount of optical feedback to maximise the gain available to signal channels Figure 5-13 shows that knowledge of the possible input power fluctuations is necessary for optimal design of the feedback lasing cavity.

Changing the feedback wavelength changes the range of FCL values with which transient suppression is possible by changing the gain of the lasing cavity. Moving to regions of the EDFA gain spectrum with lower gain is equivalent to increasing the cavity losses. Hence, in terms of maximizing the gain available to signal channels the optimum feedback wavelength should be chosen in the gain peak around 1530nm. The question of whether or not the choice of wavelength has any impact on the signal quality of the surviving channel and the optimum FCL was assessed with BER/Q measurements described in section 5.3.7.

5.3.7 **Q-factor measurements**

Sections 5.3.3 and 5.3.4 show measurement and characterization of the primary impairments of propagating channels in optically gain-clamped EDFAs across a full range of gain clamping scenarios controlled by the loss of the lasing cavity, the lasing wavelength and the burst channel power. Previously, the presence of ROs and SSPF has been characterized as function of these parameters. In this section, the aim is to determine the optimum configuration by assessing the signal quality of surviving channels as a function of FCL and

feedback wavelength using the DC-coupled digital receiver with a fixed decision threshold.

Figure 5-14 shows the Q-factor penalty across the full range of FCLs for the probe channel when 4 bursts are simultaneously added and dropped at 200μs intervals and demonstrates how the trade-off between signal gain and transient suppression is reflected in probe channel signal quality. The optimum Q-factor performance occurs for a FCL of 30dB, and there is a Q-factor penalty for both the extreme low and high values of FCL. At low FCL, a Q-factor penalty compared to the optimum value is observed because of the reduced signal gain due to excess power in the feedback channel. At high FCL, Q-factor degradation occurs due to both SSPF and RO as the feedback channel possesses insufficient power to clamp the gain of the probe channel and it becomes susceptible to input power fluctuations from burst add and drop.

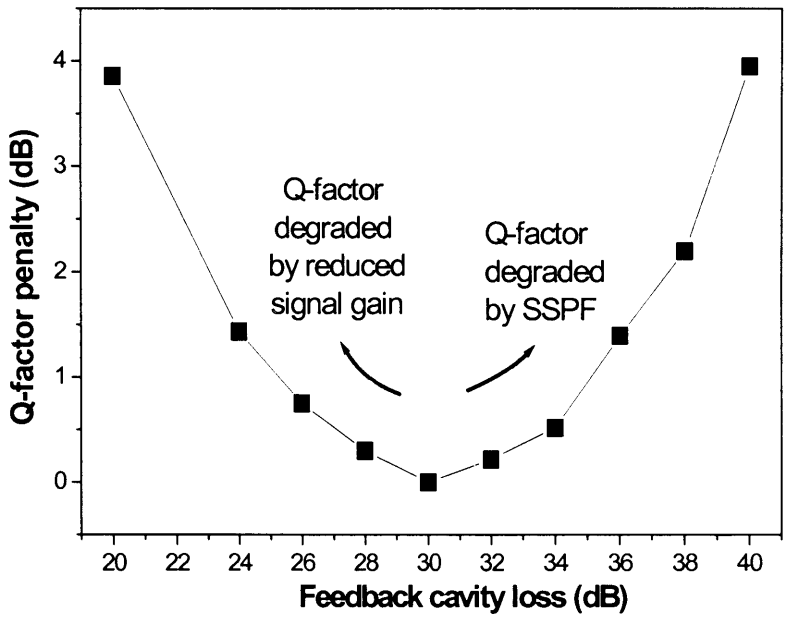

Figure 5-14 Q-factor of surviving channel as a function of FCL after 4 burst add/drop and 1528nm feedback wavelength

Figure 5-15 shows the measured correlation between the Q-factor-penalty and the SSPF when 1, 3 and 16 bursts were added and dropped with a feedback wavelength of 1528nm. In each case the required FCL for the minimum Q-factor penalty, at around 32, 30 and 26 dB for 1, 3 and 16 bursts respectively, corresponds to onset point for the SSPF. This highlights the trade-off between the amplifier gain and transient suppression. As the number of burst channels

added and dropped increases the required FCL for optimum performance reduces as more gain in the feedback channel is required to suppress the increasing input power fluctuations. It is also noted that the maximum amplitude of the relaxation oscillations occur for a FCL of 36, 34 and 30 dB for 1, 3 and 16 bursts respectively. In each case, this is in the region where the Q-factor penalty is increasing with FCL due to the onset of SSPF. The correlation between Q-factor penalty and SSPF in Figure 5-15 shows that SSPF is the dominant signal degradation mechanism when there is insufficient power in the lasing channel to compensate for input power fluctuations as predicted by the relative magnitude of the two effects shown in Figure 5-9.

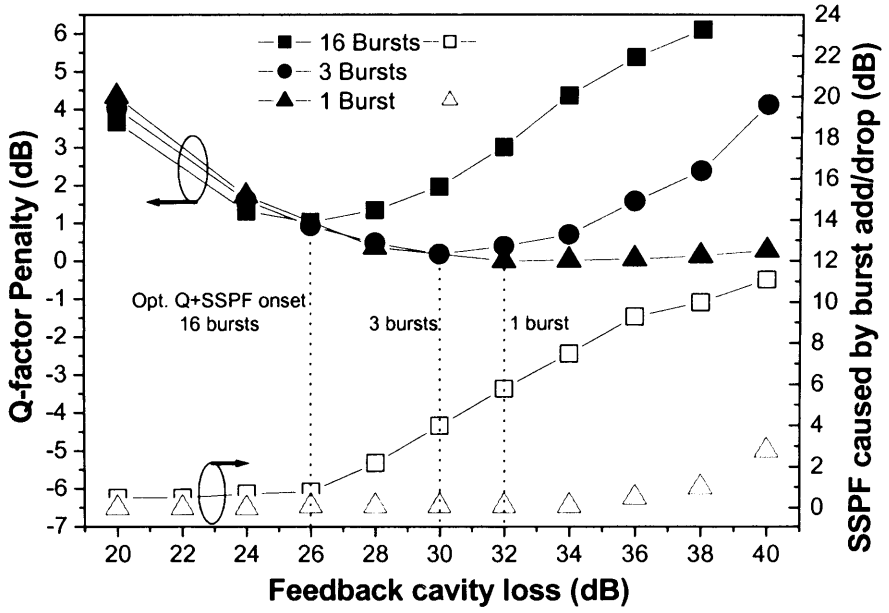

Figure 5-15 Q-factor and SSPF of surviving channel for 1, 3, and 16 burst add/drop for a feedback wavelength of 1528nm

Figure 5-15 shows that for specific input power fluctuation, an optimum FCL may be set to balance the penalty caused by reduced gain at low FCL and SSPF at high FCL. How the choice of feedback wavelength affects this optimum point was then investigated by determining this optimum point as a function of feedback wavelength. Previously in [Luo98], the wavelength dependence of RO and SSPF caused by SHB has been studied for GC-EDFAs with high gain compression. Here, how the choice of feedback wavelength affects the BER of propagating channels with the gain compression minimized by control of the FCL is investigated. For each feedback wavelength there was little or no variation in the absolute value of the optimum Q-factor for each burst channel

power but the FCL loss for which the optimum Q-factor value occurred was dependent on the feedback wavelength due to gain variations across the EDFA gain spectrum. The optimum FCL values with the highest measured Q-factor for 3 feedback wavelengths with decreasing gain (1528, 1538 and 1551nm) are shown for 1, 3 and 16 dropped bursts in Figure 5-16.

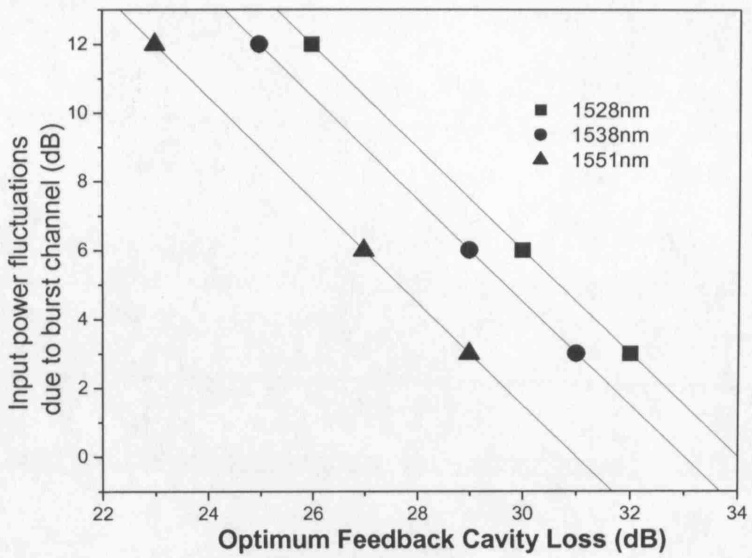

Figure 5-16 Optimum FCL for feedback wavelengths at 1528, 1538 and 1552nm for 1, 3 and 16 added/dropped bursts in a single GC-EDFA

Figure 5-16 shows that the optimum FCL also varies linearly with the magnitude of input power fluctuations, as predicted in equation (5.34). Figure 5-16 also shows that selecting a feedback wavelength on or close to the gain peak, in this case just outside the C-band at 1528nm, requires a lower FCL for optimum performance and, hence, requires less optical feedback allowing for more of the amplifier gain to be used for amplification of the propagating signal channels. Additionally, the use of the gain peak for the feedback wavelength, which should be filtered from the amplifier output, allows for the entire C-band and flat region of the gain spectrum to be used for burst signal amplification.

Once the feedback wavelength is selected the results in Figure 5-15 show that the optical feedback cavity design is then dependent on the maximum range of the input power fluctuations that must be accommodated. This power range is determined by network considerations such as the number of wavelengths in use or the router port count and in turn sets the optimum value of the most

important control parameter, the FCL, which should be minimized whilst ensuring the feedback channel is able to lase with all channels present.

5.4 Summary

This chapter investigated the available technology to realise burst-mode optical amplification in dynamic burst switched networks. Using a realistic network scenario, incorporating the burst transmitter and receiver described in the previous chapters, measurements of the BER of transmitted bursts were used to optimize GC-EDFA performance. The new approach revealed that the feedback cavity loss is the key control parameter in minimizing the BER of transmitted bursts and it is shown that the optimum feedback level is not in the region of high gain compression that was the focus of much of the previous work.

The results presented showed that optimum performance of an optically gain-clamped EDFA depends on a number of network-wide parameters. For a single GC-EDFA between 2 core routing nodes with burst add/drop, the results show that for a given feedback wavelength and input power fluctuation, there is an optimum feedback level for which the received signal quality, quantified by the Q-factor, is maximised. The amount of optical feedback required to suppress gain transients is dependent on the magnitude of the input power fluctuations. Hence, for a given GC-EDFA the required optical feedback is dependent on knowledge of the maximum input power fluctuations. This may be determined by the limits of physical network parameters such as the port count at a preceding router or number of wavelengths used in the network. The optimum choice of feedback wavelength occurs at the 1528nm gain peak as this minimizes the feedback power required to provide transient suppression whilst maximizing the gain for the signal channels. It also allows the entire C band and the flatter part of the EDFA spectrum to be used for signal channels.

The experimental results presented demonstrate the potential of a GC-EDFA to reduce the impact of gain transients on transmitted bursts caused by the adding and dropping of co-propagating bursts across and OBS network path. In particular, it is shown that the optimal design of a GC-EDFA requires consideration of both the number of wavelengths in use, maximum input power

variations and the network size. The performance and amount of gain clamping required for EDFAs cascaded over a network path is investigated in chapter 6 using an OBS network link test-bed.

5.5 References

Agr02 **Fibre-Optic communication systems third edition**
G.P.Agrawal, Pub. John Wiley and sons, 2002, ISBN 0-471-21571-6
(a) Quantisation Noise Pg8-10
(b) Optical Amplifiers Chap. 8 Pg 361-416

Ahn04 **All-optical gain-clamped erbium-doped fibre amplifier with improved noise figure and freedom from relaxation oscillation**
Joon Tae Ahn, Kyong Hon Kim. IEEE Photonics Technology Letters, Vol.16 (1), pp84-86, Jan. 2004

Ali94 **Performance of erbium-doped fibre amplifier cascades in WDM multiple access lightwave networks**
M.A.Ali, A.F.Elrefaie, R.E.Wagner, S.A.Ahmed. IEEE Photonics Technology Letters, Vol. 6 (9), pp 1142-1145, Sept. 1994

Bah03 **Investigation of relaxation-oscillation behaviour of erbium doped fibre lasers by semiclassical theory**
A.R.Bahrampu, P.Jamali, M.Mahjoej. Tech. Digest of IEEE/LEOS Conf. on Numerical Simulation of Semiconductor Optoelectronic Devices, pp WP10-WP0_6, Oct.14-16 2003

Bay04 **Optical burst switching: research and applications**
P.Bayvel, M.Düser. Tech. Digest of Optical Fibre Communication, Vol. 2, 23-27 Feb. 2004

Ber93 **Margin measurements in optical amplifier system**
N.S.Bergano, F.W.Kerfoot, C.R.Davidsion. IEEE Photonics Technology Letters, Vol. 5 (3), pp 304-306, March 1993

Bia03 **EDFA gain transients: experimental demonstration of a low cost electronic control**
A. Bianciotto, A. Carena, V. Ferrero, R. Gaudino. IEEE Photonics Technology Letters, Vol. 15 (10), pp 351 – 1353, Oct. 2003

Cho01 **High power gain-clamped EDFAs with flat gain**
H.B.Choi, B.S.Kim, D.Lee, S.B.Lee, S.J.Ahn. Tech. Digest of Optical Fibre Communication Conf. Vol. 3, pp WDD28-1 - WDD28-3, 2001

Chu02 **Reduction of relaxation oscillations in optical automatic gain-clamped EDFA using fast electronic feedforward**
H.S.Chung, J.C.Lee, M.J.Chu, J.H.Lee, H.H.Lee. Electronics Letters, Vol. 38 (5), pp 215-217

Chu97 **Performances of all-optical gain-clamped EDFAs with different feedback wavelengths for use in multiwavelength optical networks**
Joon Chung, Sang Yong Kim, Chang Joon Chae. Tech. Digest of Optical Fibre Communication, Conf., pp 22 – 24, 16-21 Feb 1997

Chu97 **Dynamic performance of the all-optical gain-controlled EDFA cascade in multi-wavelength add/drop networks**
Joon Chung, Sang Yong Kim. Tech. Digest of European Conference on Optical Communications Vol. 2, pp 139-142, 22-25 Sept. 1997

DeO05 **An all-optical gain controlled EDFA using a fast variable optical attenuator**
J.C.R.F.de Oliveira, J.B.Rosolem, R.F.da Silva, L.R.Monte, R.Arradi, A.A.Juriollo, A.C.Bordonalli. Tech. Digest of International Confeence on Microwave and Optoelectronics, pp 538-541, 25-28 July 2005

Des02 **Erbium-Doped Fibre Amplifiers**
E.Desurvire, Published 1994 John Wiley and Sons ISBN
(a) Erbium lifetime pg 16
(b) AOGC pg 468-480
(c) Gain tilt pg 203-207

Des91 **Dynamic gain compensation in saturated erbium-doped fibre amplifiers**
E.Desurvire, M.Zirngibl, H.M.Presby, D.DiGiovanni. IEEE Photonics Technology

Letters, Vol. 3 (5), pp 453-455, May 1991

Düs02 **Analysis of a dynamically wavelength-routed optical burst switched network architecture**
M. Düser, P. Bayvel, Journal of Lightwave Technology, vol. 20 (4), pp 574-586, April 2002

Enn05 **Power transients control in transparent WDM networks**
K.Ennser, T.Rogowski, G.Sacchi, M.Ibsen, O.Quargnolo, J.Shmulovich, G. Della Valle, S.Taccheo. Tech. Digest of International Conf. on Transparent Optical Networks, Vol.1, pp 309-314, 3-7 July 2005

Fal02 **Deployment of next generation WDM networks in Europe**
P.Falcao, E.Mannie-Corbisier, M.Moelants, P.Noel. Tech. Digest of Optical Fibre Communications Conf., paper TuH4, pp 45-46, 2002

Gil91 **Modeling erbium-doped fibre amplifiers**
C.R.Giles, E.Desurvire. Journal of Lightwave Technology, Vol. 9 (2) pp 271-283, Feb. 1991

Has02 **The characteristics of WDM systems with hybrid AGC EDFA In the photonics network**
M.Hashimoto, M.Yoshida, H.Tanaka. Tech. Digest of Optical Fibre Communication Conference, pp 517-518 17-22 Mar 2002

Ji05 **Low noise-figure gain-clamped L-band double-pass erbium-doped fibre ring lasing amplifier with an interleaver**
J.H.Ji, L.Zhan, L.L.Yi, C.C.Tang, Q.H.Ye, Y.X.Xia. Journal of Lightwave Technology, Vol. 23 (3) pp 1375 – 1379, March 2005

Kar00 **Gain stabilization in gain-clamped EDFA cascades fed by WDM burst-mode packet traffic**
M.Karasek, A.Bononi, L.A.Rusch, M.Menif. Journal of Lightwave Technology, Vol. 18, (3), pp 308-313, March 2000

Kar01 **Output power excursions in a cascade of EDFAs fed by multichannel burst-mode packet traffic: experimentation and modeling**
M.Karasek, M.Menif, L.A.Rusch, Journal of Lightwave Technology, Vol. 19 (7), pp 933-940, July 2001

Kim99 **Cavity loss measurement from the relaxation oscillation frequency**
Bong Kyu Kim, Young Min Jhon, Myong-Wook Kim, Jyung Chan Lee, Sang Kuk Kim, Sang Sam Choi. Tech. Digest of The Pacific Rim Conference on Lasers and Electro-Optics, Vol. 2, pp 481-482, 30 Aug. 3 -Sept. 1999

Kro98 **Gain variations in optically gain-clamped erbium doped fibre amplifiers**
M.F.Krol, Y.Liu, J.J.Watkins, M.J.Dailey. Tech. Digest of European Conference on Optical communication, Vol.1, pp 43 – 44, 20-24 Sept. 1998

Lie06 **Transmission and interactions of WDM burst signals in cascaded EDFAs**
A.Lieu, T.Cechan, T.Naito, Optical Fibre Communication Conf., 5-10 March 2006

Liu99a **Transient gain control in EDFA's by dual-cavity optical automatic gain control**
Y.Liu, M.F.Krol, IEEE Photonics Technology Letters, Vol.1, pp 1381-1383, Nov.1999

Liu99b **Optical gain control of EDFAs using time-dependent feedback loop**
Y.Liu. Electronics Letters Vol. 35, (16), pp 1371-1373, 5 Aug. 1999

Luo97 **Performance degradation of all-optical gain-clamped EDFAs due to relaxation-oscillations and spectral-hole burning in amplified WDM networks**
G.Luo, J.L.Zyskind, Y.Sun, A.K.Srivastava, J.W.Sulhoff, C.Wolf, M.A.Ali. IEEE Photonics Technology Letters, Vol. 9 (10), Oct. 1997 pp:1346 – 1348

Luo98 **Experimental and theoretical analysis of relaxation-oscillations and spectral hole burning effects in all-optical gain-clamped EDFA's for WDM networks**
G.Luo, J.L.Zyskind, J.A.Nagel, M.A.Ali. Journal of Lightwave Technology, Vol. 16 (4) pp 527-533, April 1998

Muk00 **WDM optical communication networks: progress and challenges**
B. Mukherjee. IEEE Journal of Selected Areas in Communications, Vol.18 (10), pp 1810-1824, 2000

Na99 **Rate equation model for gain-clamped erbium-doped fibre amplifiers**
K.W.Na, W.J.Lee, J.Y.Choi, W.W.Yoon, K.K.Lee. Electronics Letters, Vol. 35 (8), pp 663-664, 15 April 1999

Oik07 **Ultra fast Automatic gain control Amplifier with unique and simple transient control**
Y. Oikawa, N. Shiga, M, Shiga, Y. Horiuchi, H. Nagaeda. Tech. Digest of European Conference on Optical Communications, pp017, 2007

Oka05 **Optical burst amplification using EDFA with fast feedback control**
K.Okamura, E.Otani, T.Yoshikawa, T.Uchino, M.Fukushima, N.Kagi. Tech. Digest of Optical Fibre Communication Conf. Vol. 2, 6-11 March 2005

Poo04 **ASE spectral slice gain-clamping of EDFA**
P.Poopalan, H.Haoken, N.Tamchek, S.W.Harun, T.Subramaniam, H.B.Ahmad. IEEE Photonics Technology Letters, Vol. 16 (12), Pp 2604-2606, Dec. 2004

Ric97 **A theoretical investigation of dynamic all-optical automatic gain control in multichannel EDFA's and EDFA cascades**
D.H.Richards, J.L.Jackel, M.A.Ali. IEEE Selected Topics in Quantum Electronics, Vol. 3 (4), pp 1027-1036, Aug. 1997

Ric98(a) **A theoretical investigation of dynamic automatic gain control in multi-channel EDFA cascades**
D.H.Richards, M.A.Ali, J.L.Jackel. Tech. Digest of European Conf. on Optical Communications, Vol. 3 (4), pp1027-1036, Aug. 1997

Ric98b **Multichannel EDFA chain control: a comparison of two all-optical approaches**
D.H.Richards, J.L.Jackel, M.A.Ali. Tech. Digest of IEEE Photonics Technology Letters, Vol. 10 (1), pp 156-158, Jan. 1998

Sal90 **Modeling of gain in erbium-doped fibre amplifiers**
A,A,M.Saleh, R.M.Jopson, J.D.Evankow, J.Aspell. Tech. Digest of IEEE Photonics Technology Letters, Vol. 2 (10), pp 714 – 717, Oct. 1990

Shi00 **Fibre optic communication systems in Japan**
H. Shinohara. Tech. Digest of 13th Annual Meeting of IEEE Lasers and Electro-Optics Society, vol.1,pp 3-4, Puerto Rico, November 2000

Siv04 **Optical fibre networks and systems in India**
K.N. Sivarajan. Tech. Digest of Optical Fibre Communication Conf., Vol.1, pp 705-706, 2004

Son99 **An analytical formulation of the transient response of gain-clamped EDFA's**
K.Song, R.D.T.Lauder. IEEE Photonics Technology Letters. Vol. 11 (11), pp 1378-1380, Nov. 1999

Sri97 **EDFA transient response to channel loss in WDM transmission system**
A.K.Srivastava, Y.,Sun, J.L.Zyskind, J.W.Sulhoff. IEEE Photonics Technology Letters, Vol. 9 (3), pp 386 – 388, March 1997

Tho05 **Dynamic gain-fluctuations in gain-clamped EDFA in packet switched optical transmissions**
D.H.Thomas, J.P.Von der Weld. Tech. Digest of Optical Fibre Communication Conf., Vol. 4, 6-11 March 2005

Tho05 **Impairments of EDFA dynamic gain-fluctuations in packet-switched WDM optical transmissions**
D.H.Thomas, J.P.Von der Weld. IEEE Photonics Technology Letters, Vol. 17 (5), pp 1097-1099, May 2005

Tra05 **EDFA transient control based on envelope detection for optical burst switched networks**
A.V.Tran, C.Chang-Joon, R.S.Tucker, W.Yang Jing. IEEE Photonics Technology Letters, Vol. 17 (1), pp 226-228, Jan. 2005

Wei99 **The evolution of China's optical fibre networks**
L.P.Wei, Y.Chen, G.G.Wong. Bell Labs Technical Journal Vol. 4 (1), pp 125-144, Jan-Mar 1999

Xia00 **A novel compensating light injection configuration for gain-clamped EDFA's**
Yanhong Xiao, Xiaoming Liu, Jiangde Peng. IEEE Photonics Technology Letters, Vol. 12 (7), pp 789 – 791 July 2000

Yi04 **Improvement of gain and noise figure in double-pass L-band EDFA by incorporating a fibre Bragg grating**
L.L.Yi, L.Zhan, J.H.Ji, Q.H.Ye, Y.Z.Xia. IEEE Photonics Technology Letters, Vol. 16 (4), pp 1005-1007, April 2004

Yoo00 **Link-control gain clamping for a cascaded EDFAs link using differential ASE monitor**
Hosung Yoon, Jaehyoung Park, Seong Joon Ahn, Namkyoo Park. IEEE Photonics Technology Letters, Vol. 12 (10), pp 1334-1336, Oct. 2000

Yoo99 **Reference level free multichannel gain equalization and transient gain suppression of EDFA with differential ASE power monitoring**
Hosung Yoon, Sungho Bae, Seong Joon Ahn, Namkyoo Park. IEEE Photonics Technology Letters, Vol.11 (3), pp 316-318, March 1999

Yos06 **WDM burst-mode signal amplification by cascaded EDFAs with transient control**
T.Yoshikawa, K.Okamura, E.Otani, T.Okaniwa, T.Uchino, M.Fukushima, N.Kagi. Optics Express, Vol. 14 (11), pp.4650-4655 (2006)

Zho00 **Influence of power transients from gain-clamped EDFA on optical receiver BER performance**
L.Zhou, S.Wang, Q.Yu, Z.Jiang, H.Wang, C.Fan. Tech. Digest of International Conf. on Communication Technology, Vol.1, pp 406-409, 21-25 Aug.2000

Zir91 **Dynamic gain compensation in saturated erbium-doped fiber amplifiers**
E.Desurvire, M.Zirngibl, H.M.Presby, D.DiGiovanni, IEEE Photonics Technology Letters, Vol. 3 (5), pp 453 – 455, May 1991

Chapter 6 End-to-end transmission and sub-system inter-operability

6.1 Construction of an end-to-end OBS link model

The previous chapters have described and investigated the operation of the 3 key sub-systems of a dynamic optically burst-switched network. In this chapter, the investigation shifts to the interoperability of these subsystems and the construction of an end-to-end OBS link test bed. The test-bed combines each of the sub-systems described thus far together with a recirculating transmission loop and wavelength routers to make a realistic OBS link model. A schematic of the test-bed is shown in Figure 6-1.

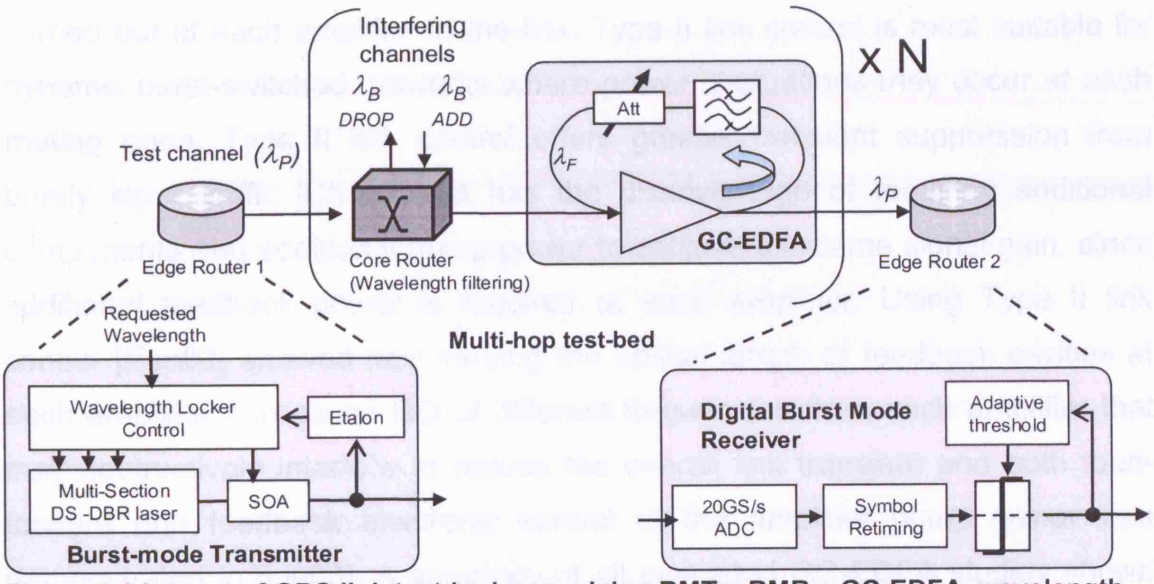

Figure 6-1 Layout of OBS link test-bed comprising BMTx, BMRx, GC-EDFA, wavelength router and recircualting transmission loop

After a review of the impact of wavelength routers on network performance, the investigation extends the work described in the previous chapter to the case of cascaded routers and amplifiers. The OBS link test-bed is used to study the effect of transients accumulated across a varying number wavelength-routing nodes linked by amplified fibre spans where, in contrast to existing work, bursts are added and dropped at each node. Finally, the role of the additional receiver processing in reducing the amount of optical feedback and the inherent BER penalty of burst-mode EDFA operation is also studied.

6.1.1 Review of EDFA cascades with bursty input traffic

The role of EDFAs in future optical networks has also been investigated in cascaded operation as found in network links. As described by Richards et al

[Ric97, Ric98a,b], there exist two approaches for EDFA link control for dynamic traffic. The first approach, referred to as Type I link control, is to apply optical feedback or electronic control schemes only at the first amplifier in the chain and allow the lasing signal to propagate through the amplifier chain to remove input power fluctuations in subsequent amplifiers. This approach has been demonstrated to reduce bursty traffic induced gain transients by up to 3 times compared to unclamped operation [Kar01, Kar00a] for optical feedback link control. Similar results for type 1 link control were shown for an electronic feedback loop controlling the power of a dummy laser [Bia03].

Not so widely studied is Type II link control where transient suppression is carried out at each amplifier in the link. Type II link control is most suitable for dynamic burst-switched networks where power fluctuations may occur at each routing node. Type II link control offers greater transient suppression from bursty input traffic [Chu97] but has the disadvantage of requiring additional components and additional pump power to achieve the same signal gain, since additional feedback power is required at each amplifier. Using Type II link control [Enn03] showed how varying the optical length of feedback cavities at each amplifier can cause RO of different frequencies from each amplifier that may destructively interfere to reduce the overall link transient and both feed-forward and feedback electronic control of the amplifier pump power was demonstrated in [Lie06]. A summary of all cascaded GC-EDFA studies shown in Table 6-1.

Table 6-1 Summary of gain transient control schemes for cascaded operation

Ref	Control Scheme (Type I/II)	Burst length	Cascade length *	Max.no channels add/drop	Max trans amp	Comment
Chu97	Opt .FB - (II)	100ms	4*80km	7 out of 8	0.6dB	
Yoo00	Opt. FB – (I)	5ms	3*VOA	7 out of 8	0.15dB	1st EDFA in link of 3
Ric98a	Opt. FB - (I&II)	n/a	6*VOA	4 out of 8	0.8dB	Simulation only
Kar01	Opt .FB - (I)	2ms	5*20dB	3 out of 4	2dB	
Enn05	Opt. FB - (II)	500μs	4 *VOA	15 out of 16	1.5dB	Ring Network, add /drop@each node
Sri97b	Elec FF - (I)	500μs	8*80km	7 out of 8	1dB	2.5Gb/s. El. Circuit response 4μs
Yos06	Elec. FF+FB - (II)	1.6ms	45*80km	3 out of 4	5.1dB	
Lie06	Elec. FF+FB-(II)	7ms		20 out of 21	0.8dB	

* Where applicable fibre length is given, otherwise the attenuation used to replicate span loss is given where provided.

With the exception of [Enn05] which describes a link control technique for ring networks using propagating ASE in the EDFA gain peak to suppress transients, all the studies of cascaded EDFA operation have assumed that the input power fluctuations only occur at the beginning of the link. However, this situation only applies to the case of point-to-point transmission across multiple spans and is not a realistic link model in a dynamic burst switched network. To build a realistic experimental link model of a dynamic burst switched network it is necessary to allow the adding and dropping of bursts at each node as is the case with the experimental investigations described here. A recirculating transmission loop was used to set up as an OBS link model where transmitted bursts traverse a number of amplified fibre spans linking wavelength routing network nodes with bursts added and dropped at each hop. This test-bed was then used to investigate how the conclusions obtained for a single amplifier extend to cascaded operation and whether impairments caused by burst add/drop accumulate across an entire OBS link where bursts are asynchronously added and dropped at each network node.

Once in place, the OBS test-bed and measurement system was then used to characterize the performance of the adaptive threshold burst-mode receiver described in chapter 4. By comparing the amount of optical feedback required in a cascade of wavelength routers and fibre spans amplified with GC-EDFAs, the performance of the receiver is compared to a standard fixed threshold optical receiver.

6.1.2 Review of wavelength routers

This section describes the available technologies envisaged for use in wavelength routers in the network core and required in the OBS link test-bed. Although additional complexity such as wavelength converters may well be incorporated in router design here only simple optical routers suitable for use as a transparent, bufferless core network router of a DON are considered. In general, optical routers fall into 2 categories with different implications for the network design. The first of these is wavelength routers where the output port of from any specified input port is determined by the carrier wavelength. These are generally diffraction based devices and require the network to have complete knowledge of the chosen path before laser tuning and therefore suitable for an

acknowledgement based network such as WR-OBS. The second category is active routers where the router must be configured in advance of burst arrival. For a Type II OBS network this could require an additional control packet to be sent after a received resource is requested and the reconfiguration time then becomes a factor determining achievable network performance.

Arrayed waveguide gratings (AWGs) were initially developed for optical multiplexing/ de-multiplexing [Smi96a,b]. The basic principle behind the AWG is the spatial separation of the constructive interference fringes of wavelength components dispersed and collected in slab waveguides and transmitted between each through a series of waveguides with a fixed path length difference. In general, AWGs are 1XN devices but may be combined with a star coupler [Dra91, Dra89] to construct NxN routing devices [Ber00].

Free space optics has the potential for higher port count optical routers and multiplexers due to better performance in terms of coherent cross talk that has been shown to limit the size and performance of AWG based devices [Kam00] since any stray light caused from material aberration is distributed in a solid angle rather than the 2 dimensional confinement in AWGs based on planar light-wave circuits. Concave grating based devices are particularly attractive since a single optical element can provide both dispersing and focusing functionality [Chu99].

The routing functionality of both devices is very similar with the output port of any given input put being determined by the input wavelength as shown in Figure 6-2.

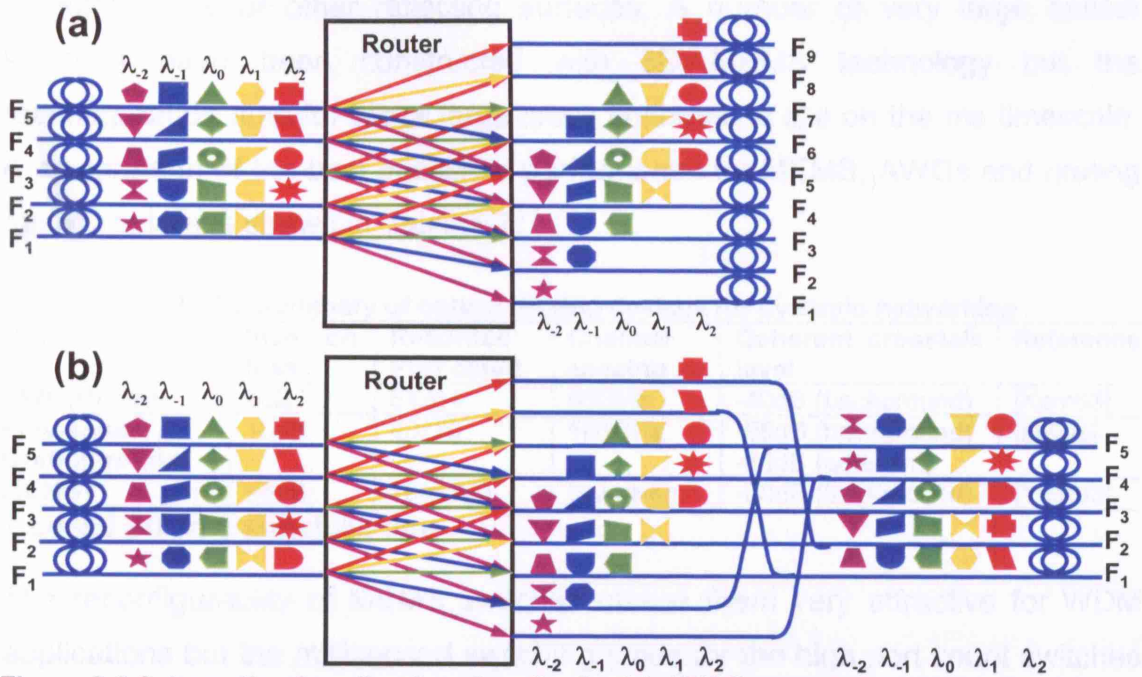

Figure 6-2 Schematic of routing functionality for (a) AWG/free-space wavelength router with 5 input fibre and (b)) AWG/free-space wavelength router with 5 input fibre and cyclic routing functionality

As shown in Figure 6-2(b), the output ports may be coupled together to achieve cyclic routing at the expense of 3dB higher loss. A routing table for such a device employing cyclic routing is shown in Figure 6-3.

		Input Port					
	Port	1	2	3	4	5	N
	1	λ_1	λ_2	λ_3	λ_4	λ_5	λ_1
	2	λ_2	λ_3	λ_4	λ_5	λ_6	λ_2
Output Port	3	λ_3	λ_4	λ_5	λ_6	λ_7	λ_3
	4	λ_4	λ_5	λ_6	λ_7	λ_8	λ_4
	5	λ_5	λ_6	λ_7	λ_8	λ_9	λ_5
	N	λ_N	λ_1	λ_2	λ_3	λ_4	λ_{N-1}

Figure 6-3 Routing table for the NxN port UCLF AWG with N wavelengths

The alternative to passive optical routers is the reconfigurable optical switch. The key performance characteristic as regards optical networking is the time needed to configure the switch for the incoming burst or packet. In general the requirement of OBS networks is for the reconfiguration time of the core nodes to be of the same order of magnitude as the switching time of the tunable lasers in the edge router. This requirement generally rules out thermal tuned devices [Hen03] and the requirement for high port count devices rules out electro-optics effects [Pap03]. The most feasible technology is the micro-electrical-mechanical system (MEMS). MEMS use tiny reflective surfaces to redirect light beams to

outgoing ports or other reflecting surfaces. A number of very large optical switches have been constructed with 3D MEMS technology but the reconfiguration time for these large cross connects is still on the ms timescale. A comparison of the best published performance for MEMS, AWGs and grating based routers is shown in Table 6-2.

Table 6-2 Summary of optical routing devices for dynamic networking

Device	Insertion loss	Recorded Port count	Channel spacing	Coherent crosstalk level	Reference
AWG(UCLF)	6dB	64x64	50GHz	-40dB (background)	[Kam03]
Free-space Grating router	10dB	40x70	100GHz	-55dB (background) -38dB (adjacent)	[Mik03]
MEMS†	<4dB	100x100	Not given	-60dB (background)	[Yam03]

† based on 3ms switching time

The reconfigurabilty of MEMS switches makes them very attractive for WDM applications but the millisecond switching times for the high port count switches make them less practical for optical burst switching architectures such as WR-OBS without an order of magnitude improvement in switching time. Free-space routers have shown superior crosstalk performance to AWGs but have yet to be presented as robustly packaged with available prototype versions suffering from high insertion loss and vibration sensitivity. For this reason, all subsequent routing measurements described in this chapter use AWGs to perform the wavelength routing functionality.

6.2 Interoperability of burst transmitter and wavelength routers

The interaction of the tunable lasers and wavelength routers has been studied previously in chapter 2 and 3 but is reviewed here to invite a re-interpretation of these results as a study of the interaction between these 2 edge and core network sub-systems. In chapter 2, the transmission stability requirement of tunable lasers experiencing thermal drift after a high tuning current switch was investigated by measuring the Q-factor penalty of bursts passing through narrow wavelength routers. These measurements, performed with 2 AWGs of different channel spacing and free-space grating router, revealed stability targets that were then used as inputs to the design of the burst transmitter in chapter 3. Additionally, these stability targets were verified at the end of chapter 3 with a repeat of these Q-factor measurements comparing locked and unlocked bursts transmitted through the same routers. These results show that the requirements of each sub-system are set both by the characteristics of the

other key sub-systems and the demands of the entire network. This is explored further in the subsequent sections which investigate the interaction of the key sub-systems using a dynamic optical network test-bed.

6.3 Performance of GC-EDFA in cascaded network operation

The results in chapter 5 showed that for a single GC-EDFA there exists an optimum FCL for which the signal quality of the transmitted burst experiencing gain transients caused by add/drop is maximized and the optimal cavity loss value may be simply determined once the maximum number of dropped bursts and feedback wavelength is known. In this section, the study is extended to a cascade of amplifiers as would be found in a DON link. Previous studies have shown that the suppression of transients across an entire link, comprising multiple amplifiers, is possible by gain clamping only the 1st amplifier in the cascade, if the feedback channel is allowed to propagate through the rest of the link with the signals [Lie06, Kar01 Yoo00, Ric98, Chu97, Sri97]. However, this only applies to the case where channels are added and dropped at the start of the link only as would be the case in point to point WDM link. For dynamic networks, such as WR-OBS, bursts may be added and dropped asynchronously at all stages across the link. To model this situation a recirculating transmission loop was used to set up an end-to-end OBS link model where bursts may be asynchronously added and dropped at each node as shown schematically in Figure 6-4.

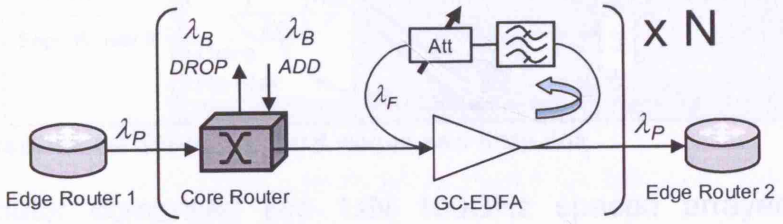

Figure 6-4 OBS link representation

6.3.1 Experimental set up for network operation

The experimental implementation was based on a single core node with recirculating transmission to emulate a network consisting of multiple core routers as shown in Figure 6-5. The transmission link comprised 40km of standard single mode fibre (SMF) fully compensated by an additional 7km of dispersion compensating fibre (DCF) with a total span loss of 13.5dB. Two ingress edge routers housed the tunable wavelength transmitters and were used to generate a probe channel (λ_P) and the add/drop burst channel (λ_B). As

with the single amplifier measurements the probe channel was generated from Tx_1 at λ_P (1542.6nm) and was modulated with a 10Gbit/s NRZ PRBS of length 2^{15}-1. This was transmitted through a specified number of router, GC-EDFA and fibre transmission stages in bursts of 250μs, set to fill one complete loop span, before being received by the digital burst-mode receiver (Rx_A) in the egress edge router. The add/drop channel (λ_B) from Tx_2 was an ON-OFF burst signal at a wavelength of 1535nm (λ_B). To ensure a complete cycle fitted within the transmitted burst length the switching period was reduced to 200μs with a 50% duty cycle. The optical power of the burst add/drop channel was set to exceed the probe channel by 9dB to emulate the effect of 8 co-propagating bursts of equal power being added or dropped simultaneously. The span EDFA was optically gain-clamped, as in the single amplifier measurement, with a minimum cavity loss of 20dB and variable attenuator to control the FCL. As shown in chapter 5, the best GC-EDFA performance is obtained by exploiting the natural EDFA gain peak, hence a feedback wavelength, λ_F, of 1528nm was used for all measurements.

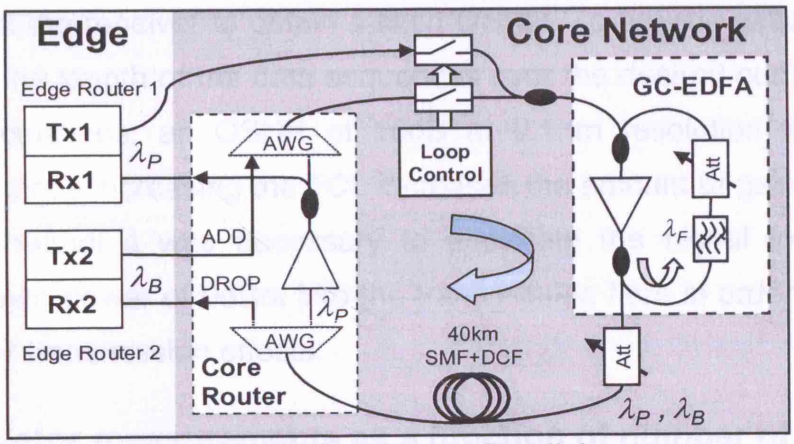

Figure 6-5 Experimental Set-up for OBS nodes and fibre link

The core router comprised two 1xN 100GHz spaced arrayed waveguide gratings (AWGs). These performed the wavelength routing functionality, dropping the bursts at λ_B whilst forwarding the bursts at λ_P on to the next core node before adding new bursts at λ_B. To compensate for the additional loop and router component losses the core router contained an additional EDFA. This was placed between the drop and add ports, where only the low power (-21dBm) continuous probe channel at wavelength λ_P propagated, and was operated in the linear regime. Operating in the linear regime ensured that there

was no gain saturation which might suppress the power fluctuations on the probe channel and removes the requirement for gain-clamping in this amplifier.

The impact of the FCL on an end-to-end network path comprising multiple GC-EDFAs with asynchronous adding and dropping of bursts at intermediate nodes was studied by monitoring the probe channel, as the number of traversed nodes was increased. This enabled the measurement of the Q-factor penalty arising from gain transients accumulated from multiple asynchronous burst add/drop events to find the optimal FCL for varying numbers of node hops.

To count the number of received errors the digital receiver was again operated with a fixed decision-threshold. The optimum receiver threshold was set to minimize the BER of the entire 250μs loop output sequence. As with the single amplifier measurements, to allow for error counting over the limited sequence length and to remove the degradations arising from accumulated amplified spontaneous emission (ASE) as the number of hops is increased; optical noise was added at the receiver to obtain a fixed OSNR. To provide acceptable error statistics for the length of the data sequences over the desired number of noise adding recirculations, an OSNR of 16dB at 0.1nm resolution was chosen. Additionally, since increasing the FCL increases the amount of gain available to the signal channel it was necessary to attenuate the signal to maintain a constant launch power of 0dBm into the transmission fibre in order to eliminate any nonlinear transmission effects.

6.3.2 Q-factor measurements as a function of number of hops

The Q-factor penalty, measured as a function of FCL for 1, 5, 15, and 25 hops is shown in Figure 6-6(a) and exhibits a number of important features. Firstly, a Q-factor penalty occurs as the number of hops is increased even with the FCL minimized at 20dB, where the best transient suppression performance is obtained. This arises from small power excursions caused by the adding and dropping of bursts at each node which are not completely suppressed, and accumulate as the number of hops increases.

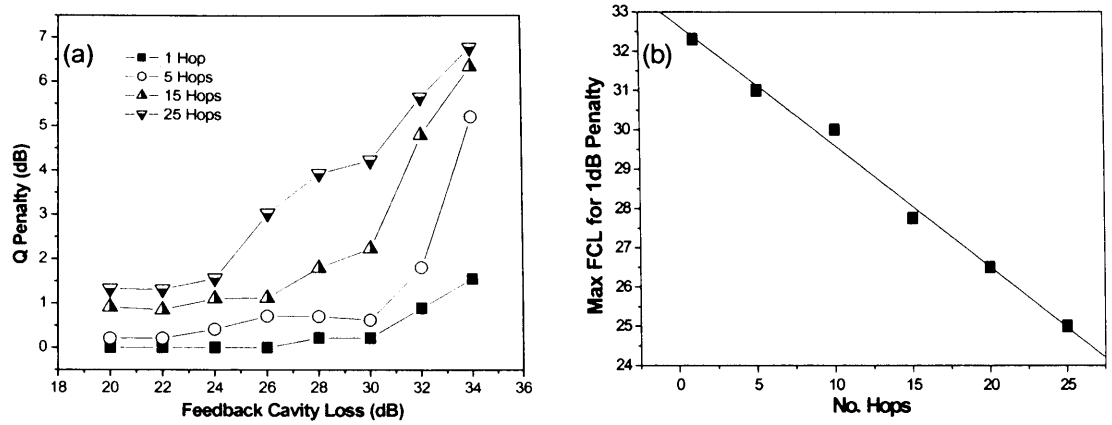

Figure 6-6 (a) Impact of FCL on Q-factor penalty with increasing number of hops and (b) required FCL for 1dB penalty with increasing number of hops for fixed and adaptive receiver thresholds

To understand the shape of the curves shown in Figure 6-6(a) it is useful to note that the Q-factor penalty due to the reduced amplitude seen at low FCL for a single amplifier in chapter 5 (Figure 5-15), is not seen for the cascaded results. This is an artefact of the requirement to maintain a constant fibre launch power for all measurements so that the increased gain due to reduced FCL was compensated for by an additional loss at each node hop. Comparison of the results shown in Figure 6-6(a) with Figure 5-15 shows that the increase in the noise figure as the FCL decreases does not cause a significant Q-factor penalty. Had the Q-factor penalty seen in Figure 5-15 at low FCL been the result of the increase in noise figure, then this trend should also be present in Figure 6-6(a). However no discernible Q-factor penalty is seen at low FCL and thus, the penalty seen in Figure 5-15 can be attributed to the reduced gain which is compensated for in the results shown in Figure 6-6(a).

Consistent with Figure 5-15, what can be observed in Figure 6-6(a) is the penalty caused by insufficient gain transient suppression as the feedback cavity losses increase which leads to SSPF. In Figure 5-15 the onset of this penalty can be used to determine the FCL required to maximize the measured Q-factor. In Figure 6-6(a), it can be seen that the point at which this penalty starts to increase sharply due to insufficient gain transient suppression shifts to lower values of FCL as the number of hops traversed increases. This occurs because there is insufficient power in the feedback channel to compensate for the increasing amplitude fluctuations, which reach over 15dB for unclamped operation and 25 hops, as more nodes are traversed. Thus, the transients

caused by adding and dropping of bursts sharing link amplifiers accumulate with each hop and a lower FCL is required to achieve optimum performance as the network size grows. To quantify the amount of additional feedback required as a function of the network size, Figure 6-6(b) shows the maximum required FCL for a 1dB penalty for each value of the number of hops considered. This metric was chosen to identify the point before the penalty caused by insufficient gain-clamping begins to significantly degrade the BER whilst maximizing the gain of the transit signals. As described in section 5.4, this may be considered to be the FCL value for optimum performance. By considering a 1dB penalty compared to the highest measured Q-factor for each number of hops, Figure 6-6(b) shows that the optimum FCL increases by approximately 0.3dB per hop. This figure can be used to estimate the amount of additional feedback power required as a function of network size and used to provide a comparison with measurements using the adaptive threshold receiver described in the next section.

6.4 Performance of an adaptive threshold receiver in GC-EDFA cascades

In this section, the interoperability of the GC-EDFA used for burst amplification and the adaptive threshold digital burst-mode receiver is investigated. The Q-factor/BER measurements presented in chapter 5 and in section 6.3 were based on a standard optical receiver configuration where the decision-circuit sets a fixed decision-threshold determined from the entire received sequence. For such a receiver the gain transients induced in surviving channels due to fluctuating amplifier input powers is particularly damaging since they result in changes to both the received signal amplitude and can add a DC offset or base line wander (BLW) error that can lead to BER degradation. Such impairments may be easily dealt with for a continuous signal by AC coupling of the received waveform but as described in Chapter 4, this presents additional issues in burst-switched networks since the capacitive time constant limits the response of the threshold setting causing large BLW swings when receiving signals with burst-to-burst power variations. The aim of this section is to investigate how the adaptive threshold and power equalization algorithms implemented by the digital receiver described in chapter 4 may also be used to correct for gain transients caused by burst-mode transmission through EDF amplified transmission links.

The use of the adaptive threshold receiver was investigated, both for a single amplifier and in cascaded operation, using identical set-ups to those described for the fixed threshold receiver. Indeed, since the receiver design requires storage of the digital waveform to implement the threshold and equalization algorithm it was possible to process the same received data sequences as those described in previous sections to provide a direct comparison of the performance between fixed and adaptive threshold receivers. Hence, the receiver hardware used for these measurements was identical to that described for the fixed threshold receiver, using a 10GHz DC–Coupled photodiode and 20Gs/S ADC.

The adaptive threshold and equalizer was implemented in 2 stages. Firstly, as for the fixed threshold measurements, the symbol timing information was recovered from the asynchronous input samples and the signal was interpolated to produce a correctly sampled signal. Then, unlike the fixed receiver measurements, the receiver processing described in chapter 4 was employed. Firstly, the BLW filter and feedback equalizer were used to correct for amplitude fluctuations and BLW before the adaptive threshold decision-circuit was used to recover the data. A schematic of the adaptive receiver is shown in Figure 6-7. As in Chapter 4, the BLW loop filter was averaged over 256 samples.

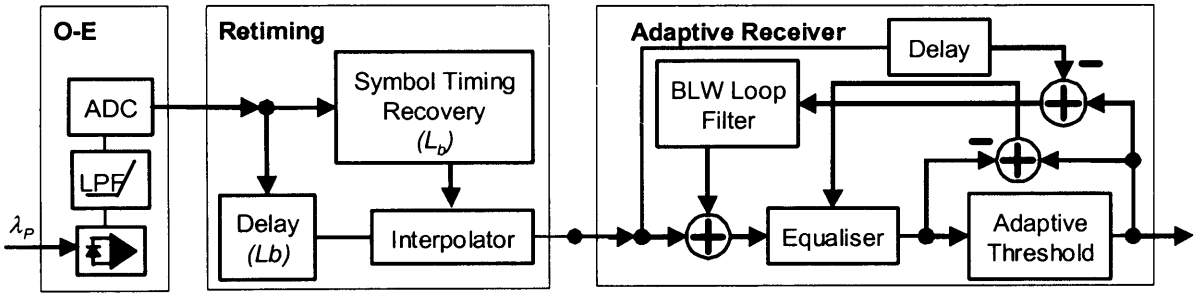

Figure 6-7 Adaptive receiver used to correct BLW from burst-mode operation of EDFA

6.4.1 Performance of adaptive receiver with single GC-EDFA

To investigate the performance of the adaptive threshold receiver with a single amplifier the experimental set-up described in section 5.3 of the previous chapter and shown in Figure 5-5 was used. Figure 6-8 shows the measured Q-factor penalty of the received bursts as a function of FCL for 1, 3 and 16 dropped bursts at a feedback wavelength of 1528nm for the adaptive receiver.

Included for comparison are the equivalent results for a fixed threshold receiver presented in Figure 5-15.

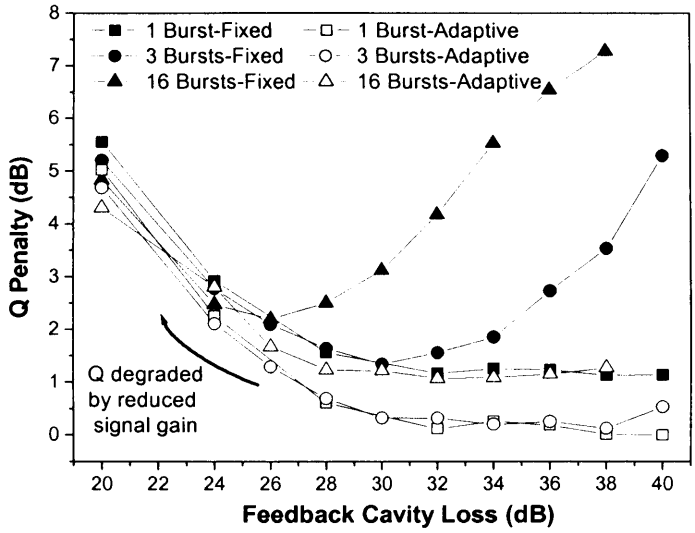

Figure 6-8 Comparison of fixed and adaptive threshold receivers for a single GC-EDFA

Figure 6-8 shows that implementing the adaptive threshold and equalizer at the receiver provides an improvement in signal quality and a reduced BER. The improvement is particularly significant at FCL values above those shown to be optimum for the fixed threshold receiver. In this region, as also shown in Figure 5-15, SSPF caused by insufficient optical feedback are prevalent. For a burst channel power equivalent to a single added or dropped burst, use of the adaptive threshold improves the measured Q-factor of the received burst by approximately 1dB, reducing to 0.5 dB at the minimum FCL where the feedback channel dominates the input power spectrum. As the burst channel power increases, the Q-factor degradation seen at low FCLs caused by reduced signal gain is still evident, with a 0.5dB offset. In contrast to the fixed threshold receiver, there is almost no Q-factor degradation caused by SSPF induced by insufficient optical gain clamping at higher burst channel powers. At low FCL, there is sufficient feedback channel power to suppress gain transients and the penalty observed with the fixed receiver is caused by reduced signal gain as explained in section 5.3. Hence, there is little improvement gained by the adaptive receiver in this region.

This is a significant result since it implies that, assuming induced gain transients do not exceed damage power thresholds of downstream amplifiers,

performance monitoring equipment or the receiver photodiode, an adaptive threshold receiver could negate any requirement for optical feedback to suppress them and allow for maximum gain for signal channels. Whether the adaptive receiver is able to recover data affected by accumulated gain transients from multiple hops across a dynamic burst switched network was then investigated in a network context using the OBS link test bed.

6.4.2 Adaptive receiver and impairments from cascaded GC-EDFAs

The performance of an adaptive threshold receiver in cascaded operation was investigated using the OBS link test-bed described in section 6.3 and shown in Figure 6-5. The performance of the adaptive threshold receiver compared to the fixed threshold receiver for 1, 5, 15 and 25 hops is shown in Figure 6-9 which shows the measured Q-factor penalty as a function of the FCL.

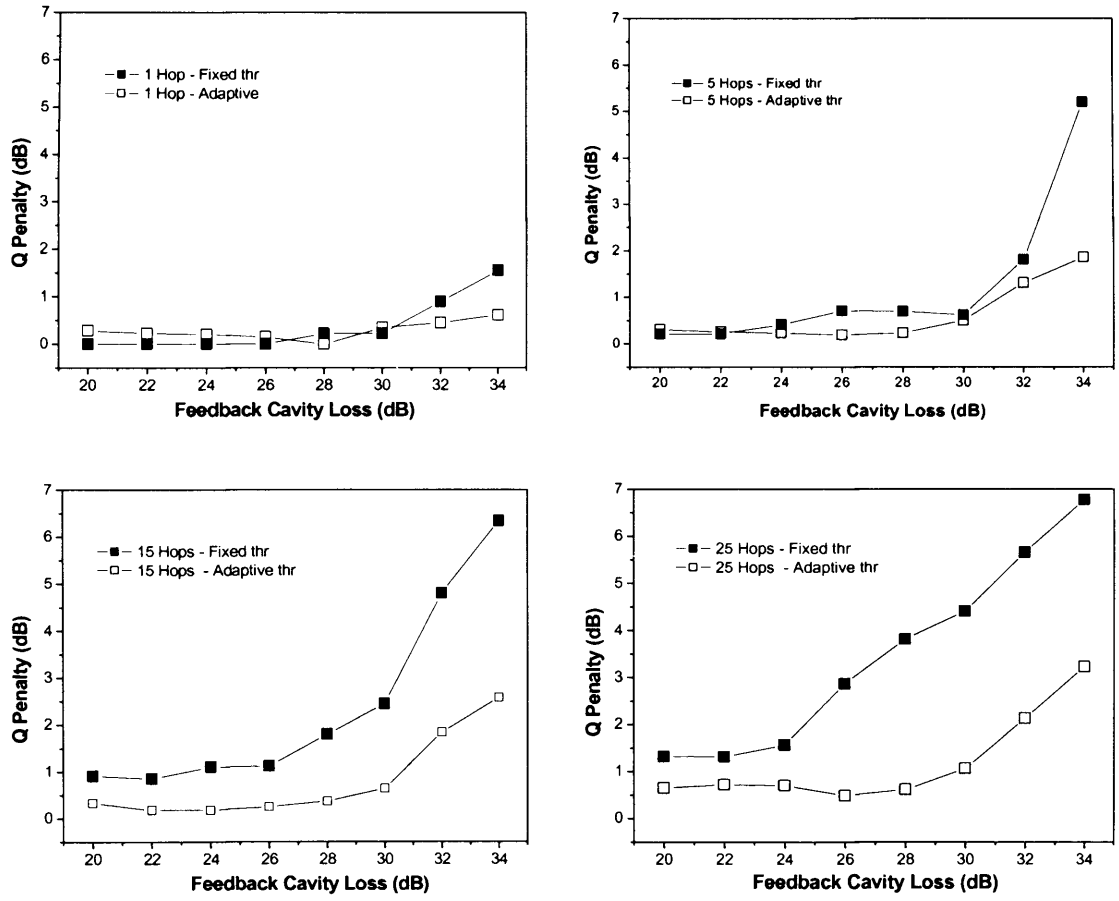

Figure 6-9 Comparing Q-factor penalty of fixed and adaptive threshold receivers as a function of FCL for 1, 5, 15 and 25 hops

For the adaptive threshold receiver the Q-factor penalty is again dependent on the number of traversed nodes and FCL but with the Q-factor penalty reduced by up to 4.5dB compared to the case of the fixed threshold receiver. At the

lowest FCL value, where maximum feedback power is coupled back to the amplifier input, there is almost no discernible Q-factor penalty for a network size of up to 15 hops and a small penalty of 0.5dB for a 25 hop network compared to 1.5dB for the fixed threshold receiver. For less than 5 hops, the maximum penalty for the adaptive receiver was less than 1dB showing that for most networks [Bar97], use of an adaptive threshold could remove all gain clamping requirements.

To further compare the performance of the receivers the maximum required FCL to ensure a Q-factor penalty of less than 1dB was used as a performance metric. Figure 6-10 shows this metric as a function of the number of hops for both the fixed and adaptive receivers. This metric was chosen to identify the point before the penalty caused by insufficient gain clamping begins to significantly degrade the BER whilst maximizing the gain of the throughput signals. This may be considered to be the required FCL value for optimum performance.

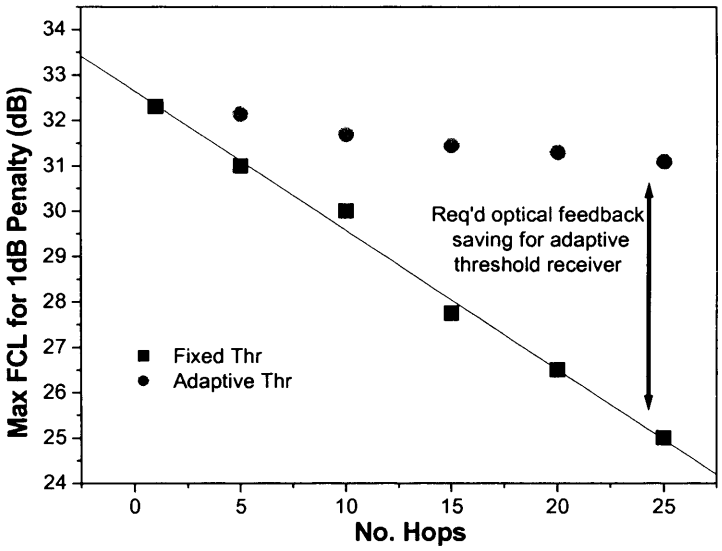

Figure 6-10 Required FCL for 1dB penalty with increasing number of hops for both fixed and adaptive receiver thresholds

Figure 6-10 shows that the adaptive threshold receiver/equalizer requires less feedback compared to the fixed threshold receiver. This arises from the adaptive receiver's ability to respond quickly to the amplitude and offset fluctuations and adapt the decision-threshold appropriately. For the fixed threshold receiver, the optimal FCL increases by 0.3dB per hop compared to 0.05dB for the adaptive receiver. Hence, the use of such an adaptive threshold

receiver not only allows for a larger amplifier spacing (as the amplifiers can tolerate a higher FCL, and hence, provide more gain) but also allow for more hops, increasing the total network size. For the system described here and a network of 25 nodes, use of the adaptive threshold receiver provides additional signal gain of over 3.1dB per amplifier due to the reduced optical feedback requirement. Assuming 0.2dB/km fibre loss, this would allow an additional 15.5km of fibre per span, an increase of 39%.

Figure 6-9 and Figure 6-10 shows that for transmitted bursts impaired by EDFA gain transients caused by asynchronous burst add/drop, the adaptive receiver both reduces the BER of data extracted from the same digital waveform and reduces the transmission penalty. Additionally, the results show that it may be possible to correct or compensate for gain transients arising from burst-mode operation of multiple cascaded EDFAs at the end of the link and not at each amplification stage. Such a scheme would not only maximise the signal gain and transmission distance across burst networks, but provide a universal correction of DC offsets acquired in transmission, prior to reception. Figure 6-9 shows that there is still a distance (no. hops) dependent penalty when no optical feedback is used to clamp the gain with the maximum measured Q-factor penalty of 3dB for 25 hops. However, for networks comprising fewer than 5 nodes or with smaller input fluctuations to the 8 bursts used here the adaptive receiver offers the potential to remove the optical feedback requirement entirely. This would allow the network operator to minimize the number of amplifiers or pump power requirement at the cost of a tolerable Q-factor penalty assuming that the maximum power transients are not sufficient to damage downstream components. Since, only a single burst channel power was used in these measurements, application of quantitative limits to this conclusion requires additional measurements.

6.5 Summary

This chapter described the construction of an end-to-end OBS test-bed incorporating the burst transmitter and receiver with a recirculating transmission loop enabling multiple routing and amplification stages. The test bed, which enabled adding and dropping of bursts at each node allowed the study of accumulated gain transients from cascaded in a realistic DON environment for

the first time. The test bed also allowed the study of interoperability of the key sub-systems described in this thesis and the results show that the performance requirements of each are inter-dependant and determined by the demands of the entire network.

The performance of cascaded amplifiers with burst add/drop at each node was studied in section 6.3 and showed that the impairments caused by insufficient optical gain clamping accumulate across a network path. In an experimental model of an OBS network path comprising multiple routing and amplification stages with bursts asynchronously added and dropped at each hop, it was shown that additional optical feedback is required to compensate for the accumulated gain transients in propagating bursts. The accumulation of power transients shifted the optimal FCL by 0.3dB for each node hop. Hence, the feedback cavity design can limit the number of hops a burst is able to traverse for a fixed performance metric and hence limit the network size.

Section 6.4 investigated the use of the digital, burst capable receiver described in chapter 4 and showed that this can significantly reduce the Q-factor penalty of transmitted bursts due to burst add/drop using the same experimental OBS model described in section 6.3. This was achieved through digital signal processing to compensate for BLW and amplitude fluctuations induced by accumulated gain transients. Compared to a fixed threshold receiver the use of an adaptive threshold allowed a 6-fold reduction in the amount of additional optical feedback required at each amplifier. This improvement allows for both an increase in the span length, by 39% for a 25 node network, and the maximum number of hops for the same feedback cavity loss and Q-factor penalty. Hence, for a network employing optically gain-clamped EDFAs, an adaptive burst-mode receiver is able to maximise achievable network size and for some network configurations may be able to remove the requirement for gain clamping all together.

6.6 References

Bar97 **Wavelength requirements in arbitrarily connected wavelength-routed optical networks**
S.Baroni, P.Bayvel. IEEE Journal of Lightwave Technology, Vol.2, pp 242-251, 1997

Ber00 **Large N x N waveguide grating routers**
P.Bernasconi, C.Doerr, C.Dragone, M.Cappuzzo, E.Laskowski, A.Paunescu.

Journal of Lightwave Technology, Vol. 18 (7), pp 985 –991, July 2000

Bia03 **EDFA gain transients: experimental demonstration of a low cost electronic control**
A. Bianciotto, A. Carena, V. Ferrero, R. Gaudino, IEEE Photonics Technology Letters, Vol. 15, (10), pp 351 – 1353, Oct. 2003

Chu97 **Performances of all-optical gain-clamped EDFAs with different feedback wavelengths for use in multiwavelength optical networks**
Joon Chung, Sang Yong Kim, Chang Joon Chae. Tech. Digest of Optical Fibre Communication, Conf., pp 22-24, 16-21 Feb

Chu97 **Dynamic performance of the all-optical gain-controlled EDFA cascade in multi-wavelength add/drop networks**
Joon Chung, Sang Yong Kim. Tech. Digest of European Conference on Optical Communications Vol. 2, pp139-142, 22-25 Sept. 1997

Chu99 **Design of free space WDM router based on holographic concave grating**
E.G.Churin, P.Bayvel. IEEE Photonics, Technology Letters, Vol. 11 (2), pp 221-223, Feb.1999

Dra89 **Efficient N×N star couplers using Fourier optics**
C.Dragone. Journal of Lightwave Technology, Vol. 7 (3), pp 479 – 489, March 1989

Dra91 **Integrated optics N×N multiplexer on silicon**
C.Dragone, C.A.Edwards, R.C.Kistler, IEEE Photonics Technology Letters, Vol. 3 (10), pp 896 - 899, Oct. 1991

Enn03 **Investigation of transient response in cascaded gain-clamped erbium-doped fibre amplifiers**
K.Ennser, S.Taccheo. Electronics Letters Vol. 39 (24), pp 1716-1717, 27 Nov. 2003

Enn05 **Power transients control in transparent WDM networks**
K.Ennser, T.Rogowski, G.Sacchi, M.Ibsen, O.Quargnolo, J.Shmulovich, G. Della Valle, S.Taccheo. Tech. Digest of International Conf. on Transparent Optical Networks, Vol.1, pp 309-314, 3-7 July 2005

Hen03 **Laser-activated optical bubble switch element**
S.Hengstler, J.J.Uebbing, P.McGuire.Tech. Digest of IEEE/LEOS International Conference on Optical MEMS, pp 117-118, 18-21 Aug. 2003

Kam03 **64X64-channel uniform-loss and cyclic-frequency arrayed-waveguide grating router module**
S.Kamei, M.Ishii, M.Itoh, I.Shibata, Y.Inoue, T.Kitagawa. Electronics Letters, Vol. 39 (1), pp 83 – 84, 9 Jan. 2003

Kar00 **Gain stabilization in gain-clamped EDFA cascades fed by WDM burst-mode packet traffic**
M.Karasek, A.Bononi, L.A.Rusch, M.Menif. Journal of Lightwave Technology, Vol. 18, (3), pp 308-313, March 2000

Kar01 **Output power excursions in a cascade of EDFAs fed by multichannel burst-mode packet traffic: experimentation and modeling**
M.Karasek, M.Menif, L.A.Rusch. Journal of Lightwave Technology, Vol. 19 (7), pp 933-940, July 2001

Lie06 **Transmission and interactions of WDM burst signals in cascaded EDFAs**
A.Lieu, T.Cechan, T.Naito. Tech. Digest of Optical Fibre Communication Conf., 5-10 March 2006

Mik03 **Ultra low coherent crosstalk, high-port count free-space wavelength router**
V.Mikhailov, C.R.Doerr, P.Bayvel, Tech. Digest of Optical Fibre Communications Conference, pp 257-258, 23-27 March 2003

Pap03 **Optical switching: switch fabrics, techniques, and architectures**
G.I.Papadimitriou, C.Papazoglou, A.S.Pomportsis. Journal of Lightwave Technology, Vol. 21 (2), pp 384-405, Feb. 2003

Ric97 **A theoretical investigation of dynamic all-optical automatic gain control in multichannel EDFA's and EDFA cascades**
D.H.Richards, J.L.Jackel, M.A.Ali. IEEE Selected Topics in Quantum Electronics, Vol. 3 (4), pp 1027-1036, Aug. 1997

Ric98(a) **A theoretical investigation of dynamic automatic gain control in multi-channel EDFA cascades**
D.H.Richards, M.A.Ali, J.L.Jackel. Tech. Digest of European Conference on Optical Communications, Vol. 3 (4), pp1027-1036, Aug. 1997

Ric98b **Multichannel EDFA chain control: a comparison of two all-optical approaches**
D.H.Richards, J.L.Jackel, M.A.Ali. IEEE Photonics Technology Letters, Vol. 10

(1), pp 156-158, Jan. 1998

Smi96a **PHASAR-based WDM-devices: Principles, design and applications**
M.K.Smit, C.Van Dam. IEEE Journal of Selected Topics in Quantum Electronics, Vol. 2 (2) , pp 236 – 250, June 1996

Smi96b **Fundamentals and applications of phasar demultiplexers**
M.K.Smit. Tech. Digest of European Conference on Optical Communication, Vol. 1, 30 Sept.-4 Oct. 2001

Sri97 **Fast-link control protection of surviving channels in multiwavelength optical networks**
A.K.Srivastava, J.L.Zyskind, Y.Sun, J.Ellson, G.Newsome, R.W.Tkach, A.R. Chraplyvy, J.W.Sulhoff, T.A.Strasser, C.Wolf, J.R.Pedrazzani. IEEE Photonics Technology Letters, Vol. 9 (12), pp 1667-1669, Dec. 1997

Yam03 **A three-dimensional MEMS optical switching module having 100 input and 100 output ports**
T.Yamamoto, J.Yamaguchi, N.Takeuchi, A.Shimizu, E.Higurashi, R.Sawada, Y.Uenishi. IEEE Photonics Technology Letters, Vol. 15 (10) pp 1360-1362, Oct. 2003

Yoo00 **Link-control gain clamping for a cascaded EDFAs link using differential ASE monitor**
Hosung Yoon, Jaehyoung Park, Seong Joon Ahn, Namkyoo Park. IEEE Photonics Technology Letters, Vol. 12 (10), pp 1334-1336, Oct. 2000

Yos06 **WDM burst-mode signal amplification by cascaded EDFAs with transient control**
T.Yoshikawa, K.Okamura, E.Otani, T.Okaniwa, T.Uchino, M.Fukushima, N.Kagi. Optics Express, Vol. 14 (11), pp.4650-4655 (2006)

Chapter 7 Summary and future work

This thesis describes the investigation of technologies and subsystems required for physical layer implementation of a range of dynamic optical networks (DONs) with a specific focus on Type II optical-burst-switching (OBS) architectures where burst lengths are in the millisecond regime. The key subsystems were identified and examined both individually and in terms of their interoperability to identify the feasibility of existing studies and where appropriate new sub-systems and control systems were developed. Finally, the key sub-systems were combined with recirculating transmission loop to form an OBS link test-bed.

The successful implementation of a DON, depends on a number of complex sub-systems operating over a range of timescales determined both by the demands of the network architecture, the inter-play between sub-systems and the physics of the underlying technology. This is particularly relevant for Type II OBS networks with burst lengths in the millisecond range. At the transmitter, in addition to switching at the nanosecond carrier lifetime limit of the tunable laser to reduce network overheads, control systems are also required to prevent transmission penalties caused by thermal effects on the millisecond scale that occur in response to high tuning current switches. The magnitude of these transmission penalties are set by the wavelength stability of the transmitter and the bandwidth of the core network wavelength routers. Similarly, the timescale of the EDFA gain dynamics determined by the erbium lifetime, result in a gain reconfiguration that is also measured in milliseconds. In dynamic networks, this means that gain transients occur in response to input power fluctuations typical of burst-switched data that are particularly crucial for Type II OBS networks. These transients may be reduced by electronic or optical control loops or compensated for at the receiver by real time processing. The results presented show that with consideration of these timescales and the inter-dependence of the key sub-systems, physical layer implementation of dynamic burst-switched optical networks is feasible.

7.1 Research summary

A survey of the main categories of optical network architecture, (OPS, OBS and WRONs) was carried out and the key sub-systems required for their implementation were identified. It was revealed that the characteristics of the key sub-systems and their component technologies are common among many of the proposed dynamic network architectures with the primary difference being the network reconfiguration time. Hence, although Type II OBS architectures were the focus of the research, the results may be equally applicable to OPS, WRONs and PONs.

For the wavelength-agile transmitter, housed in the edge router, it was found that the required performance in terms of wavelength switching time, tuning range and practical implementation left only widely tunable semiconductor lasers as a realistic candidates. The main multi-section tunable laser designs proposed to date were investigated using an automated characterisation technique which showed that detailed device specific characterisation is crucial for identification of sets of operating points with desirable switching characteristics across the desired tuning range.

The investigation of the switching characteristics was then focused on the more common and available DBR-based devices and quantified the problems of adapting these lasers for dynamic optical networks. It was found that that the emission of spurious lasing modes during the switching transition generates background crosstalk across its entire tuning range of over 50 nm. Using the probe channel BER measurements developed in this work, to replicate a WDM system, it was found that this crosstalk can cause severe impairment to other WDM channels. Additionally, the impact of long-term wavelength drift, caused by high current switching, in WDM networks was investigated in terms of interference on adjacent channels and on the burst channel, for the first time. The typical laser and TEC thermal time constants, in the ms regime, mean that this effect is particularly important over the timescales envisaged for Type II OBS networks and overlooked in studies focusing on shorter burst length schemes. Further probe channel BER measurements showed that wavelength drift due to high current switching in SG-DBR lasers can interfere with

neighbouring channels separated by 50GHz. Finally, the signal impairment caused by thermal wavelength drift on the burst channel itself as it passes through narrow wavelength routers was investigated with novel BER measurements. Q-factor penalties of up to 3dB were observed with a standard AWG router with 100GHz channel spacing due to thermal wavelength drift. For the 25GHz router, a Q-factor penalty of 16dB was observed. For a 1dB Q-factor penalty, it was found that wavelength drift of up to 2GHz was required for a minimal penalty in 50GHz and 100GHz spaced WDM system compared to 1GHz for a 25GHz spaced system. These results are important because they quantify the requirement of the control systems required to address these problems in burst transmitters.

Hence, these impairments were addressed in the development of a tunable burst transmitter, based on a DS-DBR device, which is suitable for DONs and described in chapter 3. The transmitter, capable of switching between 80 x 50GHz-spaced ITU channels, used SOA blanking to block the emission of switching crosstalk and employed a wavelength locking control loop based on an integrated wavelength locker and PI control circuit optimized using a linearised theoretical model. The switching time of the transmitter, including blanking and wavelength locking was 5μs for all the switching events measured. The loop locking time alone was 2μs limited by the bandwidth of laser current drivers. The wavelength stability was measured to be less than 1GHz below that required for a 25GHz spaced WDM system calculated in chapter 2. These results are a three order of magnitude improvement in locking speed and five-fold increase in wavelength stability over previous experimental demonstrations with DS-DBR lasers as shown in chapter 3.

To address the problems of burst data reception, a new kind of burst-mode receiver was developed to meet the needs of dynamic optical networks. The receiver allowed the use of an AC coupled photo-detector without the penalty caused by base line wander resulting input power fluctuations characteristic of burst data. The receiver used asynchronous digital sampling at twice the bit rate and digital signal processing to implement an adaptive equaliser to correct for

base line wander caused by AC-coupling in the receiver signal path and other impairments.

The characterisation of the digital burst-mode receiver (DBMRx) showed that no measurable penalty is observed when operating the receiver in burst-mode compared to continuous operation with the only necessary overhead being the 32bit preamble. Additionally, the receiver was able to cope with fluctuations of ±14MHz in the asynchronous sampling rate. Without any burst equalisation before the ADC the dynamic range of the receiver in burst-mode was measured to be 7dB for a 1dB penalty in required OSNR for a BER>10^{-3} limited by the quantisation noise at the ADC. Initially electrical burst equalisation was investigated using bursts of equal power to remove the clipping effect caused by AC-coupling in adjacent bursts with large power variations. This technique eliminated the limitation of quantisation noise and made the receiver sensitivity the limiting factor to the receiver dynamic range. Next, optical burst equalisation, based on drive current control of an SOA, was shown to increase the dynamic range for burst-to-burst power variations to over 16dB. This figure was approximately equal to the sum of the 7dB quantisation noise limited dynamic range and the SOA gain. Finally, both electrical and optical gain control were employed to recover adjacent bursts with up to 28dB power variation, the largest measured burst-to-burst dynamic range measured to date. The limitation to further dynamic range improvement in this case was both the photodiode sensitivity and the optical and electrical amplifier gain. The guard band of 100ns used for all measurements was a limited by the tuning speed of the transmitter and subsequently has potential for further reduction.

The design of the developed receiver was able to meet all the requirements of Type II OBS networks and the short preamble and guard band make this type of receiver applicable to other dynamic optical network architectures including OPS and PONs. The diverse range of applications and BMRx designs mean that no single performance metric exists for comparison of the BMRx but the burst efficiency (ratio of usable payload to control information) was 99.8%, the highest of all published BMRx studies.

In the network core, the question of gain transients caused input power fluctuations in EDFAs was addressed with a full experimental investigation of optically gain-clamped EDFAs in the context of a dynamic burst switched network. The investigation, described in chapter 5, used a realistic network scenario, incorporating the burst transmitter and receiver, to optimize GC-EDFA performance by measuring the signal quality of transmitted bursts. This new approach identified feedback cavity loss as the key control parameter in minimizing the BER of transmitted bursts and showed that the optimum feedback level occurs where the feedback channel is just able to lase with all channels present and not in the region of high gain compression, the focus of much of the previous work.

The results presented showed that optimum performance depends on a number of network-wide parameters. For a single GC-EDFA between 2 core routing nodes with burst add/drop, the results show that for a given feedback wavelength and input power fluctuation, there is an optimum feedback level for which the received signal quality, quantified by the Q-factor, is maximised. The amount of optical feedback required to suppress gain transients is dependent on the magnitude of the input power fluctuations. Hence, for a given GC-EDFA the required optical feedback may be determined by the limits of physical network parameters such as the port count at a preceding router or number of wavelengths used in the network. The optimum choice of feedback wavelength occurs at the 1528nm gain peak as this minimizes the feedback power required to provide transient suppression whilst maximizing the gain for the signal channels. It also allows the entire C-band and the flatter part of the EDFA spectrum to be used for signal channels.

Finally, the interoperability of each of the sub-systems was tested in a recirculating loop transmission experiments. In contrast to previous GC-EDFA studies, the OBS link model used allowed bursts to be added and dropped asynchronously at each node. It was shown that additional optical feedback is required to compensate for the gain transients that accumulate in propagating bursts along a network path. The accumulation of power transients shifted the optimal FCL by 0.3dB for each node hop. This result is important since it implies

that the feedback cavity design can also limit the number of hops a burst is able to traverse and ultimately limit the network size.

Using the same OBS link test-bed, the capability of the BMRx to use digital signal processing to compensate for base line and amplitude fluctuations was then exploited to reduce the requirement for optical feedback in OBS network paths. Compared to a standard fixed threshold receiver the DBMRx use of an adaptive threshold allowed a 6 fold reduction in the amount of additional optical feedback required at each amplifier. This improvement allows for both an increase in the span length, by 39% for a 25 node network, and the maximum number of hops for the same feedback cavity loss and Q-factor penalty. It was also shown that for most networks, where transmitted bursts experience fewer than 5 hops, the use of the DBMRx can remove the requirement for optical feedback to suppress gain transients. This is a significant result since compensating for the transmission impairment at the receiver would allow for significant component savings and allow for maximum signal channels gain, increasing the achievable length of each fibre span.

Overall, the results presented demonstrate that it is possible to develop sub-systems, based on existing technology, to solve existing problems and meet the demands of Type II OBS networks. These sub-systems have been shown to interact successfully on the timescales of a Type II OBS network in the first experimental demonstration of a WR-OBS network architecture, but may equally be adapted to meet the demands of other dynamic optical network architectures. Although there is scope for further development of the sub-systems described, the results presented in this thesis show that the physical layer implementation of the networks investigated is feasible for networks of up to 25 nodes.

7.2 Future work

For each of the key sub-systems described, there exist a number of avenues for further study and extension of the work presented. At the transmitter, attention should focus on improvements to the laser current drivers. Both the switching and locking of the burst transmitter described in chapter 3 was limited to the microsecond regime by driver bandwidth limitations. As demonstrated in the

fast switching measurements in chapter 2, improving the driver bandwidth can push the switching time to the fundamental carrier lifetime limit in the nanosecond regime and broaden the application range of the transmitter to the shorter burst length regimes of Type I OBS or optical packet switching. This work is currently underway and initial results have shown record switching times of under 10ns for DS-DBR lasers and it hoped that the rest of the burst-mode transmitter functionality will scale to these new timescales. Secondly, as previously reported for SG-DBR lasers, the operating points of the devices could be stored on a FPGA or programmable chip to enable construction of a software controlled module. This work will have significant impact on the type of system experiment possible using the existing test-bed. For example, improvements in switching time allows reduction of the guard band required at the receiver and the ability to program long sequences of varying power bursts allows better characterization of the both GC-EDFA and DBMRx in a more realistic context.

At the receiver, a number of areas for further research remain. The receiver was characterized for all input power variations in a worst case scenario by generating alternating bursts of maximum power variations. However, the experimental set-up used was only able to receive relatively few adjacent bursts due to storage limitation of the real-time oscilloscope and processing requirements of the offline DSP with a single machine. Whilst this allowed study of the received bursts by measurement of the BER of the received payload, the measurements were only based on bursts where the header detection based on reception of the preamble had been successful and did not allow measurement of the percentage of bursts lost due to corruption of the burst preamble. As currently being investigated, measurement of the burst loss probability is possible by improving the post processing procedure to enable reception of bursts in sufficient numbers to measure the burst lost probability (BLP).

To enable this, the processing time need to be reduce from minutes to seconds or below and may also use distributed computing resources to process many received bursts simultaneously. Significant reductions in the required processing may be obtained by only considering the burst control information since, as shown in chapter 4, the BER of received payloads can be accurately

predicted from the signal-to-noise ratio once a burst is successfully detected. Measurement of the BLP would allow better optimization of the receiver software implementation and allow an investigation of the required preamble length and minimum burst overhead.

The results reported for an experimental prototype of a digital receiver with the DSP performed offline but the possibility of a real time hardware implementation remains. A real time receiver would require not only sufficient processing power but a real-time ADC able to operate at twice the bit rate and it is the availability of these components that is the biggest limitation to a hardware implementation. Currently a hardware implementation based on commercially available products could be possible with a programmable FPGA and high-speed ADC which are currently available at speeds up to 12.5GS/s enabling a DBMRx suitable for bursts with 6.35Gb/s data payloads.

In the network core, there is a need to quantify the benefits of optical gain clamping compared to other gain clamping techniques in terms of the required optical components, gain reductions and induced impairments. These features may vary with the specific network context. Specifically concerning the GC-EDFA, it would be interesting to investigate the possibility of varying the feedback cavity design across the link. The use of the recirculating loop meant that the same amplifier was used for all node hops across the link making individual cavity design impossible. Since, the impairments were shown to accumulate across the link the optical feedback required to completely suppress gain transients is likely to vary as a function of number of hops. Hence, the signal gain and, subsequently, transmission distance could be maximized by individually setting the FCL of each link amplifier. The review of wavelength routers revealed that only passive optical routers such as AWGs or grating routers are suitable for both OBS and OPS networks due to the rigid timing constraints. Hence, future work on the routing nodes could consider the feasibility and optimisation of wavelength conversion, which could be based on the same technology as the burst transmitter, at all or some of the core routing nodes.

Appendix A GCSR and MG-Y tunable lasers

A.1 Operation of tunable lasers – GCSR and MG-Y

This section describes the operation principles of the less common widely tunable semiconductor lasers, the grating coupler with rear sampled grating reflector (GCSR) and the modulated grating- Y-branch (MG-Y) lasers. Samples of these devices were characterised using the set-up described in section 2.2 and the summary data appears in section 2.2.3.

A.1.1 GCSR

The GCSR laser has an operation principle similar to the DS-DBR. It has a widely tunable coupler transmission peak to select one of the reflected peaks from a rear sampled grating for lasing [Wes01, Wes02a]. A schematic of the GCSR laser design is shown in Figure A-1. The corresponding reflectance spectra of the main tuning sections are shown in Figure A-2. The advantage of the GCSR design is that the output light does not to pass thought the front reflector which has been shown to cause tuning current dependent absorption in SG-DBR lasers that leads to output power variations across the tuning range of several dB. However, the long cavity required for the coupler, reduces the cavity mode spacing and reduces the achievable side mode suppression ratio [Wes04].

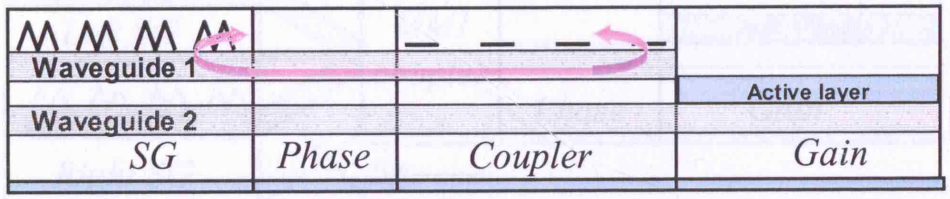

Figure A-1 Schematic of GCSR tunable laser

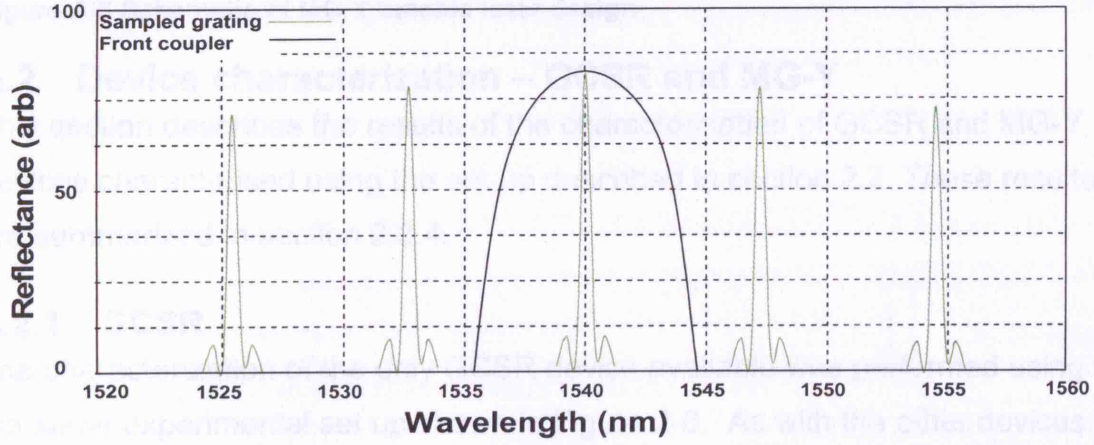

Figure A-2 Reflectance spectra of front coupler and rear sampled grating in GCSR tunable laser

A.1.2 MG-Y

The aim of solving the power uniformity problem caused by tuning current dependent absorption in the tuning sections without compromising the achievable SMSR led to development of the modulated grating Y-branch (MG-Y) laser diode. These devices operate in a similar manner to the SG-DBR but with the 2 sampled gratings joined to the gain and common phase section with a multi-mode interferometer in structure similar to half of a Mach-Zender interferometer [Kus93, Wes02], as shown in Figure A-3. In such an interferometric design problems of wavelength control and stability lead to a trade-off between tuning range and achievable SMSR [Ama98f]. Despite this such devices have been demonstrated with attractive output power, SMSR and power uniformity characteristics [Wes04]. As with the state of the art versions of all the lasers described thus far, the problem of carrier density dependent absorption in the tuning sections that leads to power variations across the tuning range may be solved by inclusion of an external SOA outside the laser cavity but how coherency between the 2 reflector arms is solved is unclear. An MG-Y laser has not yet been used in experimental dynamic optical networking studies although the ability to reliably measure reflector currents enables unique wavelength stabilization techniques, as discussed in chapter 3.

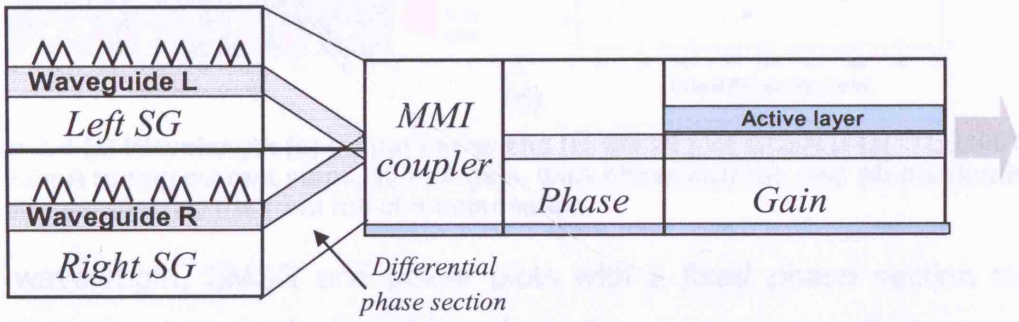

Figure A-3 Schematic of MG-Y tunable laser design

A.2 Device characterization – GCSR and MG-Y

This section describes the results of the characterisation of GCSR and MG-Y devices characterised using the set-up described in section 2.2. These results are summarized in section 2.2.4.

A.2.1 GCSR

The characterization of the only GCSR device available was performed using the same experimental set up shown in Figure 2-6. As with the other devices an initial analysis of the tuning characteristics was obtained by studying the

impact of the primary tuning sections, front coupler and reflector, without tuning of phase and gain currents. Figure A-4 shows the wavelength, power and SMSR plots with varying tuning section currents and the summary plot including additional phase control using the same operating point selection algorithm described in section 2.2.2.

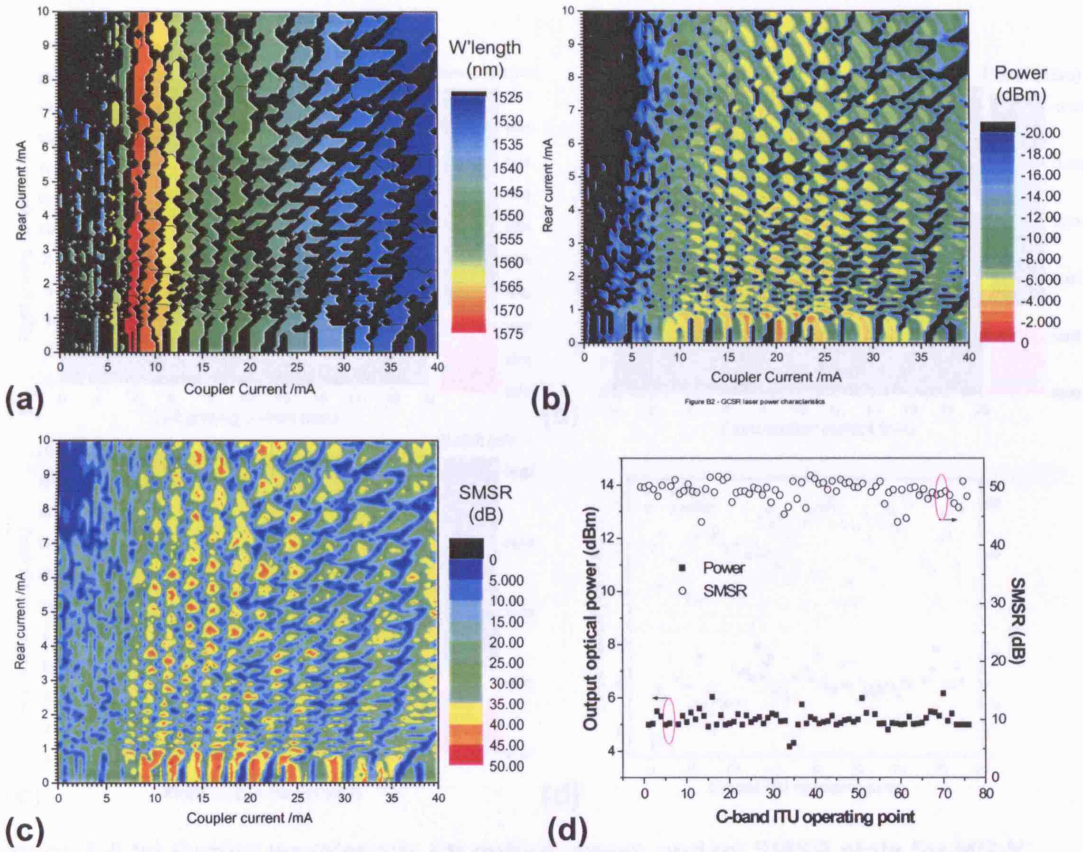

Figure A-4 (a) Wavelength (b) output power and (c) SMSR plot GCSR laser (TLG1001) with 0.2mA tuning current steps, 100mA gain, 5mA phase current. And (d) distribution of C-band operating points from full characterisation

The wavelength, SMSR and power plots with a fixed phase section current show how the design principle of broad coupler and sampled reflector provide a different tuning map structure. As with the SG-DBR and MG-Y lasers the wavelength plots show regions of similar wavelength output separated by longitudinal and super mode boundaries but because the front coupler operates to select a sub-band from the wavelength comb generated by the rear sampled grating reflector, the super-mode boundaries are vertical, meaning that tuning within a single super-mode is possible with only 1 tuning current. Such a feature can be attractive for simplifying device characterization algorithms.

A.2.2 MG-Y

The operating point summary shows that the output power of the device was around 10dB below that of the other DBR based lasers with a standard deviation of output power and SMSR across the C-band being 0.32 and 3.26. A comparison and discussion of all the device characterizations is provided in section 2.2.4.

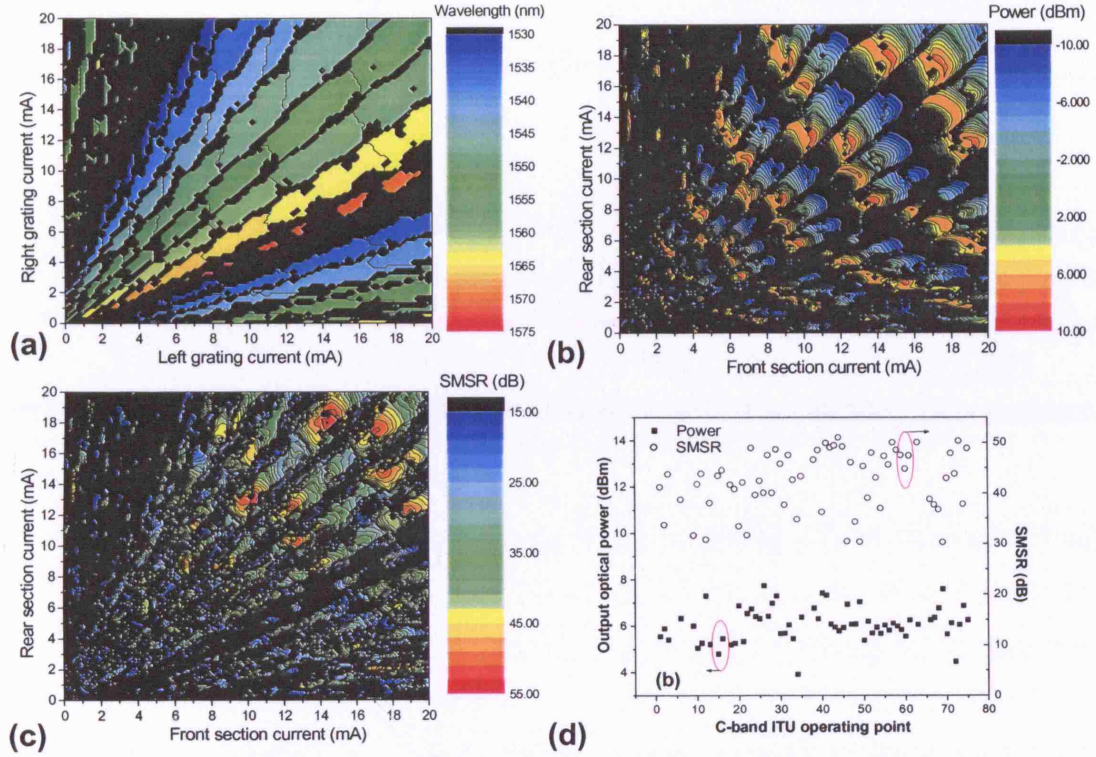

Figure A-5 (a) Output wavelength, (b) output power, and (c) SMSR plots for MG-Y (TLY1001) with 0.2mA tuning current steps, 150mA gain and 0.5mA phase current, (d) distribution of C-band operating points

The primary difference between the wavelength plot shown in Figure 2-7 is the width of the super-mode boundaries which show that when mode competition exists between 2 adjacent reflector peaks the SG-DBR is more able to suppress competing modes to select a single lasing wavelength. This is also evident in the output power and SMSR plots, which shows that although the maximum output powers are similar for both lasers, the SG-DBR is able to maintain higher output powers and SMSR closer to the super-mode boundary.

This is reflected in the distribution of operating points for both devices. Using this method acceptable operating points were identified at 75 of the 76 C-band ITU wavelengths were identified for the SG-DBR laser compared to 65 for the MG-Y device. In addition to accessing more ITU wavelengths across the C-

band the characterisation results show greater uniformity of both power and SMSR. The standard deviation of output power was 0.3 for the SG-DBR compared to 1.72 for the MG-Y. The standard deviation of SMSR was 0.74 for the SG-DBR compared to 5.96 for the MG-Y. A comparison of all the devices characterized with the best published studies is given in Table 2-4.

All references from this appendix can be found in section 2.8.

Appendix B Derivation of optimal control coefficients

B.1 Generating the photocurrents

The integrated wavelength locker design, shown in Figure B-1(a), uses a transflective etalon to split the signal between 2 photodiodes (PD), one each for the transmitted and reflected signals.

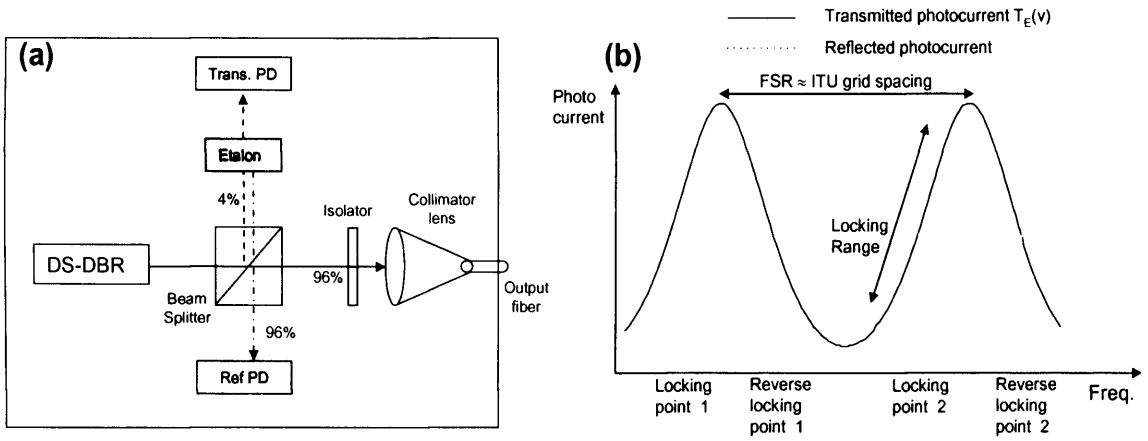

Figure B-1(a) Schematic of DS-DBR laser package containing DS-DBR and internal wavelength locker and (b) transmission spectra for transmitted and reflected photodiodes

At the laser output, a beam splitter is used to direct 4% of the optical signal generated by the laser sections to the etalon which further splits the signal into transmitted and reflected components. The etalon is designed to generate 2 photocurrents at the photo-detectors which are approximately equal at the locking points which are periodic and equally spaced in frequency. For the transmitted etalon response $T_E(\nu)$, shown in Figure B-1(b), the photocurrents of the 2 photodiodes (i_{tra} and i_{ref}) can be as a function the instantaneous optical frequency (ν) which is a small fraction, α_s, tapped from the laser output.

$$i_{trans}(\nu) = \alpha_s P_0 R_{tra} T_E(\nu) = i_{tra} T_E(\nu) \quad \textbf{(B.1)}$$

$$i_{ref}(\nu) = \alpha_s P_0 R_{ref}[1 - T_E(\nu)] = i_{ref}[1 - T_E(\nu)] \quad \textbf{(B.2)}$$

Where P_0 is the output optical power, $R_{E1,2}$ are the photodiode responsivities, and $T_E(\nu)$ is an ideal Airy function defined as:

$$T_E(\nu) = \frac{1}{1 + F_E \sin^2(\pi \frac{\nu - \nu_{ITU}}{\Delta\nu_{ITU}} - \phi_{ITU})} \quad \textbf{(B.3)}$$

Where ν_{ITU} is an ITU-T grid frequency, $\Delta\nu_{ITU}$ is the ITU grid spacing, ϕ_{ITU} is a phase shift term to ensure an ideal match with the ITU grid and F_E is the etalon finesse. The finesse (r_E) is a measure of the sharpness of the transmission

peaks and equivalent to the extinction ratio between maximum and minimum transmission, defined for a normalised maximum power as:

$$r_E = \frac{\max\{T_E(\nu)\}}{\min\{T_E(\nu)\}} = \frac{1}{\min\{T_E(\nu)\}} \quad \textbf{(B.4)}$$

The phase term and finesse parameter in equation (B.3 can be obtained by imposing the simple boundary conditions. Firstly, the extinction ratio must match the one specified in the device datasheet, that is

$$\min\{T_E(\nu)\} = \frac{1}{1+F_E} = \frac{1}{r_E} \quad \textbf{(B.5)}$$

$$\text{Thus, } F_E = r_E - 1 \quad \textbf{(B.6)}$$

And secondly, since the photocurrent are designed to be equal at the locking point we can say

$$[1 + F_E \sin^2(\phi_{ITU})]^{-1} = 1 - [1 + F_E \sin^2(\phi_{ITU})]^{-1} \quad \textbf{(B.7)}$$

Which by rearrangement gives $F_E \sin^2(\phi_{ITU}) = 1$ and an expression for the phase term of:

$$\phi_{ITU} = \sin^{-1}\left(\sqrt{1/F_E}\right) \quad \textbf{(B.8)}$$

B.2 Control circuit

The next stage is to develop the input to the wavelength locking circuitry. The structure of the proposed feedback loop is shown in Figure 3-3.

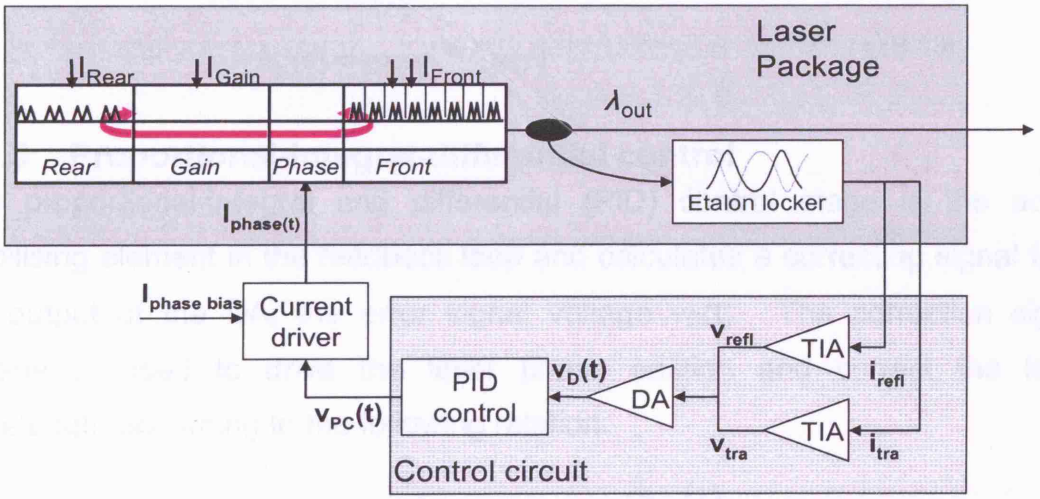

Figure B-2 Structure of wavelength locking loop comprising integrated wavelength locker and proposed control circuit

With the loop enabled the photocurrents are a function of the laser output frequency which by the compensating action of the loop become a function of

time. Hence, to simplify later expressions the photocurrents are expressed only as function of time.

B.2.1 Transimpedance amplifier stage

The first stage is the transimpedance amplifier (TIA) stage that converts the currents to time dependent voltage signals, $v_{tra}(t)$ and $v_{ref}(t)$, expressed as:

$$v_{tra}(t) = R_{tra}.i_{tra}(t) * h_T(t) \quad \text{(B.9)}$$

$$v_{ref}(t) = R_{ref}.i_{ref}(t) * h_T(t) \quad \text{(B.10)}$$

Where $R_{T1,2}$ are the transimpedance values which are assumed equal and $h_T(t)$ is the impulse response of a single pole low pass filter with cut-off angular frequency $\omega_T=2\pi f_T$ introduced to represent the bandwidth restriction of the TIAs

$$h_T(t) = \omega_T.e^{-\omega_T.t}.u(t) \quad \text{(B.11)}$$

B.2.2 Differential amplifier

The differential amplifier (DA) calculates a voltage, $v_D(t)$, which is proportional to the difference between the 2 TIA voltages, v_{T1} and v_{T2} from the wavelength locker. In addition to calculating the difference between the inputs ($v_D(t)$) the DA also provides am amplification factor (G_D) and has a zero value at an ITU wavelength.

$$v_D(t) = G_D[v_{tra}(t) - v_{ref}(t)] \quad \text{(B.12)}$$

$$h_T(t) = \omega_T.e^{-\omega_T.t}.u(t) \quad \text{(B.13)}$$

B.2.3 Proportional-integral-differential control

The proportional-integral and differential (PID) control stage is the active stabilising element in the feedback loop and calculates a correcting signal from the output of the DA, the error signal voltage $v_D(t)$. The correction signal voltage is used to drive the laser phase section and correct the laser wavelength according to the following relation:

$$v_{PC}(t) = k_P v_D(t) + k_I \int_{t_{RST}}^{t} v_D(t)d\tau + k_D \frac{\partial v_D(t)}{\partial t} \quad \text{(B.14)}$$

where K_P, K_I and K_D are the coefficients for proportional, integral and differential controls and weight the contribution of each control to the final phase section tuning correction.

The phase correction voltage V_{PC} is then passed through the current driver (CD) which converts the signal and applies the appropriate conversion to match it to tuning characteristics of the laser phase section. The CD also applies any bias current, usually the original tuning current, I_P.

$$i_P(t) = I_P + G_P.V_{PC}(t) * h_P(t) = I_P + i_{PC}(t) \quad \textbf{(B.15)}$$

where G_P is the conductance gain and h_p is the bandwidth limitation of the current driver modelled as a low pass filter step response

$$h_P(t) = \omega_P.e^{-\omega_P.t}.u(t) \quad \textbf{(B.16)}$$

B.3 Linearising the WLL

In order to optimise the performance of the wavelength locking loop and derive optimal values for the PID coefficients it was first necessary to simplify the analytical model. The first stage of this was to assume a simple linear model for the wavelength locking loop described thus far.

The electrical components of the loop, the TIAs, DA and current driver may be assumed to be linear by the relationships described in equation (B.9) to (B.15) but this is not the case for the laser phase section or the etalon response. However, these loop elements only need to operate linearly in specified operating range around the locking point. This locking range was determined experimentally using DS-DBR laser (TLD1001) by studying the phase section tuning characteristics and the measured response of the etalon locker as shown in Figure B-3.

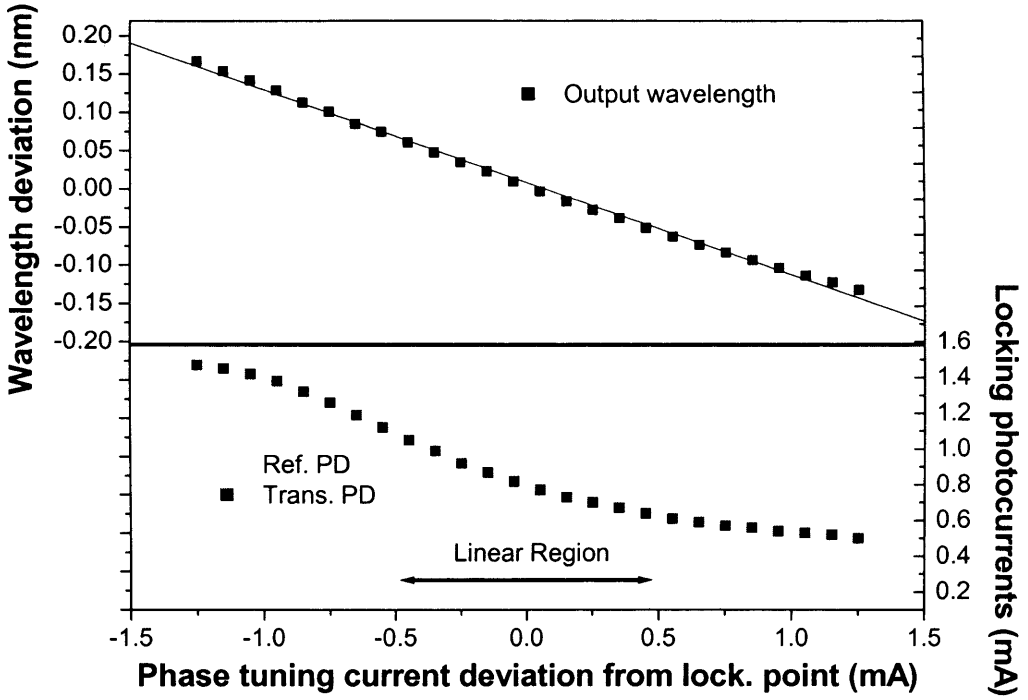

Figure B-3 Linearization of phase section and etalon response with phase section tuning current

Figure B-3 shows the measured wavelength deviation locker photocurrents as a function of phase section current around an ITU locking point. The phase section tuning current is seen to be approximately linear across the entire measured range which is limited at the extremes by degraded SMSR and ultimately by a cavity mode hop. Over this range the wavelength deviation may be written linearly as a function of the phase section tuning current i_{PC} with slope k_{ph}.

$$\Delta\lambda_P(t) = k_{ph} i_{PC}(t) \tag{B.17}$$

The etalon response may also be assumed linear over smaller range corresponding to 1mA tuning current range or a wavelength deviation of almost 0.2nm (25GHz) which is almost twice the largest measured wavelength deviation for the same device in chapter 2. Hence, the etalon response can be considered linear around the ITU wavelength in question with the slope calculated from the derivative of the etalon spectral response given in equation (B.3) with respect to the carrier frequency ν at one of the crossing points and assuming $i_E = i_{tra} = i_{ref}$.

$$k_{E_V} = \left.\frac{\partial i_{E1}(v)}{\partial v}\right|_{v=v_{ITU}} = \left.\frac{\partial i_{E2}(v)}{\partial v}\right|_{v=v_{ITU}}$$
$$= -\frac{2\pi I_E F_E \sin(\phi_{ITU})\cos(\phi_{ITU})}{\Delta v_{ITU}(1+F_E \sin^2(\phi_{ITU}))^2} \quad \textbf{(B.18)}$$

The slope of the etalon may then be translated into a wavelength expression as follows:

$$k_{E\lambda} = -\frac{v_{ITU}^2}{c} k_{Ev} \quad \textbf{(B.19)}$$

This then enables rewriting of the expressions for the photocurrents (B.1) and (B.2) in a linear form by substituting for the non-linear Airy expression:

$$i_{tra}(t) = \frac{1}{2} I_E + k_{E\lambda} \Delta\lambda_O(t) \quad \textbf{(B.20)}$$

$$i_{ref}(t) = \frac{1}{2} I_E + k_{E\lambda} \Delta\lambda_O(t) \quad \textbf{(B.21)}$$

Assuming linear performance of all of the elements of the feedback loop allows treatment of the feedback loop as a standard negative feedback scheme with system and control blocks. The periodic nature of the etalon locker allows modelling of a general case in which all wavelengths in this model are expressed as deviations from the nearest ITU wavelength with the wavelength correction induced by phase section tuning current correction, $\Delta\lambda_P$, being an adjustment to initial lasing wavelength $\Delta\lambda_L$ to give the instantaneous lasing wavelength $\Delta\lambda_O$. For this model, as developed below, the instantaneous lasing wavelength $\Delta\lambda_O$ may be considered the input to the system block comprising etalon, TIAs and DA using standard control theory [Bro91]. The differential signal voltage in turn may be considered the input to the control block comprising the PID control and current driver.

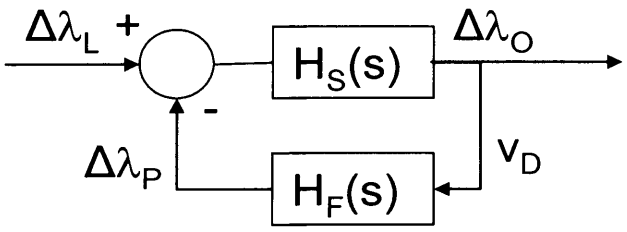

Figure B-4 Linearised model of wavelength locking control loop

Once linearised, with all key parameters expressed as a function of time the variables described thus far may be written in the Laplace domain and ultimately formulated in to a single loop transfer function from which the

optimum control coefficients may be derived. For example the etalon photocurrents become:

$$i_{tra}(s) = \frac{1}{2} I_E + k_{E\lambda} \Delta\lambda_O(s) \quad \textbf{(B.22)}$$

$$i_{ref}(s) = \frac{1}{2} I_E + k_{E\lambda} \Delta\lambda_O(s) \quad \textbf{(B.23)}$$

Whilst the voltage output of the TI and differential amplifiers become:

$$V_{tra}(s) = R_{T1} H_T(s) I_{E1}(s) \quad \textbf{(B.24)}$$

$$V_{ref}(s) = R_{T2} H_T(s) I_{E2}(s) \quad \textbf{(B.25)}$$

$$V_D(s) = G_D[V_{T1}(s) - V_{T1}(s)] \quad \textbf{(B.26)}$$

This gives an expression for voltage output of the PID controller of

$$V_{PC}(s) = (k_P + \frac{k_I}{s} + k_D s) V_D(s) \quad \textbf{(B.27)}$$

and current output of the current driver and wavelength correction of:

$$I_{PC}(s) = G_P H_P(s) V_{PC}(s) \quad \textbf{(B.28)}$$

$$\Delta\lambda_P(s) = k_{ph} I_{pc}(s) \quad \textbf{(B.29)}$$

Where $H_T(s)$ and $H_P(s)$ are the transfer functions of the transimpedance amplifiers and the current drivers given in equation (B.30) and (B.31).

$$H_T(s) = L\{h_T(t)\} = \frac{\omega_T}{s + \omega_T} \quad \textbf{(B.30)}$$

$$H_P(s) = L\{h_P(t)\} = \frac{\omega_P}{s + \omega_P} \quad \textbf{(B.31)}$$

The remaining elements of the feedback path without a specific bandwidth limitation are included in a general feedback block with a transfer function $H_f(s)$

$$H_F(s) = \frac{\Delta\lambda_P(s)}{\Delta\lambda_O(s)}$$

$$= k_F \frac{k_D s^2 + k_P s + k_I}{s} \frac{\omega_T}{s + \omega_T} \frac{\omega_P}{s + \omega_P} \quad \textbf{(B.32)}$$

Where k_F is a general coefficient covering the physical parameters of the remaining loop elements:

$$k_F = 2 k_{eta} k_{ph} k_{E\lambda} G_P G_D R_T \quad \textbf{(B.33)}$$

With k_{eta} being a coefficient describing the type of etalon and taking a value of 1 for the transflective etalon used in the DS-DBR.

The feedback loop transfer function, equation. (B.32), may be simplified by imposing a condition on the bandwidth of the entire loop based on the assumption that all loop elements will operate with a low pass cut off frequency of the entire loop equivalent to a generic loop angular frequency ω_L equivalent to both ω_T and ω_P.

$$H_F(s) = k_F \frac{k_D s^2 + k_P s + k_I}{s} \frac{\omega_L^2}{(s+\omega_L)^2} \quad \textbf{(B.34)}$$

This may then be used to define a transfer function for the entire wavelength locking loop, H_L, acting on the initial lasing wavelength $\Delta\lambda_L$.

$$H_L = \frac{\Delta\lambda_o(s)}{\Delta\lambda_L(s)} = \frac{1}{1+H_F} \quad \textbf{(B.35)}$$

Which by substitution of the expression for H_F becomes:

$$H_L = \frac{s(s+\omega_L)^2}{s(s+\omega_L)^2 + k_F\omega_L^2(k_D s^2 + k_P s + k_I)} \quad \textbf{(B.36)}$$

As discussed in chapter 2, a typical switching transition results in a region of mode competition before the estimate of the final lasing wavelength where it is desirable to block the laser output. Similarly, a WLL needs to be disabled over this region before being activated after the mode competition is over. At this point the wavelength deviation may be modelled as a step function having an expression in the Laplace domain of:

$$\Delta\lambda_L(s) = \frac{\Delta\lambda_0}{s} \quad \textbf{(B.37)}$$

Where, λ_0 is the initial wavelength deviation from the target wavelength when the loop is activated. Equation (B.37) may be then combined with the wavelength locking loop transfer function to give an expression for the output wavelength $\Delta\lambda_{out}\,(= H_L(s)\Delta\lambda(s))$:

$$\Delta\lambda_{out} = \frac{\Delta\lambda_0 s(s+\omega_L)^2}{s(s+\omega_L)^2 + k_F\omega_L^2(k_D s^2 + k_P s + k_I)} \quad \textbf{(B.38)}$$

B.4 Definition of locking time and target response

Equation (B.38) is important since it contains the control coefficients to be optimised and its equivalent in the time domain may be used to define the wavelength locking time, as shown in Figure B-5. The objective of the wavelength locking loop is to lock to the output wavelength in the shortest possible time. Hence, as with the definition of switching time defined in chapter 2, the locking time, t_L, may be defined such that the output wavelength falls and remains within a specified wavelength range, $\Delta\lambda_T$.

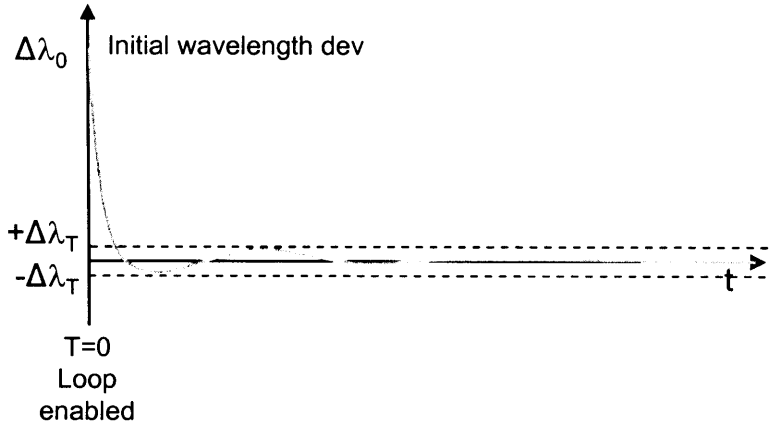

Figure B-5 Typical loop response to step wavelength deviation

Hence, at the instant the output wavelength is first within the locking range equation (B.38) may be set equal to this wavelength deviation ($\Delta\lambda_{OutT}(t_L) = \Delta\lambda_T$) and the optimal control coefficients, (and locking time) may be derived by comparison with a optimal target response to represent desirable locking characteristics.

This target response may be estimated from the initial conditions and the observed characteristic of PID control systems. In order to ensure a fast and non-oscillating response, the step response may be simplified to obtain a more manageable expression such as the single pole low pass expression in equation (B.39)

$$\Delta\lambda_{OutT}(t) = \Delta\lambda_0 e^{-\omega_N t} \qquad \textbf{(B.39)}$$

where ω_N is the natural angular frequency of the target low pass response. Hence, the formulation of the target function, equation ((B.39), allows the derivation of an expression for the minimum locking time which is defined at the

point where the target response reaches the specified wavelength deviation $\Delta\lambda_T$.

B.5 PID coefficient optimisation

By considering equation (B.39) in the Laplace domain by using the expression for the loop response already derived equation (B.38) and converting the target response it becomes possible to identify expressions for the optimal coefficients for PID controller by applying some simplifying assumptions. In the Laplace domain equation (B.39) becomes:

$$\frac{\Delta\lambda_0 s(s+\omega_L)^2}{s(s+\omega_L)^2 + k_F\omega_L{}^2(k_D s^2 + k_P s + k_I)} = \frac{\Delta\lambda_0}{(s+\omega_N)} \qquad \textbf{(B.40)}$$

This expression may then be used to derive expressions for the control coefficients K_P, K_I and K_D but first requires some additional manipulation and assumptions based on the matching condition. It should be noted that the denominator contains 2 terms. The first of which has a zero which is the loop frequency and the second of which is a polynomial containing the PID coefficients. If, it is assumed both terms have the same zeros, the step response may be simplified to an expression matching the target response. The zeros of the quadratic term may be determined by solving by the formula $k_D s^2 + k_P s + k_I = 0$ to give 2 frequency solutions ω_1 and ω_2 as follows

$$\omega_{1,2} = -\frac{-k_P \pm \sqrt{k_P^2 - 4k_D k_I}}{2k_D} \qquad \textbf{(B.41)}$$

Assuming a real solution that is also equivalent to the loop frequency ω_L we obtain the expression

$$k_D s^2 + k_P s + k_I = k_D(S+\omega_L)^2 \qquad \textbf{(B.42)}$$

This then allows extraction of the conditions:

$$\begin{aligned} k_P^2 - 4k_D k_I &= 0 \\ k_P / 2k_D &= \omega_L \end{aligned} \qquad \textbf{(B.43)}$$

This may then be substituted back into equation (B.38) to simplify it to:

$$\Delta\lambda_{Out}(s) = \frac{\Delta\lambda_0}{s + k_D k_F \omega_L^2} \qquad \textbf{(B.44)}$$

Equation (B.44) may then be equated to the target expression equation (B.40) to obtain an expression for the differential coefficient:

$$\omega_N = k_D k_F \omega_L^2 \quad \textbf{(B.45)}$$

This may then be combined with the conditions in equation (B.43) to give expressions for the proportional and integral coefficients.

$$k_P = \frac{2\omega_N}{k_F \omega_L} \quad \textbf{(B.46)}$$

$$k_I = \frac{\omega_N}{k_F} \quad \textbf{(B.47)}$$

$$k_D = \frac{\omega_N}{k_F \omega_L^2} \quad \textbf{(B.48)}$$

These expressions may be further simplified by the assumption that $\omega_L=\omega_N$. Hence, it is possible to obtain optimal values for the PID coefficients using the derived equations (B.46), (B.47) and (B.48).

$$k_P k_F = 2 \quad \textbf{(B.49)}$$

$$k_I k_F = \omega_L \quad \textbf{(B.50)}$$

$$k_D k_F = 1/\omega_L \quad \textbf{(B.51)}$$

B.6 PI control coefficient optimization

As can be deduced from equation (B.51) and is shown by numerical simulation in section 3.3, the differential coefficient in a PID control can become almost negligible for this application, being inversely proportional to the loop bandwidth. As a result, implementation of a PID control may be beyond practical implementation and it is, therefore, necessary to consider the optimal control coefficients of a PI control.

By following the same procedure as in the PID case the optimal proportional and integral coefficients may be derived. Without the differential coefficient, equation (B.38) can be re-written as:

$$\Delta\lambda_{out} = \frac{\Delta\lambda_0 s(s+\omega_L)^2}{s(s+\omega_L)^2 + k_F \omega_L{}^2 (k_P s + k_I)} \quad \textbf{(B.52)}$$

And the factor of $(s+\omega_L)$ can be simplified if:

$$k_P s + k_I = k_P(s+\omega_L) \Rightarrow \frac{k_I}{k_P} = \omega_L \quad \textbf{(B.53)}$$

Assuming that the proportional coefficient is non-zero, meeting this condition enables the step response equation (B.38) to be re-written as:

$$\Delta\lambda_{out}(s) = \frac{\Delta\lambda_0(s+\omega_L)}{s(s+\omega_L)+k_P k_F \omega_L{}^2} \tag{B.54}$$

This expression may then be reduced to the target step function by factorization of the denominator as:

$$s(s+\omega_L)^2 + k_P k_F \omega_L^2 = (s+\omega_N)^2 = s^2 + 2\omega_N s + \omega_N^2 \tag{B.55}$$

This can then be translated into the following 2 conditions:

$$\begin{aligned} \omega_L &= 2\omega_N \\ \omega_N^2 &= k_P k_F \omega_L^2 \end{aligned} \tag{B.56}$$

Equation (B.56) shows that a fixed relationship exists between the loop bandwidth and natural angular cut-off frequency that was not present in the PID case. The final optimised PI coefficients may then be obtained by combining equations (B.53) and (B.56) as follows.

$$k_P = 1/4k_F \tag{B.57}$$

$$k_I = \omega_L/4k_F \tag{B.58}$$